PATHOGEN IDENTIFICATION USING PEPTIDE NANOTUBE BIOSENSORS AND IMPEDANCE AFM

by

ROBERT I. MacCUSPIE

A dissertation submitted to the Graduate Faculty in Chemistry in partial fulfillment of the requirements for the degree of Doctor of Philosophy, The City University of New York

2006

UMI Number: 3231963

Copyright 2006 by
MacCuspie, Robert I.

All rights reserved.



UMI Microform 3231963
Copyright 2006 by ProQuest Information and Learning Company.
All rights reserved. This microform edition is protected against
unauthorized copying under Title 17, United States Code.

ProQuest Information and Learning Company
300 North Zeeb Road
P.O. Box 1346
Ann Arbor, MI 48106-1346

© 2006

ROBERT IAN MacCUSPIE

All Rights Reserved

Approval Page

This manuscript has been read and accepted by the
Graduate Faculty in Chemistry in satisfaction of the
dissertation requirement for the degree of Doctor of Philosophy.

Professor Hiroshi Matsui

Date — Chair of Examining Committee

Professor Gerald Koeppl

Date — Executive Officer

Professor Hiroshi Matsui

Professor C. Michael Drain

Professor Robert Engel
Supervision Committee

THE CITY UNIVERSITY OF NEW YORK

Abstract

PATHOGEN IDENTIFICATION USING PEPTIDE NANOTUBE BIOSENSORS AND IMPEDANCE AFM

by

Robert I. MacCuspie

Advisor: Professor Hiroshi Matsui

Pathogen identification at highly sensitive levels is crucial to meet urgent needs in fighting the spread of disease or detecting bioterrorism events. Toward that end, a new method for biosensing utilizing fluorescent antibody nanotubes is proposed. Fundamental studies on the self-assembly of these peptide nanotubes are performed, as are applications of aligning these nanotubes on surfaces. As biosensors, these nanotubes incorporate recognition units with antibodies at their ends and fluorescent signaling units at their sidewalls. When viral pathogens were mixed with these antibody nanotubes in solution, the nanotubes rapidly aggregated around the viruses. The size of the aggregates increased as the concentration of viruses increased, as detected by flow cytometry on the order of attomolar concentrations by changes in fluorescence and light scattering intensities. This enabled determination of the concentrations of viruses at trace levels (10^2 to 10^6 pfu/mL) within 30 minutes from the receipt of samples to the final quantitative data analysis, as demonstrated on Adenovirus, Herpes Simplex Virus, Influenza, and Vaccinia virus. As another separate approach, impedance AFM is used to study the electrical properties of individual viruses and nanoparticles used as model systems. The design, development, and implementation of the impedance AFM for an

Asylum Research platform is described, as well as its application towards studying the impedance of individual nanoparticles as a model system for understanding the fundamental science of how the life cycle of a virus affects its electrical properties. In combination, these approaches fill a pressing need to quantify viruses both rapidly and sensitively.

Acknowledgements

This work could not have been successfully completed without generous assistance from many sources, including several people and funding sources.

The author would like to thank advisor Professor Hiroshi Matsui for his guidance and leadership by example. Tremendous challenges were overcome with his suggestions and understanding, all while his example of how to be a successful scientist quietly led the way. The author would also like to thank the members of the thesis advisory committee including chair Prof. Hiroshi Matsui, and Prof. C.M. Drain of Hunter College/CUNY, Prof. Huixin He of Rutgers University, Prof. Robert Engel of Queens College/CUNY, and Dr. Phil Krause of FDA/CBER. Their continued thoughtful suggestions provided a pathway to building more convincing results.

The author would like to thank the faculty in the Hunter College Chemistry Department. The author would especially like to acknowledge the tremendous assistance from the Graduate Student advisor Prof. Klaus Grohmann.

The author would like to acknowledge all of the assistance from the esteemed colleagues in Professor Hiroshi Matsui's research lab, including past and present graduate students Dr. Lingtao Yu, Yung-fou "Chris" Chen, Precila Poratta, Nurxat Nueraji, Stewart Hung, Chris Pejoux, Hanying Bai, Germaine Muniz, Laurence Bensaid, and Lillian Yuan, past and present undergraduate students Jacopo Samson, Amit Haboohsheh, and Andy Chen, and past and present postdoctoral researchers Dr. Ipsita Banerjee, Dr. Ramin Djalali, Dr. Xueyun Gao, Dr. Chris Spedaliere, Dr. Anne Runge, Dr. Sang-Yup Lee, and Dr. Linglu Yang. The author would also like to acknowledge the assistance from colleagues in Professor C.M. Drain's research lab, including graduate

students Jacopo Samson, Giorgio Bazzan, Gabreilla Smeureanu, Ija Likhtina, Alex Falber, Ivana Radivojevic, and AlessandroVarotto. The author would also like to acknowledge fellow graduate student Stephanie Wolfe for help proofreading and insightful discussions, as well as insightful discussions with fellow graduate students Stewart Bachan, Tal Hassan, and Amanda Pustam.

The author would like to acknowledge the exciting collaboration with Asylum Research, including contributions from David Beck, Keith Jones, Jason Li, and Jason Bemis in developing the impedance AFM for the Asylum Research MFP-3D AFM platform.

The author would like to acknowledge Dr. Jackie Muller for instrument time at the FDA TEM Imaging Facility, and Howard Mostowski for tremendous assistance with the flow cytometry data collection and interpretation. The author would like to thank Andrea Bertke for the gracious donation of the HSV-1 and HSV-2 native and GFP mutant viruses, as well as Amita Patel, Dr. Geetha Jayan, and Dr. J.P. McWatters for insightful discussions. Also, Drs. Andrew Lewis, Zhiping Ye, and Michael Merchlinsky (all at FDA/CBER), for generous donation of virus stocks used in these studies.

The author would like to thank the Queens College Core Imaging Facility for extensive use of the Transmission Electron Microscope. The author would like to thank Dr. Karl Fath and Dr. Areti Tsiola of the Queens College Biology Department for their time and effort in maintaining and troubleshooting the TEM.

The author would like to acknowledge travel funding to perform the collaborative research with the FDA/CBER at the NIH campus from the ORISE/IRTA program. A

total of three months of time was spent over a two year period in part due to this travel funding.

Several funding agencies have provided financial support. The author would like to graciously thank the National Institutes of Health (2-S06-GM60654) and the National Science Foundation (IGERT-9972892). Additional support has been provided by the Food & Drug Administration and the National Vaccine Program Office. The work in Chapter 4 describing peptide nanotube biosensors was performed in collaboration with the Food & Drug Administration's Center for Biologics Evaluation and Research, Office of Vaccine Review & Research, Division of Viral Products.

Hunter College Chemistry infrastructure is supported by the National Institutes of Health, the RCMI program (G12-RR-03037).

The author would like to thank his parents for their constant advice and support, as well as his late grandfather Norman E. MacCuspie for his encouragement to study chemistry and nanotechnology, especially in this program, and for his financial support to pursue this degree.

Finally, the author would also like to thank his wife, Heather, for her endless understanding and support, and especially for enduring the author's rigorous travel schedule involved over the last three years of this research. Her love and support helped fuel the author's passion to discover something new every day, and to make it through.

Table of Contents

Abstract Page iv
Acknowledgements Page vi
Table of Contents Page ix
List of Figures Page xi
List of Tables Page xvii

Chapter 1 – Introduction Page 1

Chapter 2 – Self-Assembly of Peptide Nanotubes Page 12

Chapter 3 – Nanolithography and Peptide Nanotube Alignment Page 30
3.1 Biological bottom-up assembly of antibody nanotubes on patterned antigen arrays Page 30
3.2 Thiolated peptide nanotube assembly as arrays on patterned gold substrates Page 36
3.3 Self-assembly of gold nanoparticle-containing peptide nano-rings on surfaces Page 42

Chapter 4 – Multiplexed Peptide Nanotube Biosensor Pathogen Assay Page 53
4.1 Introduction Page 53
4.2 Single Virus Detection
4.2 a) Structure of nanotube-virus aggregates Page 56
4.2 b) Detection by flow cytometry using FSC vs. FL-1 data channels Page 57
4.2 c) Lack of detection using flow cytometry and SSC vs. FL-1 data channels Page 84
4.3 Multiplexed Detection Using Flow Cytometry Page 110
4.4 Materials and Methods Page 118

Chapter 5 – AC Impedance Spectroscopy on the Atomic Force Microscope - Instrument Design and Verification Page 122
5.1 Failure of DC Conductive Measurements with DI AFM Page 122
5.2 AC Phase Shift Analysis with DI AFM and Krohn-Hite Phase Analyzer Page 125
5.3 AC Amplitude and Phase Change Measurements With DI AFM and Solartron FRA Page 141
5.4 AC Impedance with Asylum AFM and Solartron Frequency Response Analyzer
5.4 a) In General Page 145
5.4 b) Reproducible contact between AFM probe

and samples with constant tip force *Page 147*
5.4 c) Checking the tip's metal coating with impedance spectra *Page 156*
5.4 d) AC impedance measurement of model systems – bare gold substrates and gold nanoparticles *Page 156*
5.4 e) Circuit modeling of impedance AFM *Page 162*
5.4 f) Conclusion *Page 168*
5.5 Experimental Details
5.5 a) Installing the frequency response analyzer *Page 168*
5.5 b) SMaRT software *Page 170*
5.5 c) Writing custom software for Igor Pro on the Asylum MFP-3D system *Page 176*
5.5 d) AC Impedance AFM Tip Holder *Page 177*
5.5 e) Sample prep *Page 182*
5.5 f) Process of collecting Impedance Spectra *Page 188*
5.6 Future Applications of AC Impedance Measurements In Solution *Page 192*

Chapter 6 – Impedance AFM for Biosensing Page 195
6.1 Introduction *Page 195*
6.2 AC Impedance Studies of PS, PMMA, and Silica Nanoparticles in Three Different Sizes
6.2 a) Polystyrene (PS) *Page 197*
6.2 b) Polymethylmethacrylate (PMMA) *Page 203*
6.2 c) Silica *Page 209*
6.3 AC Impedance Studies of Polystyrene and Silica Nanoparticles with Different Surface Chemistries
6.3 a) Polystyrene, 100nm *Page 236*
6.3 b) Polystyrene, 200nm *Page 243*
6.3 c) Silica, 110nm *Page 247*
6.4 Point to Plate Model for Capacitance of Air Gap *Page 253*
6.5 AC Impedance Spectroscopy Studies of Viruses
6.5 a) In general *Page 262*
6.5 b) HSV-1 *Page 269*
6.5 c) HSV-2 *Page 274*
6.5 d) Adenovirus 3 *Page 280*
6.5 e) Adenovirus 5 *Page 285*
6.6 Conclusion *Page 291*
6.7 Experimental Details *Page 292*
Chapter 7 – Conclusion Page 297

References Page 309

List of Figures

Figure 1-1. Illustration of chip-based microfluidic biosensor Page 2

Figure 1-2. Illustration of peptide nanotube biosensors Page 6

Figure 2-1. Chemical structure of Bis(N-α-amido-glycylglycine)-1,7-heptane dicarboxylate Page 12

Figure 2-2. Raman Spectra of peptide nanotubes Page 15

Figure 2-3. Three-dimensional hydrogen bonding network Page 16

Figure 2-4. Dynamic light scattering of a C7 solution at pH 5 Page 20

Figure 2-5. Diagram of hypothesized mechanism of nanotube formation by ribbon tightening Page 22

Figure 2-6. TEM images of striated nanotubes Page 23

Figure 2-7. TEM images of nanotubes self-assembled after 1 day at pH 5 Page 24

Figure 2-8. TEM images of the micelle elongation mechanism of tube formation Page 26

Figure 2-9. TEM images of defective peptide nanotubes Page 27

Figure 2-10. Beta sheets in various stages of rolling into nanotube structures Page 28

Figure 2-11. Scheme of self-assembly of peptide nanorings Page 29

Figure 3-1. Schematic diagram of antibody nanotube assembly Page 33

Figure 3-2. AFM images of antibody nanotube assembly Page 35

Figure 3-3. AFM image of the aligned antibody nanotubes Page 35

Figure 3-4. Schematic diagram of thiolated peptide nanotube assembly Page 37

Figure 3-5. AFM images of thiolated peptide nanotube assembly Page 39

Figure 3-6. AFM images of multiple thiolated peptide nanotubes attached inside one large gold trench Page 41

Figure 3-7. Illustration of gold nanorings assembly Page 44

Figure 3-8. TEM and AFM images of the same gold nanorings Page 44

Figure 3-9. Scheme for alignment of gold nanorings Page 46

Figure 3-10. AFM images of assembled peptide nanorings Page 47

Figure 4-1. Illustration of peptide nanotube biosensor pathogen detection Page 55

Figure 4-2. Images of peptide nanotube biosensors detecting pathogens Page 57

Figure 4-3. Flow cytometry data for Adenovirus Type 3 (AV3) Page 59

Figure 4-4. Flow cytometry data for Influenza A Page 62

Figure 4-5. Flow cytometry data for Influenza B Page 64

Figure 4-6. Flow cytometry data for Vaccinia Page 67

Figure 4-7. Flow cytometry data for biosensors against AV3, assaying for AV3 Page 69

Figure 4-8. Flow cytometry data for biosensors against AV3, assaying for AV5 Page 71

Figure 4-9. Flow cytometry data for biosensors against AV5, assaying for AV3 Page 73

Figure 4-10. Flow cytometry data for biosensors against AV5, assaying for AV5 Page 75

Figure 4-11. Flow cytometry data for biosensors against large T antigen, assaying SV40-spiked samples Page 77

Figure 4-12. Flow cytometry data for biosensors against small and large T antigen N-terminus, assaying for SV40-spiked samples Page 80

Figure 4-13. Limit of detection determinations from standard curves Page 82

Figure 4-14. Side scattering Flow cytometry data for HSV-2 virus Page 87

Figure 4-15. SSC flow cytometry data for AV3 biosensors, assaying for AV3 Page 90

Figure 4-16. SSC flow cytometry data for AV3 biosensors, assaying for AV5 Page 93

Figure 4-17. SSC flow cytometry data for AV5 biosensors, assaying for AV3 Page 95

Figure 4-18. SSC flow cytometry data for AV5 biosensors, assaying for AV5 Page 98

Figure 4-19. SSC flow cytometry data for large T antigen of SV40 biosensors, assaying for SV40-spiked samples Page 101

Figure 4-20. SSC flow cytometry data for small and large T antigen N-terminus biosensors, assaying for SV40-spiked samples Page 103

Figure 4-21. SSC flow cytometry data for Influenza A Page 105

Figure 4-22. SSC flow cytometry data for Influenza B Page 107

Figure 4-23. SSC flow cytometry data for Vaccinia (MVA) Page 109

Figure 4-24. Mixture of HSV2 and SV40 sample analysis Page 113

Figure 4-25. TEM image of an intermediate structures Page 116

Figure 4-26. Saturation effects Page 117

Figure 5-1. DC Conductive AFM measurements Page 124

Figure 5-2. AFM of Gold-coated Vaccinia virus (MVA) Page 125

Figure 5-3. Illustrations of early instrumentation setups Page 126

Figure 5-4. Test probe clip attached to the AFM tip holder Page 128

Figure 5-5. Sample puck configuration Page 129

Figure 5-6. Photograph of an early setup Page 131

Figure 5-7. Multimode AFM base Page 134

Figure 5-8. AFM tip pushed down into surface Page 135

Figure 5-9. Periodic noise in AFM image Page 137

Figure 5-10. Six hour scan of 58 nanometer polystyrene beads in contact mode Page 141

Figure 5-11. AC signals passing through a dielectric sample Page 143

Figure 5-12. Impedance Data from Solartron Demonstration Page 144

Figure 5-13. AFM illustrations Page 149

Figure 5-14. Impedance spectra of various increasing contact forces Page 154

Figure 5-15. Height images before and after impedance spectra collection Page 155

Figure 5-16. Bare gold and gold nanoparticle impedance spectra Page 158

Figure 5-17. Impedance spectra of resistors with different connections Page 160

Figure 5-18. Schematic layout Page 163

Figure 5-19. Bode plot of air gap Page 164

Figure 5-20. Bode plot of negative silica nanoparticle Page 165

Figure 5-21. Scheme of SPM-Impedance Spectroscopy. Page 166

Figure 5-22. Photographs of how to install Solartron Instruments Page 169

Figure 5-23. Initial configuration of the SMaRT software Page 171

Figure 5-24. Initial screens of the SMaRT software Page 172

Figure 5-25. Screen shots from SMaRT Page 174

Figure 5-26. AC Impedance AFM tipholder Page 178

Figure 5-27. Photos of loading the AC Impedance AFM tipholder Page 180

Figure 5-28. Side view of the Asylum MFP-3D AFM head Page 182

Figure 5-29. How to prepare a sample Page 183

Figure 5-30. How to shim a slide, step by step Page 185

Figure 5-31. How to connect a sample Page 187

Figure 5-32. Screen shot of the auto tune process Page 188

Figure 5-33. Thermal tune screen shots Page 190

Figure 6-1. Illustration of the impedance AFM configuration Page 196

Figure 6-2. Impedance spectra for three sizes of polystyrene nanoparticles Pages 197-8

Figure 6-3. AFM images of three sizes of polystyrene nanoparticles Page 200

Figure 6-4. Illustrations of capacitance models Page 201

Figure 6-5. Impedance spectra of three sizes of PMMA Pages 203-4

Figure 6-6. Impedance vector quantity Page 205

Figure 6-7. AFM images of three sizes of PMMA Page 208

Figure 6-8. Silica nanoparticles at three different sizes. Pages 210-1

Figure 6-9. AFM images of three sizes of silica Page 213

Figure 6-10. Change from plate to sphere model. Page 215

Figure 6-11. Z of 3 materials of small size Page 218-9

Figure 6-12. Z of 3 materials of medium size Page 221-2

Figure 6-13. Z of 3 materials of large size Page 224-5

Figure 6-14. Normalized of Z & C, small Page 227-8

Figure 6-15. Normalized of Z & C, medium Page 230-1

Figure 6-16. Normalized of Z & C, large Page 233-4

Figure 6-17. Impedance spectra of three surface chemistries of 100nm polystyrene Pages 237-8

Figure 6-18. AFM images of three surface chemistries 100nm polystyrene Page 240

Figure 6-19. Impedance spectra for three surface chemistries of 200nm polystyrene Pages 244-5

Figure 6-20. AFM images of three surface chemistries of 200nm polystyrene Page 247

Figure 6-21. Impedance spectra for three surface chemistries of 110nm silica Pages 249-50

Figure 6-22. AFM images of three surface chemistries of 110nm silica Page 252

Figure 6-23. Air gap impedance spectra Pages 255-6

Figure 6-24. Illustrations of field lines and double layer charge effects, and COMSOL Multiphysics predictions Page 258

Figure 6-25. Impedance spectra for all viruses characterized Pages 265-6

Figure 6-26. AFM height and section analysis data for 3 viruses Page 268

Figure 6-27. Impedance spectra for three types of HSV-1 virions Pages 271-2

Figure 6-28. AFM images of three types of HSV-1 virions Page 274

Figure 6-29. Impedance spectra for three states of HSV-2 virions Pages 276-7

Figure 6-30. AFM images of three types of HSV-2 virions Page 280

Figure 6-31. Impedance spectra for two types of AV3 Pages 282-3

Figure 6-32. AFM images of two types of AV3 Page 285

Figure 6-33. Impedance spectra for two types of AV5 Pages 287-8

Figure 6-34. AFM images of two types of AV5 Page 289

Figure 6-35. DC sweep from -5V to +5V, of HSV-1+GFP mutant Page 291

List of Tables

Table 4-1. Peptide Nanotube Biosensor Assay Limit of Detection Examples. Page 83

Table 5-1. Summary of Results from AFM Vendor Demonstrations Page 146

Table 6-1. Capacitance of Different Sizes of Materials Page 215

Table 6-2. Normalized Capacitance of Materials Page 235

Table 6-3. Capacitance of Different Surface Chemistries Page 253

Table 6-4. Capacitance of Viruses at 10 kHz. Page 267

Chapter 1

INTRODUCTION

Pathogen identification is of continued importance in the areas of medical diagnostics and biological warfare defense. Toward this end, multiple approaches will be developed in this work to identify pathogens more efficiently and robustly, and with greater sensitivity. One primary approach would be to imagine a system that allows identification of viruses based on the three criteria of physical size, biological recognition, and electrical properties. Such a chip-based microfluidics system, depicted in Figure 1-1, could be imagined as a potential solution. Utilizing three levels of recognition, including physical size, biological recognition and electrical properties, would maintain selectivity and sensitivity and improve upon existing approaches that rely on fewer criteria. Biological recognition is well known and enabled through commercially available antibodies. Physical size is well known through extensive electron microscopy studies in the literature[1]. However, the electrical properties of single virions are largely unexplored. Therefore, before constructing such a chip-based detector, a fundamental understanding of such electrical properties is required.

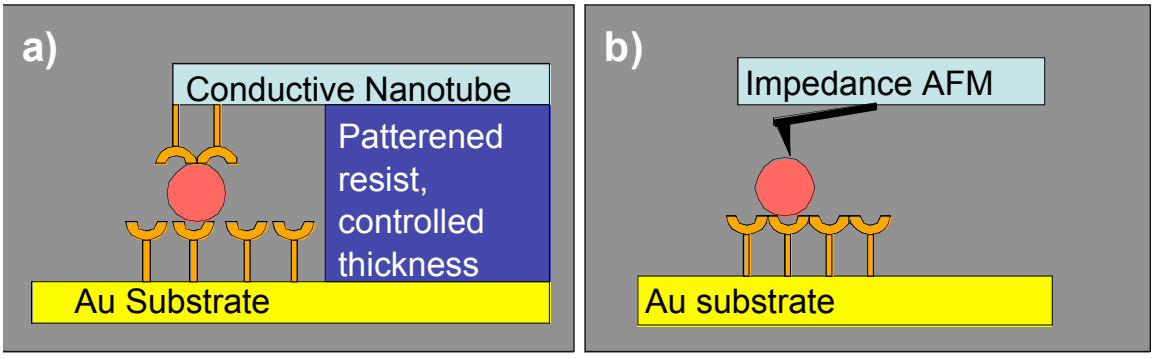


Figure 1-1. a) Cartoon of chip-based microfluidic biosensor that utilizes three levels of pathogen identification and discrimination including biological specificity through antibodies, physical size, and electrical properties. b) Impedance AFM model system for studying the fundamental science behind nanoscale electrical characterization of single virions.

Another key component of the chip-based biosensor described in Figure 1-1 is the conductive peptide nanotube. The self-assembly and properties of peptide nanotubes to make ribbon or tube-like structures and even macroscopic structures have been reported[2-6]. These nanotubes can act as templates for functionalization with porphyrins[7], metals[8-10], and proteins[11]. Further, these nanotube templates can be functionalized in a location-specific fashion such that proteins or antibodies are directed to the ends of the nanotubes only[12]. These peptide nanotubes can be directed to align on self-assembled monolayers (SAMs) deposited on gold substrates[13, 14]. Host-guest switchable photochemistry can be addressed to these nanotubes as well[15, 16]. Biomineralization peptides can be used to fabricate metal nanowires from nanoparticle coatings with tunable properties such as nanoparticle size, shape, or packing density[17-21]. Copper nanoparticles were demonstrated to have tunable sizes when growth was templated on peptide nanotube scaffolds, while silver nanoparticles were shown to have a shape specific growth. Silver nanoparticles' shape could be controlled based on peptides binding preferential faces of the growing nanocrystals, thereby restricting growth on those bound faces to generate shape control. Nickel and platinum were shown to have tunable packing densities of nanoparticles on peptide nanotube templates by changes in reaction conditions. Peptide nanotubes can also be directed to align on surfaces through nanolithography techniques[22, 23].

To exploit the versatility of peptide nanotubes while solving the need for better pathogen identification, multifunctional peptide nanotube biosensors have been developed for high-throughput, rapid, highly sensitive detection of pathogens. Such nanotube biosensors have further importance in the areas of bioterrorism response and regulation of biological products such as blood products and vaccines. Many techniques are currently being studied as potential solutions.

- Fluorescent polymers offer increased fluorescence intensity at every pathogen binding site, yet often rely on carbohydrates, which lack the ability to use antibodies to gain added pathogen specificity, to bind pathogens[24].
- Quantum dots have been conjugated to pathogens immobilized on substrates in sophisticated detection schemes[25].
- Quantitative PCR allows detection of single copies of DNA, yet is only capable of detecting available nucleic acids, and thus requires extraction steps and is subject to sample contamination concerns.
- Carbon nanotubes have been functionalized with antibodies as potential detectors[26].
- Attempts to create circuit elements in biosensing electronics have been made[27, 28].
- Electron microscopy reveals detailed structure information yet requires sample concentrations as high as 10^7 particles per mL to be time-efficient[29].

- Traditional plaque assays, while capable of detecting one single infectious unit, require several days in order to produce sensitive results.
- Studies using atomic force microscopy to characterize detailed morphology of pathogens have succeeded[30], but detection has focused on high sample concentrations[31].

Flow cytometry is a clinical diagnostic tool and basic research technique[32] used to identify, analyze and sort cells of interest. Recent advances in multiplex systems[33-35] have made flow cytometry assays advantageous by requiring low sample volumes and the ability to run multiple tests on the same sample. One challenge to the flow cytometry technique is detecting particles smaller than 0.5μm, and thus it has traditionally been used to detect cells that are infected by virus[36]. The need to rapidly and non-destructively detect intact cell-free virus in solution is currently underserved. The ability to perform such tests could provide quick analysis on whether potentially infectious virus is present in a sample. The potential benefits from a one-step, rapid (less than 30 minute), and sensitive (near attomolar concentration) screening of samples are significant. Benefits include, for example, analysis of blood samples of patients potentially exposed to pathogens recently enough that they may not yet be exhibiting symptoms allowing targeted courses of treatment in the case of limited supplies of anti-viral drugs to only those patients who did in fact contract the virus. This kind of information on how to allocate limited on-scene resources most effectively could prove invaluable for on-scene commanders.

As one solution to the challenge of better pathogen identification, a nanotube-based flow cytometry assay is developed to rapidly, sensitively, and efficiently detect the

presence of a variety of viruses in solution. The versatility of the peptide nanotube-based assay is demonstrated by detecting a range of viruses encompassing enveloped and non-enveloped DNA and RNA viruses ranging in size from 55nm to 360nm. Additionally, the multiplex ability of this assay is demonstrated by quantifying two different virus concentrations simultaneously in the same sample. Finally, demonstration of the retention of antibody selectivity is performed by testing for cross-reactivity between antibodies against different viruses in a multiplexed text. An illustration of the mechanism of this detection is shown in Figure 1-2.

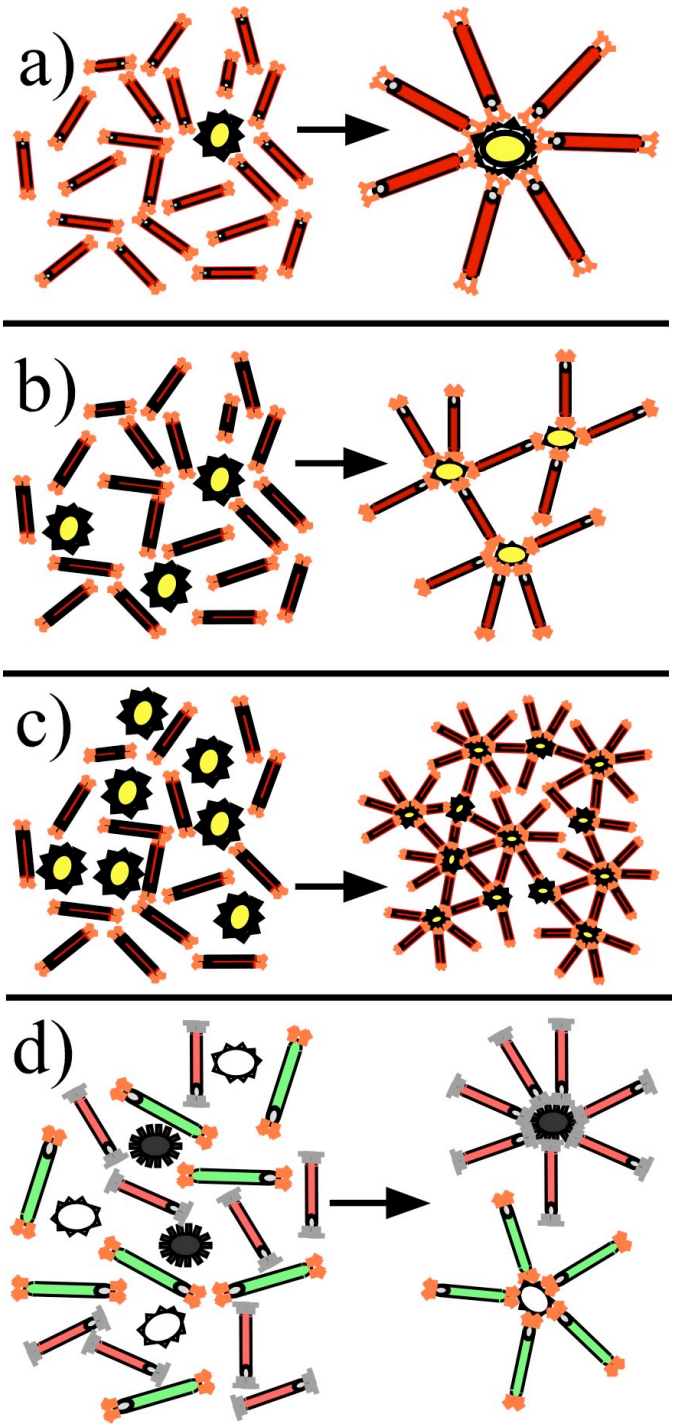


Figure 1-2. Illustration of peptide nanotube biosensors. a) Low virus concentrations cause the peptide nanotubes to aggregate around viruses in a sea-urchin or hub-and-spoke like structure. b) As the virus concentration increases, larger networks of nanotubes and viruses begin to form. c) The size and fluorescence intensity of the nanotube-virus networks is dependent on the virus concentration. d) A multiplexed test is possible by assigning each antibody a unique fluorophore emission wavelength, then combining several types of nanotube biosensors in the assay.

When considering building a microfluidics chip-based sensor like that depicted in Figure 1-1a, the ability to direct the attachment of conductive peptide nanotubes will be a crucial step. Nanofabrication will be a key step to successfully constructing such a device. Recently improved two- and three-dimensional nanofabrication techniques allow one to build precisely designed structures for various photonic applications[37-39]. While the top–down approach has been applied for photonic crystal fabrication, the bottom–up approach via self-assembly of photonic nano-building blocks is also showing promise[40-48]. For bottom–up approaches in optics fabrication to be successful, synthesis and alignment of photonic nanomaterials needs to be accomplished efficiently and precisely. Biomineralization processes, where peptides or proteins are utilized to mineralize metals and semiconductors, have been shown to produce various types of nanocrystals[49-61]. Since the amino acid sequences are very sensitive to elements for their mineralization, optimized peptide sequences can produce nanocrystals efficiently[10]. In addition to the effective crystal growth, the amino acid sequences of mineralizing peptides could also influence the size, alignment, and shape of resulting nanocrystals[19, 20, 62, 63]. Furthermore, in some cases peptides can cause nanocrystals that do not grow under ambient conditions to mineralize in solution at room temperature[64, 65]. Because the size, alignment, shape, and crystalline structure of photonic nanocrystals control the optical properties of assembled nanocrystals, the tunabilities of these features and the potential of new material synthesis by using peptides will provide a significant advantage to apply peptides for photonic material syntheses. One approach to create photonic materials by using mineralizing peptides is to pattern these peptides on surfaces based on photonic device designs and grow photonic crystals

on the patterned peptides. For example, a hologram was applied to pattern silica-mineralizing peptides as an array and resulting silica nanostructures exhibited a nearly fifty-fold increase in diffraction efficiency over a comparable polymer hologram[50]. Recently, microfluidics and lithography were also used to pattern silica- and silver-mineralizing peptides for photonic applications[63, 66].

The bottom-up approach has been gaining significant momentum in the field of nanometer-sized device fabrication, and it has led to development of a variety of smart nanoscale building blocks. Among the various nanoscale building blocks, nanotubes and nanowires have been synthesized with desired physical properties to be incorporated in electronic and optical devices. Whereas nanotube material syntheses have been explored extensively, efforts to address those nanotubes to specific locations on substrates for device fabrication have just begun. Recently, nanotubes were addressed to particular directions by using external forces such as microfluidics, magnetic fields, electric fields, and the Langmuir-Blodgett technique[67-73]. In another approach, nanotubes were addressed by chemical/biological interactions. For example, nanotubes coated with proteins were addressed onto the complimentary ligand-patterned substrates in solution[12, 13, 22]. Molecular recognition motifs, hydrogen bonding, hydrophobic interactions, and electrostatic interactions were also applied to locate nanotubes in the specific regions on substrates[14, 15, 74-77].

One approach described in this work is the directed assembly of thiolated peptide nanotubes on a surface by using the thiol-gold interaction. The thiol-gold interaction is stronger as compared to biological, hydrophobic, and electrostatic interactions. Thus, peptide nanotubes whose sidewalls were chemically modified to contain thiol groups

show a strong affinity toward gold substrates, and the nanotubes were only attached to exposed gold regions on the substrates. Because of the strong affinity, the nanotube assembly could be scaled up to form nanotube arrays by patterning gold pads on the substrates with AFM-based nanolithography[78-80]. This technique may lead to an alternative nontraditional fabrication method for electric circuits because the physical properties of aligned peptide nanotubes can be tuned after the targeted positioning with semiconductor/metal coatings on the nanotubes with simple chemical procedures[17-21].

Aside from thiol nanotube to gold alignment, the bottom-up approach in nanofabrication has been studied extensively due to the potential to develop devices such as electronics, actuators, and sensors more efficiently and economically compared to existing technologies[81-83]. Applications of biotechnology to nanofabrication also has an advantage because it affords functional building-block materials that may not be synthetically accessible and use much milder experimental conditions, such as room temperature and ambient pressure[64]. Various building blocks have been developed for the biological bottom-up approach[62, 63, 84-89]. However, it is necessary for these building blocks to be addressed to the exact locations with high precision and reproducibility to function in the nanometer scale devices[81, 90, 91]. Recently, carbon nanotubes were assembled on regions coated with the polar chemical groups on a large scale[76].

Once nanotubes have been aligned to appropriate locations on a chip, other considerations such as the metallization of the nanowires, and functionalization of the nanotube with antibodies at only the ends or porphyrin coatings, have been the topic of approaches described in the literature[7, 12, 18]. Microfluidic chip design using the

fabrication techniques just described could provide the physical size and biological discrimination previously mentioned, and even provides a direct conductive path to the target virus. However, since electrical characterization of single viruses remains largely unexplored, electrical measurements made by such chips would not be clearly understood. The lack of knowledge about electrical properties of single virions warrants study by impedance AFM.

Impedance AFM has been explored by several researchers interested in the properties of thin films that are on the order of nanometers in thickness. Nanoscale electrical characterization of materials can provide fundamental information on a material's composition and has potential utility in nanoelectronic devices such as sensors. While DC conductive AFM and STM techniques that measure current typically require conducting or semiconducting samples, AC impedance AFM techniques allow characterization of any conducting or insulating material. Several authors have successfully attempted to make impedance measurements at the nanoscale using the AFM[92-98]. Alternatively, EFM has been used to characterize the changes in forces from electric fields applied to nanoparticles to indirectly measure electrical properties[99-101]. However, all of these methods only characterized thin films of a few nanometers thickness, or measured impedance across grain boundaries. Both of these thin-film techniques were fundamentally different from measuring the impedance directly through individual nanoparticles.

The ability to electrically characterize individual nanoparticles while simultaneously exploiting the variety of data collected by AFM creates a powerful and efficient instrument for characterizing materials[102]. The impedance response of

polymer nanoparticles and viruses was investigated to demonstrate the potential of this instrument as a robust biosensor. Impedance AFM enables fundamental studies of nanomaterials like single nanoparticles with potential applications toward biosensing. This instrument has the potential to improve on current methods of virus detection in terms of sensitivity and ability to detect in-tact virions[24, 27, 29, 34, 36, 103]. This indicates that using the impedance AFM as depicted in Figure 1-1b is an excellent model system. Antibody substrates can be used for immobilizing virions on gold electrodes for AFM imaging, or alternatively antibody functionalized AFM tips can be used. Also, the physical size gap between the AFM tip and the substrate can be controlled down to the angstrom level. Further, by using conductive metal-coated AFM tips, it provides an extremely precise nanopositioning system for electrical measurements.

In regards to the application of impedance AFM directly as a biosensor, the size and shape is obtained from the AFM topography images, while the biological recognition can be obtained through an antibody-functionalized gold electrode substrate or an antibody-functionalized AFM tip, and the electrical properties can be characterized using the frequency response analyzer to obtain the complex impedance, capacitance, and other values such as electrical permittivity, dielectric loss or tan delta, and dielectric constant.

As a whole, this work describes significant progress in these multiple approaches to building a better biosensor. By gaining a fundamental understanding of the science required to achieve these goals, this work aims to provide the foundations that could lead to more robust applications and solutions to sensing problems in the future.

Chapter 2

SELF-ASSEMBLY OF PEPTIDE NANOTUBES

Self-assembled peptide nanotubes provide a versatile scaffold for a variety of interesting chemistries and applications[6]. The peptide nanotubes chosen for this thesis work were self-assembled from heptane bolaamphiphile monomers. Bis(N-α-amido-glycylglycine)-1,7-heptane dicarboxylate monomers were synthesized by previously described methods[104]. The chemical structure of this molecule, whose molecular formula is $C_{17}H_{28}O_8N_4$ and has a molecular weight of 416.42, is given in Figure 2-1. The typical method used to synthesize each batch of monomer is described in the following paragraph.

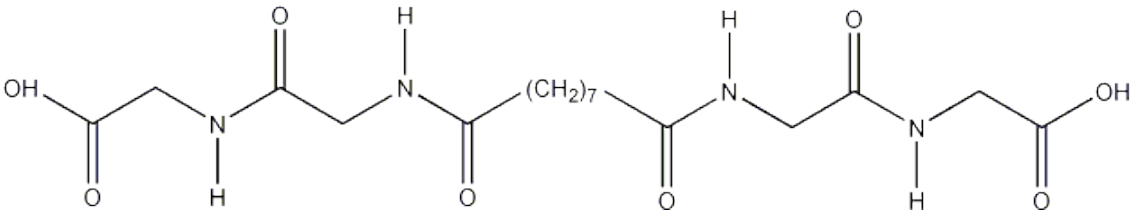


Figure 2-1. Chemical structure of Bis(N-α-amido-glycylglycine)-1,7-heptane dicarboxylate, the monomer used to self-assemble the peptide nanotubes

MATERIALS AND METHODS

In a round bottom flask, dissolve 0.5 g of azelaic acid and 0.65 g of 1-hydroxybenzotriazole(HOBT) in 100 mL of dimethylformamide(DMF). Separately, dissolve 0.92 g of 1-[3-(dimethylamino)propyl]-3-ethylcarbodiimide hydrochloride(EDAC) in 10 mL of chloroform. Mix the chloroform solution with the DMF solution on ice for 1 hour, using a magnetic stirrer for mixing. After one hour, separately dissolve 1.88 g of glycylglycine-benzyl ester in 10 mL of methanol(MeOH)

and then add 0.67 mL of triethylamine(TEA). Mix this methanol solution with the DMF solution on ice. Cover flask with parafilm, label and date the flask, and refrigerate for 12 hours or overnight. Next, remove the DMF solvent using a rotary evaporator under reduced pressure and 70 °C water bath. Leave about 5 - 10 mL solvent inside the round bottom flask. The remaining slurry appears creamy white when purest. A yellow to brown color indicates increasing amounts of contaminating side products. Let this slurry cool to room temperature for 10 minutes and then cool on ice for 15 minutes. Optionally, depending on the intensity of brown color in the intermediate, a recrystallization can be performed here using DMF as the solvent. Vacuum filter the slurry using Whatman filter paper and a Buchner funnel. Next, wash the cake with about 50 mL of 50 mM citric acid and about 50 mL of 50 mM sodium bicarbonate solution. Let the vacuum pressure pull air to dry the cake to a powder, and then weigh the dry intermediate. Typically, the intermediate weighs about 0.6 g or approximately 1.0 millimole, which is approximately a 25% yield. The intermediate is stable for at least one week, if stored in an airtight glass vial. However, it is best if the intermediate is used immediately or on the next day. In a three-neck round bottom flask, dissolve the intermediate in a minimum amount of DMF in preparation for base-hydrolysis; the amount of solvent required will typically be about 70 – 85 mL. Using a heating mantle, heat the solution to 75 – 85 °C and add 35 mL of 0.1 N sodium hydroxide. Allow the hydrolysis to proceed for 4 hours, keeping the temperature within the range of 75 – 85 °C during the entire time. Let the solution and flask cool to room temp (<30 °C) then add 5 mL of 1 N hydrochloric acid. Remove the DMF under reduced pressure as described previously. Vacuum filter the slurry, then wash it with two to three 5 – 10 mL portions of ice cold distilled water. Follow these

washes with two to three ice cold acetone washes, again using about 5 – 10 mL each portion. Weigh the final dry product and store in a labeled vial in a desiccator or other cool dry place. Characterize the powder by 300 MHz NMR (a few crystals in a 0.6 mL ampule of deuterated dimethylsulfoxide (DMSO) is sufficient) and optionally on the mass spectrometer.

This method typically produced a 0.3g actual yield, or about 0.7 millimoles, or approximately a 70% yield on the hydrolysis step and a 15% yield overall. The theoretical yield of 0.992 g is based on the glycylglycine benzyl ester being the limiting reagent at 4.7 millimoles. This batch-synthesis protocol could be doubled to produce a 0.5 to 0.6g yield. It is crucial that the rotary evaporation of the DMF solvent is done quickly, so as to avoid side reactions that produce yellow, brown, and black contaminants. Most rotary evaporations of the DMF should take less than twenty minutes. Figure 2-2 shows the Raman spectrum of the self-assembled nanotubes compared to the Raman spectrum of the monomer crystals.

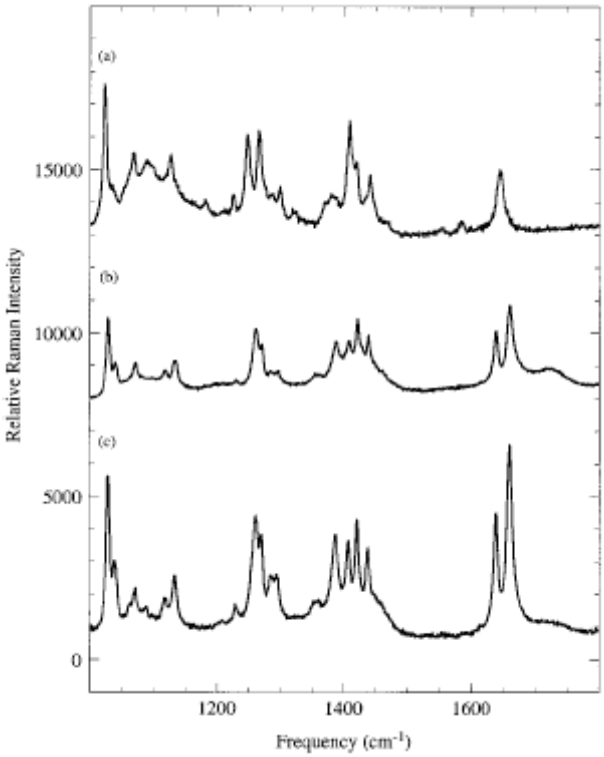


Figure 2-2. Raman Spectra of a) helical ribbon, b) nanotube, c) bolaamphiphile monomer crystal, taken from [2].

These heptane bolaamphiphile monomers will be abbreviated as "C7" monomers to represent the seven carbon alkyl chain linking the glycylglycine moeities at each end of the molecule. Under appropriate conditions, these monomers self-assembled into hollow peptide nanotubes. It was hypothesized that these nanotubes were held together by a three dimensional network of intermolecular hydrogen bonds. A proposed diagram of these three dimensional hydrogen bonding networks is shown in Figure 2-3. It was commonly observed under transmission electron microscopes that multi-walled nanotubes were formed, since the thickness of the nanotube walls were usually several nanometers thick. The average monomer molecular dimensions estimated by ChemDraw

were found to be approximately 0.4nm x 0.6nm x 2.8nm for the fully extended conformation.

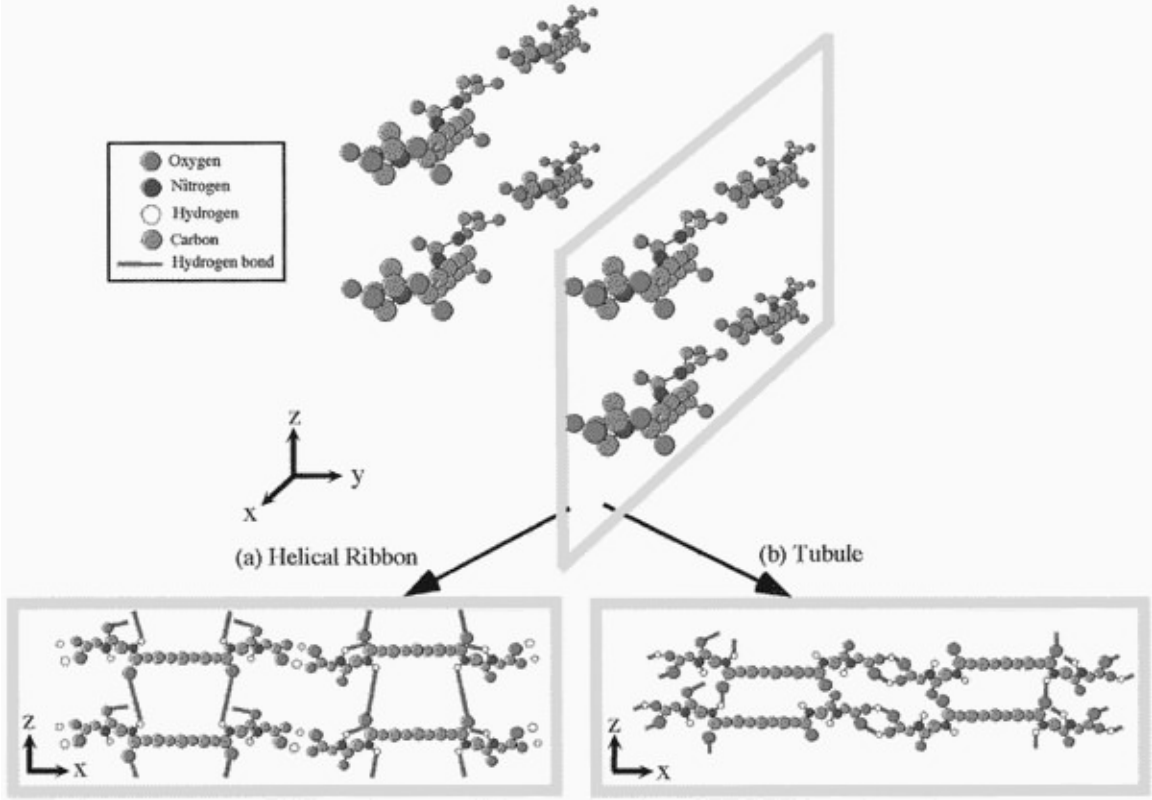


Figure 2-3. Three-dimensional hydrogen bonding network, taken from [2].

Several different self-assembly conditions were studied in an attempt to discover if subtle modifications to the solutions could produce a dramatic shift in self-assembly rates. Under normal conditions, 10mL of a 3mg/mL monomer solution dissolved in 0.1N sodium hydroxide was adjusted to pH 4.5 with citric acid and the nanotubes were allowed to grow for two weeks. When higher yields of nanotubes per mL were required, 10mg/mL monomer concentrations were used. Frequently, large crystals of the monomer must be sonicated from a few seconds up to five minutes in order to dissolve the monomer completely. It was found that if the monomer crystals floated on the surface of the sodium hydroxide solution, and could not break the surface tension to dissolve into

the aqueous phase, there would be significant or complete inhibition of nanotube formation. Such monomer batches were discarded.

In order to qualitatively determine if one set of growth conditions could produce a higher concentration of nanotubes, different concentrations of monomer, and different pH conditions were studied. Monomer concentrations of 1mg/mL, 3mg/mL, 5mg/mL, 10mg/mL, and 20mg/mL were studied first, with all solutions being adjusted to a pH of 4.50 for nanotube self-assembly. After as few as five days, precipitated material could be seen in the solutions of 10mg/mL and 20mg/mL. While less than 100% of the precipitated material contained nanotubes, this precipitated material will be referred to as nanotubes from here forward. After seven days, nanotubes could be seen in the 5mg/mL solution. After two weeks, the 3mg/mL solution had visible quantities of nanotubes, while the 5mg/mL had slightly more nanotubes, and the 10mg/mL and 20mg/mL contained significantly more nanotubes, but appeared to contain the same quantities of nanotubes by eye. Determinations were made qualitatively by swirling the vials containing the settled nanotubes, and judging by eye the density of the suspension.

Next, the pH conditions for self-assembly were studied with a 3mg/mL monomer solution. Citric acid was used to adjust the pH to 3.5, 4.0, 4.5, 5.0, 5.5, 6.0, and 7.0. Interestingly, at pH 3.5 and 4.0, there was formation of star-shaped aggregations visible to the eye in approximately one hour. These star-shaped or snowflake-shape aggregates were found to disappear when the solution was returned to pH 12 with sodium hydroxide. These solutions could then be adjusted to pH 4.5 and produce a smaller yield of nanotubes than the solutions that were adjusted directly to pH 4.5, however this technique can recover solutions that would otherwise have been unusable. However, it should be

highlighted that these snowflake aggregates likely had a very high surface area structure. This high surface area structure could become a template for making high surface area metal structures. One potential application could include creation of high surface area platinum or palladium catalysts through a biomineralization peptide coating on these snowflake structures.

Using the same experimental technique of swirling the vials containing settle nanotubes and judging the density of the suspensions by eye and side-by-side comparisons, it was found that the pH of 4.5 was the lowest pH that nanotubes could form at the pH at which the highest yield of nanotubes occurred. It was found that nanotubes could form in as few as five days, while pH 5.0 required at least ten days, pH 5.5 required two weeks to see small numbers of nanotubes, and pH 6.0 required two months to see small numbers of nanotubes. Nanotubes were never observed to self-assemble in the two months of the study of pH 7.0, at which point the study was halted.

The conclusions of the qualitative studies were that the conditions of pH 4.5 and 10mg/mL of C7 monomer were the best growth conditions, maximizing the yield of nanotubes per mL of solution. Since all of these studies were conducted at small volumes (5-10mL of monomer), it was next attempted to scale-up these self-assembly processes. Batches containing 20mL, 50mL, 100mL, 200mL, and 300mL of monomer at 10mg/mL were prepared. In all cases, after two weeks they had an equally high yield of nanotubes when quantified side by side and swirling the vials. Further qualitative evidence was provided by centrifuging 1mL of solution from each stock and comparing the size of the pellets by eye. The size of the pellets was indistinguishable when compared to the original stock solutions.

Once the scale-up discovery was made, all nanotubes were self-assembled in large batches. The greatest concern of this technique is keeping the solutions sterile and free of biological contamination. By having a large aqueous stock of peptide nanotubes, it was found that molds and fungi in the air would contaminate stocks that were frequently opened and closed. This loss due to biological contamination was minimized by fractioning the large stock into several smaller stocks of the sizes needed on a regular basis, or simply using the large volume all at once.

To further study the self-assembly of these C7 nanotubes, dynamic light scattering (DLS) studies were performed at several time points on one self-assembling solution that contained 10mL 3mg/mL of C7 monomer adjusted to pH 5 with citric acid. The results from this preliminary study are summarized in Figure 2-4. A 1mL fraction of the solution was added to the cuvette for the study and then returned to the solution, so as to minimize the disturbance to the solution and as closely mimic the actual conditions as possible. If future studies are performed, several initial conditions should be studied, and the self-assembly should be allowed to proceed entirely in the cuvette used for DLS analysis, and it should be left in the instrument with continuous sampling so as to have a complete set of time points rather than the limited results of this preliminary study.

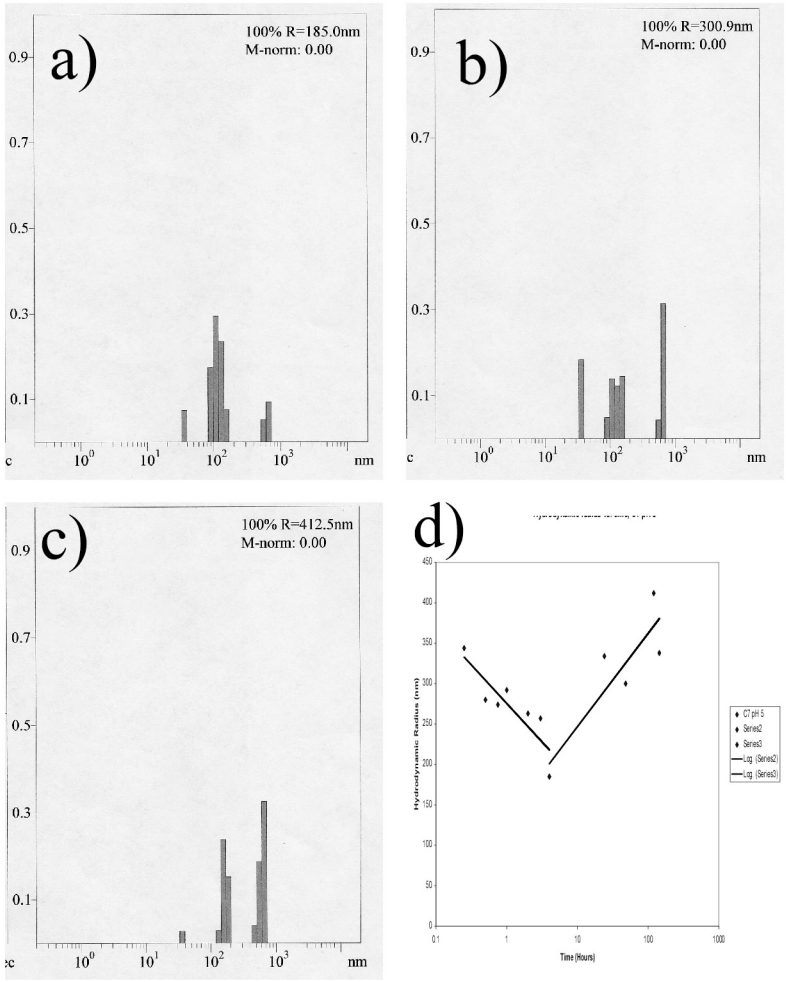


Figure 2-4. Dynamic light scattering of a C7 solution at pH 5 after a) 4 hours, b) 4 days, c) 5 days; d) plot of hydrodynamic radius vs. time for a C7 solution at pH 5, with trendlines showing decreasing size during day 1 then increasing size from day 2 to day 6.

It was discovered that the sodium hydroxide and citric acid play key roles in producing a high yield of nanotubes. While potassium hydroxide could produce small yields of tubes, sodium hydroxide worked better. Further, when hydrochloric acid was used to adjust the pH of the sodium hydroxide, nanotube formation was inhibited. While no systematic study of the acid and base combinations was performed, this could provide some interesting chemical information about the nanotubes and their hydrogen bonding

networks that could lead to a better fundamental understanding of how the nanotubes self assemble. This could imply that the citric acid is in fact part of the nanotube structure.

It was also discovered that collecting the supernatant from the first wash of the nanotubes could be set aside for two weeks and used to grow more nanotubes, thereby increasing nanotube self-assembly yield per gram of monomer. This enhanced recovery of nanotubes provided lower concentrations of nanotubes that the original 10mg/mL monomer solution, however it is more environmentally friendly because one could reuse solutions before disposal is necessary. While the focus of these studies was not developing green chemistry methods, finding greener methods and chemistries is something that should always be present in the minds of chemical researchers.

In an attempt to understand better the mechanism of the self-assembly process, the self-assembly was observed at many different time points by transmission electron microscopy (TEM). The three dimensional network of hydrogen bonds that forms the tubes is hypothesized in previous studies and is previously shown in Figure 2-5. The proposed mechanism of tube formation was the formation of a helix or twisted ribbon structure in basic conditions, which then tightened its coils until it formed a hollow tube.

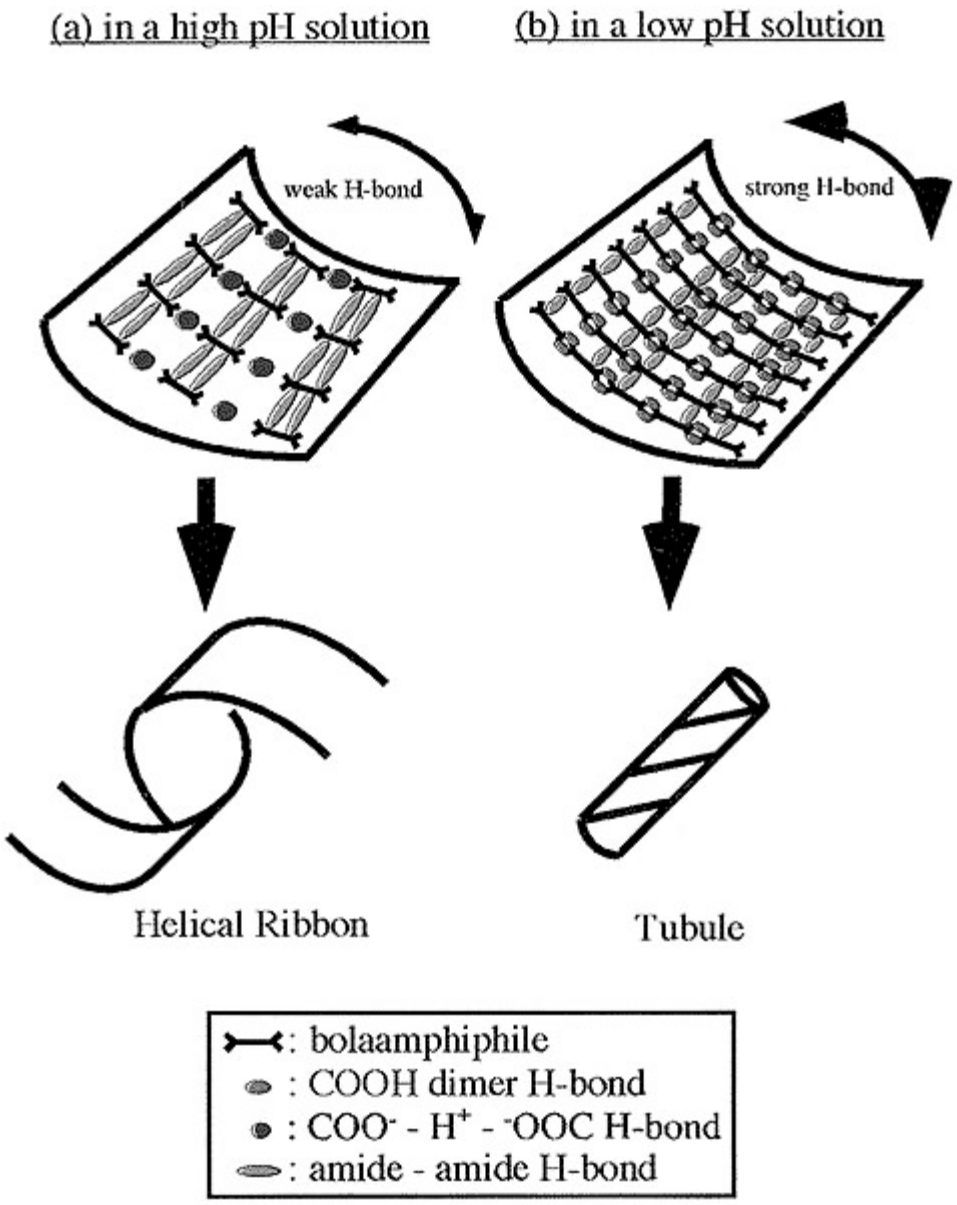


Figure 2-5. Diagram of hypothesized mechanism of nanotube formation by ribbon tightening, taken from [2].

Evidence supporting this mechanism was observed during TEM studies. The ribbon structures could be found in the basic solutions the monomers were dissolved in. At time intervals less than one hour from addition of citric acid, some striated nanotubes could be observed as shown in Figure 2-6. These structures help confirm the ribbon-tightening hypothesis. While it was beyond the scope of this particular study, it could be

beneficial to re-examine the details of these ribbons and striated nanotubes, specifically the right- or left-handed nature of the turns, the pitch of the turns, the thickness of the ribbons and the striations, and how these relate to the final diameter of the nanotube and the initial growth conditions. Variations to the initial growth conditions could include starting with tap water or nanopure water, selection of bases or acids, monomer concentrations, self-assembly temperature, stirring of solutions, pH, electric fields or magnetic fields to attempt to align the free monomers.



Figure 2-6. Striated nanotubes, suggesting ribbon-tightening hypothesis is correct.

Normal self-assembly results in large hollow nanotubes. Raw stock solutions of C7 peptide nanotubes yield polydisperse lengths and diameters. Examples of the range of polydispersity are shown in Figure 2-7b, with a large and small nanotube in the same field of view. The various sections of the large nanotube in Figure 2-7b are shown in the

higher magnification images in Figures 2-7a,c,e. A higher magnification image of the smaller nanotube in Figure 2-7b is shown in Figure 2-7d. Notice that both nanotubes have a thick outer wall and hollow interior, as evidenced by the dark bands along the edges of the nanotubes and the lighter contrast in the center. These images suggest the tubes must be multi-walled to obtain such a thickness of several nanometers.

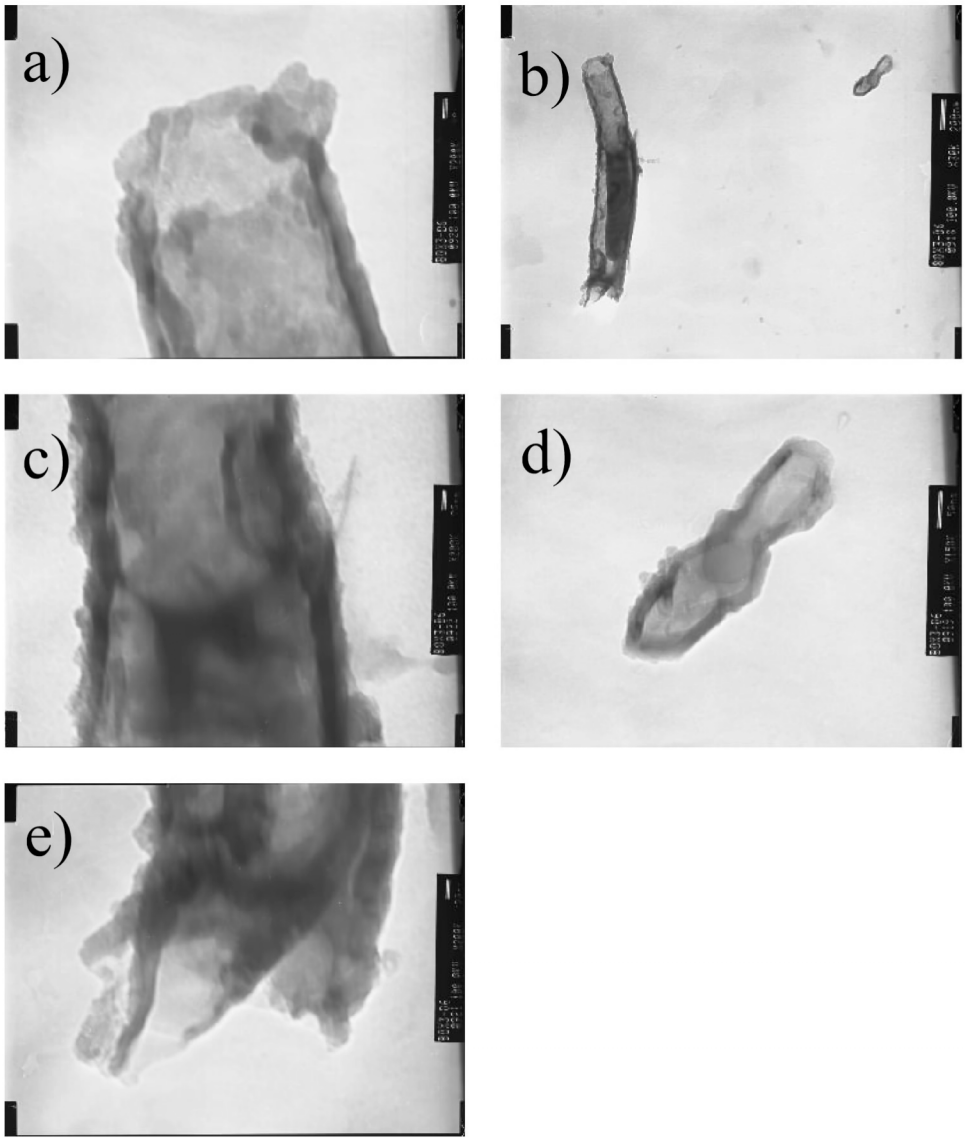


Figure 2-7. Transmission electron micrographs of b) two different sized tubes, self-assembled after 1 day at pH 5. High magnification images of the larger tube's different sections, a) top, c) middle, e) bottom, and of the d) smaller tube.

While evidence was found that supports the existing proposed mechanisms of helical ribbons tightening into tubes, data was also obtained that suggests there could be alternative mechanisms of tube formation taking place simultaneously. There were several micelle-like spheres observed to form early on, like those shown in Figure 2-8a-b. In these micelle-like structures, there is a very narrow band of contrast in the shape that the edges of grown nanotubes appear to have. This structure could be a precursor to the nanotube, and an alternate mechanism of formation. These structures were found to elongate into oval-like structures, like those shown in Figure 2-8c-d. They still retain that characteristic nanotube-end appearance, and the direction of elongation appears to be along what would be the length (z-axis) of the nanotube. These structures then elongated further into a short nanotube structure, like the one shown in Figure 2-8e, and eventually into the full grown nanotube like one shown in Figure 2-8g.

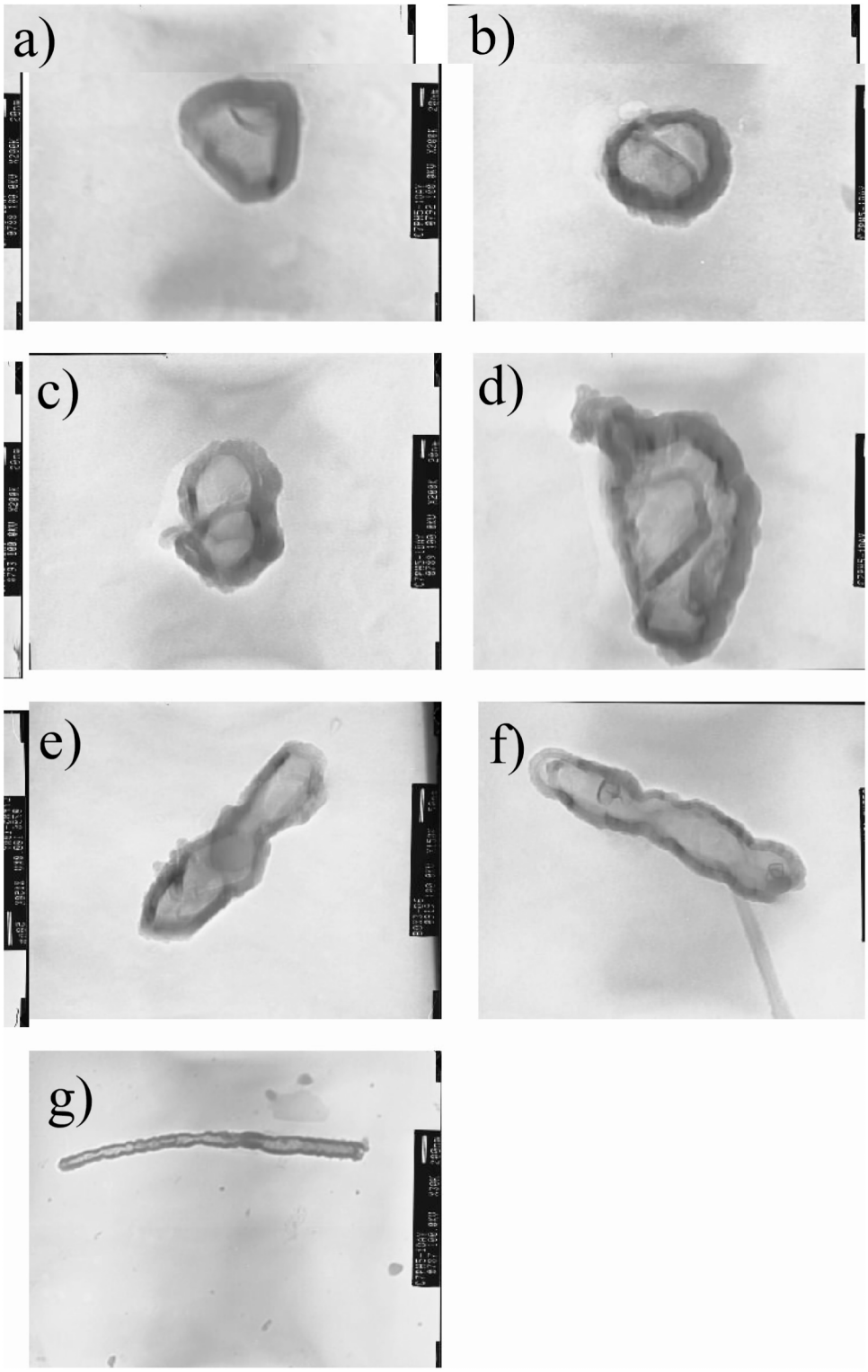


Figure 2-8. Different structures observed to support the micelle elongation mechanism of tube formation hypothesis. a) small micelle with small end curvature, b) medium micelle with full end curvature, notice the thin band of dark contrast through the middle of the

micelle circle, c) elongated micelle, d) larger elongated micelle, e) short nanotube, f) medium length nanotube, g) full grown high aspect ratio nanotube.

It was also observed that multiple nanotubes could merge together to form longer tubes. Structures that appear to be an intermediate of this process were found to occur, like those shown in Figure 2-9e, although it was not clear if this was from the drying effects of preparing the TEM grids or if this was in fact a real phenomenon. Nanotubes that appeared to have two segments with different diameters were found as well, like those shown in Figures 2-9c and 2-9d. Further, nanotubes that have branches were found as well, like those shown in Figure 2-8f and 2-9a.

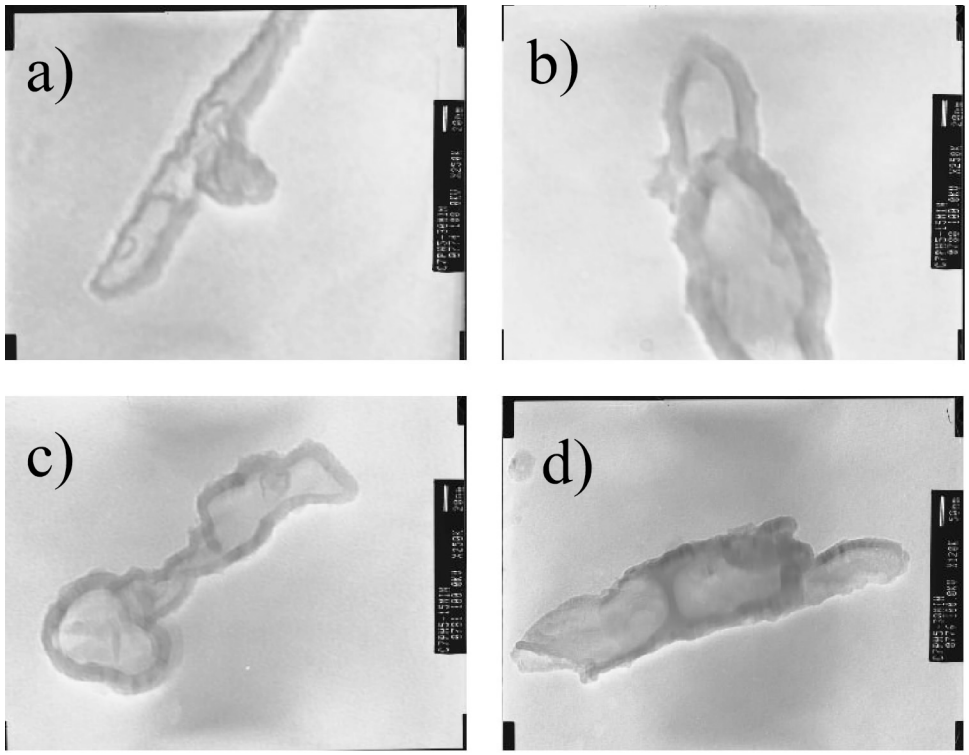


Figure 2-9. a) point defect on growing nanotube; b) micelle elongating defectively, or an elongated micelle merging with a larger micelle; c) micelle merging with the end of a growing nanotube; d) defective nanotube, perhaps a miss-folded beta sheet; e) large diameter nanotube with small diameter extension.

However, this data by itself is inconclusive to make the claim that the nanotubes can merge together to form longer tubes or branched tubes. It is possible that these defects in the nanotubes are seeded by defects in the alignment of the monomers in the three dimensional network of hydrogen bonding, such as shown in Figure 2-9a, but without computational modeling to confirm how such defects would affect the final structure, it will remain speculation.

Another alternative model is that of a beta sheet of monomers rolling up into a tube structure. Limited evidence of intermediate structures of this mechanism has been found under the transmission electron microscope, and is shown in Figure 2-10.

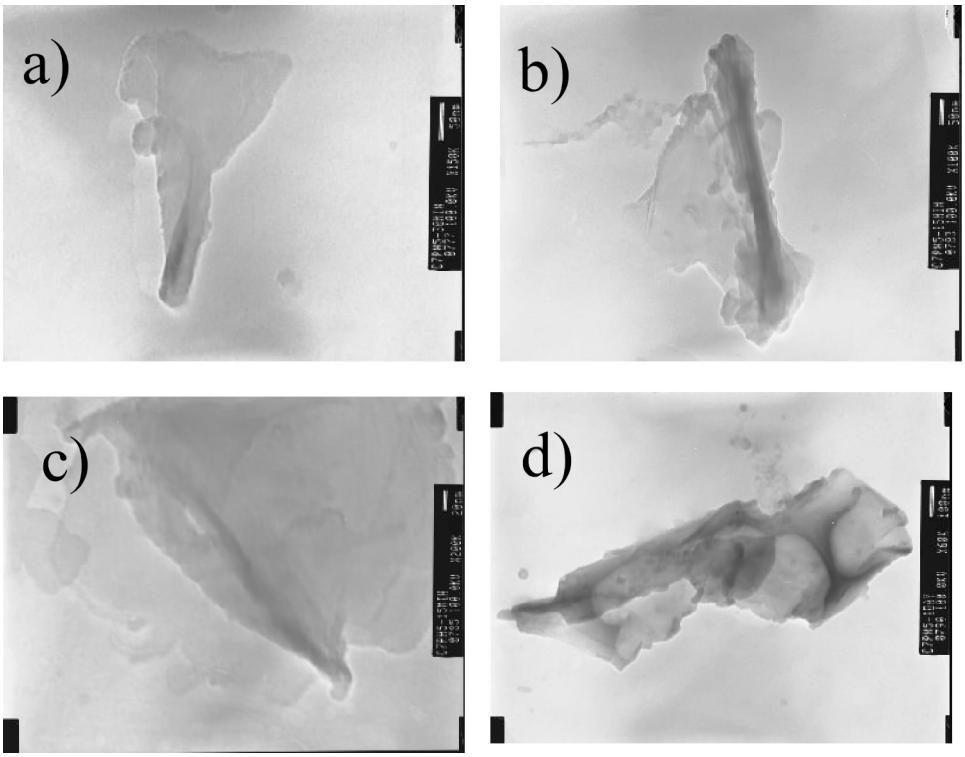


Figure 2-10. Beta sheets in various stages of rolling into nanotube structures.

Computational modeling could assist in solving this puzzle, coupled with quantitative experiments designed to calculate the type and frequency of these nanotube

defects. Other experiments that offer insight into the mechanisms driving the self-assembly of the peptide nanotubes have shown these same monomers capable of producing ring structures when self-assembled in the presence of an organic metal salt. While these mechanisms are not clearly defined, the presence of the metal ion is clearly affecting how these monomers align themselves relative to each other, and thus having an effect on the final fate of the structure. The sodium ion may serve as an initial template of appropriate size, whereas the larger potassium ion may not be suited to template the appropriate conformation. This hypothesis may be supported by the gold ion experiments. Systematic variation of the counter ion used to self-assemble the nanostructures using otherwise identical conditions could yield informative results.

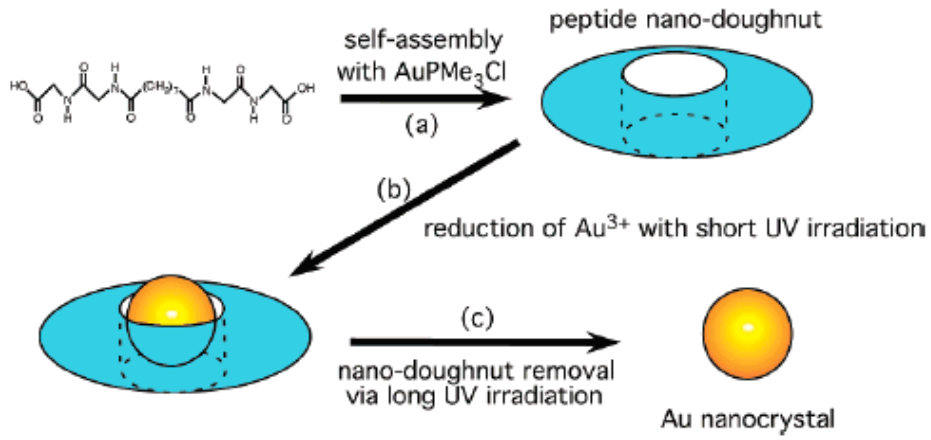


Figure 2-11. Scheme depicting self-assembly of peptide nanorings or nanodoughnuts, and application as templated growth mechanism for gold nanocrystals, taken from [105].

In conclusion, while significant progress has been made in understanding how to self-assemble these peptide nanotubes with a higher yield, much work remains to firmly elucidate the mechanism of self-assembly of the peptide nanotubes used. Computational studies should be performed, and quantitative analyses should be designed to experimentally test and reproduce the qualitative results obtained.

Chapter 3

NANOLITHOGRAPHY AND ALIGNMENT OF SELF-ASSEMBLED PEPTIDE NANOTUBE STRUCTURES

Three different methods of aligning self-assembled peptide nanotubes and nano-ring structures were developed. The first used nanolithography to create patterns of antigens on a substrate and enabled the alignment of antibody nanotubes. The second method used nanolithography to create patterns of bare gold in a self-assembled monolayer (SAM) that inhibited nanotube binding, and allowed attachment of thiol-functionalized nanotubes. The third method utilized peptide nanorings with a gold nanoparticle core, and aligned these nanorings with single spacing using a disulfide SAM. This chapter will be divided into three subsections based on each method of nanolithography-based patterning. A large portion of the material discussed in this chapter is taken from three publications to which the author of this thesis contributed significantly.

1. BIOLOGICAL BOTTOM-UP ASSEMBLY OF ANTIBODY NANOTUBES ON PATTERNED ANTIGEN ARRAYS

Here a new type of building block, antibody nanotubes, is introduced. Anchoring these nanotubes on complementary antigen arrays via antibody-antigen recognition is demonstrated. Biological recognition between the antibody nanotubes and the antigen arrays permitted recognition-driven assembly of ordered nanotube arrays. The array of antigens was written by using the tip of an atomic force microscope (AFM) on alkylthiol

self-assembled monolayer (SAM)-coated gold substrates via nanografting.[79] After antigens were immobilized onto the shaved regions of the alkylthiol SAMs with the AFM tip, antibody nanotubes, produced by incubating antibodies in template nanotube solutions, were selectively attached onto the antigen regions (Figure 3-1).

A template nanotube self-assembled from bolaamphiphile peptide monomers in NaOH / citric acid solution via three-dimensional intermolecular hydrogen bonds[2, 106] has been demonstrated to immobilize various proteins and peptides on nanotube surfaces[11, 18, 21]. This template nanotube immobilizes proteins and peptides at free amide sites on the nanotube sidewall via hydrogen bonding by means of simple incubations, the detailed procedures of which were published previously[10]. After those nanotubes were centrifuged and run through size-separation columns, a 1-mL solution of the resulting nanotubes (10 mM) with an average diameter of 100 nm were incubated with a 1-mL solution of goat anti-mouse IgG in a pH 7.2 phosphate buffer (50 ug/mL). After 48 hours, the anti-mouse IgG was coated on the template nanotubes to form the antibody nanotubes. The anti-mouse IgG nanotubes were washed with Nanopure water and centrifuged twice to remove unbound anti-mouse IgG before mixing with the antigen-coated substrates. The attachment of anti-mouse IgG on the nanotube was confirmed by fluorescence microscopy. The fluorescein-labeled anti-mouse IgG on the nanotube was also confirmed to recognize and bind the mouse IgG in solution. These results are shown in Figure 3-1e and 3-1f. To observe the selective immobilization of antibody nanotubes on the mouse-IgG arrays, systematic AFM analyses for the resulting substrates were performed (Figure 3-2). After 1-octadecanethiol (0.01 mM) was self-assembled on gold substrates in 99% ethanol at room temperature for 24 hours (Figure 3-

2a), a series of trenches (400 nm by 4 um) were made by shaving the alkylthiol SAM with a Si_3N_4 tip (Veeco Metrology) of the AFM (Nanoscope IIIa and Multimode microscope, Digital Instruments), as shown in Figure 3-2b (left). These trenches were patterned by using customized Nanoscript software written by the author. The section analysis of the trenches in Figure 3-2b (right) shows the depth of all trenches (marked by black dotted lines) is 10 nm. The substrate was washed sequentially first with ethanol and then with hexane, but the alkylthiol molecules removed by the AFM tip were still partially piled up and remained at the edges of trenches as shown in Figure 3-2b. After the mouse IgG was incubated with the resulting substrates for 1 hour at room temperature, the mouse IgG was deposited on the trenches via the thiol-gold interaction, as shown in Figure 3-2c[107]. The average height of trenches was observed to increase from -10 to +10 nm after incubating the mouse IgG, indicating the deposition of mouse IgG in the trenches[108]. When the anti-mouse IgG coated nanotubes were incubated in the buffer solution containing the mouse IgG-patterned substrate for 5 hours, the antibody nanotubes were observed to attach to the mouse IgG regions (Figure 3-2d) after washing the substrates with Nanopure water. The section analysis of this AFM image, Figure 3-2d, also supports the biological recognition-driven nanotube immobilization by increasing the height from +0 to +100 nm, which is consistent with the diameter of template nanotube. Figure 3-2e, the magnified AFM image of Figure 3-2d, shows that the multiple antibody nanotubes in the diameter of 100 nm were attached to the mouse IgG regions. The magnified AFM image of the anti-mouse IgG nanotubes in the height mode (inset in Figure 3-2e) shows that the antibody nanotubes were aligned along the trench while elongated particles were also observed at the upper side of mouse IgG region. At

this point, we are still investigating whether those particles are the aggregations of mouse IgG or the nanotube fragments.

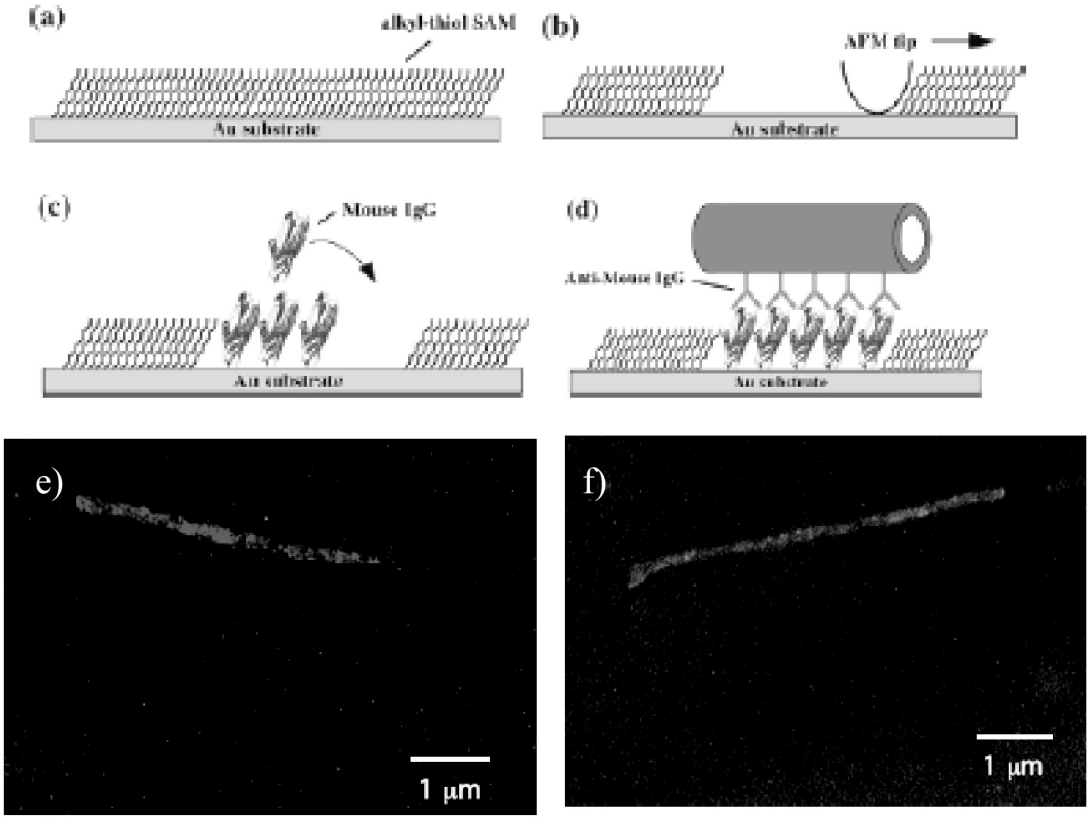


Figure 3-1. Schematic diagram of the antibody nanotube assembly on the complementary antigen substrates via biological recognition. (a) Self assembly of alkylthiol monolayers on gold substrates. (b) Shaving trenches on the alkylthiol SAM by using the AFM tip (nanoshaving). (c) Deposition of antigens in the shaved trenches (nanografting). (d) Location-specific immobilization of the antibody nanotube onto the complementary antigen regions via the biological recognition. (e) Fluorescence micrograph of the anti-mouse IgG nanotube coated with the fluorescein-labeled mouse IgG. The anti-mouse IgG nanotubes were incubated with a 1 mL solution of the fluorescein–labeled mouse IgG in a pH 7.2 phosphate buffer (50 ug/mL). After 5 hrs, the fluorescein-labeled mouse IgG was coated on the anti-mouse IgG nanotubes in the fluorescence micrograph, as shown below. This result indicates that the anti-mouse IgG on the nanotube does not lose the recognition function and binds the mouse IgG. It should be noted that this nanotube sample was not centrifuged and run through size-separation columns because the nanotube bundles were necessary to be clearly observable by fluorescence microscopy. (f) Fluorescence micrograph of the Alexa Fluor 546–labeled anti-mouse IgG-coated

nanotube. The 1 mL solution of the template nanotubes (10 mM) were incubated with a 1 mL solution of the Alexa Fluor 546–labeled goat anti-mouse IgG in a pH 7.2 phosphate buffer (50 ug/mL). After 48 hours, the anti-mouse IgG was coated on the template nanotubes to form the antibody nanotubes in the fluorescence micrograph, as shown below. It should be noted that this nanotube sample was not centrifuged and run through size-separation columns because the nanotubes were necessary to be in the form of the bundle to be clearly observable by fluorescence microscopy. Figure taken from [22].

To demonstrate that the assembly of antibody nanotubes is location-specific via biological recognition, the anti-mouse IgG coated nanotubes were incubated on the substrate patterned with the human IgG instead of the mouse IgG. As shown in Figure 3-3, no anti-mouse IgG-coated nanotubes attached to the human IgG regions patterned on the alkylthiol SAM/gold substrates via nanografting. This control experiment indicates the potential that multiple antibody nanotubes can be addressed onto patterned antigen regions respectively because the biological recognition and complexation of antibody nanotubes with complementary antigen SAMs are very specific, as observed in nature.

In summary, we observed that the biological recognition between the antibody nanotubes and the antigen arrays organized the antibody nanotubes as the ordered arrays. This technique is useful to fabricate advanced nanometer-scale devices with complex functionalities because multiple building blocks with a variety of protein functions can be addressed to specific locations on substrates in a simple process.

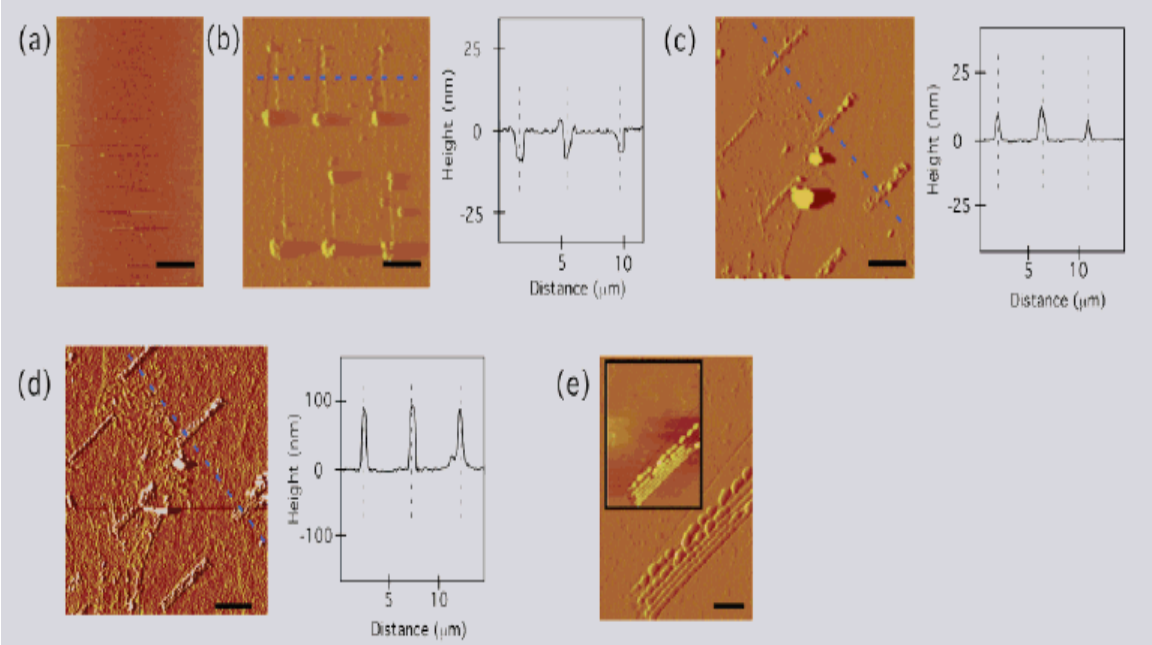


Figure 3-2. AFM images of (a) alkylthiol SAMs on gold substrate; (b) the array of trenches shaved by the AFM tip (left), the section analysis of (b) along a blue dotted line in the image (right), scale bar = 2um; (c) the array of trenches filled with mouse IgG (left), the section analysis of (c) along a blue dotted line in the image (right), scale bar = 1 um; (d) anti-mouse IgG-coated nanotubes immobilized on the mouse IgG-deposited regions (left), the section analysis of (d) along a blue dotted line in the image (right), scale bar = 1 um; (e) anti-mouse IgG-coated nanotubes immobilized on the mouse IgG-deposited regions in a higher magnification (inset: in the height mode), scale bar = 300 nm. The positions of trenches in the section analyses (b), (c), and (d), are shown by black dotted lines. Taken from [22].

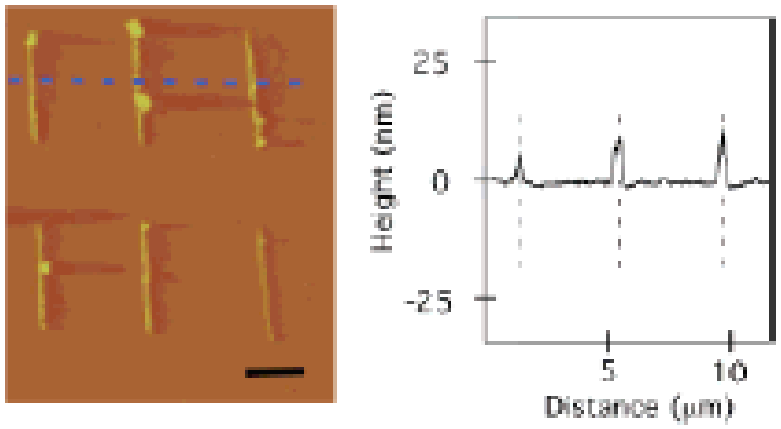


Figure 3-3. AFM image of the human IgG-deposited regions after the incubation of anti-mouse IgG-coated nanotubes. Scale bar = 2 um. No anti-mouse IgG nanotubes were

observed to attach onto the human IgG regions. Inset: The section analysis along a blue dotted line in the image. The positions of trenches in the section analyses are shown by black dotted lines. Taken from [22].

2. THIOLATED PEPTIDE NANOTUBE ASSEMBLY AS ARRAYS ON PATTERNED GOLD SUBSTRATES

In this study, the peptide nanotubes were used to examine the targeted immobilization because their sidewalls can be thiolated by simple procedures[12]. Peptide nanotubes, with average diameters of 200 nanometers, were assembled on the patterned gold pads to demonstrate the proof-of-principle of alignment. The peptide nanotubes were formed from bolaamphiphile peptide monomers in NaOH/citric acid solution[2, 106]. While the nanotubes were self-assembled via intermolecular hydrogen bonding between amide and carboxylic acid groups of the bolaamphiphile peptide monomers, the free carboxylic acid groups on the nanotube sidewalls were converted to thiols in the following two steps. First, the carboxylic acid groups of the nanotubes were substituted with NHS esters by reacting with *N*-hydroxysuccinimide (NHS) and ethyl-3-[3-(dimethylamino)propyl]carbodiimide (EDAC)[109, 110]. Because NHS esters bind amine groups covalently, the addition of 2-mercaptoethylamine to the NHS ester-functionalized nanotubes introduced thiol groups covalently linked to the nanotube surfaces[11]. The patterning of gold pads on substrates was achieved by AFM-based nanolithography (Nanoscope IIIa and Multimode microscope, Digital Instruments). For this fabrication, 1-octadecanethiol was used as a mask to prevent the nonspecific nanotube attachment and it was first self-assembled on the flat gold substrate (Figure 3-5a). This step is shown in Figure 3-4a. Then, the octadecanethiol self-assembled monolayer (SAM) was shaved by a Si_3N_4 tip (Veeco Metrology) to expose gold regions

(Figure 3-4b). The exposed gold trenches were patterned by using a customized Nanoscript software written by the author. After the gold trenches were drawn, the substrate was washed sequentially first with ethanol and then with hexane. However, in some substrates, the detached alkylthiol molecules by the AFM tip were still partially piled and remained at the edges of trenches. After the octadecanethiol (0.01 mM) was self-assembled on a gold substrate in 99% ethanol at room temperature for 12 hours, a gold trench (200 nm by 2 um) was created by the AFM tip, as shown in Figure 3-5b. In this AFM image, the brighter region represents the octadecanethiol SAM and the gold trench is darker due to their height contrast.

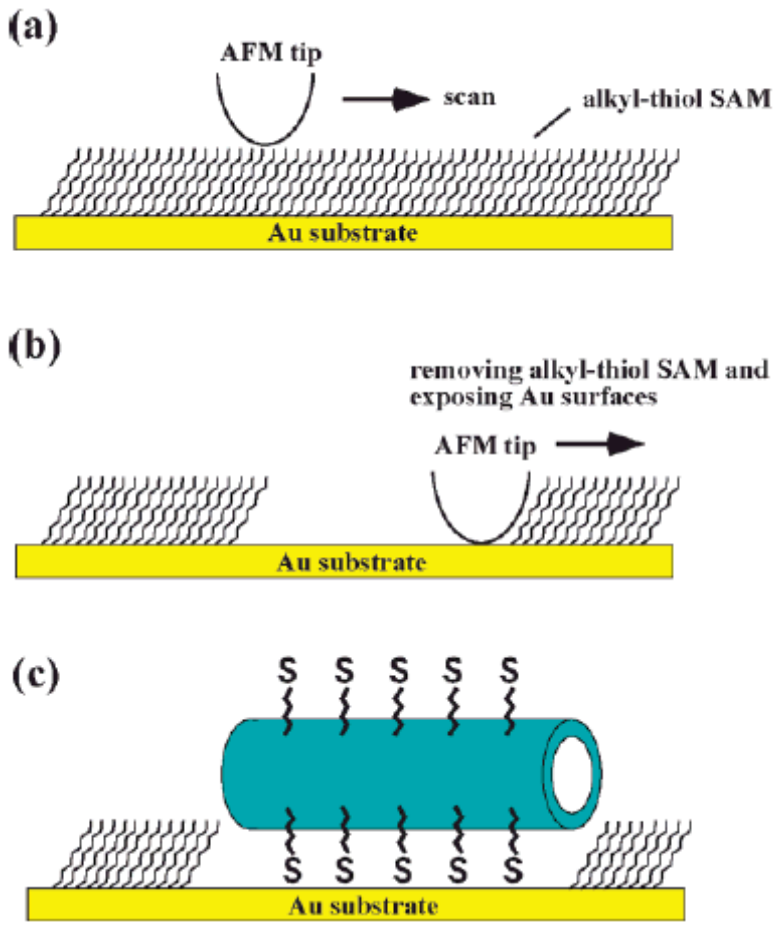


Figure 3-4. Schematic diagram of thiolated peptide nanotube assembly on the gold trench arrays. a) Self-assembly of alkylthiols on gold substrates. b) Shaving trenches on the alkylthiol SAM by using the AFM tip. c) Location-specific immobilization of the thiolated peptide nanotube onto the patterned gold trenches.

To attach the thiolated nanotubes to the patterned gold pads on the substrate, the nanotubes were incubated in solution containing the patterned substrate overnight at room temperature under nitrogen. After these substrates were washed thoroughly with ethanol/water solution, the thiolated nanotube was observed to attach selectively to the gold trench via the thiol-gold interaction, as shown in Figure 3-5c. This process corresponds to the step in Figure 3-4c. In this AFM image, the shaved region became higher as compared to the background due to the nanotube attachment because the nanotube diameter was larger than the height of octadecanethiol SAMs. This nanotube assembly on the patterned gold substrate could be scaled up with a larger number of nanotubes. When multiple gold trenches were shaved on the substrate and the nanotubes were incubated, most of the gold trenches were filled with the nanotubes, as shown in Figure 3-5d.

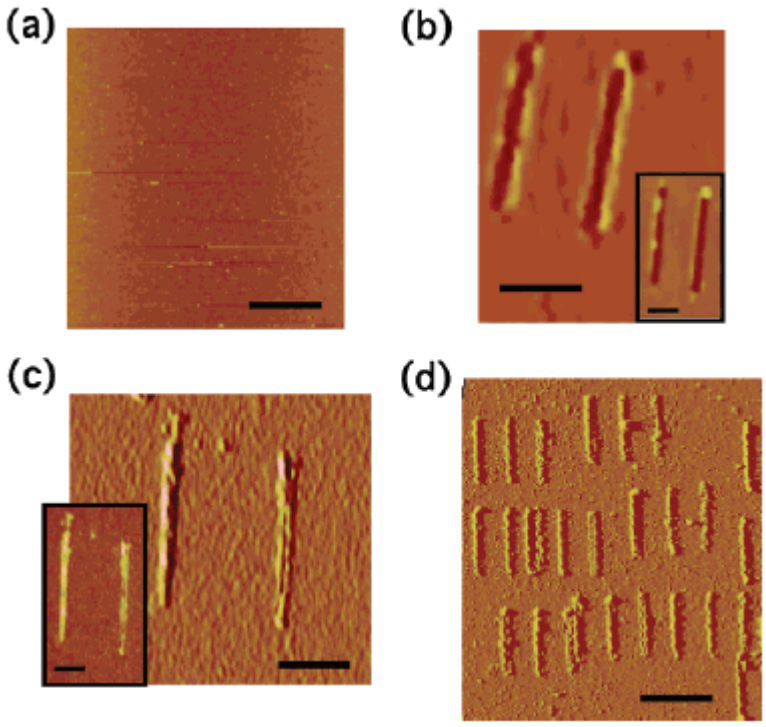


Figure 3-5. AFM images of (a) the alkylthiol SAM on the gold substrate, scale bar = 1 um. (b) The trench (200 nm x 2 um) shaved by the AFM tip, scale bar = 1 um. Inset: the AFM image in the height mode, scale bar = 500 nm. (c) The thiolated peptide nanotube attached on the trench, scale bar = 1 um. Inset: the AFM image in the height mode, scale bar = 500 nm. (d) The thiolated peptide nanotubes attached on the 200 nm-trench array, scale bar = 2 um.

Statistically, about 90% of the gold trenches were observed to have thiolated nanotubes in the AFM images. The thiolated peptide nanotubes in the diameter of 200nm were assembled effectively onto gold trenches of comparable size. But the selective attachment of the nanotube to the larger gold trenches was not demonstrated yet. We produced a 1.5 um by 3 um gold trench by the same procedure and examined how the thiolated nanotubes recognize the larger gold trenches. When nanotubes were incubated in solution containing the patterned substrate overnight at room temperature under nitrogen, the multiple nanotubes with the diameter of 200 nm were attached in the 1.5 um long exposed gold trench (Figure 3-6a). About 90% of nanotubes were aligned parallel

in a close-packed manner, and the magnified AFM images in Figure 3-6b clearly show that eight nanotubes with average diameter of 200 nm were aligned inside the trench. Previously, multiple antibody-coated nanotubes were packed in the trenches functionalized by the complementary antigens in the same alignment as observed in this system[22]. Carbon nanotubes were also aligned on the polar molecular patterns on gold[76]. In both cases, the concentrations of nanotubes and the inter-nanotube interactions seem to be important factors for alignment, and the thiolated peptide nanotube alignment in the larger trench likely occurred in the appropriate nanotube concentration. Further systematic alignment studies as a function of the nanotube concentration are necessary to understand the alignment mechanism of the thiolated peptide nanotubes.

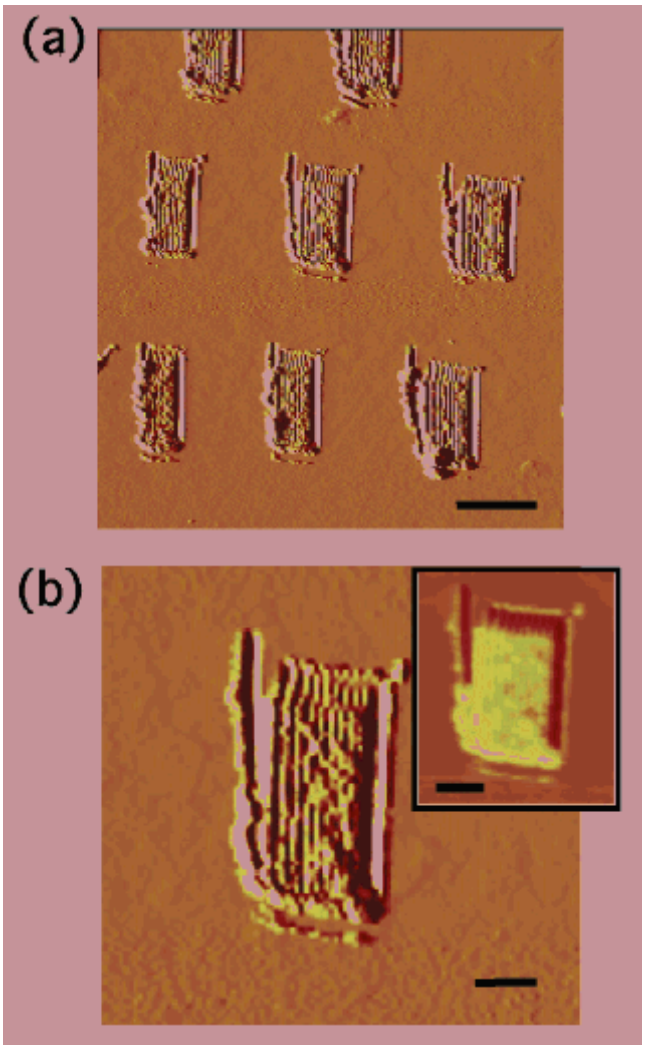


Figure 3-6. AFM images of (a) the multiple thiolated peptide nanotubes attached inside the large gold trench (1.5 um x 3 um), scale bar=2.5 um; (b) the magnified AFM image of (a), scale bar =700 nm. Inset: the AFM image in the height mode, scale bar=800 nm.

In summary, the peptide nanotubes whose sidewalls were thiolated could be assembled onto gold trenches patterned on alkylhiol SAMs. When the diameter of the nanotubes was comparable to the width of gold trench, about 90% of the trenches were attached by nanotubes. As the width of trench was increased, multiple nanotubes were observed to attach inside the large gold trench in a close-packed manner. Peptide nanotubes with diameters of 200 nm were used as a proof-of-principle to demonstrate

that this approach may lead to an alternative nontraditional fabrication method in order to address nanometer-scale building blocks for device fabrications with simple chemical procedures. However, smaller nanotube assembly is desirable to be comparable to conventional photolithographic fabrications.

3. SELF-ASSEMBLY OF GOLD NANOPARTICLE-CONTAINING PEPTIDE NANO-RINGS ON SURFACES

Ring-shaped peptide nanostructures, like those described previously[105], were assembled as an array on surfaces. By reduction of the gold ions trapped inside the cavities of nano-rings, the peptide nano-rings could template the growth of new gold nanoparticles. After the gold nanoparticles were grown, these nano-rings containing gold nanoparticles can be aligned on the chemically functionalized arrays patterned by nanolithography as shown in Figure 3-7. The peptide nano-rings were self-assembled in a close-packed manner along the array of those dithiolated self-assembled monolayers (SAMs). These gold nanoparticles were positioned with equal spacing on each line without touching each other using the peptide nano-rings as spacers. This type of alignment of nanomaterials with spacers can be very useful for improved photonic crystal designs.

When the peptide monomers were self-assembled in the presence of the water-insoluble trimethylphosphinegold chloride ($AuPMe_3Cl$) for 5 days in the dark, the ring-shaped peptide assemblies were observed in solution. The average outer diameter of nano-ring was 50nm and the average inner diameter was 15 nm[105]. Previous spectroscopic investigation showed that these peptide nano-rings were self-assembled

from the peptide monomers and the organic gold salts by chelating gold with amide groups of the peptide monomers. After 20 minutes of UV light irradiation of the nano-ring solution, gold nanoparticles were grown inside the cavities of nano-rings[18, 105].

In a TEM image of the nano-ring after reduction of gold ions, the gold nanoparticle appeared darker at the center of the nano-ring as shown in Figure 3-8a. These particles in the cavities were also confirmed as gold nanoparticles by electron diffraction before their assembly on the dithiol SAMs. When the peptide nano-rings were previously synthesized, they were observed to be stable in solution[105] however these nano-rings have not been assembled on surfaces. Therefore, it was necessary to examine their stability during the assembly process. Before fabricating the structure shown in Figure 3-7, we examined whether the gold nanoparticle-containing peptide nano-rings are rigid enough to be self-assembled on surfaces by spin-coating them on TEM grids.

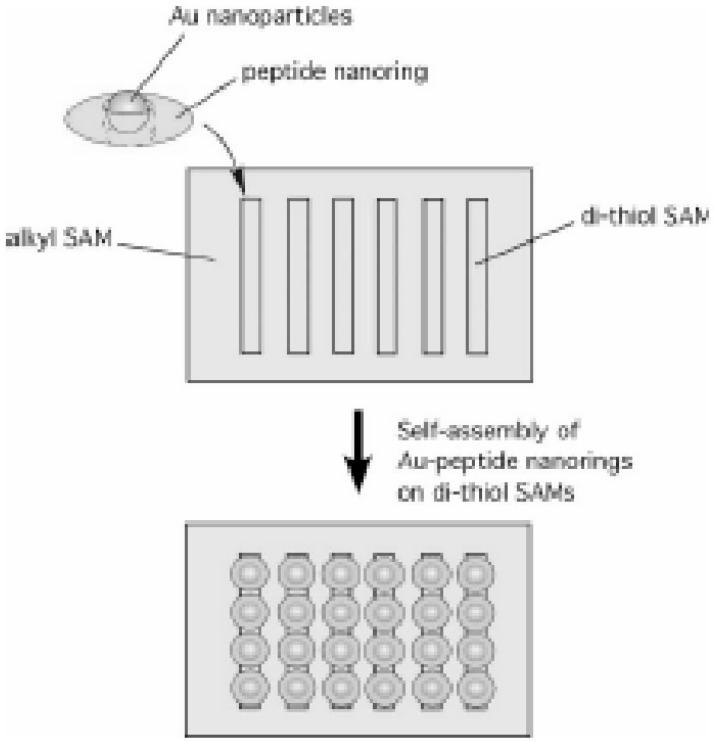


Figure 3-7. Illustration of gold nanoparticle-containing peptide nano-ring assembly on the patterned gold substrate.

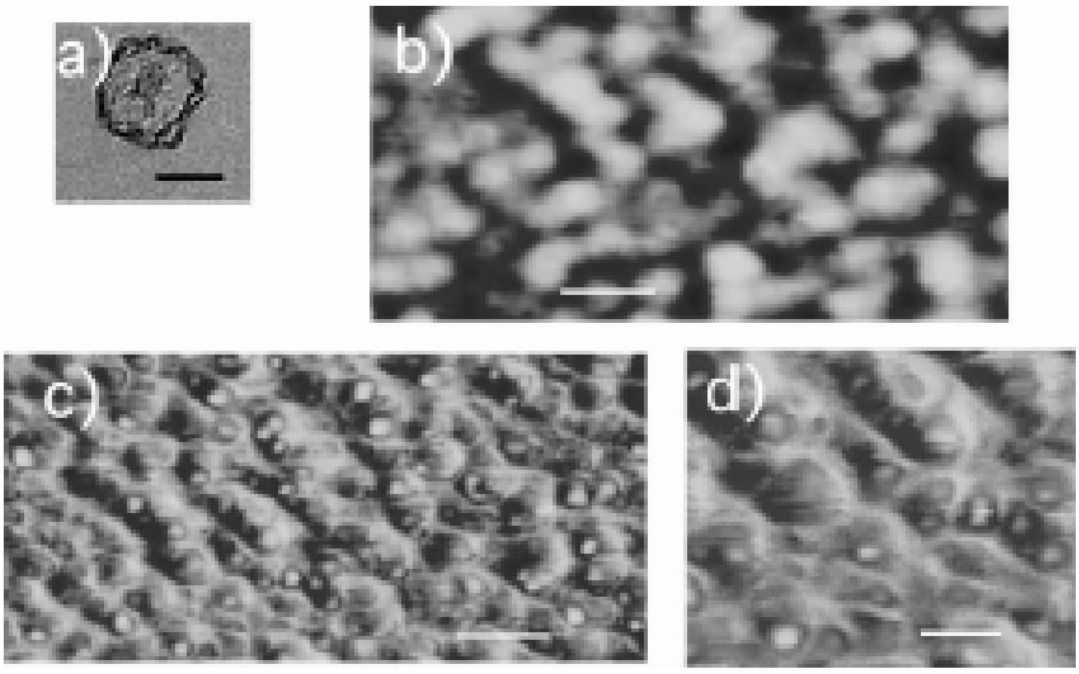


Figure 3-8. (a) TEM image of the peptide nano-ring containing a gold nanoparticle inside the cavity, scale bar=50 nm. (b) AFM image of spin-coated peptide nano-rings containing gold nanoparticles in their cavities on TEM grids in height mode, scale bar=80nm. (c) AFM image of spin-coated peptide nano-rings containing gold nanoparticles in their cavities on TEM grids in phase mode, scale bar=80nm. (d) the phase AFM phase image in high magnification, scale bar=40 nm.

An AFM height image in Figure 3-8b confirms that the nano-rings were deposited on a TEM grid. This figure imaged the assembly of the nano-rings on the surface, but the gold nanoparticles inside the nano-rings could not be resolved in this AFM height image. However, when this assembly was imaged by the phase mode of AFM as shown in Figure 3-8c, the gold nanoparticles were observed as a brighter contrast inside the nano-rings because harder surfaces of gold nanoparticles appeared brighter than softer surfaces of the outer peptide nano-rings. In the magnified phase image of Figure 3-8d, these gold nanoparticles were not exactly located at the center of the nano-rings, which may be due to the deformation of the nano-ring shape via spin-coating and the multiple orientations of the nano-rings on the TEM grid.

Since the peptide nano-rings were stable enough to be assembled on TEM grids via spin-coating, we examined the targeted self-assembly of the peptide nano-rings on functionalized surfaces. The functionalized array of dithiol SAMs was patterned by three steps. First, alkyl SAMs were deposited on a gold substrate and the array was patterned by removing the alkyl SAMs with the AFM cantilever. Then, mercaptohexadecanoic acid was assembled on the curved array where gold surfaces were exposed. The carboxylic groups on the top of these SAMs on trenches were substituted by thiol groups, as shown in Figure 3-9. To align the peptide nano-rings containing gold nanoparticles on

the dithiol SAM array patterned on a gold substrate as shown in Figure 3-7, these nano-rings were incubated with this substrate in solution for 8 hours.

Because the end groups of the SAMs on the trenches were functionalized with thiol groups (Figure 3-9), this incubation process allowed the nano-rings to self-assemble onto these trenches with the thiol-gold interaction, as shown in Figure 3-10. Figure 3-10a is the AFM image of the patterned substrate in the height mode after the nano-rings were incubated in the substrate-containing solution. The peptide nano-rings were closely packed to form the array of continuous lines along the trenches in Figure 3-10a.

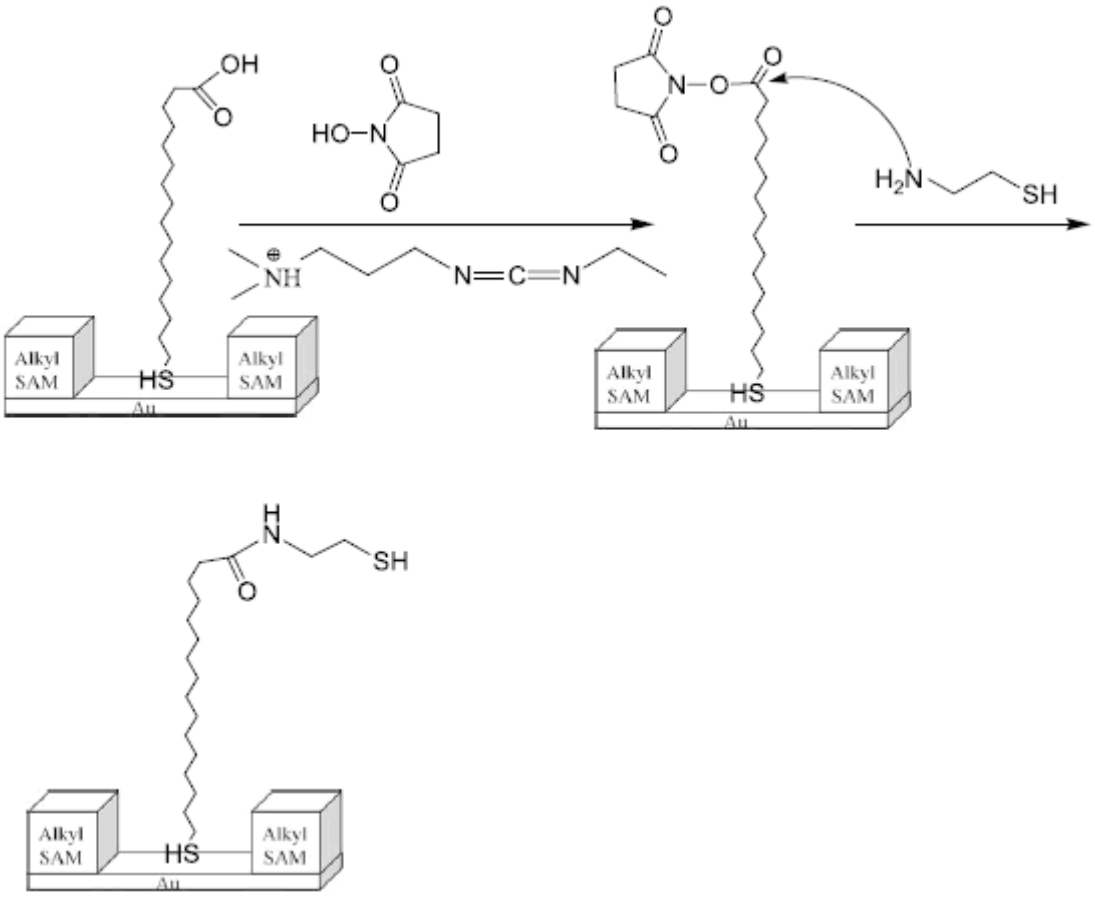


Figure 3-9. Fabrication of dithiol SAMs on patterned gold substrates.

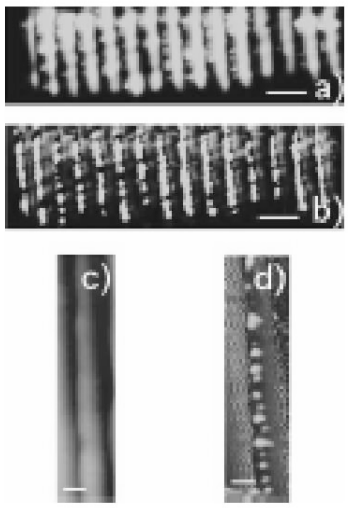


Figure 3-10. AFM images of gold nanoparticle-containing peptide nano-rings assembled on the dithiol SAM-patterned in (a) height mode, scale bar=300 nm (b) phase mode, scale bar=300 nm (c) height mode in high magnification, scale bar=50 nm, (d) phase mode in high magnification, scale bar=50 nm.

As seen in the height mode AFM image of the spin-coated samples in Fig. 3-8b, the individual gold nanoparticle inside the nano-ring could not be identified in Fig. 3-10a due to their small height difference between the peptide nano-ring and the gold nanoparticle. However, in the phase mode AFM image of this substrate, the deposited spheres on the trenches looked less continuous in Figure 3-10b since the brighter spheres in this phase image are more likely gold nanoparticles, due to their surface hardness as compared to the one for the peptide nano-rings. While these AFM images in the phase mode in low resolution do not explicitly show the discrete positioning of gold nanoparticles inside the nano-rings aligned on the trenches as shown in Figure 3-7, the high-resolution image of the single trench containing the peptide nano-rings in the phase mode assisted visualizing the peptide nano-ring alignment more clearly. When the single trench was imaged with the height mode image in high-resolution (Figure 3-10c), still only continuous packing of the nano-rings was observable as a line along the trench and

the discrete gold nanoparticles could not resolve. But when the single trench was imaged in the phase mode, discrete alignment of gold nanoparticles was observed as shown in Figure 3-10d. In this image, the harder gold nanoparticles appeared to be brighter and the spacing between these nanoparticles was visible. Most of the gold nanoparticles in Figure 3-10d were self-assembled discretely without touching each other due to the spacing of the peptide nano-rings (Figure 3-7). The darker nano-ring contrast around the gold nanoparticle, observed in the spin-coated sample in Figure 3-8b, was not observed clearly in Figure 3-10d, however this phase contrast difference between the spin-coated nano-rings and the self-assembled nano-rings may be caused by their topological differences. For the self assembled sample, the nano-rings were self assembled on rough surfaces consisting of alkyl SAMs and dithiol SAMs in different heights. The trenches were also not flat because the AFM cantilever could not shave alkyl SAMs smoothly and it further scraped the gold substrate partially. Shaved SAM molecules and gold substrate atoms were piled at the edges of trenches, which also increased the roughness of the substrate.

When neat gold nanoparticles without the peptide nano-rings were assembled on the same dithiol-functionalized trenches, those gold nanoparticles were aligned in continuous lines without spacing in their phase AFM image. This observation supports that the gold nanoparticles observed in Figure 3-10d were separated by the peptide nano-rings, otherwise the spacing between gold nanoparticles would not have been observed. It should be noted that some of these nanoparticles seem to contact each other in Figure 3-10d due to the deformation of the nano-rings during the self-assembly, which was also observed in the spin-coated sample in Figure 3-8.

Bis(N-a-amido-glycylglycine)-1,7-heptane dicarboxylate was synthesized and recrystallized as previously described in chapter 2 of this thesis. 1-Ethyl-3-[3-(dimethylamino) propyl]carbodiimide hydrochloride (EDAC), N-hydroxysuccinimide(NHS), 2-mercaptoethylamine, trimethylphosphinegold chloride, 16-mercaptohexadecanoic acid and octadecanothiol were used as received from Aldrich. Annealed gold substrates were purchased from Molecular Imaging (Agilent AFM). A series of trenches (100 nm by 1 mm) were made by shaving the alkylthiol SAM with a Si_3N_4 tip (Veeco Metrology) of the AFM (Nanoscope IIIa and Multimode microscope, Digital Instruments). These trenches were made by customized Nanoscript software written by the author. Formvar Film 200 Mesh copper TEM grids were obtained from Electron Microscopy Sciences. The UV-Lamp had a power of 14 mW/cm^2, and a wavelength of 254 nm.

After peptide monomer of bis(N-a-amido-glycylglycine)- 1,7-heptane dicarboxylate, 0.028 g, was dissolved in 10 mL of water and the pH of this solution was adjusted to 5.5 with citric acid, an excess amount of an organic gold precursor, trimethylphosphinegold chloride ($AuPMe_3Cl$) was added to this solution. After 5 days in the dark, the peptide nano-rings were observed to have an outer diameter of 50 nm and an inner diameter of 15 nm. The nano-ring solution was washed with deionized water and centrifuged at 14.5 krpm, and then gold ions trapped inside the peptide nano-rings were reduced by a UV light (14 mW/cm^2, 254 nm) for 20 min. The resulting gold nanoparticles were observed to be about 15 nm in an average diameter from AFM images.

In order to pattern the peptide nano-rings containing gold nanoparticles in their cavities as an array on gold substrates, an array of dithiolated SAMs was patterned by a cantilever of an atomic force microscope (AFM) with the following sequence. First, 1-octadecanethiol (0.01 mM) was self assembled on gold substrates in 99% ethanol at room temperature for 12 hours. Then, an array of trenches (100 nm by 1 mm) was created by removing the alkylthiol SAMs by the tip of AFM via nanolithography. On these trenches where gold surfaces were exposed, 16-mercaptohexadecanoic acid (0.01 mM) was self-assembled for overnight. After the resulting substrates were washed by deionized water, the end groups of the SAMs on trenches were functionalized by thiol via substituting carboxylic acid groups with thiol groups as shown in Figure 3-9. In Figure 3-9, the functionalized gold substrates were immersed in aqueous solution containing 400 mL of ethyl-3-[3-(dimethylamino)propyl]carbodiimide (EDAC, 75mM) and 400 mL of N-hydroxy succinimide (NHS, 15 mM) for 30 min. Then, as shown in the step 3 in Figure 3-9, 800 mL of 2-mercaptoethylamine (15mM) was incubated in the solution for 24 hours to modify the ends groups of the SAMs in trenches to thiol groups.

When the peptide nano-rings containing gold nanoparticles in their cavities were mixed with the dithiolated SAM-patterned surfaces in aqueous solution for 8 hours, the nano-rings were self assembled on the trenches with the thiol-gold interaction. After these substrates were washed with deionized water, the attachment of the peptide nano-rings on the arrayed trenches was confirmed by AFM. The height mode AFM image was used to observe the topology of the nano-ring assembly. The phase mode AFM image was used to observe the location of gold nanoparticles, since the different hardness of surfaces between gold nanoparticles and peptide nano-rings enables the ability to

distinguish each of them respectively in the trenches. We also assembled the peptide nano-rings containing gold nanoparticles on TEM grids by spin-coating to examine whether the nano-rings can be packed on surfaces without distraction. The TEM grids were fixed on the top of mica substrates, which were also attached on AFM metal sample pucks. After the gold nanoparticle-containing peptide rings were spin-coated on the TEM grids, the resulting coatings were examined by AFM.

The monomer for the self-assembled nanotubes, bis(*N*-amido-glycylglycine)-1,7-heptane dicarboxylate, was prepared as described elsewhere[104]. To self-assemble the peptide nanotubes, the monomer was dissolved in 30 mM NaOH to form a 10 mM solution. The pH of the solution was adjusted to 4.6 with 50 mM citric acid. The pH-adjusted solution was placed at room temperature and the peptide nanotubes appeared in the solution after two weeks. The resulting nanotubes were washed with deionized water and centrifuged (14,500 rpm) for 10 min.

The peptide nanotubes in 200 uL aqueous solution were mixed with NHS (15 mM), and then 200 uL of EDAC (75 mM) was added to the solution and vortexed for 30 minutes. This procedure was followed by centrifuging the nanotube solution for 1 h and then washing with water. After nitrogen was bubbled through the nanotube solution for 30 min, the nanotube sample was treated with 0.1 mM solution of 2-mercaptoethylamine. The mixture was again vortexed for 1 hour and the nanotubes were centrifuged. After the nanotube solution was left at 4 °C overnight, the nanotubes were centrifuged and washed immediately prior to the attachment to the patterned gold trenches.

gold substrates were purchased from Molecular Imaging. The substrate was washed thoroughly with 99% ethanol prior to the use. After 1-octadecanethiol (0.01

mM) was self-assembled on gold substrates in 99% ethanol at room temperature for 12 hours, the substrate was washed in ethanol for AFM-based nanolithography.

Chapter 4

MULTIPLEXED PEPTIDE NANOTUBE BIOSENSOR PATHOGEN ASSAY

1. INTRODUCTION

Rapid, sensitive, and selective detection of viruses is of continued importance in the areas of medical diagnostics and biological warfare defense. In this section of study, several viruses were used as example analytes. Herpes Simplex Virus Type 1 (HSV-1) is known to cause cold sores around the mouth, and Herpes Simplex Virus Type 2 (HSV-2) is known to cause genital herpes[1]. In both of these cases, spread of the virus can occur when patients do not actively exhibit symptoms, thereby spreading the disease unknowingly. Adenovirus is a virus that causes up to 10% of acute respiratory infections in children, with infections also possible in the eyes, intestines and urinary tract[111]. Simian Virus 40 (SV40) is a natural virus that is typically asymptomatic in otherwise healthy monkeys[112]. Interest in SV40 increased in the early 1960's after its discovery as a contaminant in some 98 million injected polio vaccines. Studies have shown SV40 associated with mesothelioma tumors, or lung cancer, as well as some brain and bone tumors[113-115]. Influenza has many strains and is the cause of the common flu, and more recently the source of much public fear of bird flu[116].

When a solution containing a low concentration of viruses was added to a nanotube biosensor solution, the nanotubes bound the target viruses in a "hub and spoke" shaped fashion (Figure 4-1a). At higher virus concentrations, multiple virus "hubs" merged together and allowed the proportional addition of more nanotube "spokes" which form larger network structures (Figures 4-1b, 4-1c). This created a proportional

relationship between the virus concentration and the size of the aggregates. Each nanotube was of approximately equal fluorescence intensity, which created a proportional relationship between the average aggregate fluorescence intensity and the virus concentration in the aggregate. A selected antibody was attached to both ends of the nanotubes and dye molecules were covalently bonded along the entire length of the nanotubes. This nanotube scaffold created a ratio of dye molecules per antibody of approximately 10^4:1, significantly improving the stoichiometry of 1:1 when dyes were covalently bonded directly to antibodies.

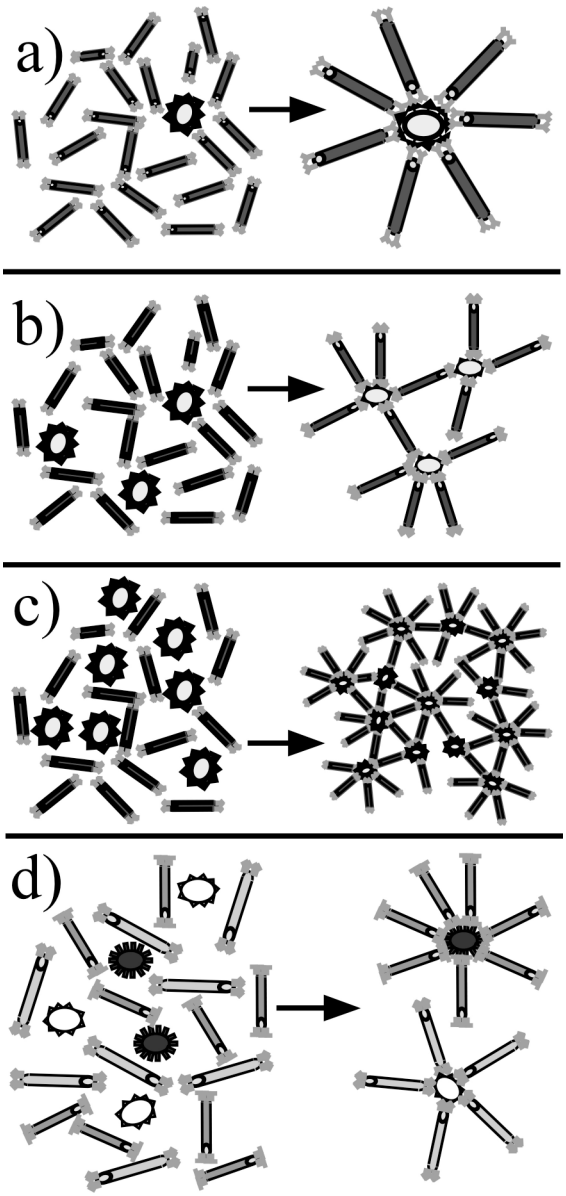


Figure 4-1. a) Illustration of the "hub and spoke" structure formed when the biosensor nanotubes bind to a single virus, shown at low initial virus concentrations. b) Illustration of the smaller network structures formed when biosensor nanotubes bind a few viruses, such as at intermediate virus concentrations. c) Illustration of the larger network structures formed when the biosensor nanotubes bind several viruses, such as at high initial virus concentrations. d) Illustration of two virus detection mechanisms, showing how red dye-labeled nanotube biosensors (dark gray) which contained antibody against the black viruses with rectangular antigens aggregated independently. Simultaneously, green dye-labeled nanotube biosensors (light gray) which contained antibody against the white viruses with triangular antigens aggregated independently.

2. SINGLE VIRUS DETECTION

a) Structure of nanotube-virus aggregates

The structure of the formed aggregates was observed by transmission electron microscopy. At 10^6 pfu/mL, large network structures like those in Figure 4-2a were observed. This result was consistent with the mechanism depicted in Figure 4-1. A unique advantage to this system was that the nanotubes allow rapid visualization by light microscopy of the presence of viruses not normally visible by light microscopy. As the aggregates grew in size by incorporating more viruses and nanotubes, a rapid qualitative observation of the presence of a target pathogen could be made by using a fluorescence microscope and observing a specific color aggregate, as depicted in Figure 4-2b. While it was not possible to precisely determine the size or fluorescence intensity of the network structures, and therefore the number of viruses in the solution or even in a given aggregation, using a bench top fluorescence light microscope provided a simple method of qualitative assessment when a low limit of detection is not required of the assay.

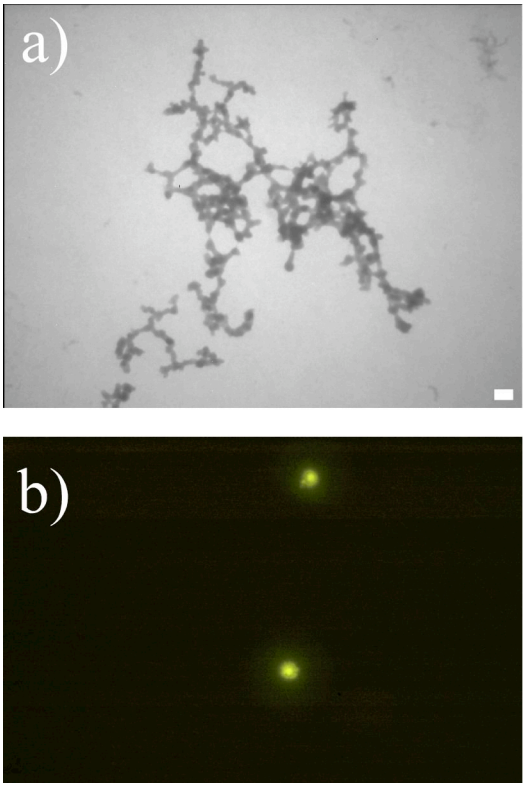


Figure 4-2. a) TEM image of high virus concentration (10^6 pfu/mL Adenovirus Type 3 added), scale bar = 1um; b) Fluorescent microscope image of high virus concentration sample (10^6 pfu/mL Adenovirus Type 3).

b) Detection by Flow Cytometry using FSC vs. FL-1 data channels

Flow cytometry allowed analysis of any suspension. The suspension was diluted upon intake to the flow cytometer to pass no more than one cell, particle, nanotube, or virus-nanotube network structure per drop through the laser detection system. This allowed the scattering and fluorescence intensity information to be gathered on each aggregate individually. Forward scattering (FSC) intensity increased as particle size and refractive index increased. Side scattering (SSC) provided surface roughness information[32]. Since the nanotubes all had the same refractive index, the change in size of aggregates was the only contribution to the change in FSC. Discussion to follow on page 86 will demonstrate why measurement of the FSC size changes and fluorescence

intensities were the preferential data channels to study. Flow cytometry simultaneously collects multiple data channels including FSC, SSC, and multiple Fluorescence data channels.

Using virus-free control samples with software gating, one could identify where the background noise from sample buffers, water, and leftover unreacted nanotubes that did not bind a virion occurred. Exploiting the strengths of the software eliminated the need for any washing steps of the samples. Removal of a washing step prevented accidental loss of viruses, reduced the number of chances for contamination to be introduced, and met the criteria of an efficient and simple testing protocol. This process of gate selection began by examining the negative control samples containing only raw peptide nanotubes before mixture with viruses (Figure 4-3a), Adenovirus stock (Figure 4-3b), and 1X PBS buffer (Figure 4-3c). The virus stocks were run to demonstrate that these particles were too small to be detected by the flow cytometer directly. The buffer solution demonstrated that there was no background fluorescence interference, nor any nanometer sized air bubbles introduced from the flow pumping system.

By next looking at the positive controls of 10^2 pfu/mL (Figure 4-3d) and $10^{5.5}$ pfu/mL (Figure 4-3e), one could draw a gated region that included the peptide nanotube biosensor networks of all sizes while eliminating the background noise factors. An example gate was shown in Figures 4-3a to 4-3e, and subsequent histograms of the fluorescence intensity of the gated regions were shown as insets below the dot plots. Notice that the gates were drawn to exclude a maximum area of unbound nanotubes while simultaneously including a maximum area where nanotube aggregates were found to occur.

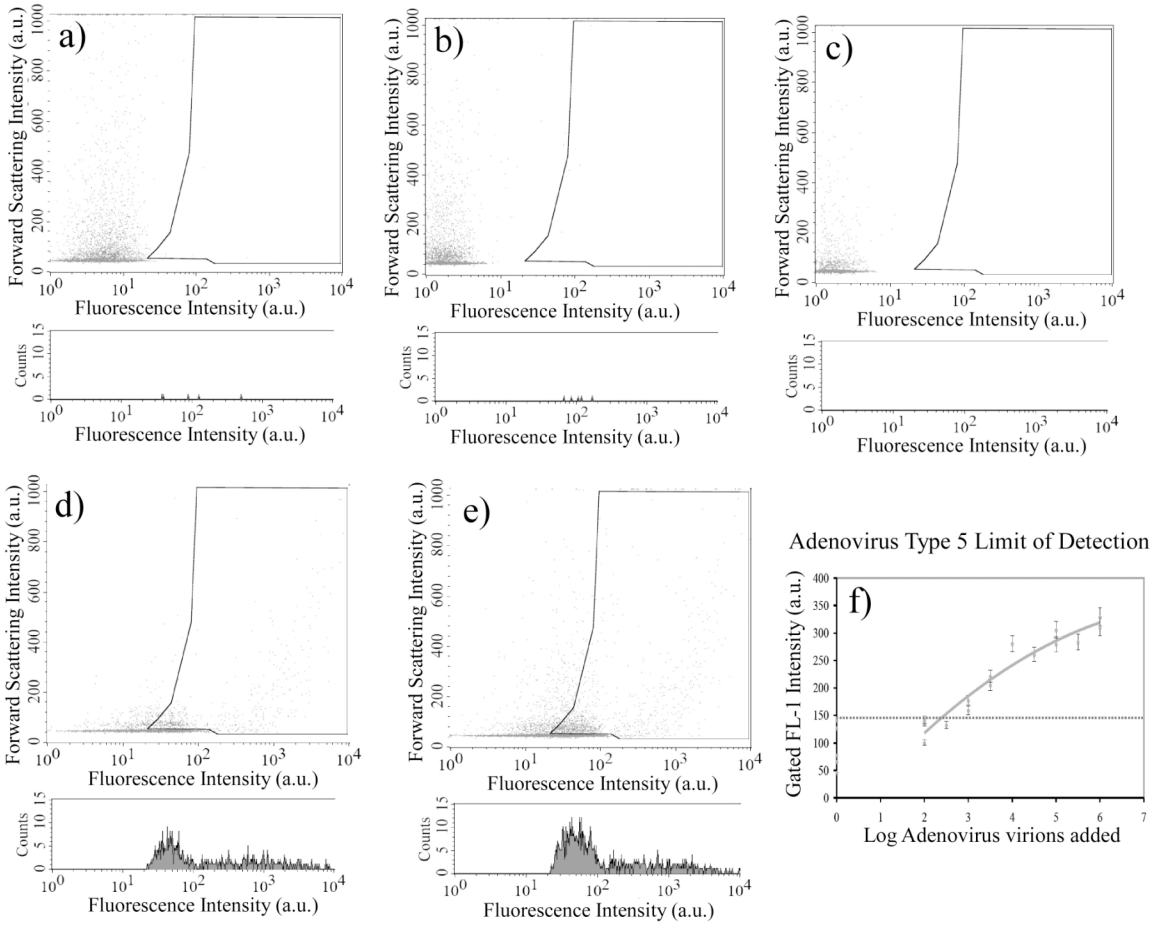


Figure 4-3. Forward Scattering (FSC) vs. Green Fluorescence Intensity (FL-1) dot plot of a) nanotubes only, b) Adenovirus stocks (10^6 pfu/mL), c) 1X PBS buffer, d) 10^2 pfu/mL AV3, e) $10^{5.5}$ pfu/mL AV3; histogram of fluorescent intensities observed for the gated region in frames a-e are shown as insets below the dot plot. f) Limit of detection standard curve plots created using average gated fluorescence intensity vs. concentration of virus added.

The process of gate selection and creating a standard curve required some preparation time in advance. Once this preliminary work was completed, a gating protocol and standard curve could be applied to many unknown samples. The limit of detection results for all virus and antibody combinations studied by flow cytometry were

summarized in Table 4-1 on page 84. In Figure 4-4, Influenza type A antigen was analyzed. In Figure 4-4a, the nanotubes were shown in a green fluorescence intensity vs. forward scattering intensity dot plot as a negative control. In Figure 4-4b, 50 nm gold nanoparticles were shown to show detection by size of small nanoparticles was not feasible. In Figure 4-4c, the undiluted Influenza A antigen stocks were shown. In Figure 4-4d, the solvent used for the dilutions in this experiment, distilled water, was shown. In Figure 4-4e, nanotube biosensors mixed with Influenza A antigen at 10^2 pfu/mL was displayed, while in Figure 4-4f, nanotube biosensors mixed with Influenza A antigen at 10^6 pfu/mL was shown. In this case, the gate was drawn to exclude a maximum number of unbound nanotubes from the negative control, yet include a maximum number of the aggregated nanotube-virus structures. However, while the solvent and virus stock background noise was entirely excluded, it was chosen to not exclude entirely the unbound nanotube events. As shown by the histogram insets below each dot plot, there were unbound nanotubes included in the gate selection which created a background average fluorescence intensity or an empty-cell fluorescence average intensity. By using this background average fluorescence intensity as a threshold criterion, the user could define positive samples as only those with average fluorescence intensities higher than the negative control. Even before examining the limit of detection plot, the histograms visually show that the positive controls in Figure 4-4e and 4-4f had a higher number of events in the fluorescence intensity ranges above 10^2 arbitrary units. These histograms included more fluorescent events between 10^2 and 10^3 arbitrary units when compared to the negative control in Figure 4-4a, and also contained significantly more events in the region above 10^3 arbitrary units when compared to the negative control. Despite the

differences in gate selection between Adenovirus Type 3 and Influenza A antigen, it did not affect the limit of detection or the quality of the measurements. The ability to resolve virus concentration without having to wash out unbound nanotubes was also retained, maintaining the simple protocol for sample handling.

It was also noteworthy that the samples provided for analysis of the Influenza A antigen and Influenza B antigen (to be described with Figure 4-5) were not whole viruses in the stocks, but rather free proteins in solution that were the antigens used when raising the antibodies against the actual viruses. In this case, the biosensors were assaying for free protein rather than for the actual virus. This led to the discovery that this assay could work equally well on whole viruses or even free proteins in solution. Future work could further determine the broader capabilities of this multifunctional peptide nanotube based assay to perhaps include all materials that can be detected by antibodies when combined with the SV40 results to be discussed on pages 77 to 81.

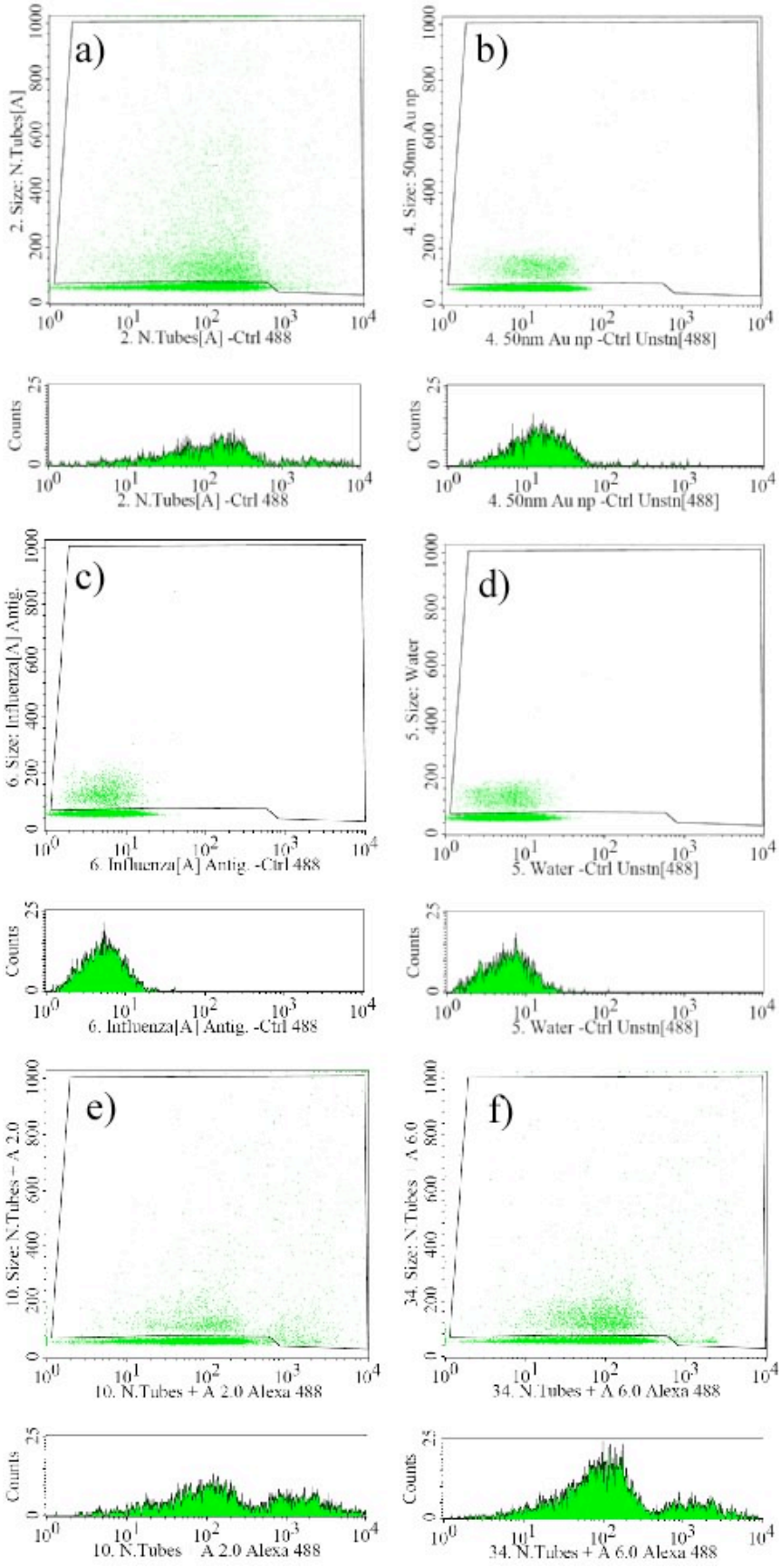

a)
2. Size: N.Tubes[A]
2. N.Tubes[A] -Ctrl 488
Counts
2. N.Tubes[A] -Ctrl 488
b)
4. Size: 50nm Au np
4. 50nm Au np -Ctrl Unstn[488]
Counts
4. 50nm Au np -Ctrl Unstn[488]
c)
6. Size: Influenza[A] Antig.
6. Influenza[A] Antig. -Ctrl 488
Counts
6. Influenza[A] Antig. -Ctrl 488
d)
5. Size: Water
5. Water -Ctrl Unstn[488]
Counts
5. Water -Ctrl Unstn[488]
e)
10. Size: N.Tubes + A 2.0
10. N.Tubes + A 2.0 Alexa 488
Counts
10. N.Tubes + A 2.0 Alexa 488
f)
34. Size: N.Tubes + A 6.0
34. N.Tubes + A 6.0 Alexa 488
Counts
34. N.Tubes + A 6.0 Alexa 488

Figure 4-4. Influenza A gate selection. a) nanotube only negative control; b) 50nm gold nanoparticles; c) Influenza A antigen stocks, 10^7 pfu/mL; d) water; e) nanotube biosensors + Influenza A 10^2 pfu/mL; f) nanotube biosensors + Influenza A 10^6 pfu/mL. Insets below each dot plot show histograms of the fluorescence intensities recorded in the gated regions.

In the case of Influenza B antigen, several controls were also used to determine the appropriate gate selection. In Figure 4-5a, the negative control of nanotubes only was shown. In Figure 4-5b, 50nm gold nanoparticles were shown, with the gated events looking remarkably similar to that of the solvent background shown in Figure 4-5d. In Figure 4-5c, undiluted Influenza B antigen stocks of 10^7 pfu/mL were shown. In Figure 4-5d, the solvent used for diluting samples, distilled water, was shown. In Figure 4-5e, the positive control of nanotube biosensors mixed with Influenza B antigen at a 10^2 pfu/mL concentration was shown. In Figure 4-5f, nanotube biosensors mixed with Influenza B antigen at a 10^6 pfu/mL concentration was shown. Inset below each dot plot was the histogram with the number of gated events at any given fluorescence intensity. Similarly to the case for Influenza A, the gate selection attempts to maximize the area where nanotube aggregates were found, while excluding the areas of noise from solvent and virus stocks and minimizing the areas including unbound nanotubes. As with the Influenza A gates, the Influenza B gates included unbound nanotubes in the calculations, however the background average fluorescence intensity for the empty cell condition of the negative control enabled the measurements to be made without washing out unbound nanotubes by using the threshold criteria of a minimum average fluorescence intensity in order for a sample to be considered positive. The data could be visualized using the inset histograms from the positive and negative controls to see the increased average fluorescence intensity between negative and positive sample conditions.

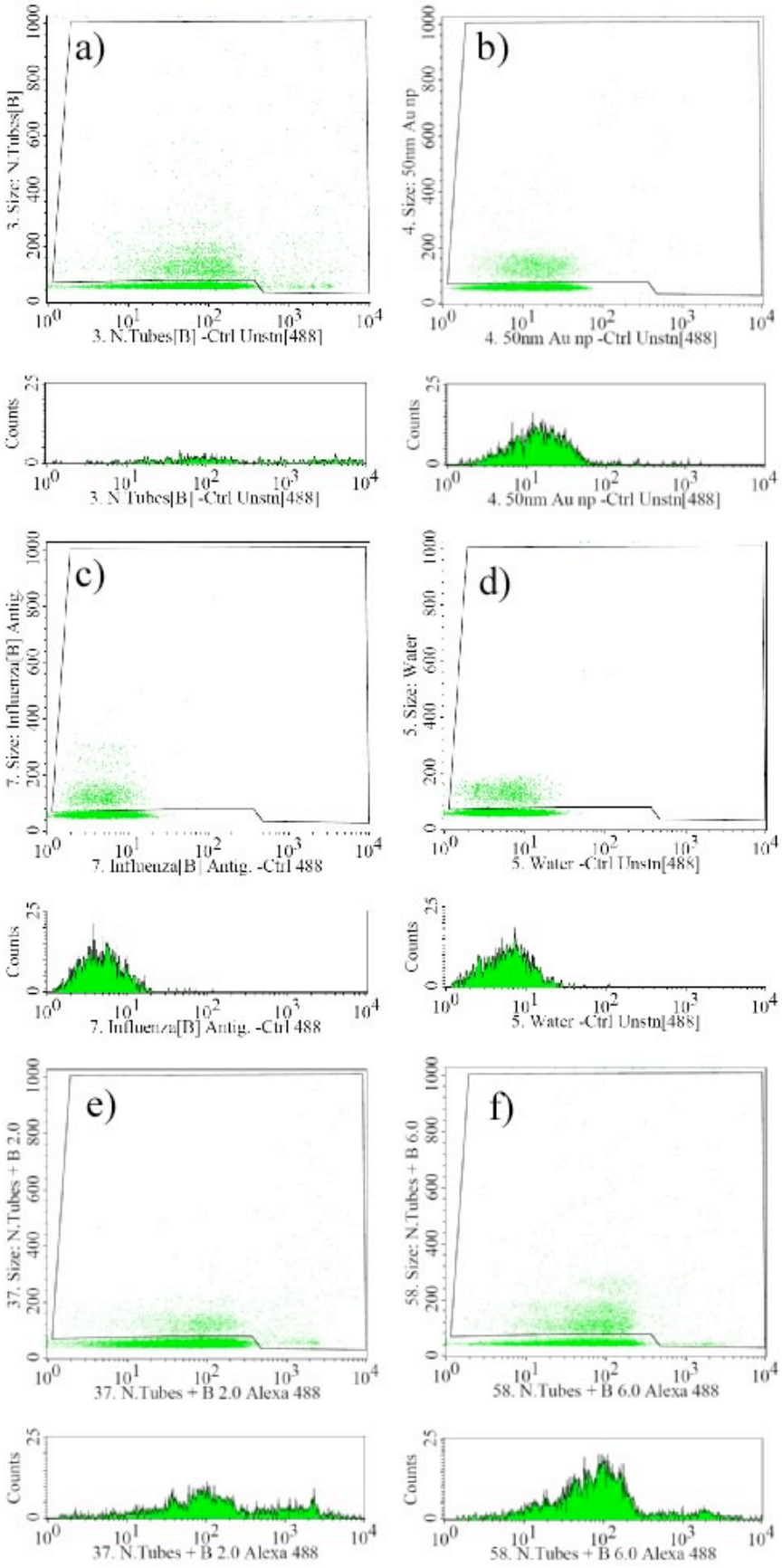

a)
3. Size: N.Tubes[B]
3. N.Tubes[B] -Ctrl Unstn[488]
Counts
3. N.Tubes[B] -Ctrl Unstn[488]
b)
4. Size: 50nm Au np
4. 50nm Au np -Ctrl Unstn[488]
Counts
4. 50nm Au np -Ctrl Unstn[488]
c)
7. Size: Influenza[B] Antig.
7. Influenza[B] Antig. -Ctrl 488
Counts
7. Influenza[B] Antig. -Ctrl 488
d)
5. Size: Water
5. Water -Ctrl Unstn[488]
Counts
5. Water -Ctrl Unstn[488]
e)
37. Size: N.Tubes + B 2.0
37. N.Tubes + B 2.0 Alexa 488
Counts
37. N.Tubes + B 2.0 Alexa 488
f)
58. Size: N.Tubes + B 6.0
58. N.Tubes + B 6.0 Alexa 488
Counts
58. N.Tubes + B 6.0 Alexa 488

Figure 4-5. Influenza B gate selection. a) nanotube only negative control; b) 50nm gold nanoparticles; c) Influenza B antigen stocks, 10^7 pfu/mL; d) solvent background of distilled water only; e) nanotube biosensors + Influenza B 10^2 pfu/mL; f) nanotube biosensors + Influenza B 10^6 pfu/mL; insets below each dot plot is a histogram showing the number of gated events at each fluorescence intensity.

The case depicted in Figure 4-6 described gate selection for analysis of Vaccinia or MVA virus using the peptide nanotube biosensors. In Figure 4-6a, the nanotube only negative control was shown. In Figure 4-6b, 50nm gold nanoparticles were shown. In Figure 4-6c, the solvent used for all dilutions, distilled water, was shown. In Figure 4-6d, nanotube biosensors mixed with Vaccinia at a concentration of 10^2 pfu/mL were characterized. This virus concentration was below the limit of detection, and thus appears similar to the negative control. In Figure 4-6e, the nanotube biosensors mixed with Vaccinia viruses at a concentration of 10^5 pfu/mL were shown as one positive control. In Figure 4-6f, nanotube biosensors mixed with Vaccinia viruses at a concentration of 10^6 pfu/mL were shown as a second positive control. Here, the gate selection was drawn such that positive events will be maximized, with less stringent efforts made to minimize the number of events from background noise sources. The behavior of Vaccinia was different from other viruses studies. This was manifested through a sharper response in number of events and average fluorescence intensity when above the threshold for the limit of detection when compared to other viruses. While it was not immediately clear why Vaccinia exhibits such a markedly different response, it could be hypothesized that due to the oval shape and larger size of Vaccinia, at 270nm by 360nm, when compared to the next largest virus studied of Herpes Simplex Virus Type 2 at a spherical diameter of approximately 120nm, the size and shape difference of the virus may have altered the nanotube-virus network formation properties of Vaccinia.

Despite the uncertainty regarding why there was a higher limit of detection and more pronounced response, the increased response of fluorescence intensity was exploited in the gate selection to maximize the area of potentially positive events. Such a high signal could have allowed for more noise in the measurement while still having an acceptable signal to noise ratio, and therefore more events were allowed to be gated in the negative control samples.

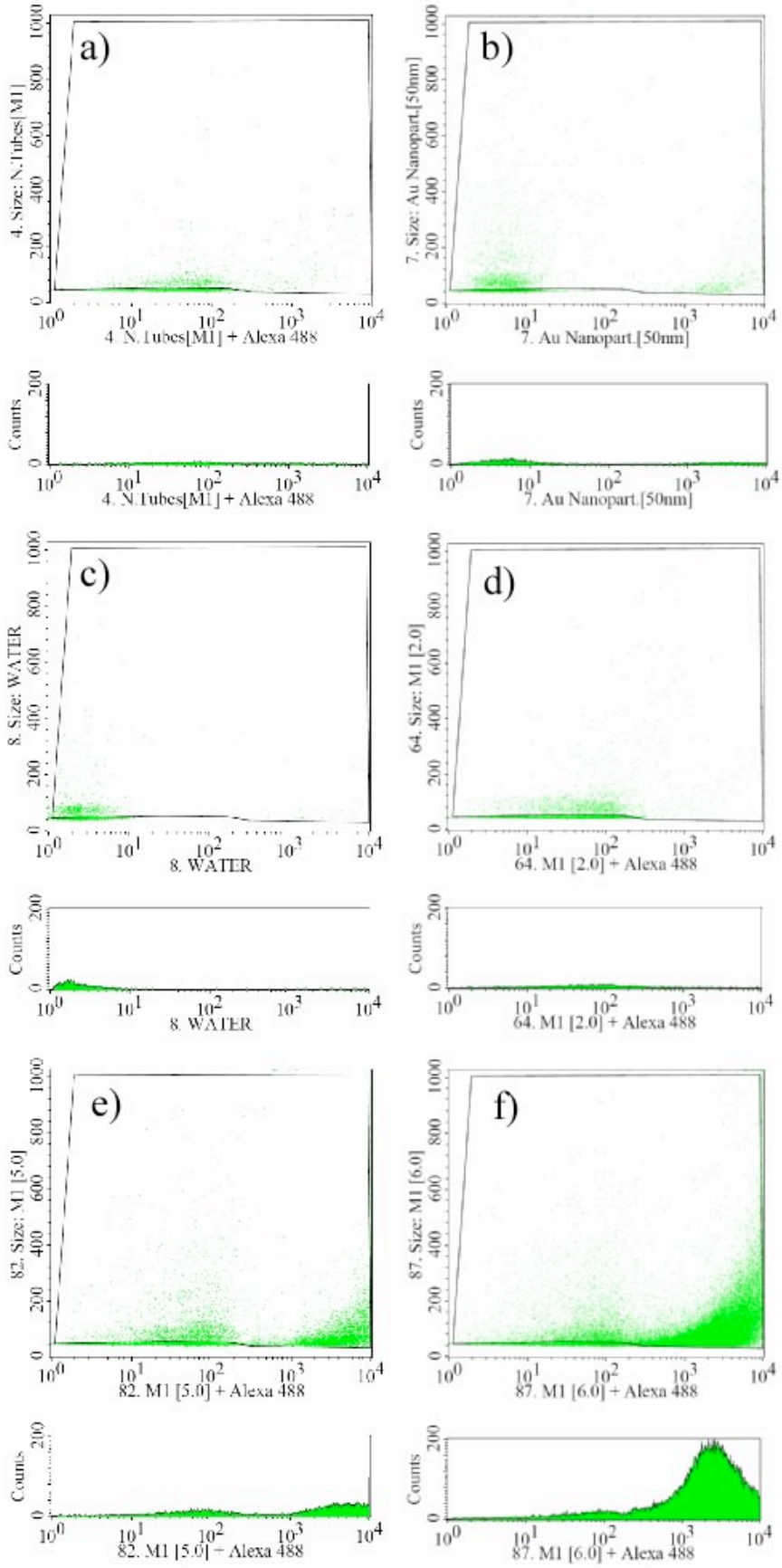

a)
4. Size: N.Tubes[M1]
4. N.Tubes[M1] + Alexa 488
Counts
4. N.Tubes[M1] + Alexa 488
b)
7. Size: Au Nanopart.[50nm]
7. Au Nanopart.[50nm]
Counts
7. Au Nanopart.[50nm]
c)
8. Size: WATER
8. WATER
Counts
8. WATER
d)
64. Size: M1 [2.0]
64. M1 [2.0] + Alexa 488
Counts
64. M1 [2.0] + Alexa 488
e)
82. Size: M1 [5.0]
82. M1 [5.0] + Alexa 488
Counts
82. M1 [5.0] + Alexa 488
f)
87. Size: M1 [6.0]
87. M1 [6.0] + Alexa 488
Counts
87. M1 [6.0] + Alexa 488

Figure 4-6. Vaccinia gate selection. a) nanotube only negative control; b) 50nm gold nanoparticles; c) solvent of distilled water; d) nanotube biosensors + Vaccinia 10^2 pfu/mL; e) nanotube biosensors + Vaccinia 10^5 pfu/mL; f) nanotube biosensors + Vaccinia 10^6 pfu/mL; insets shown below each dot plot are histograms of the number of gated events at each fluorescence intensity.

Figure 4-7a showed the nanotube only negative control for nanotube biosensors against Adenovirus Type 3 (AV3), used to assay for Adenovirus Type 3. In Figure 4-7b, 50nm gold nanoparticles were shown to have a very high number of low fluorescence intensity events, however these events mostly occurred at fluorescence intensities lower than the negative control shown in Figure 4-7a. In Figure 4-7c, undiluted Adenovirus Type 3 virus stocks at a concentration of 10^6 pfu/mL were shown. In Figure 4-7d, the solvent used for dilution in this experiment, distilled water, was shown. In Figure 4-7e, the nanotube biosensors against AV3 mixed with Adenovirus Type 3 at a concentration of 10^2 pfu/mL showed one positive control near the limit of detection. In Figure 4-7f, the nanotube biosensors against AV3 mixed with Adenovirus Type 3 at a concentration of 10^6 pfu/mL showed a second positive control. An experiment to demonstrate the specificity of antibodies was performed. Antibody specificity towards different strains of the same species of virus was retained in the biosensor assay, and was depicted in Figure 4-7. The biosensor nanotubes loaded with antibody against Adenovirus Type 3 is used to test for the concentration of Adenovirus Type 3. Clearly, this matching pair produces a positive result, with a standard curve and limit of detection that is expected. However, in Figure 4-8, the same biosensor nanotubes loaded with antibody against Adenovirus Type 3 is used to assay for concentration of Adenovirus Type 5. Since the antibodies purchased were specified to not cross-react, the expectation is no detection of Adenovirus Type 5 by the anti-Adenovirus Type 3 biosensors.

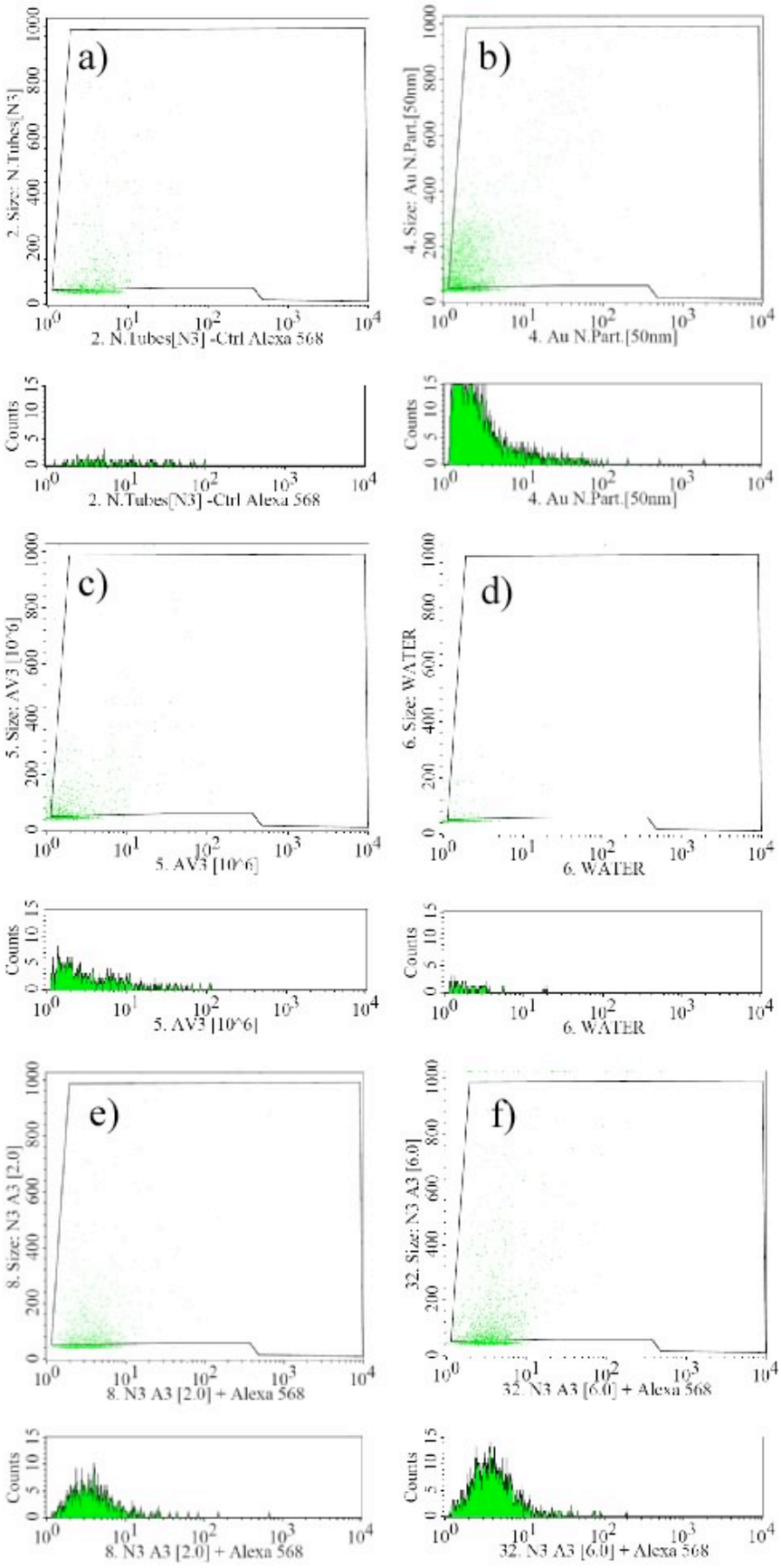

a)
2. Size: N.Tubes[N3]
2. N.Tubes[N3] -Ctrl Alexa 568
Counts
2. N.Tubes[N3] -Ctrl Alexa 568
b)
4. Size: Au N.Part.[50nm]
4. Au N.Part.[50nm]
Counts
4. Au N.Part.[50nm]
c)
5. Size: AV3 [10^6]
5. AV3 [10^6]
Counts
5. AV3 [10^6]
d)
6. Size: WATER
6. WATER
Counts
6. WATER
e)
8. Size: N3 A3 [2.0]
8. N3 A3 [2.0] + Alexa 568
Counts
8. N3 A3 [2.0] + Alexa 568
f)
32. Size: N3 A3 [6.0]
32. N3 A3 [6.0] + Alexa 568
Counts
32. N3 A3 [6.0] + Alexa 568

Figure 4-7. Nanotube biosensors against Adenovirus Type 3 (AV3), assaying for Adenovirus Type 3, gate selection. a) nanotube only negative control; b) 50nm gold nanoparticles; c) Adenovirus Type 3 virus stocks, 10^6 pfu/mL; d) solvent of distilled water; e) nanotube biosensors against AV3 + Adenovirus Type 3 10^2 pfu/mL; f) nanotube biosensors against AV3 + Adenovirus Type 3 10^6 pfu/mL; insets below each dot plot show histograms of the number of gated events at each fluorescence intensity.

Before discussing the results of the limit of detection of the non-complimentary pairing of antibody and virus, the gate selection will be examined. In Figure 4-8a, the negative control of nanotube biosensors against Adenovirus Type 3 was shown. Figure 4-8a provided the basis for the gate selection, in an attempt to remove the maximum number of unbound nanotubes from the gated calculations. Since this experiment assayed a non-complimentary pairing between antibody and virus, a low signal, if any, would be expect. Therefore, priority was placed on removing noise from the gated calculations. In Figure 4-8b, 50nm gold nanoparticles were shown, again as a control to demonstrate that detection of such small sized nanoparticles was really indistinguishable from the solvent background. In Figure 4-8c, the undiluted Adenovirus Type 5 virus stocks at a concentration of 10^6 pfu/mL were shown. In Figure 4-8d, the solvent of distilled water was shown. In Figure 4-8e, the nanotube biosensors against Adenovirus Type 3 were mixed with Adenovirus Type 5 stocks at a concentration of 10^2 pfu/mL. In Figure 4-8f, the nanotube biosensors against Adenovirus Type 3 were mixed with Adenovirus Type 5 stocks at a concentration of 10^6 pfu/mL. If the assay using the anti-Adenovirus Type 3 biosensors were to successfully detect Adenovirus Type 5 viruses, then figures 4-8e and 4-8f would be considered the positive controls. However, the data collected indicated the average fluorescence intensity and number of events for these samples were the same as for the negative control.

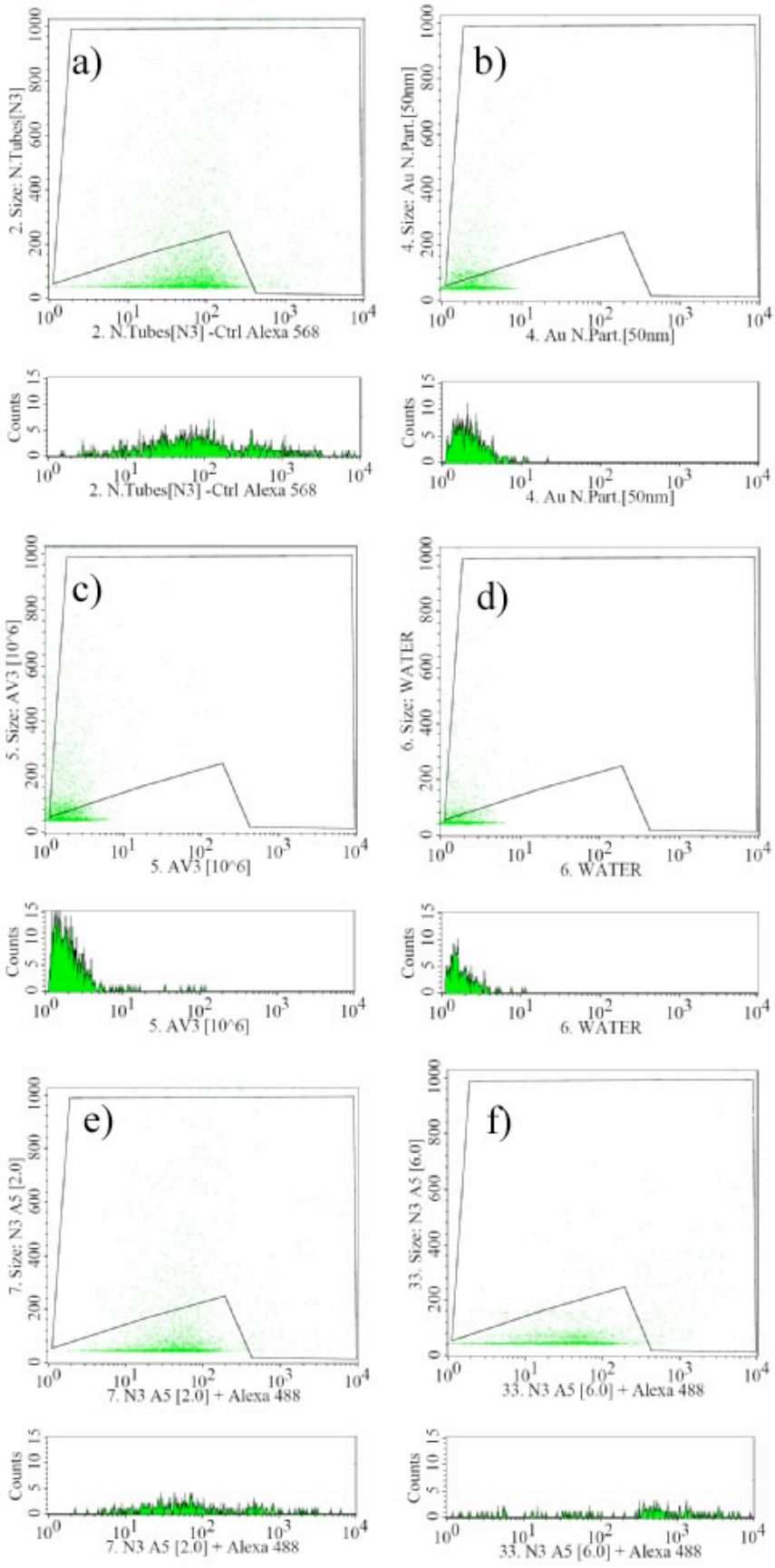

a)
2. Size: N.Tubes[N3]
2. N.Tubes[N3] -Ctrl Alexa 568
Counts
2. N.Tubes[N3] -Ctrl Alexa 568
b)
4. Size: Au N.Part.[50nm]
4. Au N.Part.[50nm]
Counts
4. Au N.Part.[50nm]
c)
5. Size: AV3 [10^6]
5. AV3 [10^6]
Counts
5. AV3 [10^6]
d)
6. Size: WATER
6. WATER
Counts
6. WATER
e)
7. Size: N3 A5 [2.0]
7. N3 A5 [2.0] + Alexa 488
Counts
7. N3 A5 [2.0] + Alexa 488
f)
33. Size: N3 A5 [6.0]
33. N3 A5 [6.0] + Alexa 488
Counts
33. N3 A5 [6.0] + Alexa 488

Figure 4-8. Nanotube biosensors against Adenovirus Type 3 (AV3), assaying for Adenovirus Type 5, gate selection. a) nanotube only negative control; b) 50nm gold nanoparticles; c) Adenovirus Type 5 virus stocks, 10^6 pfu/mL; d) solvent of distilled water; e) nanotube biosensors against AV3 + Adenovirus Type 5 10^2 pfu/mL; f) nanotube biosensors against AV3 + Adenovirus Type 5 10^6 pfu/mL; insets below each dot plot show histograms of the number of gated events at each fluorescence intensity.

In Figures 4-9 and 4-10, a similar and complimentary set of experiments to those conducted in Figures 4-7 and 4-8 were depicted. In this case, the anti-Adenovirus Type 5 antibody was used as the detection unit of the multifunctional peptide nanotube biosensors, and these biosensors were used to assay for first Adenovirus Type 3 in Figure 4-9, then Adenovirus Type 5 in Figure 4-10. As expected in Figure 4-9, no detection was observed. In regards to the gate selection, Figure 4-9a showed the negative control. In Figure 4-9b, 50nm gold nanoparticles were shown. In Figure 4-9c, undiluted Adenovirus Type 3 virus stocks at a concentration of 10^6 pfu/mL were shown. In Figure 4-9d, the solvent used, distilled water, was shown. In Figure 4-9e, nanotube biosensors against Adenovirus Type 5 were mixed with Adenovirus Type 3 at a concentration of 10^2 pfu/mL, while in Figure 4-9f, nanotube biosensors against Adenovirus Type 5 were mixed with Adenovirus Type 3 stocks at a concentration of 10^6 pfu/mL. Since this experiment assayed using an unmatched pairing of antibody and virus, the samples in Figure 4-9e and 4-9f which would normally have been positive controls showed the same average fluorescence intensity and number of events as the negative control exhibits.

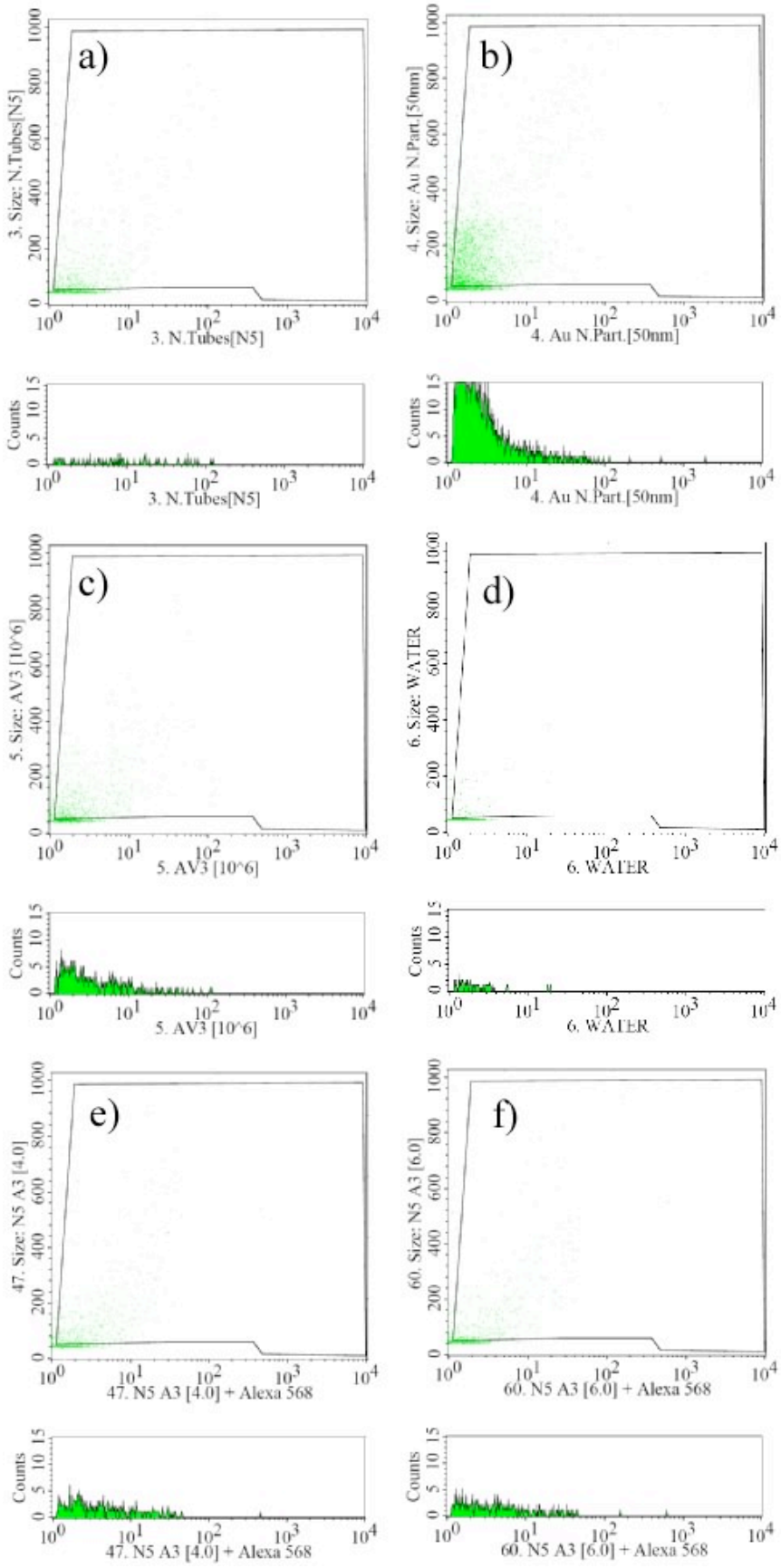

a)
3. Size: N.Tubes[N5]
3. N.Tubes[N5]
Counts
3. N.Tubes[N5]
b)
4. Size: Au N.Part.[50nm]
4. Au N.Part.[50nm]
Counts
4. Au N.Part.[50nm]
c)
5. Size: AV3 [10^6]
5. AV3 [10^6]
Counts
5. AV3 [10^6]
d)
6. Size: WATER
6. WATER
Counts
6. WATER
e)
47. Size: N5 A3 [4.0]
47. N5 A3 [4.0] + Alexa 568
Counts
47. N5 A3 [4.0] + Alexa 568
f)
60. Size: N5 A3 [6.0]
60. N5 A3 [6.0] + Alexa 568
Counts
60. N5 A3 [6.0] + Alexa 568

Figure 4-9. Nanotube biosensors against Adenovirus Type 5 (AV5), assaying for Adenovirus Type 3, gate selection. a) nanotube only negative control; b) 50nm gold nanoparticles; c) Adenovirus Type 3 virus stocks, 10^6 pfu/mL; d) solvent of distilled water; e) nanotube biosensors against AV5 + Adenovirus Type 3 10^2 pfu/mL; f) nanotube biosensors against AV5 + Adenovirus Type 3 10^6 pfu/mL; insets below each dot plot show histograms of the number of gated events at each fluorescence intensity.

In Figure 4-10a, the nanotube only negative control was shown. In Figure 4-10b, the 50nm gold nanoparticles were shown. In Figure 4-10c, undiluted Adenovirus Type 5 virus stocks at a concentration of 10^6 pfu/mL were shown. In Figure 4-10d, the solvent, distilled water, was shown. In Figure 4-10e, the nanotube biosensors against Adenovirus Type 5 were mixed with Adenovirus Type 5 virions at 10^2 pfu/mL in one positive control near the limit of detection. In Figure 4-10f, the nanotube biosensors against Adenovirus Type 5 were mixed with Adenovirus Type 5 viruses at 10^6 pfu/mL to show a second positive control. In this case, the gate selections were made with an emphasis on maximizing the number of positive events that contained nanotube-virus network aggregates. The solvent had some low fluorescence intensity noise, as did the virus stocks and gold nanoparticles. However, this low intensity noise in the fluorescence channel was of a lower intensity than the fluorescence intensity of single unbound nanotubes in the negative control in Figure 4-10a. Some small amounts of unbound nanotubes did fall into the gated regions, but as previously described these values were used to establish a threshold for the minimum average fluorescence intensity required to be considered a positive sample. Further, examination of the positive controls revealed a set of fluorescent events that began at 100 pfu/mL that were absent from the negative control. Upon addition of higher virus concentrations, an increase in the number of single-virus structures was observed by the histogram in Figure 4-10f.

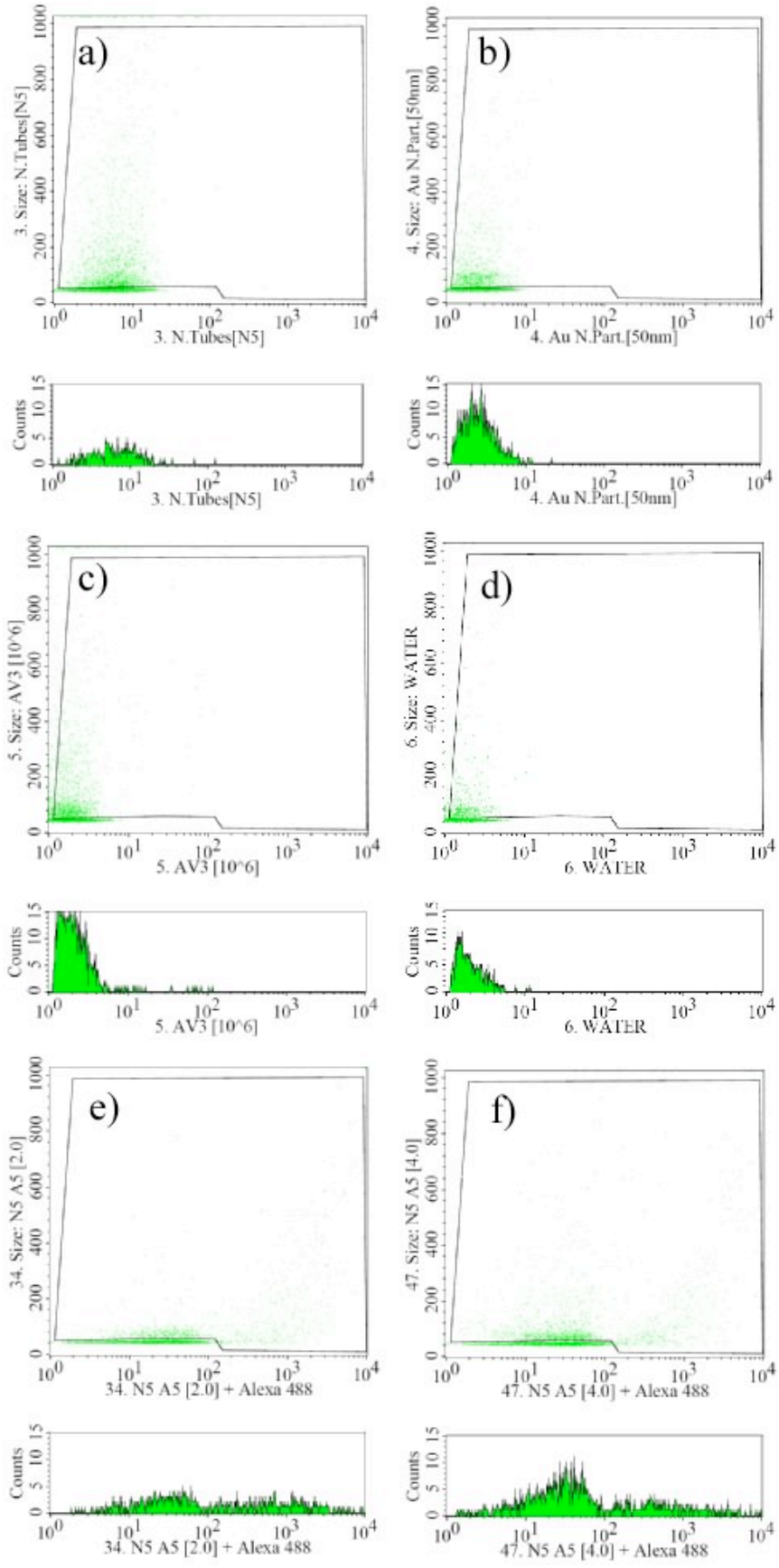

a)
3. Size: N.Tubes[N5]
3. N.Tubes[N5]
Counts
3. N.Tubes[N5]
b)
4. Size: Au N.Part.[50nm]
4. Au N.Part.[50nm]
Counts
4. Au N.Part.[50nm]
c)
5. Size: AV3 [10^6]
5. AV3 [10^6]
Counts
5. AV3 [10^6]
d)
6. Size: WATER
6. WATER
Counts
6. WATER
e)
34. Size: N5 A5 [2.0]
34. N5 A5 [2.0] + Alexa 488
Counts
34. N5 A5 [2.0] + Alexa 488
f)
47. Size: N5 A5 [4.0]
47. N5 A5 [4.0] + Alexa 488
Counts
47. N5 A5 [4.0] + Alexa 488

Figure 4-10. Nanotube biosensors against Adenovirus Type 5 (AV5), assaying for Adenovirus Type 5, gate selection. a) nanotube only negative control; b) 50nm gold nanoparticles; c) Adenovirus Type 5 virus stocks, 10^6 pfu/mL; d) solvent of distilled water; e) nanotube biosensors against AV5 + Adenovirus Type 5 10^2 pfu/mL; f) nanotube biosensors against AV5 + Adenovirus Type 5 10^6 pfu/mL; insets below each dot plot show histograms of the number of gated events at each fluorescence intensity.

In Figure 4-11, nanotube biosensors against Simian Virus 40(SV40) large T antigen were used to assay for SV40. The gate selection can be described as having criteria aimed to reduce the signal from unbound nanotubes and solvent background. In Figure 4-11a, the nanotube only negative control was shown, with the gate selection showing a histogram that revealed very few gated events. In Figure 4-11b, SV40 virus stocks were shown at a concentration of 10^6 pfu/mL with as few gated events as that of the solvent. In Figure 4-11c, the solvent, distilled water, was shown with the gate drawn to eliminate the majority of events from being gated. In Figure 4-11d, nanotube biosensors were mixed with SV40 at a concentration of 10^2 pfu/mL, while in Figure 4-11e nanotube biosensors were mixed with SV40 at a concentration of 10^4 pfu/mL, and finally in Figure 4-11f nanotube biosensors were mixed with SV40 at a concentration of 10^6 pfu/mL. These positive controls revealed an increasing average gated fluorescence intensity as well as number of gated events.

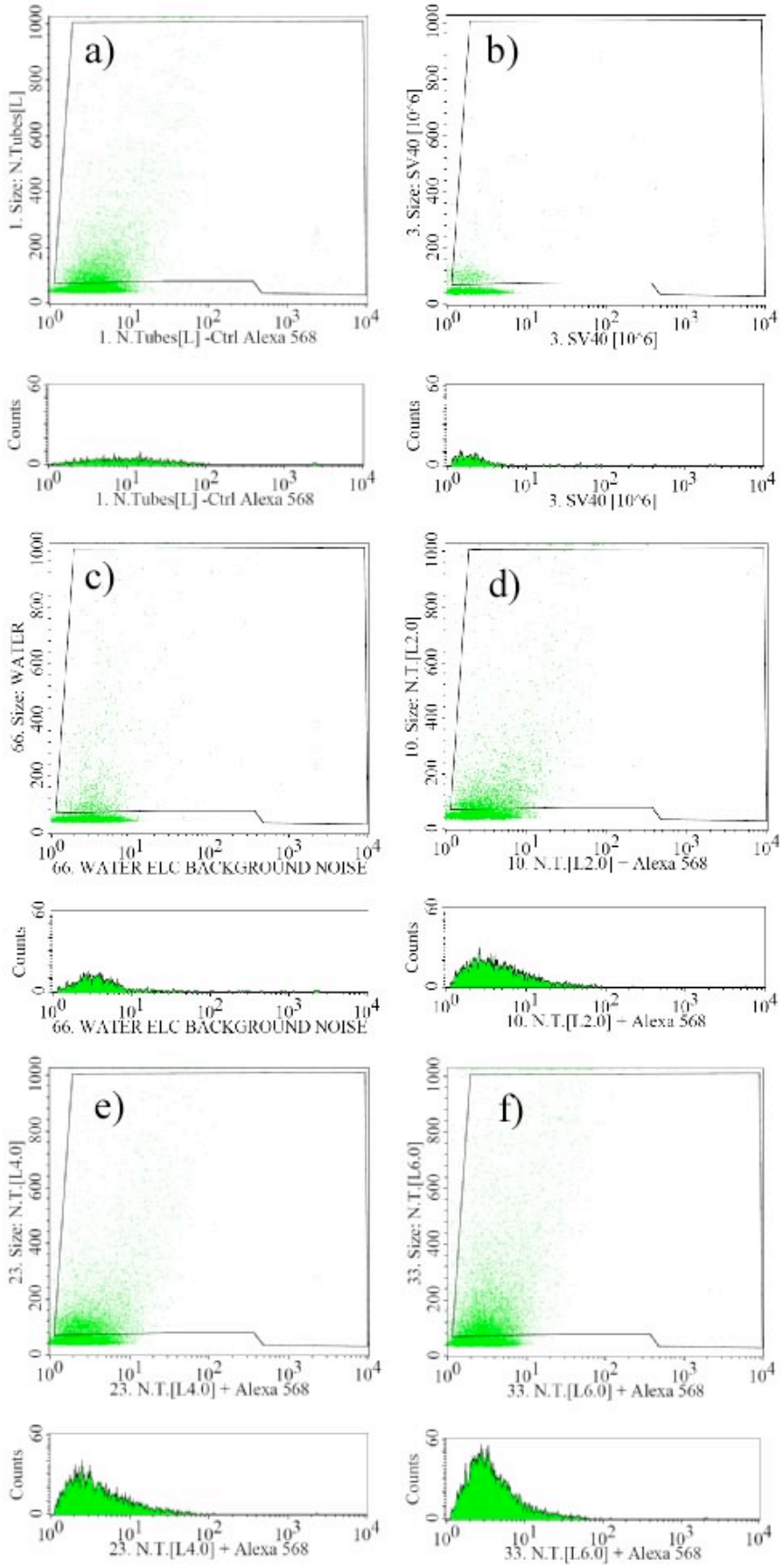

a)
1. Size: N.Tubes[L]
1. N.Tubes[L] -Ctrl Alexa 568
Counts
1. N.Tubes[L] -Ctrl Alexa 568
b)
3. Size: SV40 [10^6]
3. SV40 [10^6]
Counts
3. SV40 [10^6]
c)
66. Size: WATER
66. WATER ELC BACKGROUND NOISE
Counts
66. WATER ELC BACKGROUND NOISE
d)
10. Size: N.T.[L2.0]
10. N.T.[L2.0] + Alexa 568
Counts
10. N.T.[L2.0] + Alexa 568
e)
23. Size: N.T.[L4.0]
23. N.T.[L4.0] + Alexa 568
Counts
23. N.T.[L4.0] + Alexa 568
f)
33. Size: N.T.[L6.0]
33. N.T.[L6.0] + Alexa 568
Counts
33. N.T.[L6.0] + Alexa 568

Figure 4-11. Nanotube biosensors against Simian Virus 40(SV40) large T antigen, assaying for SV40, gate selection. a) nanotube only negative control; b) SV40 virus stocks, 10^6 pfu/mL; c) solvent of distilled water; d) nanotube biosensors + SV40 10^2 pfu/mL; e) nanotube biosensors + SV40 10^4 pfu/mL; f) nanotube biosensors + SV40 10^6 pfu/mL; insets below each dot plot show histograms of the number of gated events at each fluorescence intensity.

In Figure 4-12, nanotube biosensors against Simian Virus 40(SV40) large and small T antigen N-terminus assaying for SV40 virus were depicted. Both the large T antigen and small T antigen are proteins that are transcribed after SV40 infection occurs[117, 118]. During the course of this research project, no evidence that supported or denied the presence of either small T or large T in the structure of SV40 was found. This finding could be interpreted several ways. One possible interpretation could be as follows. Since the SV40 was grown in a cell culture, the large T antigen proteins and small T antigen proteins were left over in the virus stocks as part of the cellular debris that always remains in virus stocks. It was possible the assay was detecting the free protein concentration rather than the virus concentration directly. If this were true, however, it would be very hard to form sea-urchin structures with monoclonal antibodies able to bind only one site of a protein. Another possibility was one of the antibodies is cross-reactive with a surface protein on SV40. If the epitope "within amino acids 83-128 of the large T-antigen"[119, 120] could have cross-reacted with some other surface protein on SV40, then this detection methodology would perform similarly to other virus-antibody pairings. Another hypothesis could also be that the large T-antigen or small T-antigen perhaps remained associated with the surface of some SV40 viruses as a result of the virus stock preparation protocol. Alternatively, if, in fact, one or both of the large and small T antigens were somewhere in the internal structure of SV40, the nanotube

biosensors could have been assaying for viruses that have imperfections or have degraded. It could have been that non-pfu (plaque forming unit) virus fragments were present in the stocks in some proportion to the plaque forming unit viruses, and the antibodies were able to detect these fragments. According to further details from the antibody manufacturer's website datasheets, www.Abcam.com, both proteins have "Immunogen = Full length protein (purified) (SV40)." and "Species Reactivity = SV40 infected cells." This suggested that the antibodies may have been detecting cellular debris or free protein that remained associated with the virus stock solutions. In Figure 4-12a, the nanotube only negative control was shown. The number of gated events was very low, based on the gate selection criteria of removing the majority of events from the solvent background, and from the nanotubes themselves in the negative control. In Figure 4-12b, the number of gated events from the virus stocks were as low as water. In Figure 4-12c, distilled water was shown, and as expected there were very few gated events. In Figure 4-12d, the first positive control of nanotube biosensors mixed with samples spiked with SV40 at a concentration of 10^2 pfu/mL was shown. In Figure 4-12e, the second positive control of nanotube biosensors mixed with samples spiked with SV40 at 10^4 pfu/mL was shown. In Figure 4-12f, the third positive control of nanotube biosensors mixed with samples spiked with SV40 at 10^6 pfu/mL was shown. In all three of these positive controls, the number of gated events increased, however the average fluorescence intensity did not. Detection appeared to work in both Figures 4-11 and 4-12, however from the limit of detection plots prepared in Figure 4-13 it was clear that the antibody against large T antigen "between amino acids 83-128" was most effective.

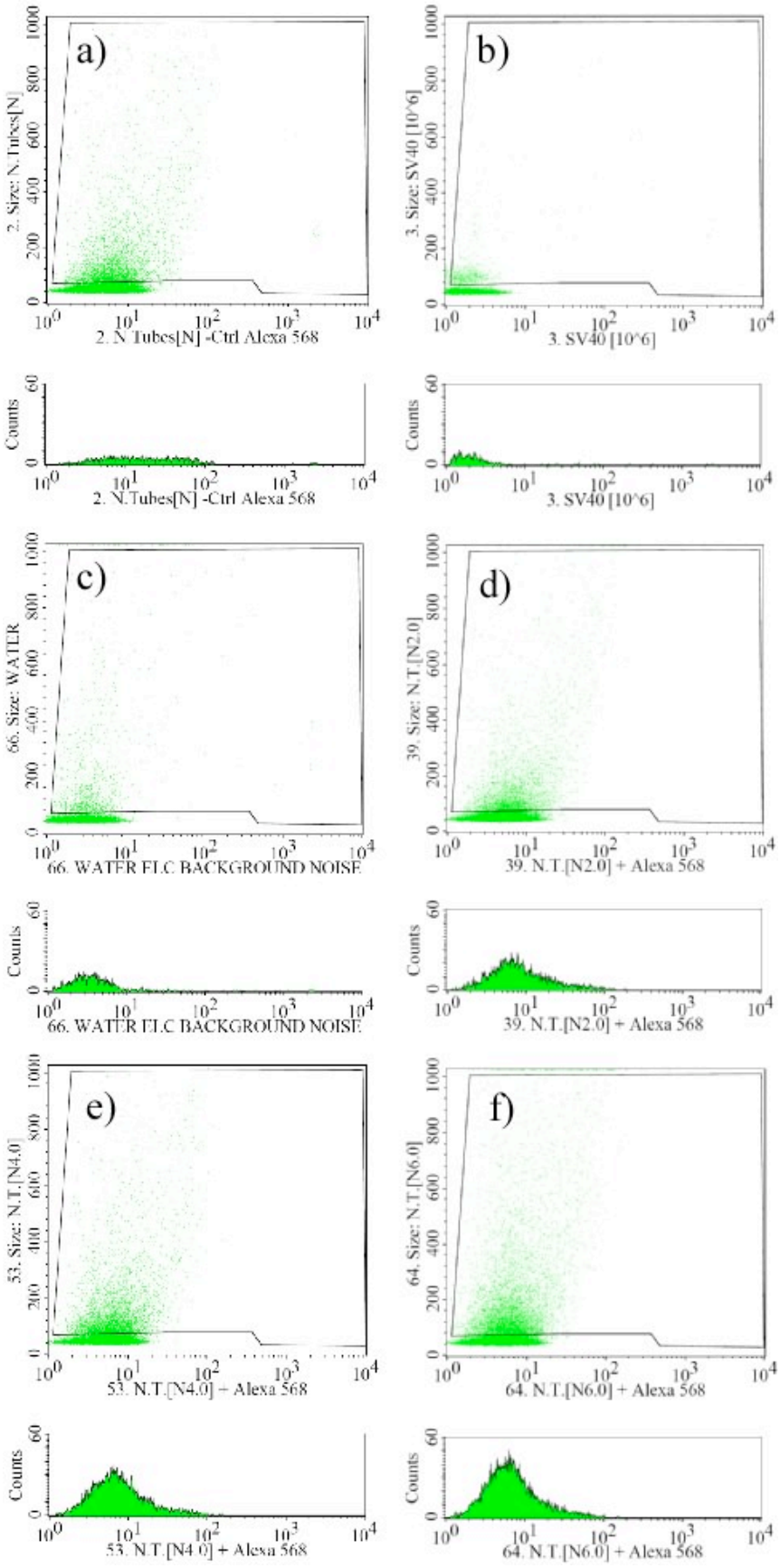

a)
2. Size: N.Tubes[N]
2. N.Tubes[N] -Ctrl Alexa 568
Counts
2. N.Tubes[N] -Ctrl Alexa 568
b)
3. Size: SV40 [10^6]
3. SV40 [10^6]
Counts
3. SV40 [10^6]
c)
66. Size: WATER
66. WATER FLC BACKGROUND NOISE
Counts
66. WATER FLC BACKGROUND NOISE
d)
39. Size: N.T.[N2.0]
39. N.T.[N2.0] + Alexa 568
Counts
39. N.T.[N2.0] + Alexa 568
e)
53. Size: N.T.[N4.0]
53. N.T.[N4.0] + Alexa 568
Counts
53. N.T.[N4.0] + Alexa 568
f)
64. Size: N.T.[N6.0]
64. N.T.[N6.0] + Alexa 568
Counts
64. N.T.[N6.0] + Alexa 568

Figure 4-12. Nanotube biosensors against Simian Virus 40(SV40) large T antigen N-terminus, assaying for SV40, gate selection. a) nanotube only negative control; b) SV40 virus stocks, 10^6 pfu/mL; c) solvent of distilled water; d) nanotube biosensors + SV40 10^2 pfu/mL; e) nanotube biosensors + SV40 10^4 pfu/mL; f) nanotube biosensors + SV40 10^6 pfu/mL; insets below each dot plot show histograms of the number of gated events at each fluorescence intensity.

Figure 4-13 showed a series of limit of detection plots. In each of these plots, the red dotted line showed the minimum fluorescence intensity, or threshold fluorescence intensity, required to distinguish a positive value from a negative. The threshold was chosen based on the negative control of only nanotube biosensors, where no virus was added to the sample. Linear fits were shown through the data points obtained. All concentrations were in a log scale on the x-axis, while all the average gated fluorescence intensity values on the y-axis were shown in arbitrary units. This limit was selected by looking at the gated fluorescence intensity of the nanotube only negative controls, a value of zero on the x-axis, and determining the highest value. The dotted red line was then drawn slightly above this highest value of the negative control, with the conservative assertion that anything above the highest negative control value must be a positive value. This threshold for the minimum fluorescence intensity then allowed the calculation of the limit of detection. The results of Figure 4-13 were summarized in Table 4-1.

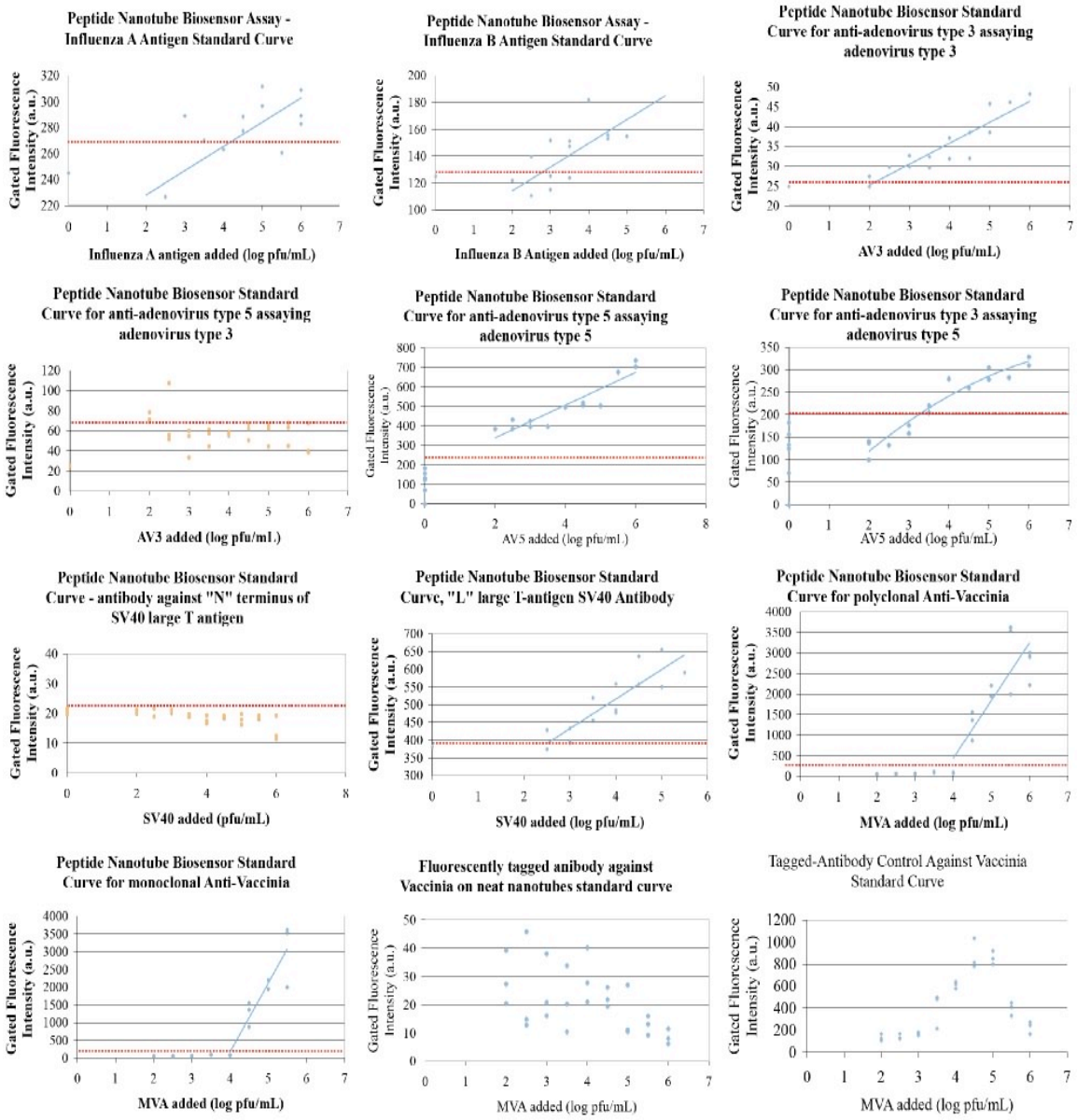


Figure 4-13. Limits of detection determination from standard curves.

Table 4-1. Peptide Nanotube Biosensor Assay Limit of Detection Examples.

Antibody (m=mono, p= polyclonal)	**Virus**	**Virus Size (nm)**	**Detection Limit (Log pfu)**
m AV5	AV3	55-65	N.D.
m AV3	AV3	55-65	2.0
m AV5	AV5	55-65	2.0
m AV3	AV5	55-65	3.5
m SV40 N	SV40	Protein (virus=80nm)	N.D.
m SV40 L	SV40	Protein (virus=80nm)	2.0
m HSV2	HSV2	110-120	2.5
p I/A/Wyo	I/A/Wyo	antigen	2.0
p I/B/Sh	I/B/Sh	antigen	2.0
m MVA marker 1	MVA	270x360	4.0
p MVA marker 2	MVA	270x360	4.0
p MVA FITC-Ab only (no nanotubes)	MVA	270x360	N.D.
Antibody (m=mono, p= polyclonal)	**Virus**	**Virus Size (nm)**	**Detection Limit (Log pfu)**

Table 4-1. Limit of detection data for several virus and antibody combinations using the peptide nanotube biosensor assay. Notice antibody selectivity is retained. Abbreviations: AV3 = Adenovirus Type 3. AV5 = Adenovirus Type 5. SV40/L = Simian Virus 40 –

Large T antigen. SV40/N = n-terminus of Simian Virus 40 – small T antigen. HSV2 = Herpes Simplex Virus Type 2. I/A/Wyo = Influenza Type A/Wyoming. I/B/Sh = Influenza Type B/Shengdong. MVA = Attenuated Vaccinia. Marker 1 = TV43. Marker 2 = polyclonal MVA antibody. MVA FITC-Ab only = FITC labeled polyclonal anti-MVA antibody only, not conjugated to nanotube biosensors; this was a control experiment. N.D. = no detection.

When designing an experiment, the careful selection of antibodies can allow discrimination between different strains of the same virus. When antibody against Adenovirus Type 5 was used to detect Adenovirus Type 3, the assay could not detect levels of AV3 present, compared to a low limit of detection of 100 pfu/mL when the antibody against AV3 was used. Conversely, antibody against AV3 could not detect low levels of AV5 compared to the antibody against AV5. Thus, the detection limit clearly was influenced by the antibody selection against the pathogen of interest. Further proof was found when an antibody against a specific amino acid sequence in a viral protein in the SV40 genome, amino acids 83-128 of the large T-antigen, was used and had a detection limit of $10^{2.0}$ pfu/mL, compared to the antibody against the entire N-terminal of the large and small T-antigens which had no detection. This suggested that the system is tunable and might even achieve lower detection limits as different choices of antibodies are developed in the future.

It was also noteworthy that the ratio of nanotubes to virus was constant at all sizes of networks, which maintained the proportional relationship between virus concentration, network size, and network fluorescence intensity. This relationship was central to the quantitative detection method that was described.

c) Lack of detection using Flow Cytometry and SSC vs. FL-1 data channels

Since the networks had large areas of free space between the hubs and spokes, the more nanotubes that were present in the network allowed for an increase in SSC as there were more surfaces to reflect the laser light at 90°. However, due to the direct proportionality between virus concentration and number of nanotubes per network, and therefore size and fluorescence intensity of the network, it made most sense to quantify the network structures by forward scattering intensity and fluorescence intensity thresholds, rather than introduce further complexity and statistical unreliability with the side scattering signal. However, since the flow cytometer collected both forward scattering and side scattering simultaneously in addition to fluorescence intensity, it was possible to display the data here to demonstrate the more complex nature of using side scattering vs. fluorescence intensity dot plots and gate selections as opposed to the forward scattering vs. fluorescence intensity previously discussed.

In Figure 4-14, side scattering vs. fluorescence intensity dot plots were shown, with insets beneath each frame that showed histograms of the number of gated fluorescence events at various intensities. In Figure 4-14a, the wash buffer negative control was displayed. As would be expected, very little background noise was observed in both the dot plots and the histogram. In Figure 4-14b, a positive control of the peptide nanotube biosensors added to a stock solution of Herpes Simplex Virus Type 2 at a concentration of $10^{3.3}$ pfu/mL was shown. It was an interesting observation that there was a linear relationship between the side scattering intensity and the fluorescence intensity, with a very uniform cigar-shaped distribution in the gated region of positive events. When compared to the negative control of only nanotubes as shown in Figure 4-14c, it became clear there were large numbers of unbound nanotubes remaining in

solution. In Figure 4-14c, there was a broad distribution of side scattering intensities that all had a very small fluorescence intensity. This suggested that the flexible rod-like nanotubes could bend, fold, and tumble in a variety of different shapes and relative angles to the laser and photodetectors in the flow cytometer. However, the low fluorescence intensity suggested that only single nanotubes were being observed, and that there was little or no auto-aggregation of the nanotubes. This distribution of side scattering intensities became very narrow when several nanotubes bound around a central virus and formed a much more ordered sea-urchin structure. As multiple sea-urchin vertices merged together in the formation of larger multiple-nanotube-multiple-virus networks, proportionality between the surface roughness and the fluorescence intensity was observed. This proportional trend was observed in both positive controls in Figures 4-14b and 4-14d. In Figure 4-14d, the virus concentration was much higher, with $10^{5.5}$ pfu/mL of Herpes Simplex Virus Type 2 added to the peptide nanotube biosensors. It was an interesting observation that the number of events increased slightly at the higher virus concentration, however the average fluorescence intensity did not increase in a statistically significant fashion. Another observation of note was that the number of events in the unbound nanotube region was much less in Figure 4-14d compared to Figures 4-14b or 4-14c. This observation suggested that nearly all of the original nanotubes were being consumed by the networks and sea-urchin structures that were forming as a result of the presence of the virus.

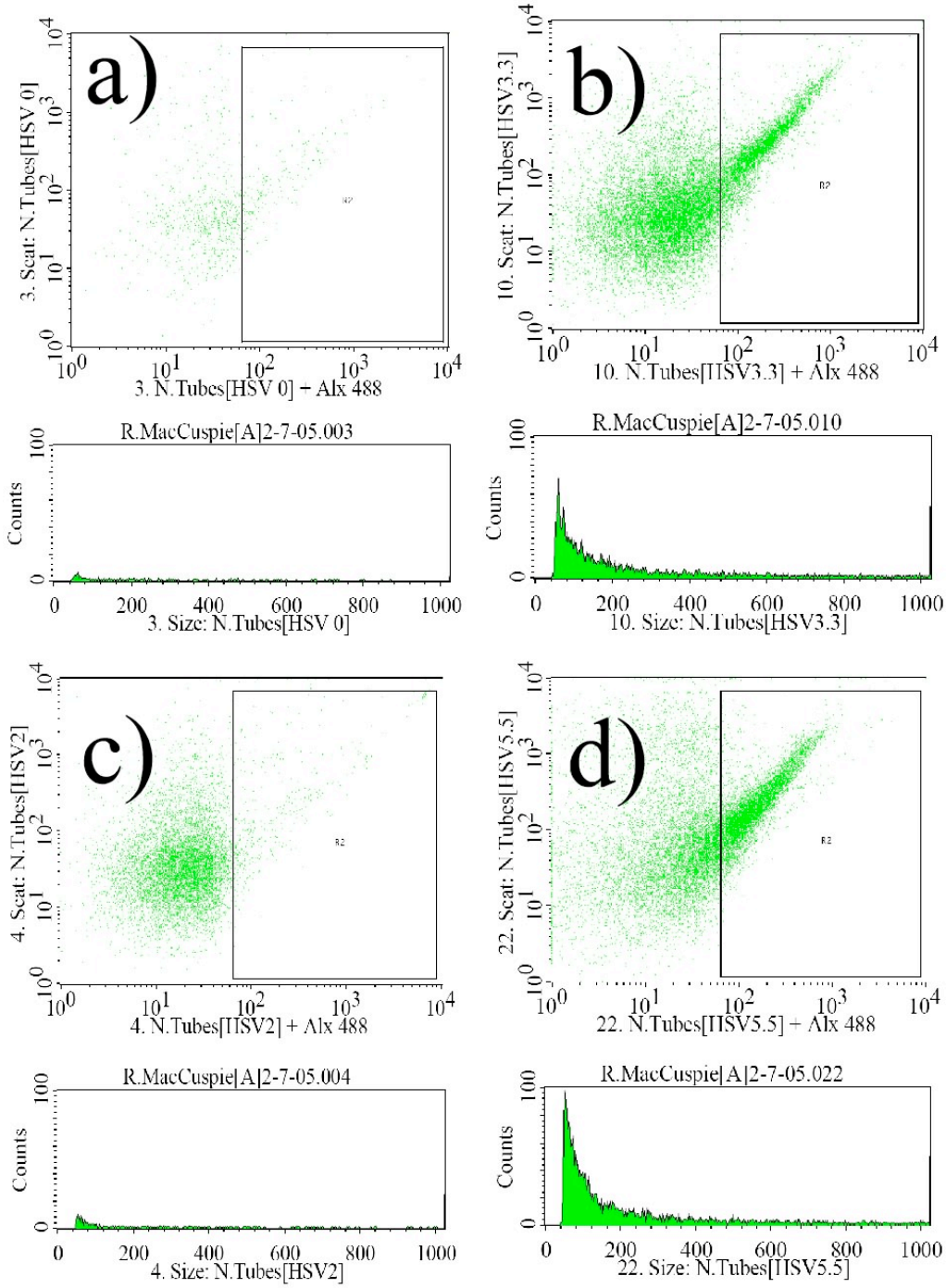


Figure 4-14. Side scattering intensity vs. fluorescence intensity dot plots of HSV-2 virus; a) wash buffer only; b) positive control with nanotubes + $10^{3.3}$ pfu/mL HSV-2 virus added; c) negative control with nanotube biosensors only; d) positive control with nanotubes + $10^{5.5}$ pfu/mL HSV-2.

Figures 4-15 through 4-18 showed the series of experiments to determine the antibody selectivity capabilities of this antibody-based assay. For two different strains of Adenovirus, complimentary and non-complimentary pairings were studied with comparisons of side scattering intensity vs. fluorescence intensity in the dot plots used to determine the gated regions. There were some positive indications that there was an increase in the average fluorescence intensity of solutions as the virus concentration increased. Further, the retention of selectivity by strain of the antibodies was reinforced, since neither of the non-complimentary antibody-virus pairings exhibited any cross-reactivity.

In Figure 4-15, gate selection was performed with the goal to eliminate the background noise from water as the only criteria. In Figure 4-15a, the negative control of just the nanotube biosensors shows some positive events occurring with minimal fluorescence intensity in the gated region. In Figure 4-15b, the Adenovirus stocks showed some very high levels of noise in terms of number of events, but the noise events all had fluorescence intensity values that were lower than the single peptide nanotube biosensors. In Figure 4-15c, the gate selection to remove the noise from water was displayed. In Figure 4-15d, the first positive control was shown. Slightly higher average gated fluorescence intensity was observed compared to the negative control, and slightly more fluorescent events were observed compared to the negative control as well. Subsequently higher average gated fluorescence intensity and numbers of fluorescent events were observed in Figures 4-15e and 4-15f. The concentrations of Adenovirus Type 3 in Figures 4-15d, 4-15e, and 4-15f were 10^2, 10^4, and 10^6 pfu/mL, respectively. These results suggested that side scattering and fluorescence intensity dot plots and gate

selections could be used to determine unknown Adenovirus concentrations, however the differences between data points on standard curves were not as statistically meaningful as for the forward scattering and fluorescence intensity dot plots and gate selections. Nonetheless, demonstration of the retention of antibody selectivity by virus strain was shown in that the complimentary pairing of virus and antibody did exhibit a mildly positive behavior.

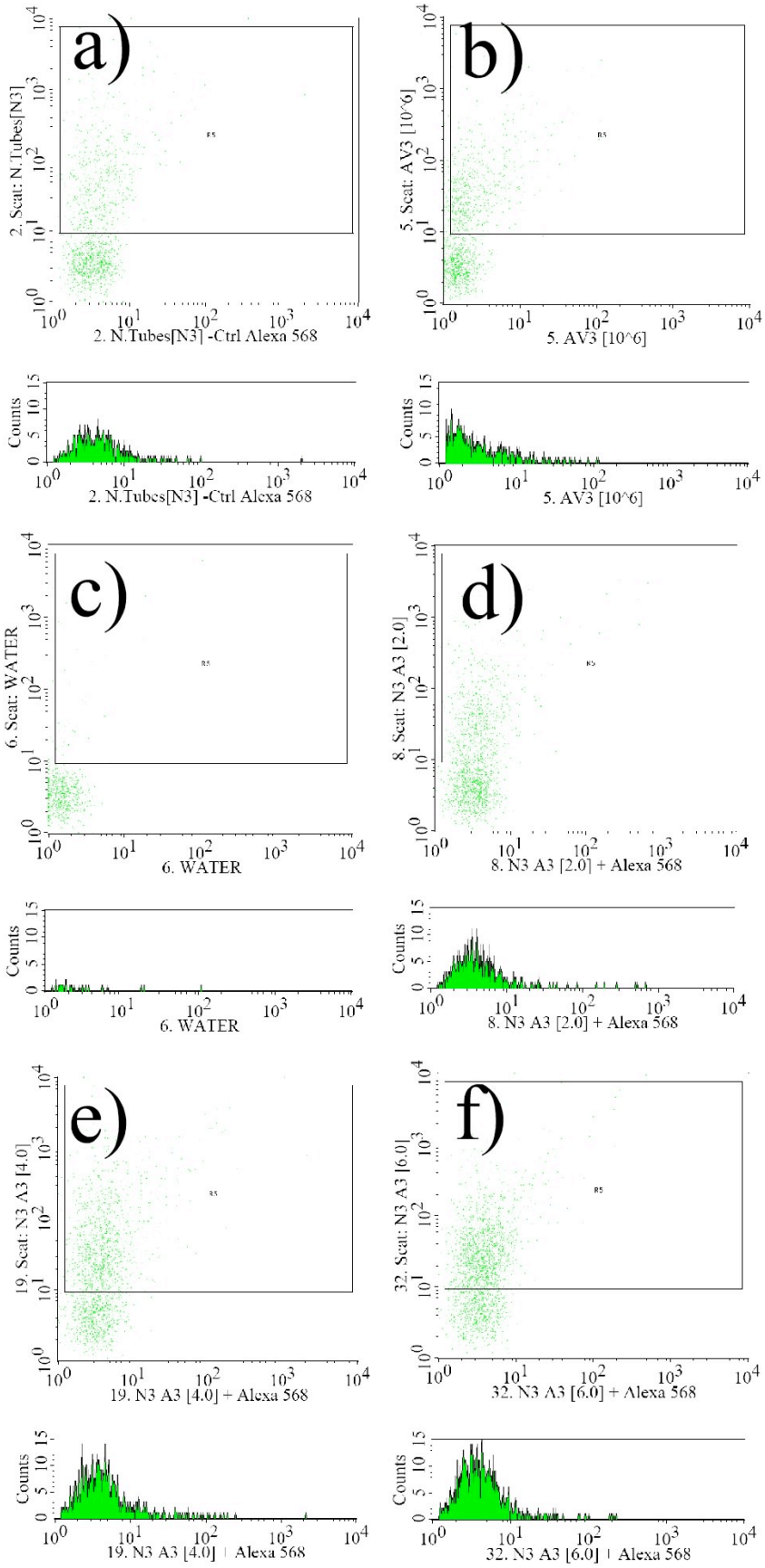

a)
2. Scat: N.Tubes[N3]
2. N.Tubes[N3] -Ctrl Alexa 568
Counts
2. N.Tubes[N3] -Ctrl Alexa 568
b)
5. Scat: AV3 [10^6]
5. AV3 [10^6]
Counts
5. AV3 [10^6]
c)
6. Scat: WATER
6. WATER
Counts
6. WATER
d)
8. Scat: N3 A3 [2.0]
8. N3 A3 [2.0] + Alexa 568
Counts
8. N3 A3 [2.0] + Alexa 568
e)
19. Scat: N3 A3 [4.0]
19. N3 A3 [4.0] + Alexa 568
Counts
19. N3 A3 [4.0] + Alexa 568
f)
32. Scat: N3 A3 [6.0]
32. N3 A3 [6.0] + Alexa 568
Counts
32. N3 A3 [6.0] + Alexa 568

Figure 4-15. Peptide nanotube biosensors with antibodies against Adenovirus Type 3, assaying for Adenovirus 3 concentration; a) nanotubes only negative control; b) Adenovirus 3 stocks; c) wash solvent of distilled water; d) nanotube biosensors added to a solution containing 10^2 pfu/mL of Adenovirus 3; e) nanotube biosensors added to a solution containing 10^4 pfu/mL of Adenovirus 3; f) nanotubes biosensors added to a solution containing 10^6 pfu/mL of Adenovirus 3.

In Figure 4-16, the non-complimentary pairing of antibodies against Adenovirus Type 3 used to assay for Adenovirus Type 5 were examined. Here again as in Figure 4-15, the gate selection was based primarily upon eliminating the noise from the water sample. In Figure 4-16a, the negative control of only the nanotube biosensors was shown. Some care was taken to remove a large number of events from the gated region using this control dot plot; however it was clear from the histogram that all of these nanotube events could not be eliminated. In Figure 4-16b, the 50nm gold nanoparticles were shown. These nanoparticles exhibited a slightly higher number of gated fluorescence events than the water control shown in Figure 4-16d, however they were also of low fluorescence intensity such that the unbound single nanotube biosensors had higher fluorescence intensity than the nanoparticles. In Figure 4-16c, the Adenovirus Type 5 stocks were shown undiluted. While there were many gated fluorescent events, they were similar in intensity to the nanoparticles and were lower than the nanotube negative control in Figure 4-16a. In Figure 4-16d, the distilled water solvent used for all dilutions was shown. The majority of the events were eliminated from the gated region based on the gate selection criteria described earlier in this paragraph. In Figure 4-16e, the first of two positive controls was shown. Adenovirus Type 5 was spiked in samples at a concentration of 10^2 pfu/mL. However, lower numbers of fluorescent events were observed in the gated region when compared to the negative control of only nanotubes.

This trend was further observed in Figure 4-16f, where samples were spiked with Adenovirus Type 5 at concentrations of 10^6 pfu/mL. While it could be speculated this down-regulation of fluorescence intensity by the presence of the viruses could be used as a mechanism to detect the viruses, it was not accompanied by an increase in average fluorescence intensity. If network structures formed in such a way that side scattering intensity decreased as the virus concentration increased, then there should have been a corresponding increase in fluorescence intensity. However, it must be considered that the decreased side scattering intensity would have lowered the positive events outside of the gated region and made them appear no different from the unbound peptide nanotubes. Since there was no increase in fluorescence intensity observed, there was no evidence the networks were forming. Therefore, no reliable determination of unknown virus concentrations could be made. This demonstrated that the antibodies retain virus strain selectivity and specificity after being loaded onto the peptide nanotube biosensors, since this experiment was assaying for a non-complimentary pairing.

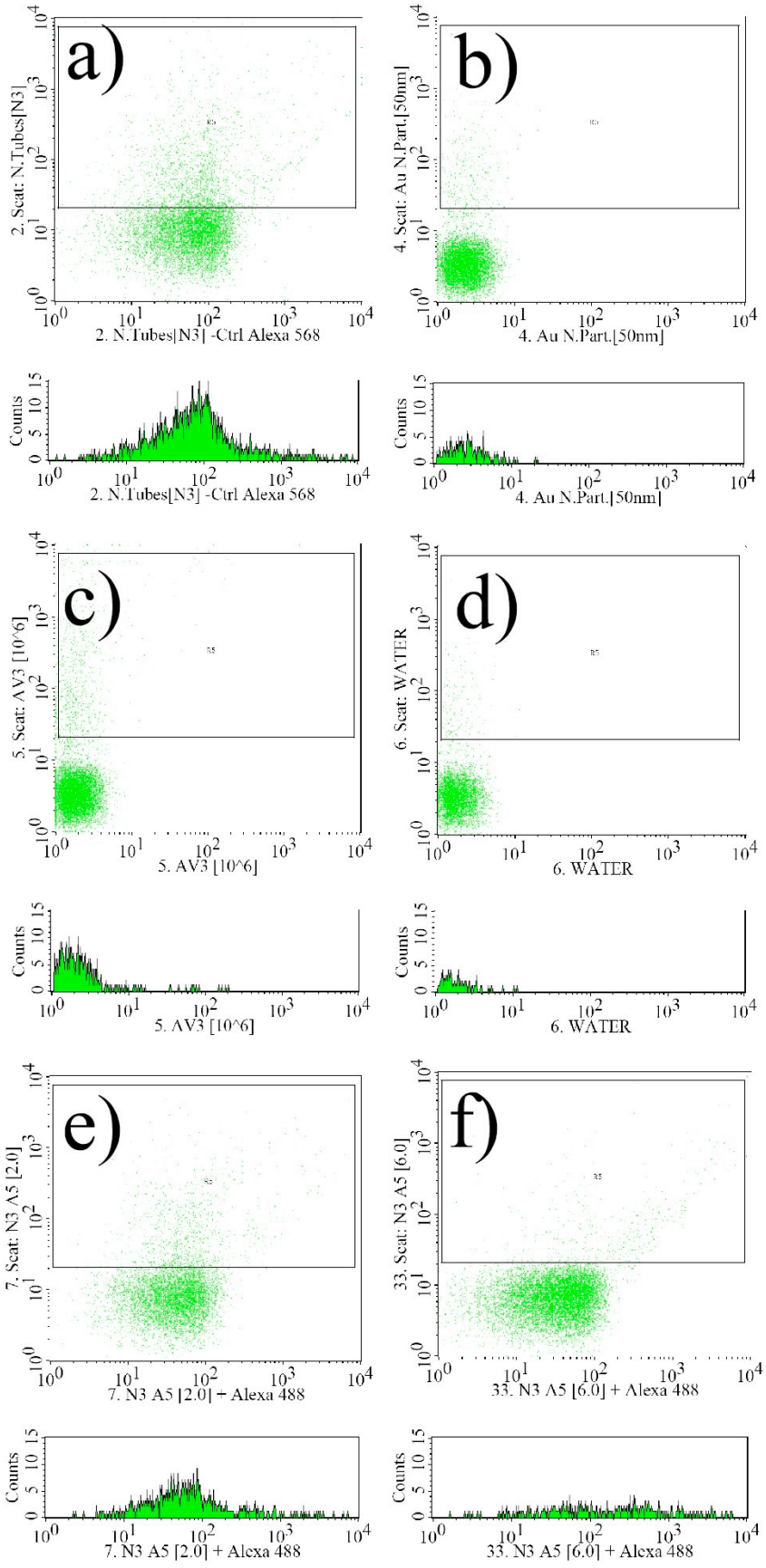

a)
2. Scat: N.Tubes[N3]
2. N.Tubes[N3] -Ctrl Alexa 568
Counts
2. N.Tubes[N3] -Ctrl Alexa 568
b)
4. Scat: Au N.Part.[50nm]
4. Au N.Part.[50nm]
Counts
4. Au N.Part.[50nm]
c)
5. Scat: AV3 [10^6]
5. AV3 [10^6]
Counts
5. AV3 [10^6]
d)
6. Scat: WATER
6. WATER
Counts
6. WATER
e)
7. Scat: N3 A5 [2.0]
7. N3 A5 [2.0] + Alexa 488
Counts
7. N3 A5 [2.0] + Alexa 488
f)
33. Scat: N3 A5 [6.0]
33. N3 A5 [6.0] + Alexa 488
Counts
33. N3 A5 [6.0] + Alexa 488

Figure 4-16. Peptide nanotube biosensors with antibodies against Adenovirus Type 3, assaying for Adenovirus Type 5. a) nanotube negative control; b) 50nm gold nanoparticles; c) Adenovirus Type 5 stocks, 10^6 pfu/mL; d) solvent used for dilutions, distilled water; e) peptide nanotubes added to sample spiked with 10^2 pfu/mL Adenovirus 5; f) positive control of peptide nanotubes added to sample spiked with 10^6 pfu/mL Adenovirus Type 5.

In Figure 4-17, the peptide nanotube biosensors were loaded with antibodies against Adenovirus Type 5, and used to assay for Adenovirus Type 3. Similarly to the Adenovirus Type 3 biosensor case, the gate selection was driven primarily by the goal of removing noise from the water. In Figure 4-17a, the nanotube negative control was shown, with some unbound nanotubes falling into the gated region with very low fluorescence intensities. In Figure 4-17b, the 50nm gold nanoparticles exhibited a large number of fluorescent events at low fluorescence intensities. The gold nanoparticles' fluorescence intensity distribution overlapped with the unbound nanotubes' distribution. In Figure 4-17c, the Adenovirus Type 3 stocks were shown. These stocks had a higher number of events than the unbound nanotubes like the gold nanoparticles, but fewer events. In Figure 4-17d, the water solvent was shown, with a histogram that reflected the gate selection choice to remove as many noise events from the water as possible. In Figure 4-17e, the first positive control was shown with Adenovirus Type 5 biosensors assaying for Adenovirus Type 3 at a spiked concentration of 10^2 pfu/mL. In Figure 4-17f, the second positive control was shown with Adenovirus Type 5 biosensors assaying for Adenovirus Type 3 at a spiked concentration of 10^6 pfu/mL. In both cases of positive controls, the distribution of fluorescent events in the histograms was statistically similar to the negative control. Therefore, antibody selectivity was retained in the case of the strain specific antibody against Adenovirus Type 5.

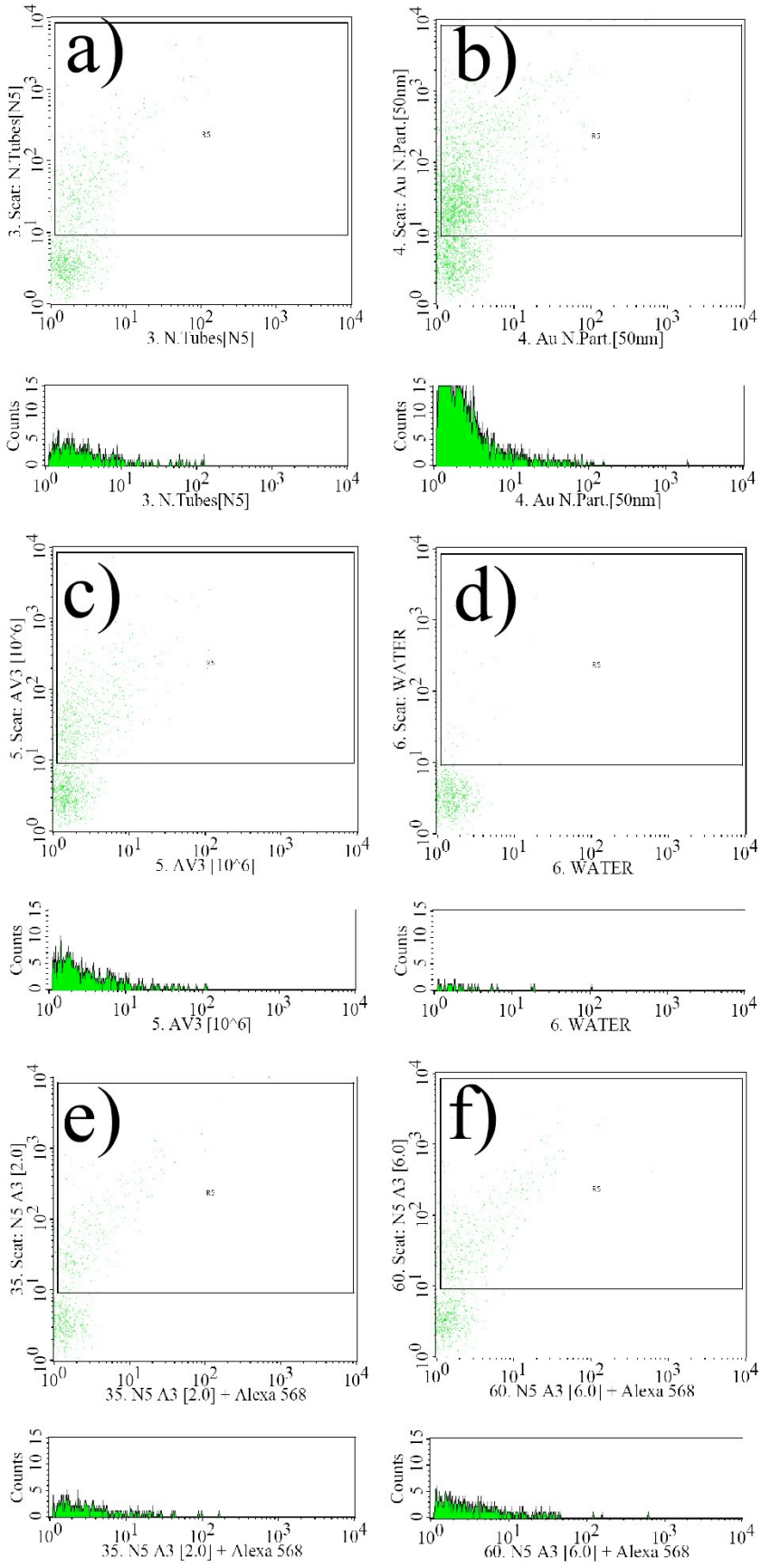

a)
3. Scat: N.Tubes[N5]
3. N.Tubes[N5]
Counts
3. N.Tubes[N5]
b)
4. Scat: Au N.Part.[50nm]
4. Au N.Part.[50nm]
Counts
4. Au N.Part.[50nm]
c)
5. Scat: AV3 [10^6]
5. AV3 [10^6]
Counts
5. AV3 [10^6]
d)
6. Scat: WATER
6. WATER
Counts
6. WATER
e)
35. Scat: N5 A3 [2.0]
35. N5 A3 [2.0] + Alexa 568
Counts
35. N5 A3 [2.0] + Alexa 568
f)
60. Scat: N5 A3 [6.0]
60. N5 A3 [6.0] + Alexa 568
Counts
60. N5 A3 [6.0] + Alexa 568

Figure 4-17. Peptide nanotubes with antibodies against Adenovirus Type 5 used to assay for Adenovirus Type 3. a) nanotube negative control; b) 50 nm gold nanoparticles; c) Adenovirus Type 3 stocks; d) solvent, distilled water; e) positive control of nanotube biosensors mixed with 10^2 pfu/mL Adenovirus Type 3 spiked samples; f) positive control of nanotube biosensors mixed with 10^6 pfu/mL Adenovirus Type 3 spiked samples.

In Figure 4-18, peptide nanotube biosensors loaded with antibodies against Adenovirus Type 5 were used to assay for Adenovirus Type 5 in the second complimentary pairing in the virus-strain selectivity series of experiments. Dot plots showing side scattering intensity vs. fluorescence intensity were shown with histograms of gated events' fluorescence intensities shown as insets below each dot plot. Similarly to the other strain selectivity experiments, the gate selection was given a primary goal of removing events caused by water, which were sources of noise. In Figure 4-18a, the negative control of only peptide nanotube biosensors was shown. There were some low fluorescence intensity events, which provided a threshold criterion that positive samples must exceed to be considered positive. In Figure 4-18b, the 50 nm gold nanoparticles were shown. These particles had very little difference in their histogram of gated events' fluorescence intensity from the histogram for water, shown in Figure 4-18d. The Adenovirus Type 5 stocks, undiluted and at a concentration of 10^6 pfu/mL, were shown in Figure 4-18c. There were a slightly higher number of fluorescence events with the Adenovirus stocks compared to water, as had been previously observed with Adenovirus stocks, however the average fluorescence intensity of these events was lower than the average gated fluorescence intensity of the unbound nanotube biosensors negative controls, and was therefore an acceptable level of noise. For both positive controls, an increased average gated fluorescence intensity as well as number of events was observed. In the lower virus concentration positive control shown in Figure 4-18e, the sample was

spiked with10^2 pfu/mL Adenovirus Type 5 and mixed with peptide nanotube biosensors. While the presence of unbound peptide nanotubes was still observed, a clear increase in the number of events that occurred at higher fluorescence intensities showed that the sea-urchin and larger network structures were forming and were detected. In Figure 4-18f, the sample was spiked with 10^6 pfu/mL of Adenovirus Type 5 and mixed with peptide nanotube biosensors. Here, the number of overlapping events was decreased compared to the first positive control and the negative control, which suggested that the majority of the nanotubes had been consumed to form some type of network or sea-urchin structure. The complimentary pairings exhibited a positive response demonstrating detection could have been possible. Comparison of the standards of deviation between side scattering and forward scattering dot plots and gate selections revealed that the forward scattering gate selections provided more reliable data sets. While it was obvious that there was a proportional relationship between increasing network size and increasing virus concentration with no upper limit other than the number of nanotubes added to the sample, it was non-obvious that the side scattering intensity provided a less proportional relationship. Since the size of the larger network structures was directly proportional to the number of nanotubes it contains, the organization of these nanotubes into the network could achieve a variety of shapes, each having its own unique surface roughness and therefore side scattering intensity. It was thus harder to distinguish accurate information about the number of viruses present in each network or aggregate of peptide nanotube biosensors and viruses using side scattering intensity as a criterion when compared to the better alternative of using forward scattering intensity.

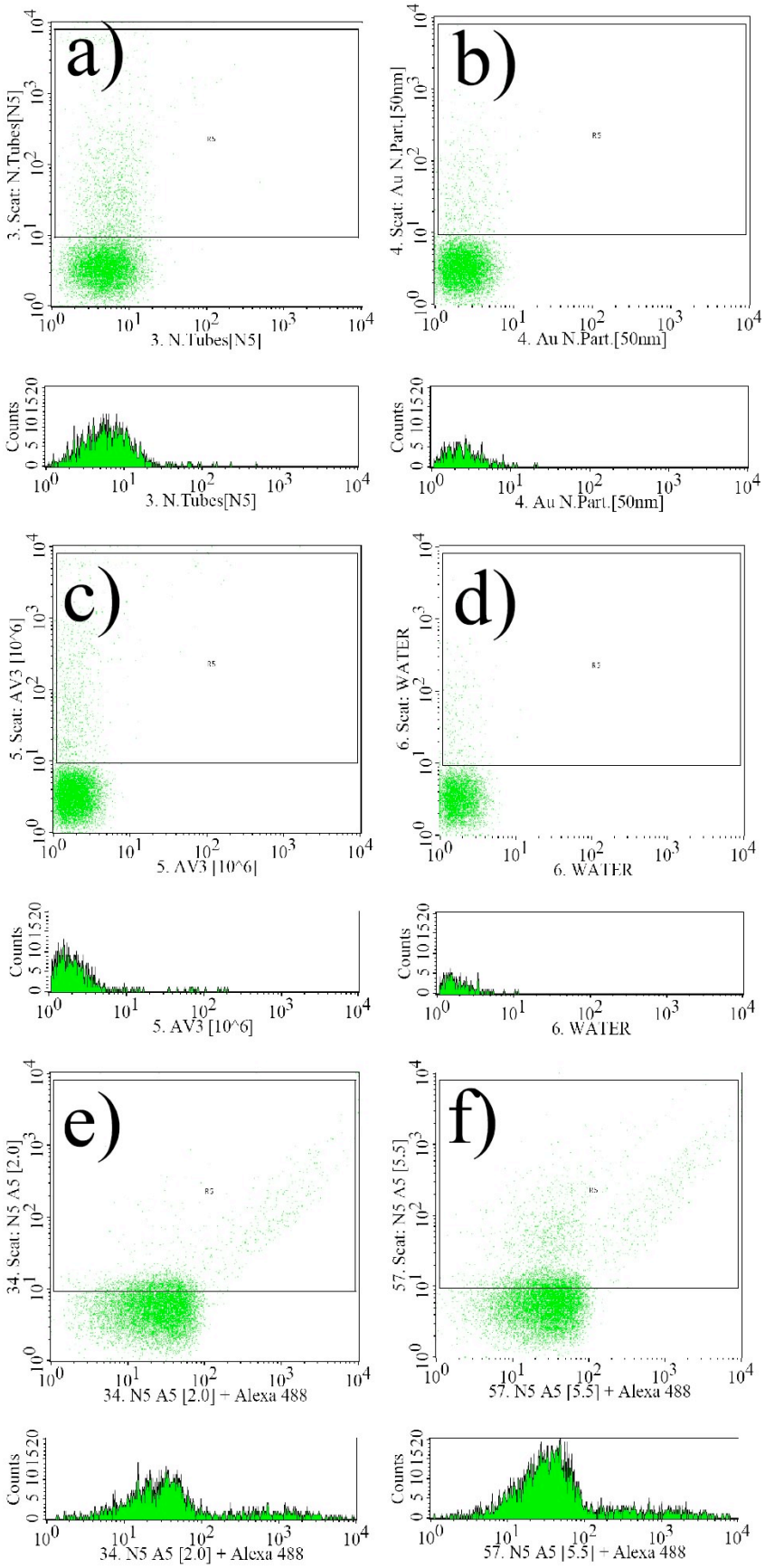

a)
3. Scat: N.Tubes[N5]
3. N.Tubes[N5]
Counts
3. N.Tubes[N5]
b)
4. Scat: Au N.Part.[50nm]
4. Au N.Part.[50nm]
Counts
4. Au N.Part.[50nm]
c)
5. Scat: AV3 [10^6]
5. AV3 [10^6]
Counts
5. AV3 [10^6]
d)
6. Scat: WATER
6. WATER
Counts
6. WATER
e)
34. Scat: N5 A5 [2.0]
34. N5 A5 [2.0] + Alexa 488
Counts
34. N5 A5 [2.0] + Alexa 488
f)
57. Scat: N5 A5 [5.5]
57. N5 A5 [5.5] + Alexa 488
Counts
57. N5 A5 [5.5] + Alexa 488

Figure 4-18. Peptide nanotube biosensors with antibodies against Adenovirus Type 5 used to assay for Adenovirus Type 5 concentration. a) nanotube negative control; b) 50nm gold nanoparticles; c) Adenovirus Type 5 stocks; d) solvent, distilled water; e) positive control of peptide nanotubes mixed with Adenovirus Type 5 at 10^2 pfu/mL concentrations; f) positive control of peptide nanotubes mixed with Adenovirus Type 5 at 10^6 pfu/mL concentrations.

In Figure 4-19, peptide nanotube biosensors loaded with antibodies against a specific domain of the large T antigen of SV40 were used to assay for SV40 concentration. More specifically, the epitope was between amino acids 83 and 128 of the large T antigen. This experiment was the first of two experiments that showed the side scattering vs. fluorescence intensity of assays for the SV40 virus. The selection of antibodies in this set was actually detecting for the T antigen of SV40, a protein that was transcribed only after infection in cells had occurred. The SV40 virus stocks were originally grown in a cell culture, with the presence of T antigen likely in the final stock along with other cellular debris. Since the T antigen concentration should be proportional to the concentration of free virus, this enabled the detection of the SV40 virus concentration. The gate selection for these side scattering vs. fluorescence intensity dot plots was performed such that background noise from water and virus stocks would be nearly eliminated. In Figure 4-19a, the nanotube only negative control was shown. There were a significant number of peptide nanotubes creating gated fluorescent events. In Figure 4-19b, the virus stocks were shown, with nearly all noise from virus stocks eliminated from the gated events, as shown by the histogram inset beneath the dot plot. In Figure 4-19c, the distilled water solvent was assayed, showing an amount of noise that was less than the nanotube negative control in terms of number of gated events, but was very similar in terms of average gated fluorescence intensity. In Figures 4-19d, 4-19e,

and 4-19f the positive controls were shown, with nanotube biosensors used to assay a sample spiked with 10^2, 10^4, and 10^6, pfu/mL of SV40 virus, respectively. In Figures 4-19d and 4-19e, the histograms showed a similar fluorescence intensity and number of events when compared to the negative control. This suggested that the side scattering intensity vs. fluorescence intensity dot plots did not provide accurate means of detecting virus concentration. In Figure 4-19f, the histogram showed a slightly larger number of fluorescence events than the negative control, however the average gated fluorescence intensity was statistically the same as the negative control. It was noteworthy that all of the side scattering data displayed in Figures 4-14 through 4-23 was collected at the same time on the same samples as shown in Figures 4-3 through 4-12. The flow cytometer had multiple photodetectors tuned to specific wavelengths, and at various angles relative to the illumination laser. Typically, a 488nm laser was used to excite the drops as they pass through the flow cytometer. If there was a cell or a nanotube in the drop, it would have created a positive signal on the detectors, and the data would have been recorded in various channels. There was a 488nm photodetector in line with the laser spot so the forward scattering could be detected and a 488nm photodetector at 90 degrees to the laser so the side scattering could be recorded. The other photodetectors for fluorescence emission peaks of fluorophores were filtered for the specific wavelengths of the fluorophores involved.

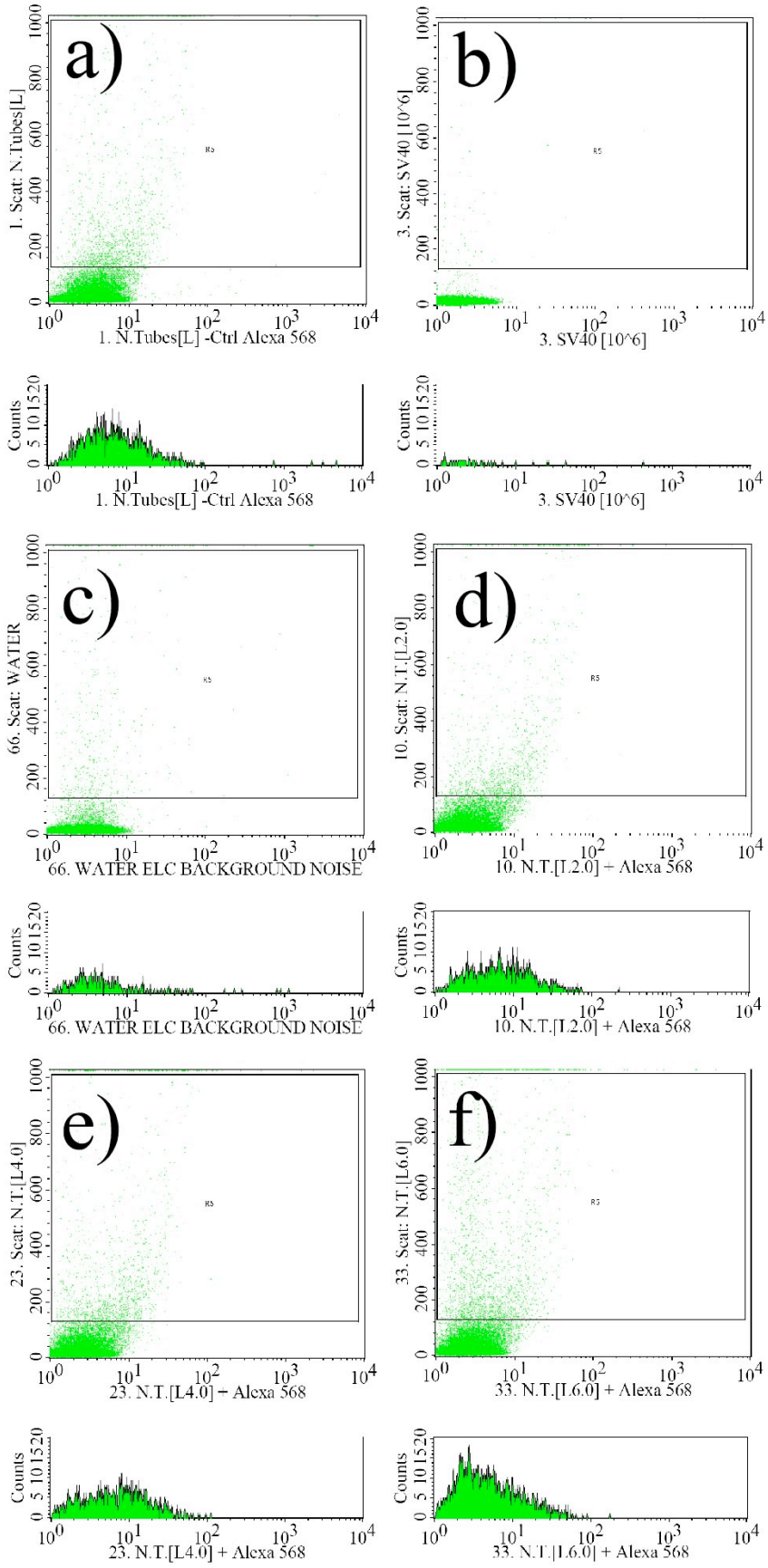

a)
1. Scat: N.Tubes[L]
1. N.Tubes[L] -Ctrl Alexa 568
Counts
1. N.Tubes[L] -Ctrl Alexa 568
b)
3. Scat: SV40 [10^6]
3. SV40 [10^6]
Counts
3. SV40 [10^6]
c)
66. Scat: WATER
66. WATER ELC BACKGROUND NOISE
Counts
66. WATER ELC BACKGROUND NOISE
d)
10. Scat: N.T.[L2.0]
10. N.T.[L2.0] + Alexa 568
Counts
10. N.T.[L2.0] + Alexa 568
e)
23. Scat: N.T.[L4.0]
23. N.T.[L4.0] + Alexa 568
Counts
23. N.T.[L4.0] + Alexa 568
f)
33. Scat: N.T.[L6.0]
33. N.T.[L6.0] + Alexa 568
Counts
33. N.T.[L6.0] + Alexa 568

Figure 4-19. Peptide nanotube biosensors with antibodies against the large T antigen of SV40 virus. a) nanotube negative control; b) SV40 virus stock, undiluted, 10^6 pfu/mL; c) solvent, distilled water; d) positive control of peptide nanotubes mixed with 10^2 pfu/mL SV40; e) positive control of peptide nanotubes mixed with 10^4 pfu/mL SV40; f) positive control of peptide nanotubes mixed with 10^6 pfu/mL SV40.

In Figure 4-20, peptide nanotube biosensors were loaded with antibodies against the N-terminus of small and large T antigen of SV40. Again, this antibody was detecting a free protein concentration in solution that was a reflection of the original virus concentration. Here, as in Figure 4-19, the main consideration in selecting the gate shape was to reduce the noise from water and virus stocks as much as possible. In Figure 4-20a, the nanotube biosensors negative control was shown. A significant number of gated fluorescence events were observed. In Figure 4-20b, the SV40 virus stock was assayed. As expected by the gate shape selection criteria, there were relatively few gated events. In Figure 4-20c, the solvent of distilled water was shown, with very few gated events displayed in the histogram inset beneath the dot plot. In Figures 4-20d, 4-20e, and 4-20f, the positive controls of the peptide nanotube biosensors mixed with samples spike with 10^2, 10^4, and 10^6 pfu/mL of SV40 were shown. If only these three histograms were examined in isolation of the other controls, the data could suggest that there was some slight increase in number of events as the virus concentration increased, however there was no statistically significant increase in the average gated fluorescence intensity. Further, when considering the negative control, there was no statistically significant difference in average gated fluorescence intensity, and therefore no claims could be made of detection by side scattering intensity and fluorescence intensity.

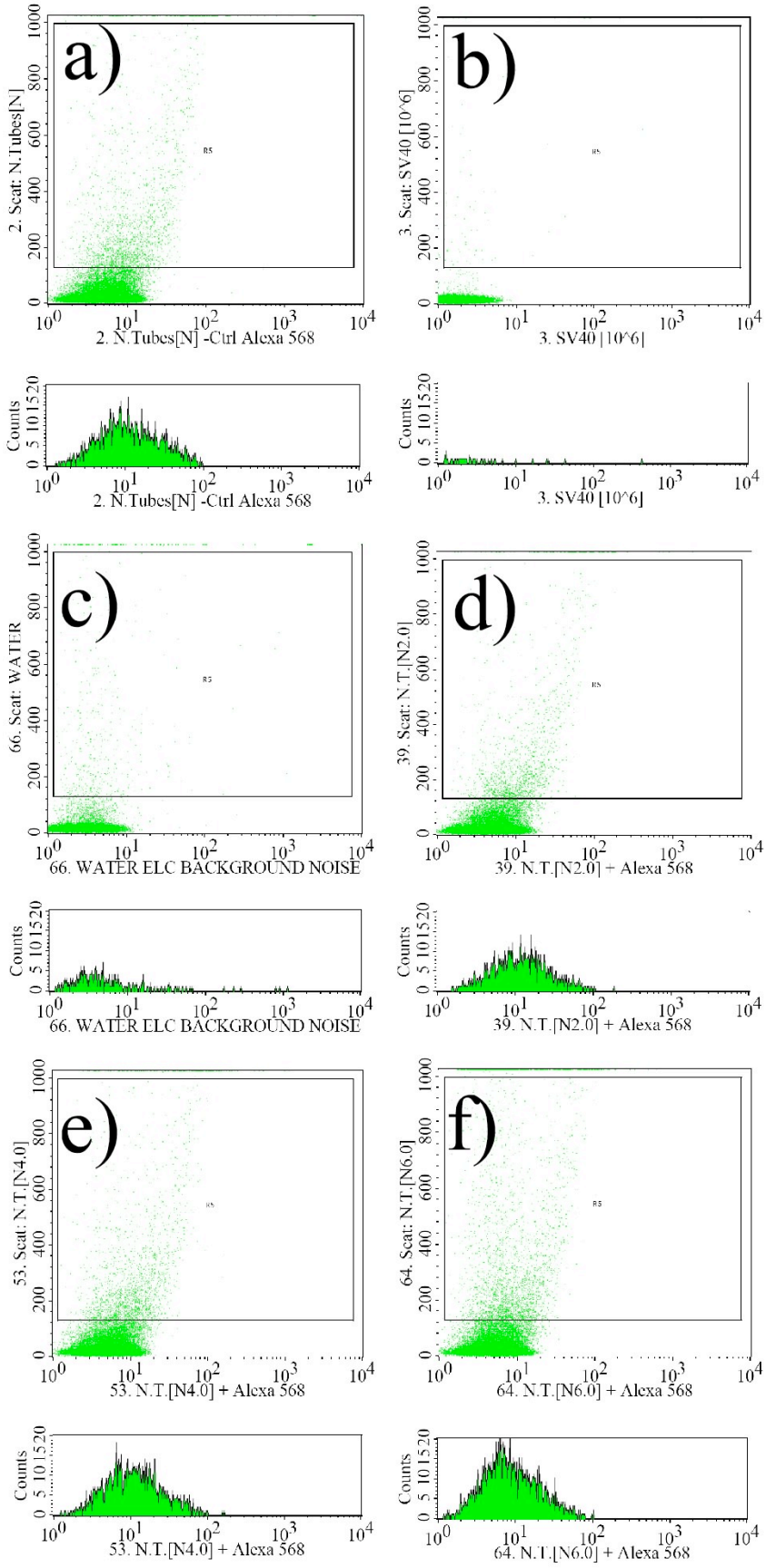

a)
2. Scat: N.Tubes[N]
2. N.Tubes[N] -Ctrl Alexa 568
Counts
2. N.Tubes[N] -Ctrl Alexa 568
b)
3. Scat: SV40 [10^6]
3. SV40 [10^6]
Counts
3. SV40 [10^6]
c)
66. Scat: WATER
66. WATER ELC BACKGROUND NOISE
Counts
66. WATER ELC BACKGROUND NOISE
d)
39. Scat: N.T.[N2.0]
39. N.T.[N2.0] + Alexa 568
Counts
39. N.T.[N2.0] + Alexa 568
e)
53. Scat: N.T.[N4.0]
53. N.T.[N4.0] + Alexa 568
Counts
53. N.T.[N4.0] + Alexa 568
f)
64. Scat: N.T.[N6.0]
64. N.T.[N6.0] + Alexa 568
Counts
64. N.T.[N6.0] + Alexa 568

Figure 4-20. Peptide nanotube biosensors with antibodies against the N-terminus of both the small and large T antigen of SV40 virus. a) nanotube negative control; b) SV40 virus stock, undiluted, 10^6 pfu/mL; c) solvent, distilled water; d) positive control of peptide nanotubes mixed with 10^2 pfu/mL SV40; e) positive control of peptide nanotubes mixed with 10^4 pfu/mL SV40; f) positive control of peptide nanotubes mixed with 10^6 pfu/mL SV40.

Figure 4-21 showed peptide nanotube biosensors loaded with antibody against Influenza A antigen used to assay for Influenza A antigen concentration. These antibodies and antigen stocks were obtained and provided as a safety precaution so that no live flu virus would need to be handled. The gate selection criteria were again driven by the goal of reducing or eliminating the background noise from the water and virus antigen stock samples. In Figure 4-21a, the nanotube negative control was displayed. A wide distribution of fluorescent event intensities was observed, with very few events in the gated region. In Figure 4-21b, the undiluted stocks of Influenza A antigen were shown. As expected, there were very few gated fluorescence events. In Figure 4-21c, distilled water was assayed, and few gated events were observed. In Figure 4-21d, the 50 nanometer gold nanoparticles were observed. The nanoparticles fell outside of the gated region and thus produced few gated fluorescence events. In Figure 4-21e, the first positive control of nanotube biosensors added to 10^2 pfu/mL of Influenza A antigen was displayed. There was little difference in the shape of the dot plot event distribution or in the histogram of gated events. The average gated fluorescence intensity was similar, as was the number of gated events. In Figure 4-21f, the second positive control of nanotube biosensors added to 10^6 pfu/mL of Influenza A antigen were displayed. Since both positive controls appeared indistinguishable from the negative control, there could be no claims of detection made using side scattering vs. fluorescence intensity.

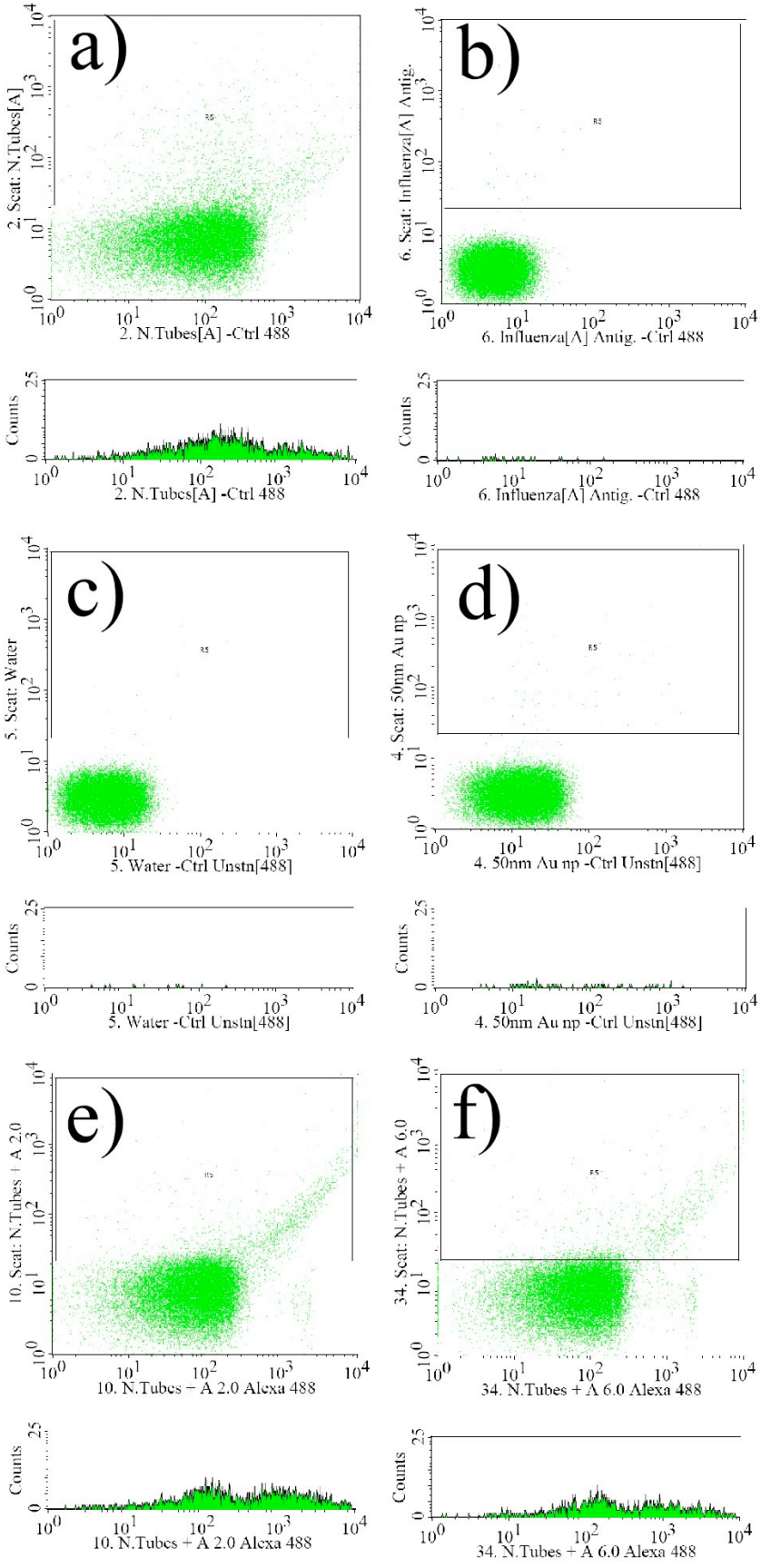

a)
2. Scat: N.Tubes[A]
2. N.Tubes[A] -Ctrl 488
Counts
2. N.Tubes[A] -Ctrl 488
b)
6. Scat: Influenza[A] Antig.
6. Influenza[A] Antig. -Ctrl 488
Counts
6. Influenza[A] Antig. -Ctrl 488
c)
5. Scat: Water
5. Water -Ctrl Unstn[488]
Counts
5. Water -Ctrl Unstn[488]
d)
4. Scat: 50nm Au np
4. 50nm Au np -Ctrl Unstn[488]
Counts
4. 50nm Au np -Ctrl Unstn[488]
e)
10. Scat: N.Tubes + A 2.0
10. N.Tubes + A 2.0 Alexa 488
Counts
10. N.Tubes + A 2.0 Alexa 488
f)
34. Scat: N.Tubes + A 6.0
34. N.Tubes + A 6.0 Alexa 488
Counts
34. N.Tubes + A 6.0 Alexa 488

Figure 4-21. Peptide nanotube biosensors with antibodies against Influenza A. a) nanotube negative control; b) Influenza A antigen stock, undiluted, 10^6 pfu/mL; c) solvent, distilled water; d) 50nm gold nanoparticles; e) positive control of peptide nanotubes mixed with 10^2 pfu/mL Influenza A antigen; f) positive control of peptide nanotubes mixed with 10^6 pfu/mL Influenza A antigen.

In Figure 4-22, peptide nanotube biosensors loaded with antibodies against Influenza B were used to assay for Influenza B antigen concentration. Similarly, the gate selection criteria used were to primarily eliminate the noise from the water and the virus stocks. In Figure 4-22a, the negative control of only nanotube biosensors was shown. A significant number of gated fluorescence events were observed. In Figure 4-22b, the 50 nanometer diameter gold nanoparticles were observed. No gated fluorescence intensity events were observed. In Figure 4-22c, the virus antigen stocks of the Influenza B antigen were observed, and in Figure 4-22d, the solvent of distilled water was observed. Since both of these two samples were used in the criteria for gate shape selection, they resulted in no gated fluorescence intensity events being observed. In Figure 4-22e, the first positive control was shown. Peptide nanotube biosensors were mixed with samples spiked with 10^2 pfu/mL Influenza B antigen. The number of gated fluorescence events was observed to decrease compared to the negative control. In Figure 4-22f, the second positive control was shown. Peptide nanotube biosensors were mixed with samples spiked with 10^6 pfu/mL Influenza B antigen. The negative control displayed a similar number and average of gated fluorescence intensity events. This result demonstrated that using side scattering vs. fluorescence intensity dot plots and gate selections was not appropriate for quantitative detection.

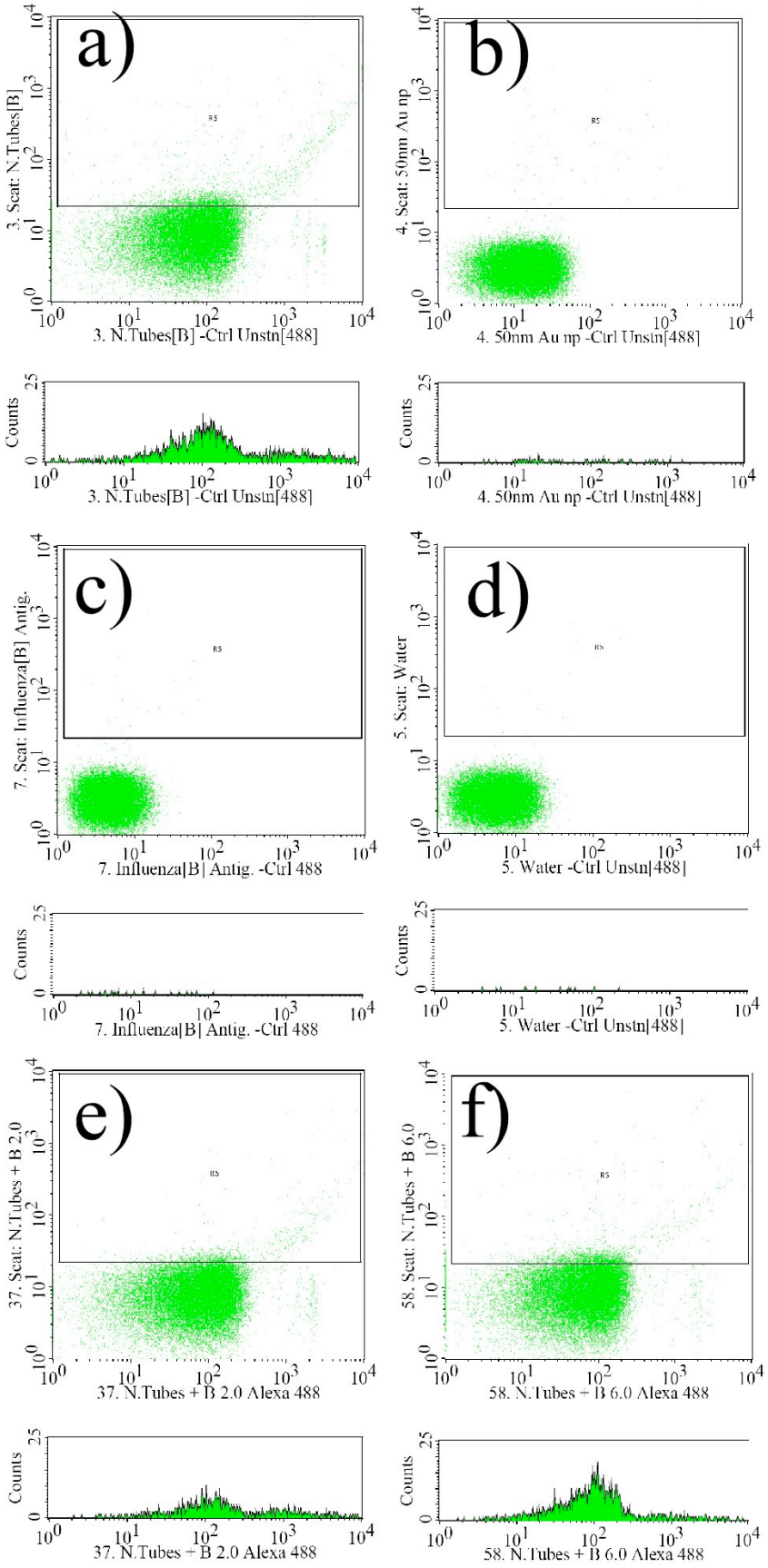

a)
3. Scat: N.Tubes[B]
3. N.Tubes[B] -Ctrl Unstn[488]
Counts
3. N.Tubes[B] -Ctrl Unstn[488]
b)
4. Scat: 50nm Au np
4. 50nm Au np -Ctrl Unstn[488]
Counts
4. 50nm Au np -Ctrl Unstn[488]
c)
7. Scat: Influenza[B] Antig.
7. Influenza[B] Antig. -Ctrl 488
Counts
7. Influenza[B] Antig. -Ctrl 488
d)
5. Scat: Water
5. Water -Ctrl Unstn[488]
Counts
5. Water -Ctrl Unstn[488]
e)
37. Scat: N.Tubes + B 2.0
37. N.Tubes + B 2.0 Alexa 488
Counts
37. N.Tubes + B 2.0 Alexa 488
f)
58. Scat: N.Tubes + B 6.0
58. N.Tubes + B 6.0 Alexa 488
Counts
58. N.Tubes + B 6.0 Alexa 488

Figure 4-22. Peptide nanotube biosensors with antibodies against Influenza B. a) nanotube negative control; b) Influenza B antigen stock, undiluted, 10^6 pfu/mL; c) solvent, distilled water; d) 50nm gold nanoparticles; e) positive control of peptide nanotubes mixed with 10^2 pfu/mL Influenza B antigen; f) positive control of peptide nanotubes mixed with 10^6 pfu/mL Influenza B antigen.

Figure 4-23 showed side scattering vs. fluorescence intensity dot plots of the peptide nanotube biosensors loaded with antibodies against Vaccinia virus. In this experiment, the gate shape selection criteria were expanded to not only reduce the background noise from virus stocks and solvent, but also from unbound nanotubes. In Figure 4-23a, the nanotube negative control was shown. Based on the gate selection criteria there were very few gated fluorescence events. In Figure 4-23b, the noise from 50 nm gold nanoparticles had been eliminated from the gated regions. In Figure 4-23c, the virus stocks of Vaccinia or MVA were assayed. A large amount of noise events remained in the gated region that could not be eliminated. This noise further complicated measurements due to its high average fluorescence intensity. In Figure 4-23d, the solvent of distilled water was shown, and based on the gate selection criteria there were very few noise events. In Figure 4-23e, the first positive control of 10^5 pfu/mL Vaccinia spiked samples was displayed, and exhibited a slight increase in the number of gated fluorescence events compared to the negative control. In Figure 4-24f, the second positive control of 10^6 pfu/mL Vaccinia spiked samples was displayed, and exhibited a marked increase in the number of gated fluorescence events. Due to the control that showed the large number of high fluorescence intensity events from the virus stocks alone, the results shown here did not allow a conclusion to be drawn that the nanotube networks were forming based solely on the SSC vs. FL-1 data. This further reinforced the selection of FSC vs. FL-1 as the method of choice for quantitative assays.

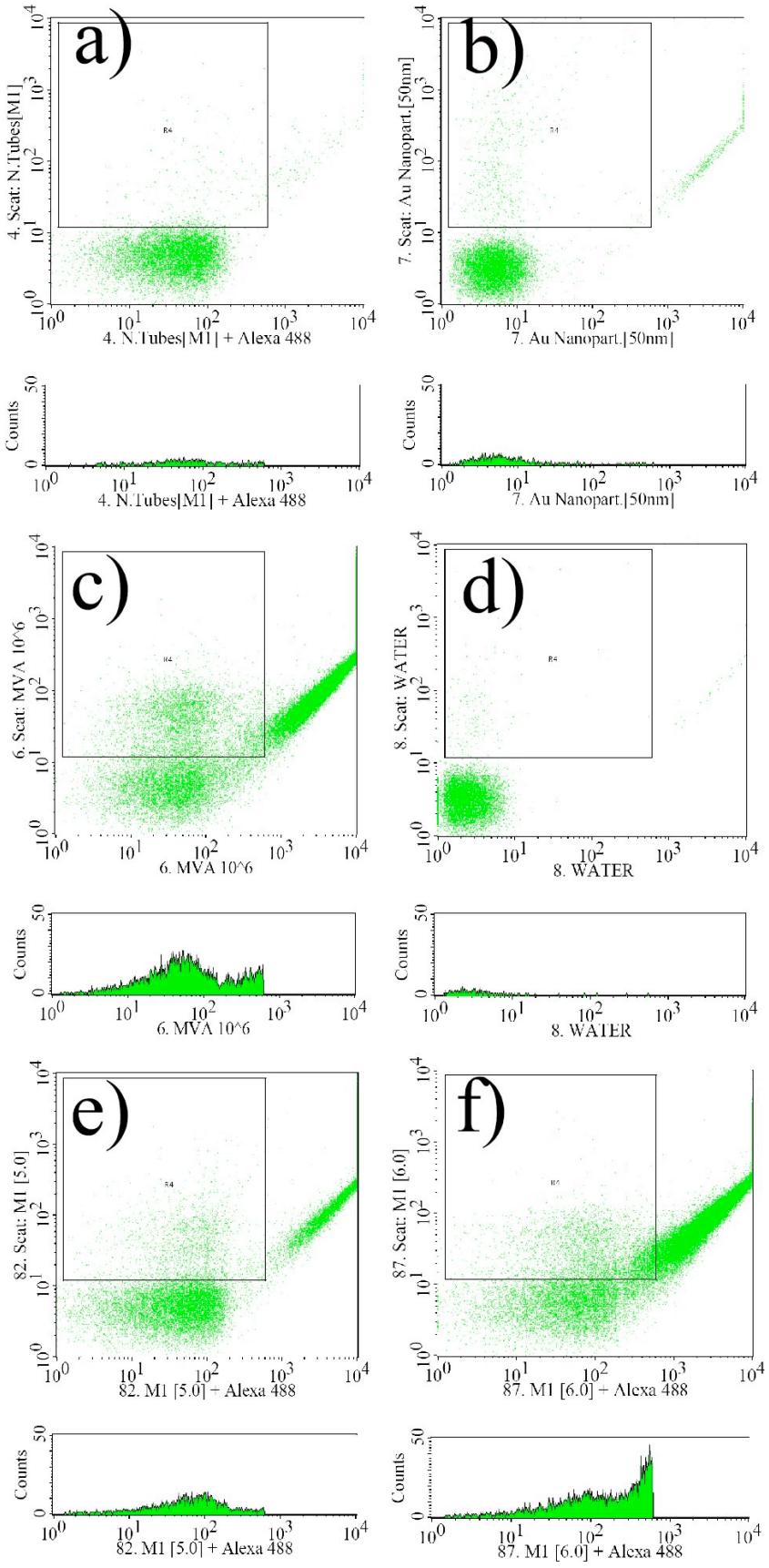

a)
4. Scat: N.Tubes[M1]
4. N.Tubes[M1] + Alexa 488
Counts
4. N.Tubes[M1] + Alexa 488
b)
7. Scat: Au Nanopart.[50nm]
7. Au Nanopart.[50nm]
Counts
7. Au Nanopart.[50nm]
c)
6. Scat: MVA 10^6
6. MVA 10^6
Counts
6. MVA 10^6
d)
8. Scat: WATER
8. WATER
Counts
8. WATER
e)
82. Scat: M1 [5.0]
82. M1 [5.0] + Alexa 488
Counts
82. M1 [5.0] + Alexa 488
f)
87. Scat: M1 [6.0]
87. M1 [6.0] + Alexa 488
Counts
87. M1 [6.0] + Alexa 488

Figure 4-23. Peptide nanotube biosensors with antibodies against Vaccinia (MVA). a) nanotube negative control; b) 50nm gold nanoparticles; c) Vaccinia stock, undiluted, 10^6 pfu/mL; d) solvent, distilled water; e) positive control of peptide nanotubes mixed with 10^2 pfu/mL Vaccinia; f) positive control of peptide nanotubes mixed with 10^6 pfu/mL Vaccinia.

The protocol to test liquid samples for viruses was developed for efficiency. By adding a 100uL aliquot of nanotubes to a 400uL aliquot of sample, mixing and incubating for 25 minutes, the samples were ready for analysis either qualitatively by light microscopy or quantitatively by flow cytometry. This simple protocol required addition of one reagent solution, and one instrumental analysis. Assuming previously prepared peptide nanotube biosensors, normal proficiency to obtain flow cytometry data in under five minutes, and standard curves previously prepared, the process only took 30 minutes from receipt of the sample in the lab until the final quantitative data was ready. Furthermore, the sensitivity of the assay was on the order of 50 virions in 0.5mL, comparable to quantitative PCR and on the order of attomolar virus concentrations. This protocol therefore met the criteria of rapid, one step, and sensitive.

3. MULTIPLEXED DETECTION USING FLOW CYTOMETRY

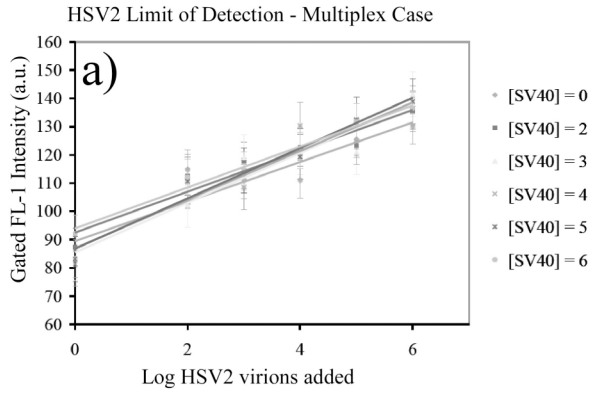
Thus far, discussion has detailed the case of analyzing a single virus at a time. However, to demonstrate the selectivity of the antibody-based assay, a multiplexed experiment was designed. Two types of nanotubes were synthesized independently, each with a unique antibody-fluorescent dye pairing. An aliquot of each type of nanotube was then added to the samples under analysis. An illustration of the mechanism of multiplex detection is shown in Figure 4-1d. In this illustration, the HSV2 was represented by the white viruses with the triangular antigens and the anti-HSV2 antibody was represented by

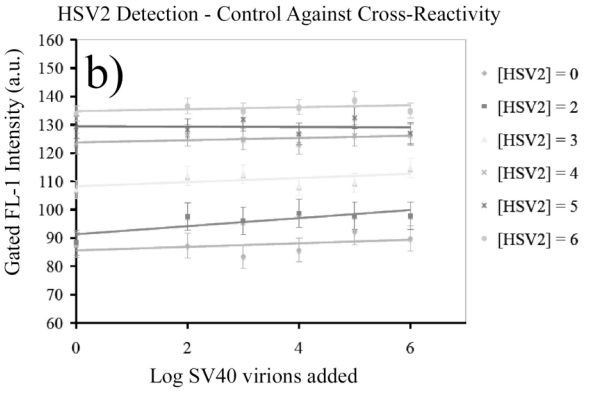
the triangular antibody. The anti-HSV2 antibody was attached at the ends of the nanotubes labeled with green dye. The SV40 was represented by the black viruses with the rectangular antigens, and the anti-SV40 antibody was represented by the rectangular antibody. The anti-SV40 antibody was attached at the ends of the nanotubes labeled with red dye. Since antibodies were chosen to prevent cross-reactivity between the two viruses, the green nanotubes aggregated only as a function of the HSV2 concentration while the red nanotubes aggregated only as a function of the SV40 concentration, thereby retaining the selectivity of the assay.

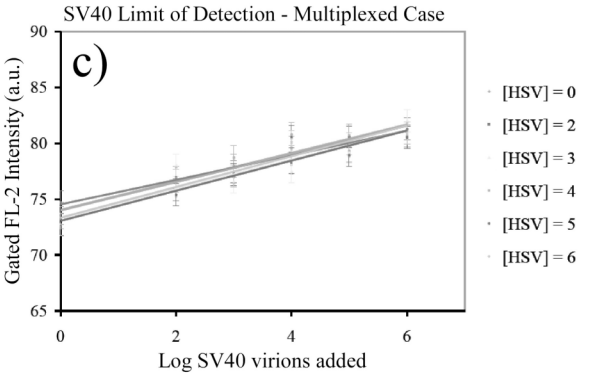
In this proof of principle experiment, nanotubes with antibodies against HSV2 virus were labeled with green Alexa 488 dye while nanotubes with antibodies against SV40 were labeled with red Alexa 633 dye, and a 1:1 mixture of these two types of nanotubes was prepared to analyze subsequent virus-spiked samples. To prove the independence of each nanotube biosensor system within the multiplex assay, a carefully designed series of controlled experiments were performed on this two virus system to confirm its validity. In order to make sure there was no inhibition of aggregation by having a mixture of nanotubes present, the mixture of both nanotubes was analyzed a single virus at a time. First studying only SV40 virus-containing samples, single color red aggregates were found to be the only structures present, with no change in limit of detection compared to using a single type of nanotube biosensor as shown in Table 4-1. Subsequent observation of only HSV2 virus-spiked samples found solely single color green aggregates and again no change in the limit of detection compared with single virus results.

An analysis of potential cross-reactivity of each antibody was also performed. First studying HSV2, the limit of detection using gated average red fluorescence intensity was determined. This limit of detection determination was performed at several unique constant background SV40 concentrations. Each of these limit-of-detection traces were overlaid onto the same plot to create Figure 4-24a. Each trace represented the limit of detection at one given SV40 background concentration. Since all of the traces fell within a very tight tolerance region of each other, this shows that the simultaneous presence of SV40 and SV40 nanotube biosensor aggregates did not interfere with the selectivity or detection of HSV2 at any concentration of either virus.

The effect of cross-reactivity between the antibodies and viruses was also tested. Figure 4-24b showed a plot of the data from Figure 4-24a, presented in a different fashion. The green fluorescence intensity values of each HSV2 concentration were plotted against the background SV40 concentration added. Since the green fluorescence intensity was a measure of HSV2 concentration, and each trace contains data points at a constant HSV2 concentration, one would have expected to see traces with a slope close to zero, with each trace offset by the appropriate level to reflect the expected fluorescence intensity at the given HSV2 concentration for that trace. This prediction was in fact observed in Figure 4-24b, further indicating the absence of cross-reactivity and retention of antibody selectivity.


HSV2 Limit of Detection - Multiplex Case
a)
Gated FL-1 Intensity (a.u.)
Log HSV2 virions added
[SV40] = 0
[SV40] = 2
[SV40] = 3
[SV40] = 4
[SV40] = 5
[SV40] = 6


HSV2 Detection - Control Against Cross-Reactivity
b)
Gated FL-1 Intensity (a.u.)
Log SV40 virions added
[HSV2] = 0
[HSV2] = 2
[HSV2] = 3
[HSV2] = 4
[HSV2] = 5
[HSV2] = 6


SV40 Limit of Detection - Multiplexed Case
c)
Gated FL-2 Intensity (a.u.)
Log SV40 virions added
[HSV] = 0
[HSV] = 2
[HSV] = 3
[HSV] = 4
[HSV] = 5
[HSV] = 6

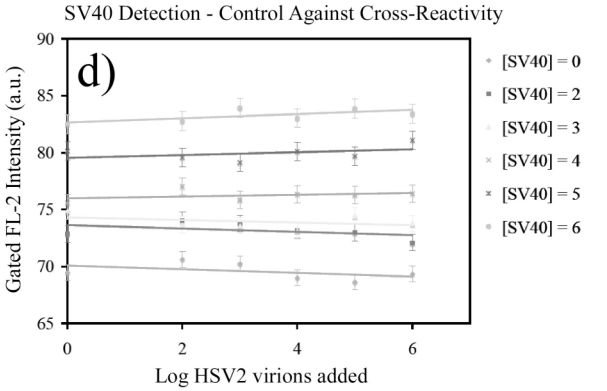

SV40 Detection - Control Against Cross-Reactivity
d)
Gated FL-2 Intensity (a.u.)
Log HSV2 virions added
[SV40] = 0
[SV40] = 2
[SV40] = 3
[SV40] = 4
[SV40] = 5
[SV40] = 6

Figure 4-24. Mixture of HSV2 and SV40 sample analysis. Red fluorescence intensity was used for SV40 detection, green fluorescence intensity was used for HSV2 detection. a) gated red fluorescence intensity vs. concentration of SV40, for SV40 limit of detection; b) gated red fluorescence intensity vs. concentration of HSV2, for cross-reactivity determination; c) gated green fluorescent intensity vs. concentration of HSV2 concentration, for HSV2 limit of detection; d) gated green fluorescence intensity vs. concentration of SV40, for cross-reactivity determination.

Similarly to HSV2, when examining SV40 in Figure 4-24c, the limit of detection using gated average red fluorescence intensity was determined at various constant HSV2 background concentrations. Again, each trace represented one unique constant background HSV2 concentration, and all of the traces fell within a very tight tolerance region of one another. To assay for cross-reactivity of the SV40 antibody in Figure 4-24d, the same data set was presented differently. Each trace represented a constant SV40 concentration and was plotted against the background HSV2 levels. This confirmed that no cross-reactivity occurred between the samples studied. These controls showed the versatility of the nanotube assay, and provided the proof-of-principle that the technique was only limited by the number of photodetectors present on the flow cytometer and the ability to resolve the individual fluorophores with minimal overlapping in their fluorescence peaks.

A unique advantage to this system was the nanotubes allow rapid visualization by light microscopy of the presence of viruses not normally visible by light microscopy. This qualitative assay was used as an alternative to the quantitative flow cytometry method. As the aggregates grew in size by incorporating more viruses and nanotubes, a rapid qualitative observation of the presence of a target pathogen was made by using a fluorescence microscope by observing a specific color aggregate. While it was not possible to precisely determine the size or fluorescence intensity of the network

structures, and therefore the number of viruses in the solution or even in a given aggregation, using a bench top fluorescence light microscope provided a simpler alternative method when a low limit of detection is not required of the assay, or if a flow cytometer was not immediately available.

The ratio of nanotubes to viruses was important in predicting the expected size of the network structures. Considering the mechanism of network formation, in the first step, a single virus bound to a single nanotube to create an intermediate structure. A TEM image of such an intermediate structure was shown in Figure 4-25a. When the concentration of the nanotubes was much higher than the concentration of the virus, this intermediate was statistically likely to encounter only unbound nanotubes until all the available nanotube binding sites on the virus had been occupied. In the case where the concentration of nanotubes approached the same order of magnitude as the concentration of the virus, the likelihood of an intermediate finding and binding to another intermediate or unbound virus increased. This allowed the formation of the larger network structures. However, if the concentration of nanotubes was less than the concentration of the virus, it was possible for nearly all of these intermediate structures to bind another virus and not bind any other nanotubes or even other intermediate structures.

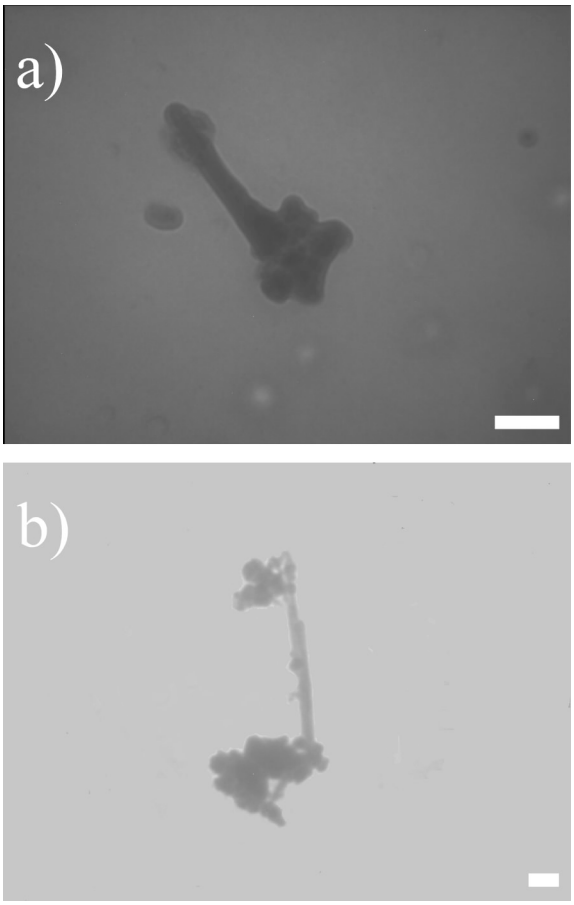


Figure 4-25. a) TEM image of an intermediate structure of a nanotube with virus bound at one end. b) TEM image of a saturated nanotube, from a solution where virus concentration exceeded the nanotube concentration tenfold.

A structure from a solution where the number of viruses exceeded the number of nanotubes ten-fold was shown in Figure 4-25b. The nanotube was saturated with a virus at both ends, yet there were no other nanotubes bound in the structure. Saturated structures could therefore yield a false negative result. This was observed in the data in Figure 4-26. In Figure 4-26a, the nanotube concentration was higher than the virus concentration by one order of magnitude. The nanotubes detected the concentration of virus accurately when the nanotubes' concentration exceeded the virus concentration, and as such were under the normal conditions for the experiments described. In Figure 4-26b,

the nanotube concentration was approximately equal to the virus concentration. As the nanotubes were diluted to a point where the virus concentration was on the same order of magnitude as the concentration of nanotubes added, the number of aggregates began decreasing and nanotubes not bound into aggregates were found to be present. In Figure 4-26c, the nanotube concentration was less than the virus concentration by one order of magnitude. As the nanotubes were further diluted such that virus concentration exceeded the number of nanotubes, the number of aggregates went essentially to zero with the individual saturated nanotubes being detected as the only species present. The presence of such a saturation point, while unlikely in a real sample, reinforced that the aggregate networks increased in size by the nanotubes binding viruses at both ends.

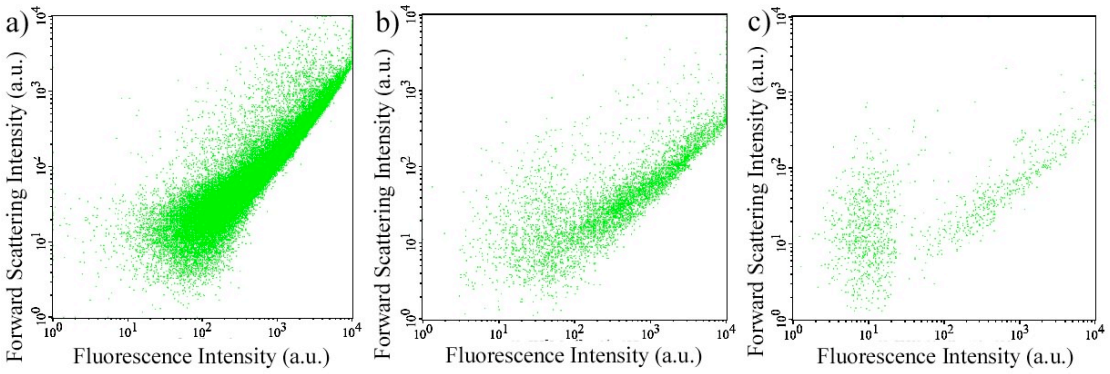


Figure 4-26. Dot plot of forward scattering vs. fluorescent intensity at a) 10^7 nanotubes/mL, b) 10^6 nanotubes/mL, and c) 10^5 nanotubes/mL, for a 10^6 pfu/mL HSV-2 spiked sample. The logarithmic nanotube dilutions are eventually saturated, with unbound nanotubes being observed as still present in the solution.

The selection of gates in the flow cytometry data was an important step in creating standard curves for quantitative analysis. A series of negative and positive controls should be examined when drawing appropriate gates. The goal should be to exclude all noise from water, and virus stocks. In some cases, including a negative control of 50nm gold nanoparticles is useful to demonstrate that 50nm sized particles

give the same signal as water, therefore the virus stocks should also give the same signal as water. Once these regions are excluded, the negative control of the fluorescent nanotubes without viruses should be considered. A careful examination to eliminate the majority of the single nanotubes should be performed. Finally, the positive controls should be included into the gate drawing process, to confirm that the regions where the small and large network structures will appear are included in the gated region.

4. MATERIALS AND METHODS

Synthesis of peptide nanotubes

Bis(*N*-α-amido-glycylglycine)-1,7-heptane dicarboxylate was prepared as previously described. These bolaamphiphile peptide monomers (10mg/mL) were dissolved in 50mM sodium hydroxide overnight, and then the pH of the resulting solution was adjusted at 4.5 using a citric acid buffer. After two weeks, the peptide nanotubes saturated the solution. Then the nanotubes were separated by size separation columns, resulting in a suspension of nanotubes with dimensions of approximately 100 nm diameter by 1 um length. The resulting nanotube solution was washed by deionized water and centrifuged three times at 14,000RPM before functionalizing them with antibodies and dyes.

Antibody fictionalization and dye attachment on the peptide nanotubes

Antibodies were immobilized at the ends of peptide nanotubes using gold nanoparticles as protective masks on the sidewalls of nanotubes[12]. To thiolate the sidewalls of nanotubes for the gold nanoparticle adsorption, 1.5mL of nanotube solution was reacted with 15 mM N-hydroxysuccinimide (50 uL) and 75mM 1-[3-

(dimethylamino)propyl]-3-ethylcarbodiimide hydrochloride (50 uL) at room temperature for three hours. Both chemicals were purchased from Sigma and used as received. After the sample was washed and centrifuged, the nanotubes were reacted with 30 μL of 2-mercaptoethylamine (5 mM) (Sigma) for 12 hours at 4 °C to complete the sidewall thiolation. After another wash, 40 μL of gold nanoparticles (50 nm) (Ted Pella) were added for 6 hours to mask the sidewalls of nanotubes. After unbound gold nanoparticles were washed out, an excess amount of selected antibody (Abcam) was incubated with the nanotubes overnight.

While the gold nanoparticle-masked nanotubes adsorbed antibodies on their entire surfaces, the chemical etching of the gold nanoparticles masks removed antibody molecules from the sidewalls but antibodies at the nanotube ends remained bound. The gold nanoparticle masks were then removed by breaking gold-S bonds with 40uL of an iodine solution (1g KI and 0.3g I_2 per 1 mL distilled H_2O). Previously published results demonstrate the retention of the activity of biological molecules using this method. After the resulting solution was washed four times, the thiol groups which remained along the sidewalls of nanotubes were applied to covalently link maleimide fluorescent dye molecules. First, those nanotubes were resuspended in 10 uM tris-(2-carboxyethyl)phosphine, hydrochloride (TCEP) to reduce disulfide bonds between nanotubes immediately, and then Alexa-Fluor 488 and 633 C_5-Maleimide (Invitrogen) was added to these solutions for two hours at room temperature. The resulting nanotube solutions were washed thoroughly to eliminate the potential background interference from unbound fluorescent dyes left over in the solution. The nanotubes were stored in light-shielding vials to prevent photobleaching of these dyes before use.

Antibody nanotube assay for virus

Antibodies were used as purchased from Abcam (Cambridge, MA). Antibodies used included anti HSV-2, anti-SV40, anti-Influenza A, anti-Influenza B, anti-Adenovirus Type 3, anti-Adenovirus Type 5, and anti Vaccinia.

Herpes simplex virus type 2 (HSV-2) strain 333 was grown in Vero cells as described[121]. Adenovirus Type 3 (ATCC# VR-847) and Adenovirus Type 5 (ATCC# VR-1516) were used as received from American Type Cell Culture.

Titered stocks of SV40, Influenza vaccine strains A & B, and Vaccinia (MVA) were obtained from Drs. Andrew Lewis, Zhiping Ye, and Michael Merchlinsky (all at FDA/CBER), respectively.

To create a series of spiked samples for analysis, 10-fold serial dilutions in 1X PBS were performed from virus stocks with known concentrations.

Flow cytometry and transmission electron microscopy (TEM)

All flow cytometry experiments were performed by a FACS-Aria (BD Biosciences) using a 100 micron tip in the low sort mode. Those tips were washed by buffers between each sampling. A 488 nm laser illumination source was used for the forward scattering (FSC). The 488 nm side scattering (SSC), 516nm Alexa-Fluor 488 peak fluorescence emission (FL-1), and 650nm Alexa-Fluor 633 peak fluorescence emission (FL-2) were detected at 90°. The flow cytometry data was analyzed using the CellQuest Pro software package (BD Biosciences).

The collected nanotube-virus networks with various virus concentrations were studied by transmission electron microscopes (Zeiss, Jeol) with an acceleration voltage of 100kV.

The concentration of stock biosensor solutions was determined by counting the number of fluorescent nanotubes in a 0.5mL aliquot, and found to be between $3.3x10^7$ and $8.6x10^7$ nanotubes/mL. All solutions had a working concentration of $5.0x10^6$ nanotubes/mL, in the final 500μL sample volume for each set of analysis experiments.

Chapter 5

AC IMPEDANCE SPECTROSCOPY ON THE ATOMIC FORCE MICROSCOPE – INSTRUMENT DESIGN AND VERIFICATION

1. FAILURE OF DC CONDUCTIVE MEASUREMENTS WITH DI AFM

Impedance AFM has been used by many researchers to study the properties of nanometer thin films and their defect sites[92, 93, 95, 96, 98, 122]. Some of the earliest pioneering work was performed by Dawn Bonnel at the University of Pennsylvania and Sergei Kalinin during his doctoral research under Dr. Bonnel at U. Penn, and later as an investigator at Oak Ridge National Lab. This work tried to measure the forces from an AC electric field applied to samples[123]. Their further work included imaging of ZnO crystals[94], ceramics[124], and polycrystalline ceramic materials[125], as well as measuring the Schottky barrier diode between p-type and n-type semiconductors[93]. Characterization of carbon nanotubes was also performed[126, 127] as well as studies of the tip gating effect[128]. Dale Teeters studied thin films for nanobattery applications by impedance spectroscopy on the AFM[92]. Bob Hamers used AC electric fields to manipulate bacteria into gaps between electrodes for characterization by impedance analysis[95]. Mark Hersam has worked towards developing better methods of impedance measurements at the nanoscale[98], as well as the Prinz group at Stanford[96, 97]. In all of these cases, researchers were studying thin films deposited on substrates. Studies sought defects of microns in size or made efforts to study grain boundaries or local effects by moving the tip point by point along larger structures. However, a lack of research focusing on characterizing single nanoparticles or single virions was found. An

advantage of the AC impedance AFM technique is the ability to electrically characterize insulating and dielectric materials at the nanoscale, an improvement over the limitations of traditional DC-based conductive AFM techniques commercially available. Despite this advantage, to date very few systems have been developed that exploit Impedance AFM.

Initially, conductive AFM measurements using a DC bias were attempted on native virus particles using a Veeco MultiMode AFM with a Nanoscope IIIa controller and a J-scanner in collaboration with Rutgers University and Professor Huixin He. Due to the high resistance of the viruses, later determined to be on the order of tens of gigaohms, the current sensors were not able to detect any current flow through the virus particles. Several other challenges were discovered to making these kinds of measurements. The contact force that one images with creates shear forces that quickly wear off the metal coatings on the AFM tips. Typical gold coatings on AFM tips are usually quite weak, and allow only a few scans before losing conductive contact. By reducing the forces applied during contact mode imaging to increase tip lifetime, the image quality deteriorates and it becomes difficult to clearly visualize where the viruses are located on the substrate. Another challenge included the tip sweeping viruses off the surface during the scanning process. When the contact force was too high and the gain was too low, loosely bound virus particles would be pushed to the edge of the scanning area on the sample. The image shown in Figure 5-1 was the best DC-conductive mapping AFM image obtained on gold-coated virus samples, and depicts the challenges of the conductive AFM method. Challenges included the gold coating of the tip wearing

off before the image could be collected, as well as the gold coating being scraped off due to the high force required during contact mode imaging.

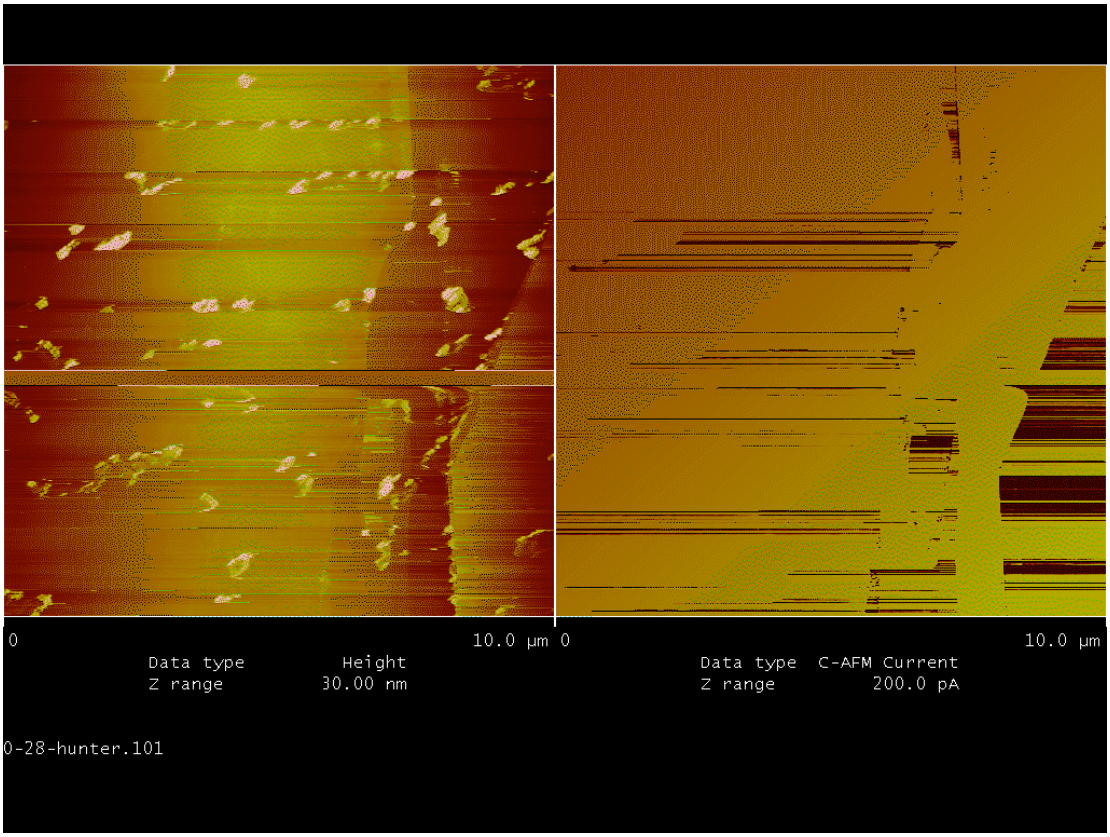


Figure 5-1. DC Conductive AFM measurements taken at Rutgers University in collaboration. The left frame is the height image, and the right frame is the current data.

A method of obtaining DC conductive AFM measurements was derived that included making a gold coating on the surface of the viruses. A solution of viruses containing approximately 10^7 pfu/mL was incubated with trimethylphosphinegold chloride ($AuPMe_3Cl$) and utilized the surface peptides of the viruses. It is thought that light was capable of reducing of the gold salt ions very slowly, and creating a gold coating of several nanometers over a period of twenty four hours. The approach of using light to reduce gold ions with affinity for peptides had been previously demonstrated with peptide nanotubes[18]. Alternatively, the reducing agent of hydrazine hydride was used

to quickly reduce the gold salt in approximately one minute. Topographical AFM images of such gold-coated viruses are shown in Figure 5-2, while conductive mapping attempted images are shown in Figure 5-1.

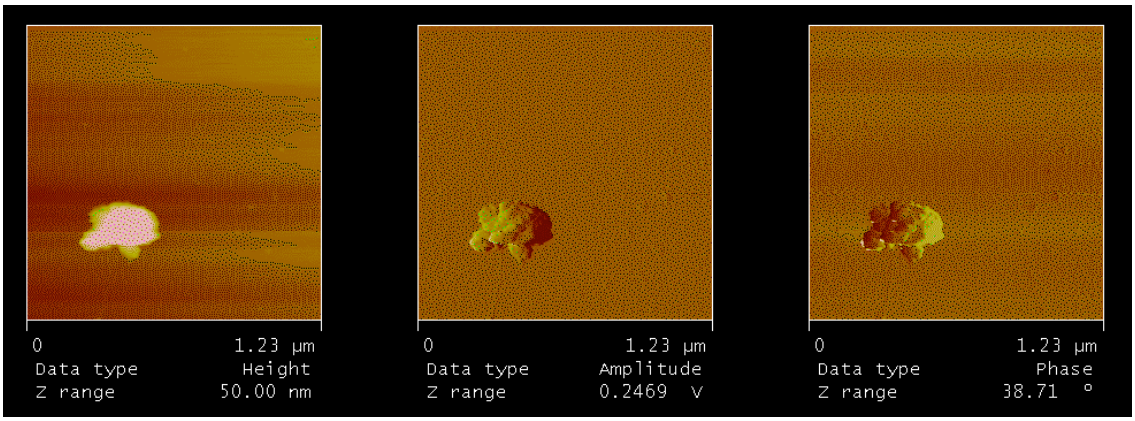


Figure 5-2. Gold-coated Vaccinia virus (MVA).

2. AC PHASE SHIFT ANALYSIS WITH DI AFM AND KROHN-HITE PHASE ANALYZER

After establishing that DC conductivity mapping measurements were not appropriate for characterizing native biological samples, it was decided to attempt AC methods of electrical characterization. A first attempt was made to determine only the phase shift of an AC bias being applied to the sample. In impedance theory, the tangent of the phase angle is equal to the difference between the reactance from inductance, X_L, and the reactance from capacitance, X_C, divided by the real resistance, R. The equation is described below in equation (5-1).

$$\tan\phi = \frac{X_L - X_C}{R} \quad (5\text{-}1)$$

A diagram of the experimental setup is shown in Figure 5-3a. These experiments were performed on the Veeco MultiMode AFM with a Nanoscope IIIa controller and J-scanner at Hunter College. The experimental setup included using a frequency or signal generator with a frequency range sweepable from 1Hz to 1MHz, and sweepable bias output from 0 to +10 V RMS for a source of AC bias. This signal was split using a T-junction BNC connector, with one half of the signal going to the reference input of a phase comparator, and the second half going to the sample. In Figure 5-3, tip bias with the sample "held to ground" is shown, although sample bias with the tip "held to ground" was tried and found to work equally as well. After passing through the sample, the output signal was routed to the phase comparator. The analog output channel of the phase comparator was then piped into the AFM controller using the Veeco Signal Access Module and the Aux D channel, which could then be used to graphically display the phase shift of the AC signal as the AFM topography image was collected.

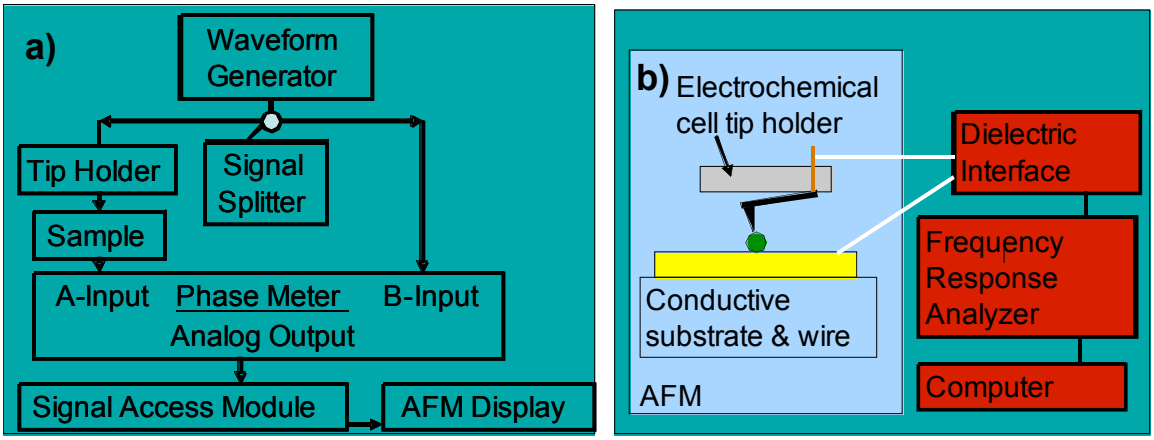


Figure 5-3. Illustrations of early instrumentation setups. a) Using a waveform generator and AC phase analyzer to compare reference signals to modified signals that passed through the sample under investigation. b) Using an impedance analyzer and plastic tip holder (electrochemical cell) to measure the impedance through a sample under investigation on the AFM.

A series of modifications were made to the AFM tip holder and sample mounting process. The goal was to create an electrically isolated path to the AFM tip, pass the signal through the sample, and then return the modified signal back to the phase analyzer. An EFM tip holder or Electrostatic Force Microscopy tip holder, or alternatively an electrochemical cell tip holder was required to obtain an electrically isolated path to the AFM tip. The EFM tipholder had appropriate electrical isolation built into its design, even though a metal chassis was used for the body of the tipholder. The electrochemical cell tip holder was constructed of plastic, and therefore unambiguously provided electrical isolation.

Three ways of connecting the signal generator and phase analyzer will be described, including clipping the wires directly to the tipholder and using the Signal Access Module. These three ways can be used individually or combined, and these three ways are not meant to be exhaustive or all-inclusive, but merely some examples provided as a starting point. While several combinations of these techniques were tried in naïve attempts to find the best way, further study could potentially improve future performance.

Wires were directly connected to the tip holder using the spring-loaded cap on the top of the tip holder and a hooked test-lead clip, filed down to be narrow enough to fit between the spring-loaded cap and top of the tip holder. The connection location of the test-lead probe to the tip holder is shown in Figure 5-4.

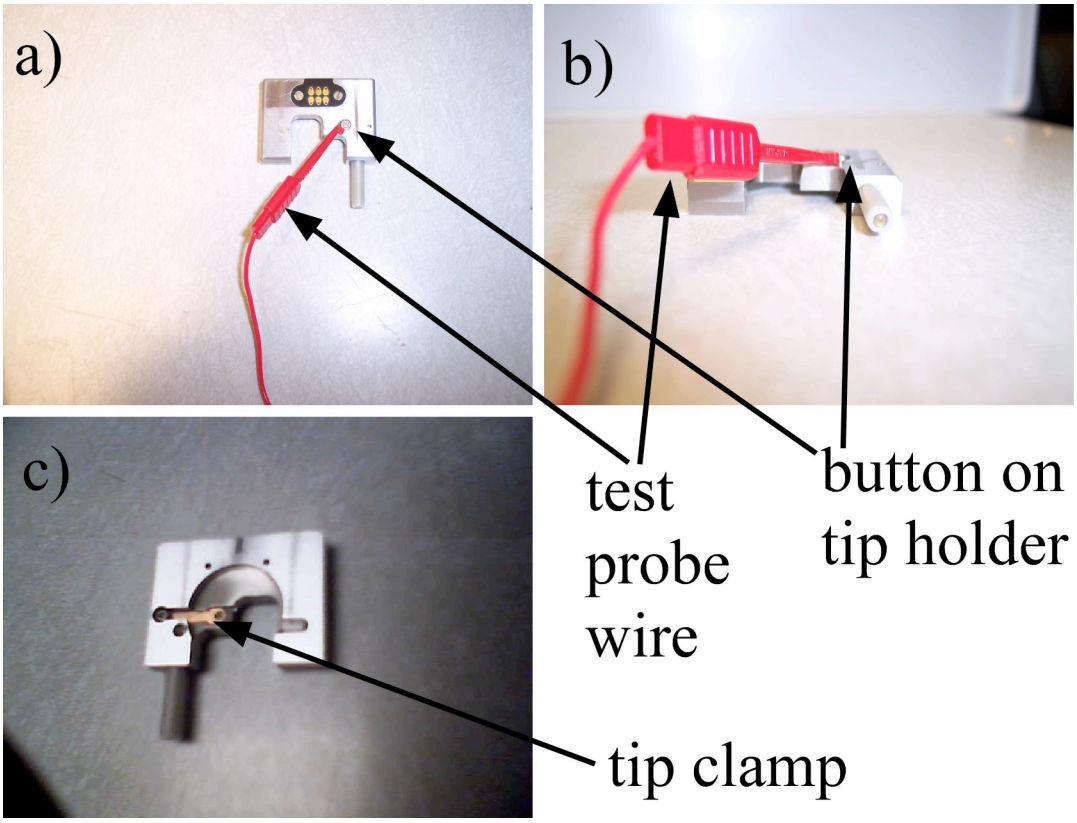


Figure 5-4. a) Top view and b) side view of how the test probe clip attached to the AFM tip holder. The round button on the right side of the tip holder was pried up so the test probe could clip to the shaft underneath the button. The round button provides direct electrical connection to the brass colored tip clamp on the c) bottom side of the tip holder.

Using a hand-held multimeter to check for electrical continuity, it was found the connection depicted in Figure 5-4 gave a direct electrical path from the red wire clipped to the tipholder, through the tip holder, and to the AFM tip itself through the spring-loaded clamp that holds the AFM tip in place. The brass colored tip clamp is shown in Figure 5-4c. Due to the design of the tip holder, by attaching the wire to the small round button on the top side of the tip holder, there is an electrical path to the tip clamp, which would be in contact with the metal coating of an AFM tip. To mount the sample, a current-limiting resistor of one kiloohm was connected to the usual stainless steel sample puck using conductive carbon tape. Above this resistor, graphite substrates or metal foil

substrates were connected with conductive carbon tape to the sample puck, as shown in Figure 5-5a. The value of the one kiloohm current limiting resistor was determined to provide protection against 10 V of bias creating a large current through a purely conducting loop, while still being small enough not to interfere with most measurements. Extra layers of conductive tape were cut to fill the void in the layer where the wire was inserted. The sample puck had electrical insulation tape placed on the bottom, as shown in Figure 5-5b.

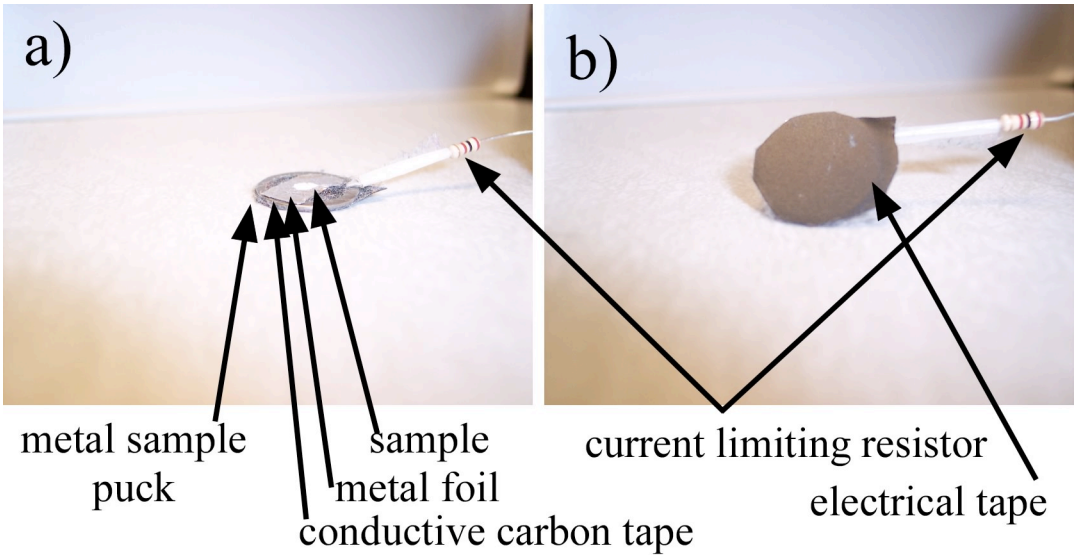


Figure 5-5. a) Top and b) bottom views of the sample puck configuration that included a metal foil substrate, conductive tape to attach the foil substrate to the stainless steel puck, and a wire (from current limiting resistor) to the sample puck, and how insulating tape was applied to the bottom of the sample puck to electrically isolate the sample from the AFM. Tape was also used on the current limiting resistor wire to prevent accidental short circuiting.

The insulating tape on the bottom of the sample puck electrically isolated the sample from the piezo cap, which was held to the ground of the AFM base and controller. This prevented extraneous current from ground loops that form when different instruments are connected but held to different ground potentials. Ground loops occur when two different ground sources are used and each has a different electrical potential.

Since the electrical potential of one is higher than the other, it acts like a battery, and generates a current flow from one ground source to the other. The current from ground loops would be added to the current already flowing through the circuits, and thus provides a source of noise. While these ground loop currents are often very small, due to the extremely low currents being studied this was an important consideration. One easy way to overcome this challenge is to ensure that all instruments using the three-pronged plugs standard in the US, where the lower centered cylindrical prong is the ground connection, are plugged into the same electrical run. In other words, if all of the outlets the instruments are plugged into can be switched on and off with the same circuit breaker, then they share a common ground. A safety step for the instruments was taken when tape was wrapped around the wire leading to the current limiting resistor to prevent accidental short circuit events.

The sample was mounted on the piezo cap, with a wire alligator clipped to the sample's current limiting resistor so that the signal to or from the sample could be accessed. The tip holder was loaded, and then the wire was connected to it by the test probe clip yielding the setup shown in the photograph in Figure 5-6.

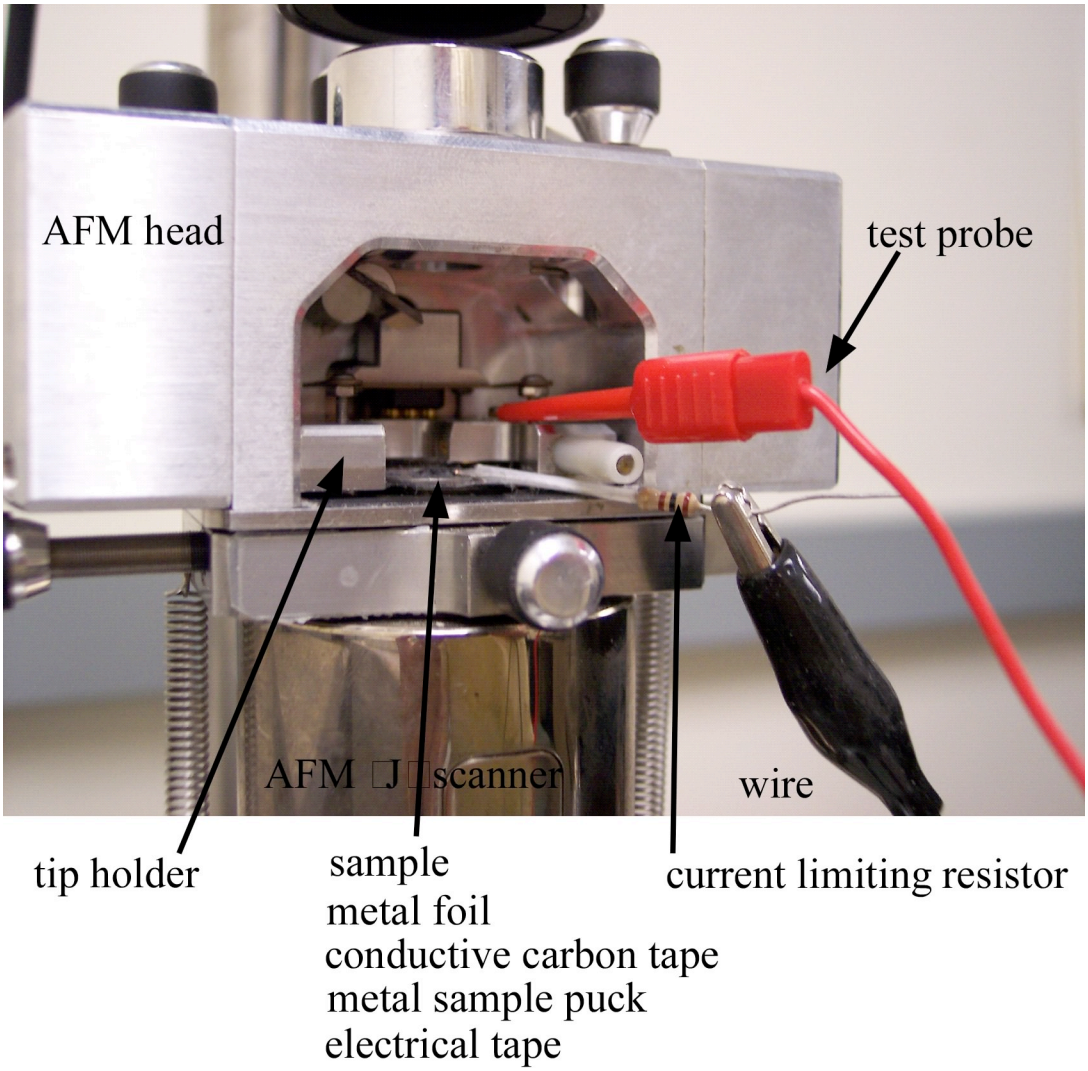


Figure 5-6. Photograph of an early method of connecting the signal generator and phase analyzer to the AFM. If tip bias is to be used, the red wire connected to the tip holder in the photo would be connected to the signal generator, and the black wire connected to the sample holder would be connected to the phase analyzer input.

A second way of electrical interfacing utilized the Veeco Signal Access Module (SAM). Using a hand-held multimeter to check for electrical continuity, it was determined which pin on the tipholder and which BNC connector on the SAM provided a direct electrical path to the tip. The same sample puck design previously constructed was used.

A third way of electrical interfacing utilized jumpers connected to the base of the AFM. This method used a graphite substrate, connected to a stainless steel sample puck with conductive graphite tape, and in direct electrical contact with the piezo cap of the J-scanner. This piezo cap is usually held to ground by the jumpers in the base of the MultiMode AFM as shown in the cartoon of the normal jumper configuration in Figure 5-7c with the Extender Module installed. The Extender Module is the small box from Veeco that is used to enable phase imaging in Tapping Mode, and is inserted in the cable between the AFM base and the controller. The pins are numbered 1 through 8 from top to bottom of the diagram, and assume the cable to the controller is on the left side when viewing the base. Pin number 1 is connected to ground, pin 2 is connected to the piezo cap, pin 3 is connected to the Analog 2 line, accessible by the Signal Access Module, pin 4 is unused or ground, pin 5 is a redundant connection to the Analog 2 line, pin 6 is connected to the AFM tip, pin 7 is connected to the Aux D channel, accessible by the Signal Access Module, and pin 8 is used for STM imaging. The Signal Access Module is essentially the breakout box that allows a user to monitor the signals being sent through the cable connecting the controller to the AFM base channel by channel. A user can also provide their own signal to override specific channels. The Aux D channel is an unused channel built into the instrument to allow the user to pipe in data output signals from measurement instruments external to the AFM controller, yet still display that data in the AFM images. In the normal configuration for imaging with the Extender module, pins 1 and 2 are jumpered together so the piezo cap is held to ground, pins 5 and 6 are jumpered together so the Analog 2 line is connected to the AFM tip, and pins number 7 and 8 are connected so STM imaging can work correctly. When pins are not jumpered together,

they are essentially a dead-end in the circuit path for that channel and have no effect on the operation of the instrument. In order to provide a direct electrical connection to the sample, the jumpers were reconfigured such that this provided a direct electrical connection to the sample. A cartoon of the jumper settings are shown in Figure 5-7d. In this case, just the Analog 2 line is connected to the AFM tip, so that a BNC connector can be used at the Signal Access Module to provide the tip bias, and the sample puck pictured in Figure 5-5 can be used for the direct connection to the substrate. The other pins were not jumpered as normal so the piezo cap would be electrically isolated by not jumpering pins 1 and 2, and since the Aux D channel was being used for data display by the phase analyzer and STM imaging was not being used pins 7 and 8 were not jumpered. The configuration of how each component and module of the AFM was connected is shown in Figure 5-7e. From the AFM base, a cable runs to the Signal Access Module. From the Signal Access Module, a cable runs to the Extender Module. From the Extender Module, a cable runs to the Nanoscope IIIa controller. From the Nanoscope IIIa controller, a cable runs to the main computer which drives the instrument and displays the data.

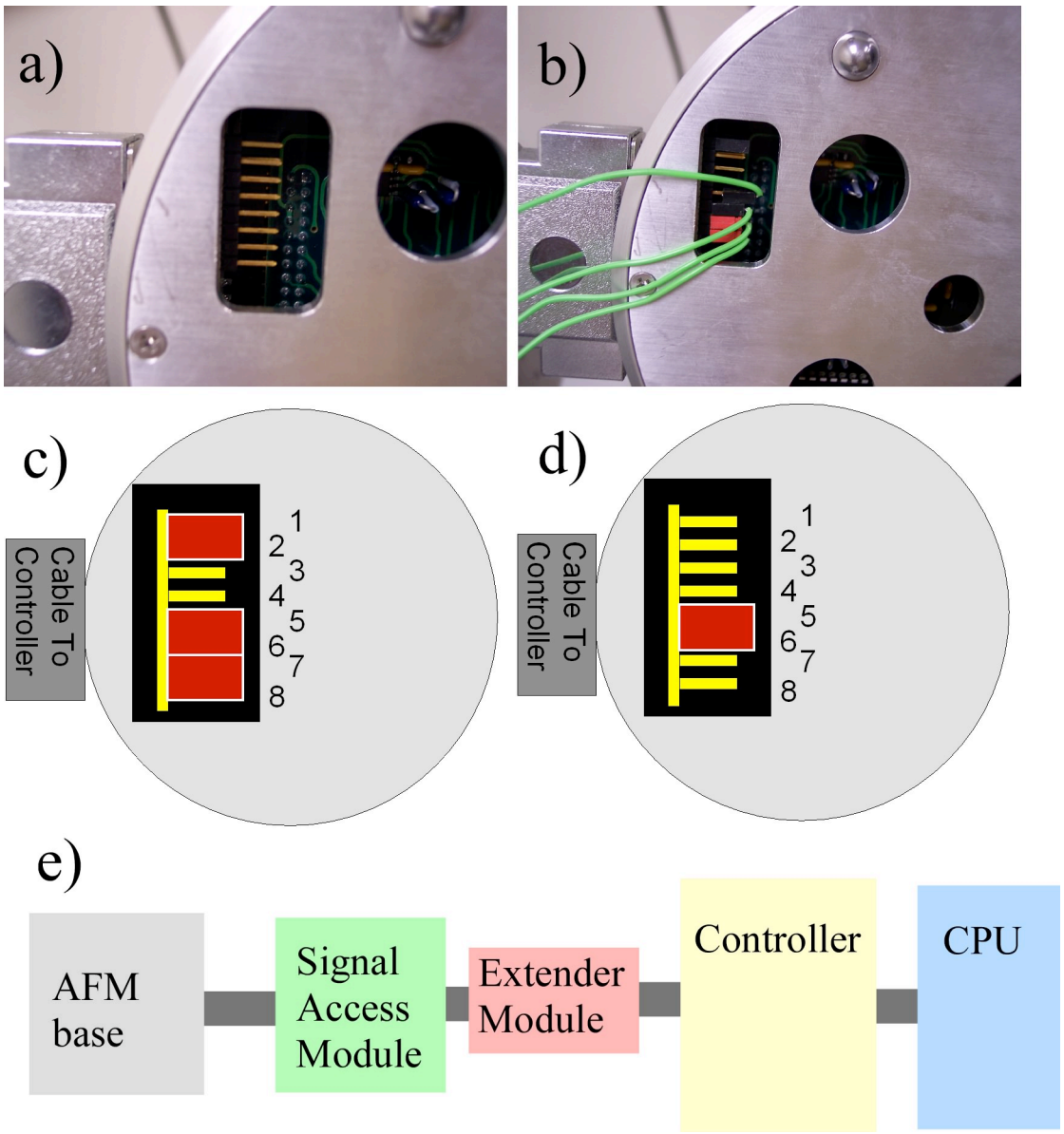


Figure 5-7. a) The pins located on the base of the Multimode AFM, with no jumpers connected. b) The jumpers and wires connected to the pins so that an external breadboard can be used to connect the appropriate pins. c) Illustration of normal jumper configuration. d) Illustration of jumper configuration to use the Analog 2 line (pin 5) from the Signal Access Module to provide a connection to the AFM tip (pin 6). e) Illustration of how each component and module was connected from the AFM base to the CPU, with dark gray rectangles between shaded boxes representing a cable.

Several problems were eventually discovered with these setups. The large lengths, nearly twelve inches, of unshielded wires used in making the connections allowed

parasitic induction from 60 Hz noise and ambient radio-frequency noise. This corresponds to electricity in the walls and power outlets in the US delivered at 60 Hz. The magnetic fields around power lines can induce small amounts of current in unshielded wires. Similarly, unshielded wires act as an antenna to pick up current from the radio frequency waves that are ubiquitous in modern life. Using faraday cages or minimizing lengths of unshielded wires is one way to overcome this challenge, or alternatively one can use longer integration times for the impedance measurements.

Other problems included the carbon tape sometimes required significant pressure to be conductive. The use of too many layers of conductive tape often created problems with the electrical measurements, while the use of too few layers of tape yielded an uneven attachment of the graphite to the sample puck. The problems with the electrical measurements included not being able to get a conductive measurement when the conductive tip was shorted onto a bare region of the conductive substrate. Using the stepper motor to drive the tip down into the surface with so much contact for the cantilever could been seen on the video camera as being greatly bent, as shown in Figure 5-8, electrical continuity was sometimes achievable.

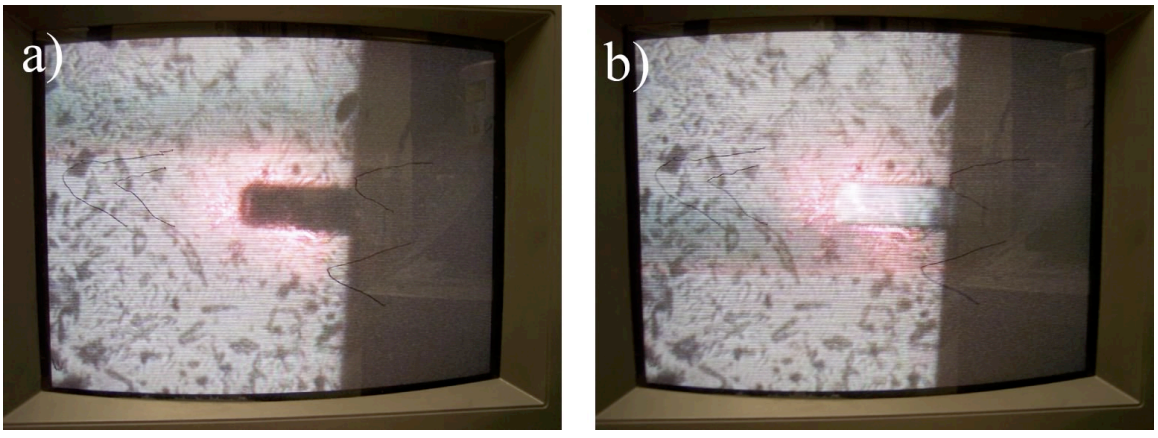


Figure 5-8. AFM tip a) before and b) after being pushed down into surface such that the tip is significantly bent.

Thermal expansion of several layers of tape often made imaging challenging, since one would engage and start scanning but within a few minutes the sample would have moved in the z-direction and the tip would be either fully extended of fully retracted and an image could no longer be obtained. This was minimized by using metal foils that could bend over the wire, however these foils are rarely atomically smooth. Alternatively, rather than using a rigid round wire, using a copper wire spun from several strands allowed the end of the wire to be splayed out, such that the thinner strands required less physical space, and also provided a more even support platform for attaching a graphite substrate above it without the need for multiple layers of conductive carbon tape.

Another problem stemmed from vibrations from the wires. Physical vibrations from being on the thirteenth floor of a building located on top of a New York City subway stop, and other sources, were amplified through lever action in the connections to the AFM sample pucks, introducing sources of noise and vibration during imaging which were sometimes prohibitive to collecting an image. This noise could be identified by diagonal lines running through the sample images, which changed slope with changes in scan rates. This periodic noise was reduced by decreasing the distance of the center of mass on the lever arm from the fulcrum point, but was still consistently a problem. An example of such noise is shown in Figure 5-9 for a sample of bare graphite.

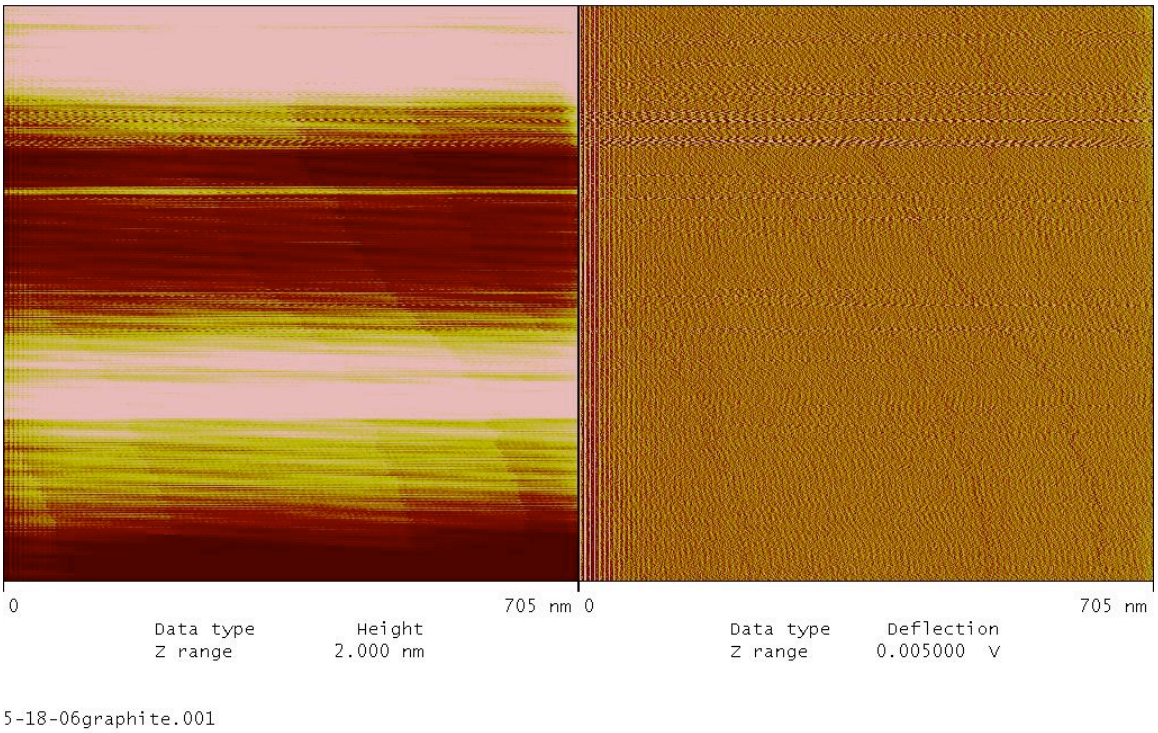


Figure 5-9. Periodic noise in AFM image, most pronounced on the left side of the image of bare graphite.

Instrumentation challenges inherent to this AFM model were also uncovered. Electrical measurements through the AFM base jumpers or signal access module are also measuring AFM electronics components in addition to the sample. The fact that the MultiMode is an open-loop scanner introduced problems with telling the tip to move to specific coordinates and the instrument not responding precisely. "Open-loop" is a term used to describe scanners that do not have sensors to measure precisely how far the piezoelectric material moved the scanner. When a voltage is applied to a piezoelectric material, it expands in a certain proportion of so many nanometers per volts applied. This proportion is dependent on operating temperature, and age of the piezoelectric

material. Since an open loop scanner has no way of knowing the precise response of the piezo when a certain voltage is applied, open-loop scanners are subject to substantial errors when zooming in. This necessitates magnifying images in very slow stepwise fashions, where one will have to zoom in repeatedly and re-center or offset the x and y coordinates after each step. By adding a sensor that measures precisely how far a scanner piezo moves in response to the applied voltage, a feedback loop is formed where the controller can adjust the voltage applied to the piezoelectric material until the precise movement distance is obtained. This sensor closes the feedback loop of the electrical circuit, which explains the origins of the terminology. The sensors typically work by using a wire that passed through a second wire coiled around the first. Since a charged wire moving through a coiled wire creates current in the coiled wire through magnetic fields inducing current, and current sensors can measure the length of time and intensity of the current generated by this motion, the controller can then calculate precisely how far the scanner moved, and send this information to the feedback loop for any small adjustments that might be necessary.

Further challenges included the fact that there was no means to control the temperature of the Multimode AFM environment. Since the piezoelectric response of materials is temperature dependent, this created sources of thermal drift that were as high as tens of nanometers per minute due to thermal expansion alone, which compounded the problems of the open loop scanner.

Despite these challenges, data was obtained using this setup with limited success at reproducibility. An example of such data can be found in Figure 5-12, which will be discussed later. Even when 10 V of AC bias was applied to the sample, less than 10 mV

was often received by the phase analyzer, a Krohn-Hite model 6500A. This instrument was purchased used and therefore is an older design requiring at least 100 mV of signal to its detectors to make a comparison. Attempts to use an op-amp on an external breadboard to boost the signal were made with inconsistent results. While the op-amp offered a gain on signal of as much as 10^6, the signal to noise ratio remained problematic. Concerns were also raised as to whether using the op-amp would alter the phase of the AC signal being measured before it is sent to the detector, which could lead to more complicated analysis of the results. This was essentially a very naïve attempt to build half of a homemade impedance analyzer, since impedance analyzers measure both the amplitude and phase differences, and the design and construction of instrumentation was discovered to be not as straightforward as it first appeared.

Figure 5-10 shows some early attempts to display height topography and AC phase shift data from the AuxD channel. The Aux D, or auxiliary channel D, is an extra data channel designed by Veeco to allow users to input data measured from instruments external to the AFM controller, yet still display this information on the real-time plots and save the data. These images show the response time of the phase analyzer was much slower than the scan rate, such that several points were being averaged for one measurement displayed in a coarse fashion. Examination of the phase analyzer integration time for measurements revealed that measurements were made at the rate of 3 Hz. This yielded the consequence of very long scan times of over six hours for even a low resolution 256 x 256 image, which required scan rates lower than 0.011 Hz to allow the phase analyzer time to sample each point during scanning.

As is shown in Figure 5-10, six hour scans do not work. Due to the previously mentioned fact the MultiMode AFM is an open-loop scanner and there was no temperature control in place at the time, significant thermal drift could take place during such a slow scan. This is demonstrated by the poor quality of the height image. At the scan size of 1.79 um and scan rate of 0.011 Hz, the scan speed was 0.021 um/s. By comparison, a normal scan rate would be 0.5 Hz to 1.5 Hz, with appropriately higher scan speeds depending on the scan size, since the scan speed is simply the product of the scan size and the scan rate. Since the spatial resolution in the topological image in the x and y coordinates depends primarily on the radius of curvature of the AFM tip, and since typical AFM tips have a radius of curvature of about 10 nm, one can typically resolve as small as 10 nm features in x and y. Smaller features, such as 1nm strands of DNA, can be resolved, although the tip broadening effect can make the DNA appear to be 10 nm across in the cross-sectional analysis, despite an accurate height measurement.

In the case of the image in Figure 5-10, with the scan size of 1.79 um and scan rate of 0.011 Hz, the scan speed was 0.021 um/s, the effects of thermal drift must be carefully considered. With thermal drift as high as ten nanometers per minute possible when operating in an ambient environment without temperature control, thermal drift of up to 4 um was possible over the course of a six hour scan. In other words, the AFM scanner could drift more than double the scanning area before the scan was completed. Further compounding the problem is the drift of the z-piezo. Ultimately, this increased resolution in AC bias phase shift was meaningless without useful topography information to determine where the target nanoparticles are located to yield a given phase shift.

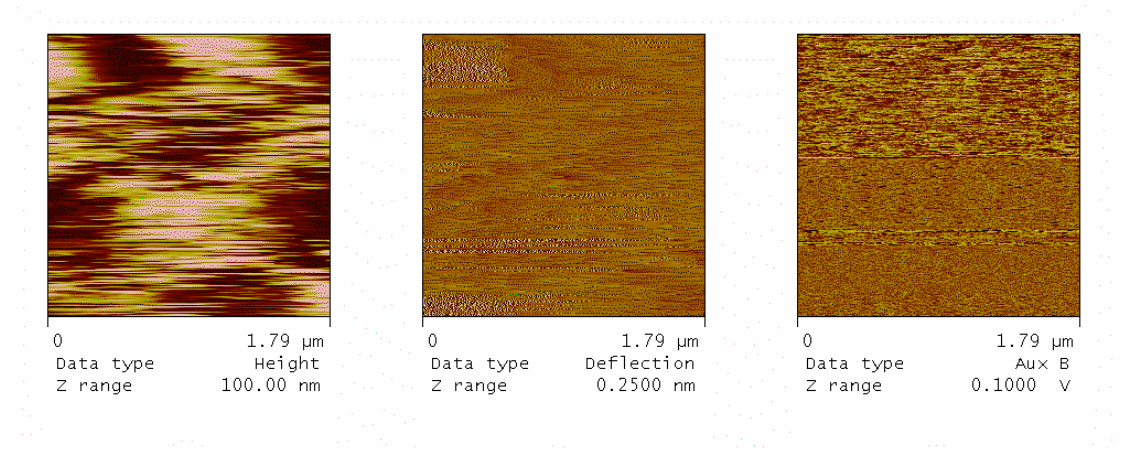


Figure 5-10. Six hour scan of 58 nanometer polystyrene beads in contact mode. Frames from left to right show height, deflection, and phase shift.

3. AC AMPLITUDE AND PHASE CHANGE MEASUREMENTS WITH DI AFM AND SOLARTRON FREQUENCY RESPONSE ANALYZER.

It was determined after further study that the complex impedance spectrum of a material provides more information than simply monitoring the phase shift of an AC signal. Despite the previously described challenges with measuring phase directly, some of these issues, especially extracting signal from noise, could be better performed with more sophisticated instrumentation. When an AC signal is applied to a sample, changes in both the amplitude and phase occur, as shown in Figure 5-11a. By comparing changes in amplitude and phase, as shown in Figure 5-11b, the determination of the real and imaginary components of impedance is possible. Imagine a signal is generated at a certain amplitude, frequency, and phase. This input wave could be described mathematically as $Asin(t+a)$, where A is the amplitude coefficient and a is the phase offset. After passing this AC signal through the sample, the process of transmitting the

signal through the different material will create a shift in the amplitude and phase of the resulting output wave. This output wave could be described mathematically as $Bsin(t+b)$, where B is the amplitude coefficient and b is the phase offset. It is possible to determine a transfer function, $G(t)$, that when operating on $Asin(t+a)$ yields $Bsin(t+b)$. It is also possible to imagine the differences in amplitude, or gain, (A-B) and differences in phase (a-b) as being two coordinates that define a vector quantity. This vector is the frequency response. To analyze the data, a user can create a plot of the magnitude of this vector and plot it as a function of frequency. Alternatively, one can plot only the real component (or only the imaginary component) as a function of frequency. This can be done automatically for only individual spectra in the SMaRT software. To plot the average of several spectra for real or imaginary impedance or impedance magnitude and display the error bars, one needs to transfer the impedance magnitude spectrum by spectrum, then incorporate the errors. Alternatively, the data values measures can be exported to Excel, and statistical analysis can be performed on the data sets of multiple spectra. Typically, the impedance magnitude was exported, averaged, and was plotted as a function of frequency. The impedance magnitude relates to these differences in that the frequency response of a circuit can be described as some transfer function acting on the initial frequency, and by determining that transfer function one can calculate the impedance of the circuit. The frequency response analyzer automatically performs these conversions and provides a measurement of the real and imaginary components of the impedance.

In studying the instrumentation typically used to measure impedance spectra, it was determined a commercial frequency response analyzer (FRA) was necessary to proceed efficiently, as most crude attempts to build frequency response analyzers failed

to deliver the performance required of this research. One advantage of the Solartron instrumentation was the ability of the software to calculate and extract the desired signal portion out of noisy data. By estimating what the frequency and amplitude of the desired signal portion was, and then calculating the second and third harmonics of that data, the ability to resolve signal that would otherwise be masked by noise became possible. This makes phase difference measurement reliable again, especially compared to the experimental setup described previously in Section 2 of Chapter 5.

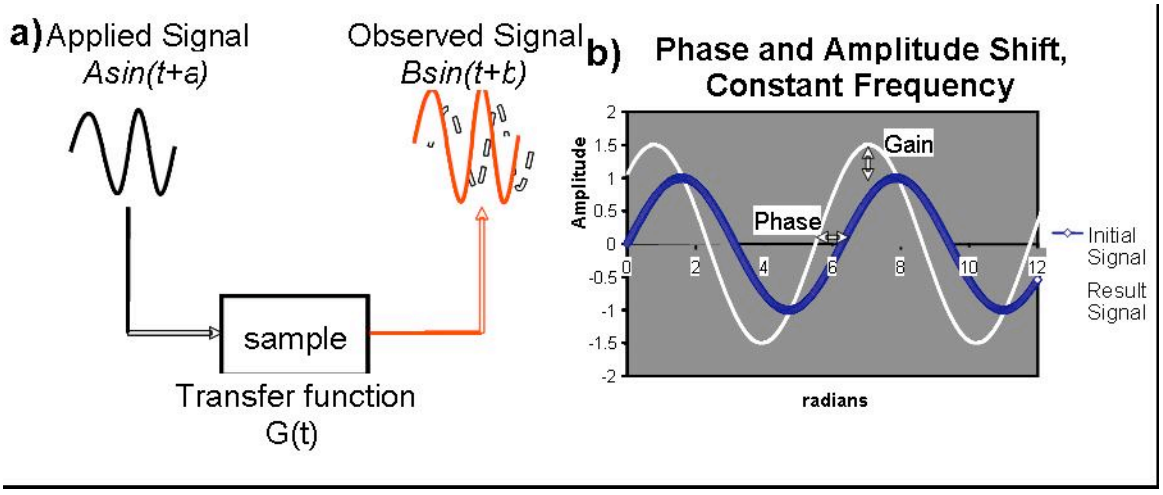


Figure 5-11. a) Example of how AC signals are affected by passing through a dielectric sample. b) Phase and amplitude shift of a sine wave at constant frequency.

A Solartron 1260 Frequency Response Analyzer (FRA) and Solartron 1296 Dielectric Interface were selected after a promising demonstration despite only having successful results one afternoon over a three week period, as shown in Figure 5-12a. A cartoon of the impedance setup is shown in Figure 5-3b. This instrument increases the ability to resolve signal from background noise tremendously compared to unfiltered results. It also provides more precise control when sweeping frequency during collection

of the impedance spectra, when compare to the signal generator used in the previously described setup in section two of this chapter.

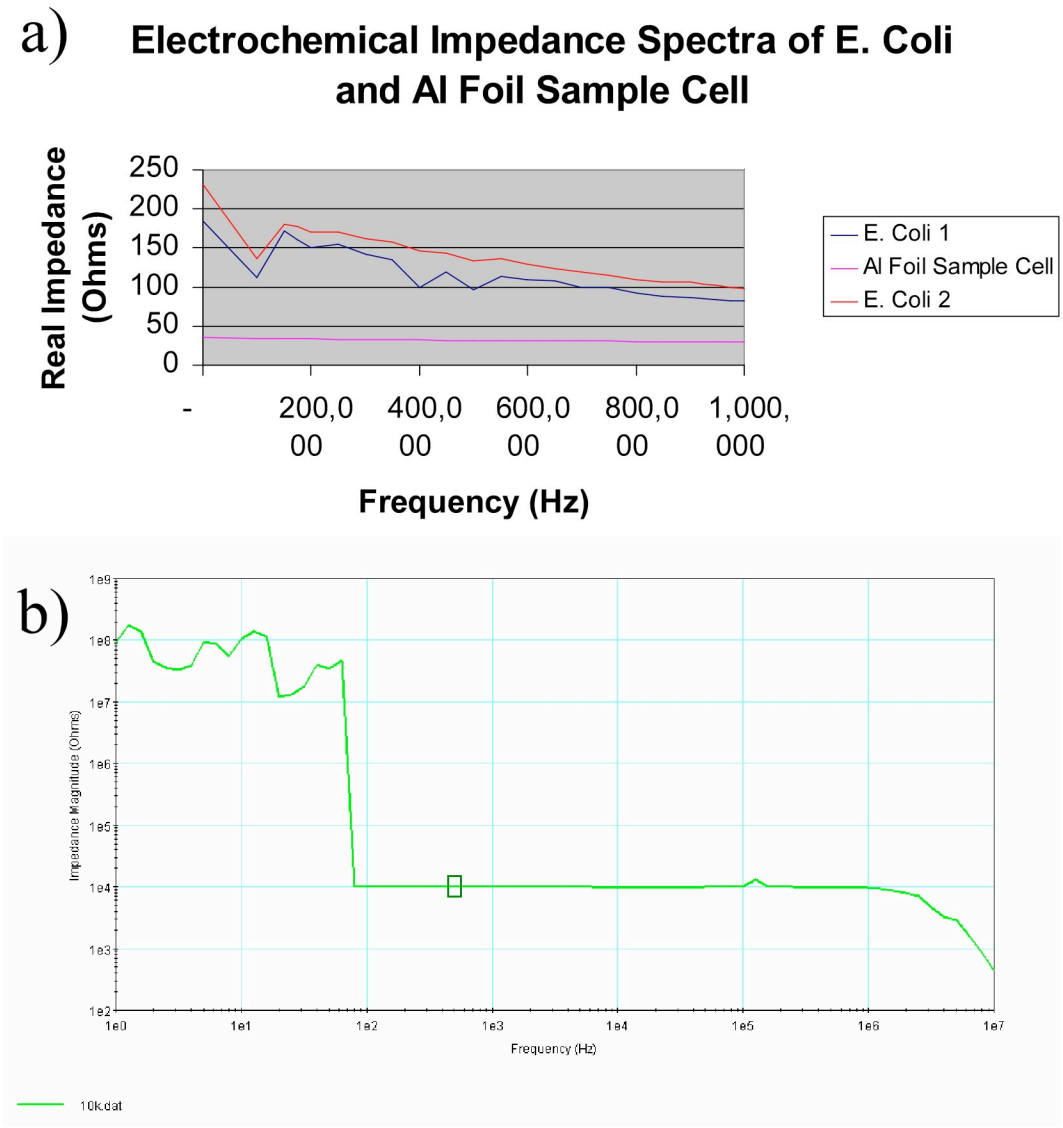


Figure 5-12. a) Impedance Data from Solartron Demonstration. b) Impedance spectra collected where the AFM tip drifted off of the nanoparticle of interest, and onto a bare gold substrate with a 10 kohm current limiting resistor in series.

The same three interfaces previously described for phase analysis were also used for the impedance analysis. Each of these connections had their own challenges as

previously described. While several months were spent attempting to make reproducible measurements, no clearly defined reasons for the lack of reproducibility observed could be determined. The problem of thermal drift was identified when it manifested itself by the tip drifting off of the insulating nanoparticle and onto the conductive substrate below and delivered a corresponding sharp drop in impedance, as shown in Figure 5-12b. Other problems included a frequent error from the FRA displayed as "Input Overload."

4. AC IMPEDANCE WITH ASYLUM AFM AND SOLARTRON FREQUENCY RESPONSE ANALYZER

a) In General

It was determined a new AFM was needed, with closed loop scanners and conductivity modules that could be modified for this custom application to avoid the challenges of reverse-engineering the MultiMode. Several vendors were researched, and the Veeco's Nanoman II Dimension system and Asylum Research's MFP-3D system were demonstrated in the lab. After a detailed comparison of the performance during the demonstrations, which are summarized in Table 5-1, and a nearly unanimous recommendation by the over twenty students and faculty in attendance during the demonstrations, Asylum Research won the bid with their MFP-3D Stand Alone AFM. Specific problems could be overcome by the Asylum AFM. It offers a closed loop scanner in the X and Y direction, and a sensored Z piezo which can roughly be described as creating a closed loop instrument with all three axes. This provides much more accurate force curves. Further, the ability of the Asylum AFM to provide easy access to an electrically isolated path to the tip holder was superior to other instruments on the

market, the details of which will be described later on page 174. This capitalized on the ORCA tip holder used for electrical measurements. Further, since this system was being designed with impedance measurements in mind it was better constructed than anything that could have been adapted in an attempt to work on the old AFM. This new design required shorter lengths of unshielded wires, which could help reduce the noise from 60Hz power lines and ambient radio frequency noise. It also included a mounting bracket on the rear of the AFM base for attaching BNC cables and providing shielded connections as close as possible to the AFM tip holder and sample. By placing the AFM inside of a metal acoustic isolation hood this also acts as a grounded shield around the unshielded wires inside.

Table 5-1. Summary of Results from AFM Vendor Demonstrations

Technique	Asylum	Veeco	Performed Equally	Advantage Asylum	Advantage Veeco
AC Impedance	☑	☑		☑	
DC Conductivity Mapping	☑	☑		☑	
I-V Curves / Force Curves	☑	☑	☑		
Liquid Imaging	☑	☑	☑		
MFM/EFM	☑	☑			☑
Closed loop XY	☑	☑	☑		
Sensored Z	☑	☑		☑	
Tech Support	☑	☑		☑	
“Dip Pen”	“☑”	“☑”	“☑”		
System ease of use – least retraining required					☑

As part of the negotiation process with Asylum Research, a collaboration was established. This enabled research to be performed at the Asylum Research headquarters

in Santa Barbara, CA. Before the system was shipped to Hunter College, preliminary experiments were performed at the factory to determine if the design of the impedance AFM interface would perform to the desired specifications. Several checks were performed against original design schematics of the electronics, including the ORCA tip holder designed for electrical measurements, to confirm again that the path from impedance analyzer to sample and back was electrically isolated from all of the AFM and its associated electronics.

The MFP-3D Standalone AFM system was setup and installed in the AFM lab at Hunter College. Considerable anti-vibration and acoustic isolation was designed into the location to house the AFM. In order to determine what the effects of each component in the system could be several setups were studied to build in a stepwise fashion models of which components could or could not be influencing the impedance spectra.

b) Reproducible contact between AFM probe and samples with constant tip force

One concern in making electrical measurements, especially on soft materials, is whether mechanical strain or physical deformation of the particles will affect the electrical properties of the material. Careful consideration was given to this problem to design the experiments such that reproducible contact could be made from particle to particle, even as tips or samples change from day to day.

Reproducible contact force is important since a good electrical contact must be made between the AFM tip and the sample. Enough force must be applied such that the AFM tip actually comes into physical contact with the sample, and is not merely compressing the air fluid layer above the surface. When engaging onto or approaching the surface, the AFM tip compresses the air in between the tip and the sample. This

compression requires a minimum amount of force, however it can be significant. If one makes an impedance measurement in this situation, the measurement will include the air gap between the tip and the sample in addition to the sample. This could introduce undesirable effects that must be compensated for in any calculation. The equivalent capacitance of a series of capacitors is shown in equation (5-2).

$$\frac{1}{C_{tot}} = \frac{1}{C_1} + \frac{1}{C_2} + \ldots \quad (5\text{-}2)$$

The air capacitance would be an order of magnitude smaller than the higher particle capacitance. By equation (5-2), this makes the smaller $1/C_{air}$ or $1/C_1$ term the dominant contribution to the observed capacitance $1/C_{tot}$. As the air gap decreases, the electric field begins to pass completely through the nanoparticle. This makes the capacitance from the nanoparticle the dominant term. The simplest way to remove any uncertainty is to maximize physical electrical contact between the tip and the sample. In order to achieve physical contact between the tip and the sample, a greater force must be applied to overcome the air/fluid compression effect.

First, it was determined how to calculate and maintain a constant contact force. One of the controls which the user can manipulate on the AFM most conveniently includes the deflection setpoint. The deflection voltage is the value on the photodetector that tells where the laser spot is located. The photo detector is divided into four quadrants, A through D, as shown in Figure 5-11a. The sum of the voltage in quadrants A and B is divided by the sum of the voltage in quadrants C and D, to create a ratio from +10 V to -10 V that tells the user whether the laser spot is at the top of the photo detector in the case of +10 V, or at the bottom of the photo detector in the case of -10 V, or anywhere in between.

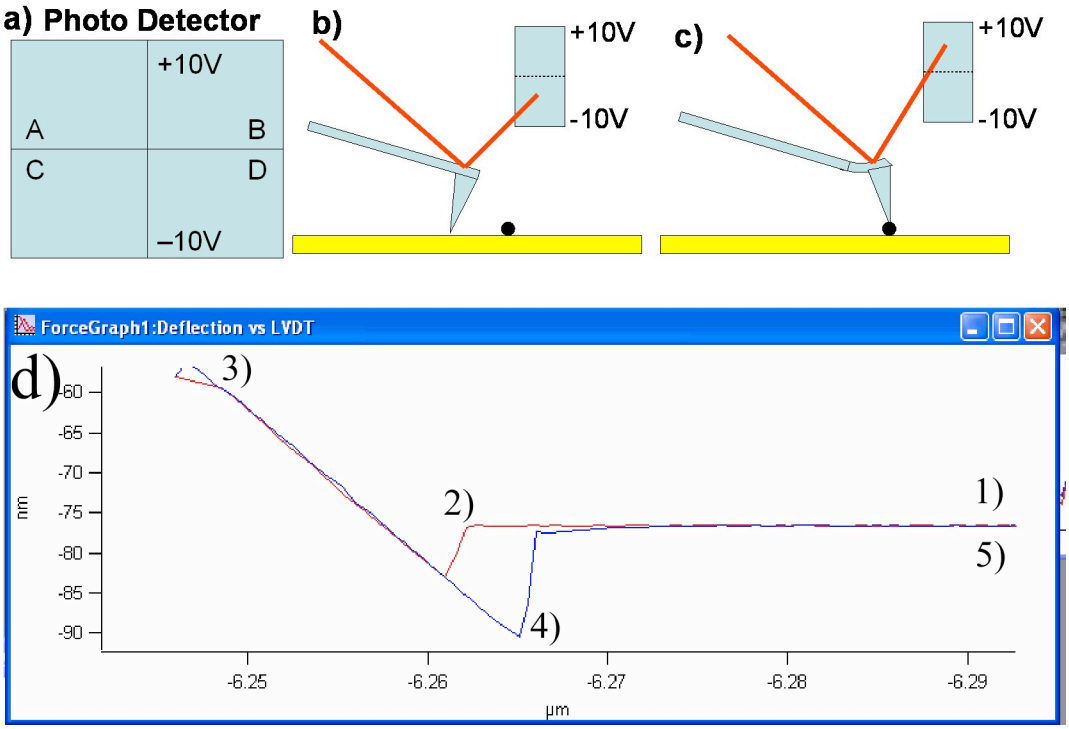


Figure 5-13. a) Cartoon of the four quadrants of the photodetector and the voltage values assigned to the y-axis. b) AFM tip scanning a surface has a laser beam that is focused on the end of the cantilever which is reflected to the photodetector to provide the deflection value in volts to the AFM controller. c) When the tip encounters a surface feature and bends, the laser is deflected, hitting the photodetector in a new spot, changing the deflection value the photodetector provides back to the AFM controller. d) Example of a force curve on a hard surface.

A more positive value means the laser was deflected higher, like the situation in Figure 5-13c compared to Figure 5-13b, while a negative value means the laser was deflected lower. These values are provided in units of volts, since that is the output of the electronics involved. The term free-air deflection will be defined as the voltage the photodetector reads when the tip is above the surface before it is engaged. For example, this may typically be around 0 V when the tip is first loaded and the user adjusted this value with the deflection wheel on the head of the Asylum MFP-3D AFM.

An understanding of how the deflection setpoint is used to control contact mode imaging will clarify future discussions. When the AFM tip is pushed down towards the surface by the z-piezo and makes contact with the surface, the cantilever begins to bend. This causes the laser spot to change position on the photodetector. Once the deflection voltage equals the deflection setpoint, the z-piezo stops, as shown in Figure 5-13b.

In contact mode imaging this deflection feedback is exploited. As the tip is scanned across the surface, the cantilever bends as surface features are encountered, as shown in Figure 5-13c. When the tip bends, the laser is reflected to a different spot on the photodetector, which in turn causes a corresponding change in deflection voltage. As a result of the change in deflection voltage, the feedback loop triggers the z-piezo to move in the appropriate direction to return the deflection voltage to the deflection setpoint value.

In the case of collecting a force curve, monitoring of the deflection is also important. First, an understanding of what data is displayed in a force curve plot should be gained. In the force curve pictured above in Figure 5-13d, the x-axis is the distance that the z-piezo is extended, and the y-axis is the deflection in nanometers of the cantilever. The red trace is the deflection of the cantilever as the z-piezo is lowered to towards the surface, and the blue trace is the deflection of the cantilever as the z-piezo withdraws away from the surface. One can imagine several sections of the force curve, numbered sequentially from beginning to end, as depicted on Figure 5-13d by the numbers one through five. At point 1), the beginning of the force curve, the z-piezo is some distance above the surface. The deflection value plotted is the free-air deflection. The term free-air deflection will be defined on page 153. As the tip is lowered towards

the surface, eventually attractive forces between the tip and the sample cause the tip to jump down suddenly to be in contact with the surface at point 2). Once in contact with the surface, the cantilever bends or deflects at a constant rate. This slope is used to calculate the optical lever sensitivity, to be discussed on page 154. At point 3) on Figure 5-13d, once a certain trigger point is reached the z-piezo reverses direction and begins to pull away from the surface. This trigger point can be a deflection value or a voltage on the photodetector or some other value defined by the user. Typically, a relative deflection voltage of 0.2 V is used. As the z-piezo pulls the tip away from the surface, the attractive forces between the tip and the surface cause the tip to stick on the surface slightly longer than would be expected, at point 4). This creates a valley in the deflection plot as the cantilever is bent in the opposite direction as when it was being pushed into the surface. Eventually, the z-piezo pulls the tip far enough away from the surface to overcome the attractive forces, and the free air deflection value is observed for the remainder of the force curve until its conclusion at point 5) on Figure 5-13d.

In the force curve panel, one can plot this deflection voltage change on the y-axis against the distance the z-piezo moved down towards the surface on the x-axis. Since for hard surfaces the deflection of the cantilever in nanometers is always equal to the distance the cantilever is pushed towards the sample by the z-piezo, using this slope of 1 in the left-most region of the force curve allows the user to calculate the deflection optical lever sensitivity. The inverse of this value is displayed to the user by the Asylum software package as the deflection inverse optical lever sensitivity, or deflection InvOLS. It has units of V/nm, and is a measure of the response in volts by the photodetector for each nanometer of deflection the cantilever undergoes.

The terms absolute deflection and relative deflection should also be defined. The absolute deflection is the raw value in volts read from the photodetector, and ranged from -10 V to +10 V on the Asylum MFP-3D. The term relative deflection describes a deviation from the free-air deflection, or the final deflection minus the free air deflection. For example, a user may load the tip and use the deflection wheel on the head of the AFM to set the free air deflection to a value of -1.00 V before engaging. If the user engaged the tip onto the surface and saw a deflection voltage of -0.80 V, the relative deflection would be (-0.80 V – (-1.00 V)) =0.20 V. The absolute deflection would be the current deflection value on the photodetector, which is -0.80 V.

It would be most expedient to convert this relative deflection value into the force applied by the tip onto the sample. To define such a conversion factor in equation (5-3), the units provided in the factor Gamma are relative deflection volts per nanonewton.

$$\Gamma\left(\frac{V}{nN}\right) \equiv \frac{1}{k\left(\frac{nN}{nm}\right) * InvOLS\left(\frac{nm}{V}\right)} \quad (5\text{-}3)$$

This equation uses the spring constant of the cantilever, k, and the inverse optical lever sensitivity, InvOLS. The spring constant is determined by the thermal tune method on the Asylum MFP-3D AFM, and provided in units of nN/nm. The InvOLS is determined from a force curve done on a hard surface, in the sloped region where the tip is being deflected. The optical lever sensitivity is the amount of movement of the laser spot on the photodetector for every nanometer the tip is pushed down towards the surface and correspondingly deflected. The distance in nanometers is known from the sensored Z-piezo on the Asylum MFP-3D AFM, while the deflection is recorded directly in volts. By taking the inverse of the optical lever sensitivity, the InvOLS term has units of nm/V.

Multiplying the spring constant and InvOLS and then taking the inverse of this term provides the term Gamma, which is unique to each cantilever used. To determine the desired relative deflection, one can multiply the desired contact force by Gamma. To determine the deflection setpoint, one simply adds the relative deflection to the free air deflection.

An example may be informative. If the spring constant was determined by the thermal tune to be 11.12 nN/nm, and the InvOLS was determined to be 62.63 nm/V, Gamma would be 1 / (11.12*62.63) = 0.001436 V/nN. If 100 nN of contact force is desired, the relative deflection would be 0.14V. If the free-air deflection was initially -0.08 V, the deflection setpoint should be +0.06 V.

Several contact forces were used in determining what force is required for good electrical contact. In a study of gold nanoparticles with an external current limiting resistor in the breadboard of 15kOhms, the contact force was systematically varied using a series of deflection setpoints. In Figure 5-14, a low contact force of 50 nN is shown to have high contact impedance and thus poor electrical contact. However, at 100 nN, 150 nN, and 200 nN all of the traces are overlaid, showing good electrical contact by measuring the value of the current limiting resistor.

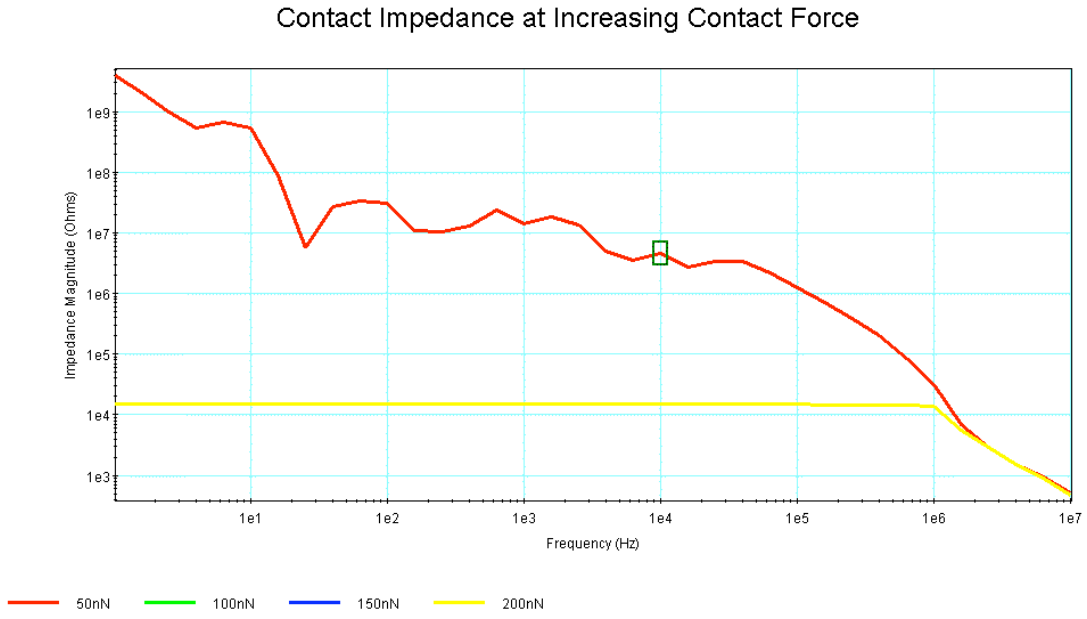


Figure 5-14. Impedance spectra of various increasing contact forces, measuring the contact impedance for gold nanoparticles, with a 15 kOhm current limiting resistor in series.

After the 100 nN target force was determined, topography images were taken before and after collection of the impedance spectra to determine whether any permanent physical deformation or nanoindentation had occurred. It was found that 100nN provided no deformation on hard materials as shown in Figure 5-15 with height images and cross section analyses before and after several impedance spectra were collected at 100 nN contact force and no deformation on soft materials. In the case of the 100 nm polystyrene nanoparticles, notice in the section analysis, shown in Figure 5-15d, of the post-impedance height image, shown Figure 5-15c, that no nanoindentations or permanent physical deformations occurred when compared to the initial section analysis, shown in Figure 5-15b, or the initial height image, shown in Figure 5-15a. In the case of the Adenovirus Type 3 the section analysis, shown in Figure 5-15h, of the post-impedance height image, shown Figure 5-15g, showed no nanoindentations were present when

compared to the initial section analysis, shown in Figure 5-15f, or the initial height image, shown in Figure 5-15e.

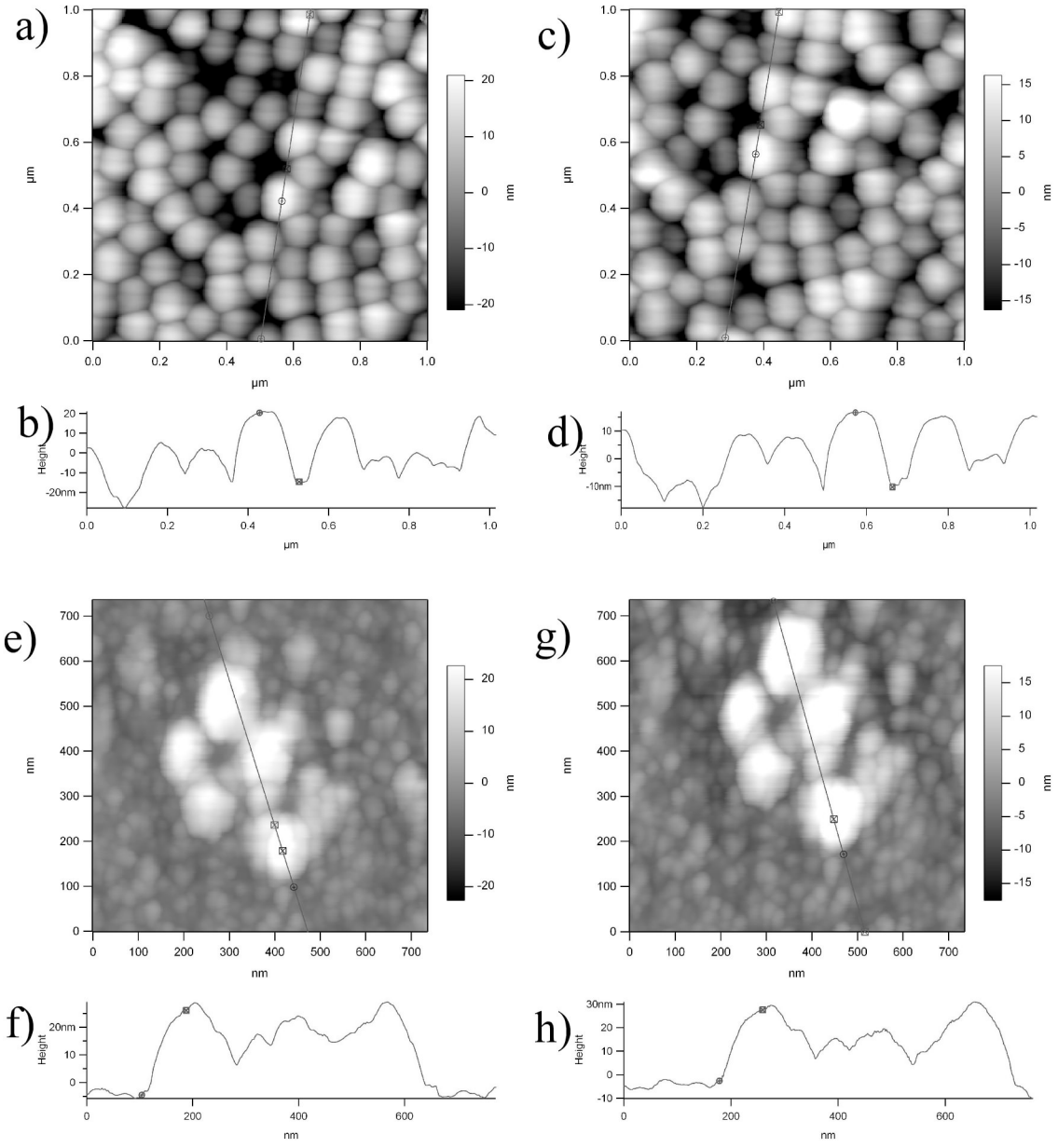


Figure 5-15. Height images a) before and c) after impedance spectra collection with 100 nN of force on 100 nm polystyrene beads. b), d) Cross-sectional analysis of red line through height images a), c) respectively, shown as inset below each topographical image. Some thermal drift of approximately 200 nm occurred between collection of the two height images, which were approximately two hours apart and taken after fifteen particles were analyzed. e) Before and g) after impedance spectra collection with 100 nN of force on Adenovirus Type 3 capsids. f), h) Cross-sectional analysis of red line through height images e), g) respectively, shown as inset below each topographical image.

c) Checking the tip's metal coating with impedance spectra

In order to check for the continuity of the metal coating on the AFM tip, it should be brought into contact with a bare region of the gold substrates, and a quick spectra collected to determine if the contact impedance is still the expected low value. When tips are worn out, the impedance spectra will look like that of an insulator as shown in Figure 5-16a, and the phase shift spectra is shown in Figure 5-16b with the worn out tip having a phase shift consistent with that of a pure resistor of zero degrees. The metal coating on most commercially available AFM tips is about 20 nm thick, with a 5 nm adhesion layer of metal beneath that to increase tip lifetime. Most platinum coated AFM tips maintain their conductive coating for only one to two hours of contact mode imaging. However, by collecting images in AC mode or tapping mode, and engaging the surface in contact mode with 100 nN and not scanning during impedance measurements, tips have maintained their conductive coatings for as long as three days of imaging and spectra collection.

Impedance spectra were collected on single gold nanoparticles of 20 nm diameter and 150 nm diameter, to determine what the contact impedance might be between a platinum tip and the gold nanoparticles. Since the gold nanoparticles are conductors, the circuit can be modeled simply as a resistor for the contact resistance.

d) AC impedance measurement of model systems – bare gold substrates and gold nanoparticles

The impedance AFM tip holder and the sample substrate were connected directly to the impedance analyzer, with no current limiting resistors. Typically, when using the

Solartron FRA and Asylum AFM, current limiting resistors of 10 kOhm were used. This arbitrary starting point was recommended by Asylum Research to be a good starting point that balanced allowing too much current to flow into the detector on the FRA and potentially damage it, while still being low enough to see the sample. Since these high instrumental resistances would mask expected contact impedances of 250 ohms, the choice was made to conduct these experiments, depicted in Figure 5-16c, without current limiting resistors. While current overload errors were displayed by the FRA during the collection of the spectra shown in Figure 5-16c, serious damage to the FRA was fortunately avoided. There is nearly identical matching in the contact impedance of the different sizes of nanoparticles, when 100 nN of contact force is used. Essentially, this configuration will be measuring the contact impedance. When thinking about the circuit model, there would be a resistance between the tip and the sample, but since the sample is a metal conductor, and all other wires and connections and even the tip are conductors, the primary source of resistance will be the contact impedance between the tip and the sample. Figure 5-16a shows the two impedance spectra for a new tip and a worn tip. In this case, a current limiting resistor of 10 kOhm was used in order to prevent current overload errors on the Solartron FRA. In Figure 5-16a, the impedance is slightly above 10 kOhm because the contact impedance of 250 ohms was also being measured. In each combination of substrate and sample and tip material, it will take trial and error experimentation to determine the best compromise for protecting the FRA and not masking the desired signal.

It may be concerning that the impedance spectra of the worn tip shown in Figure 5-16a has a constant slope, whereas measurements of other insulating nanoparticles do

not have this constant slope. The reason this slope is constant in the case of a worn tip on a bare region of substrate is that the equivalent circuit is that of a capacitor. There are not any complicating factors such as nanoparticles with complex electric fields that affect the impedance measurement.

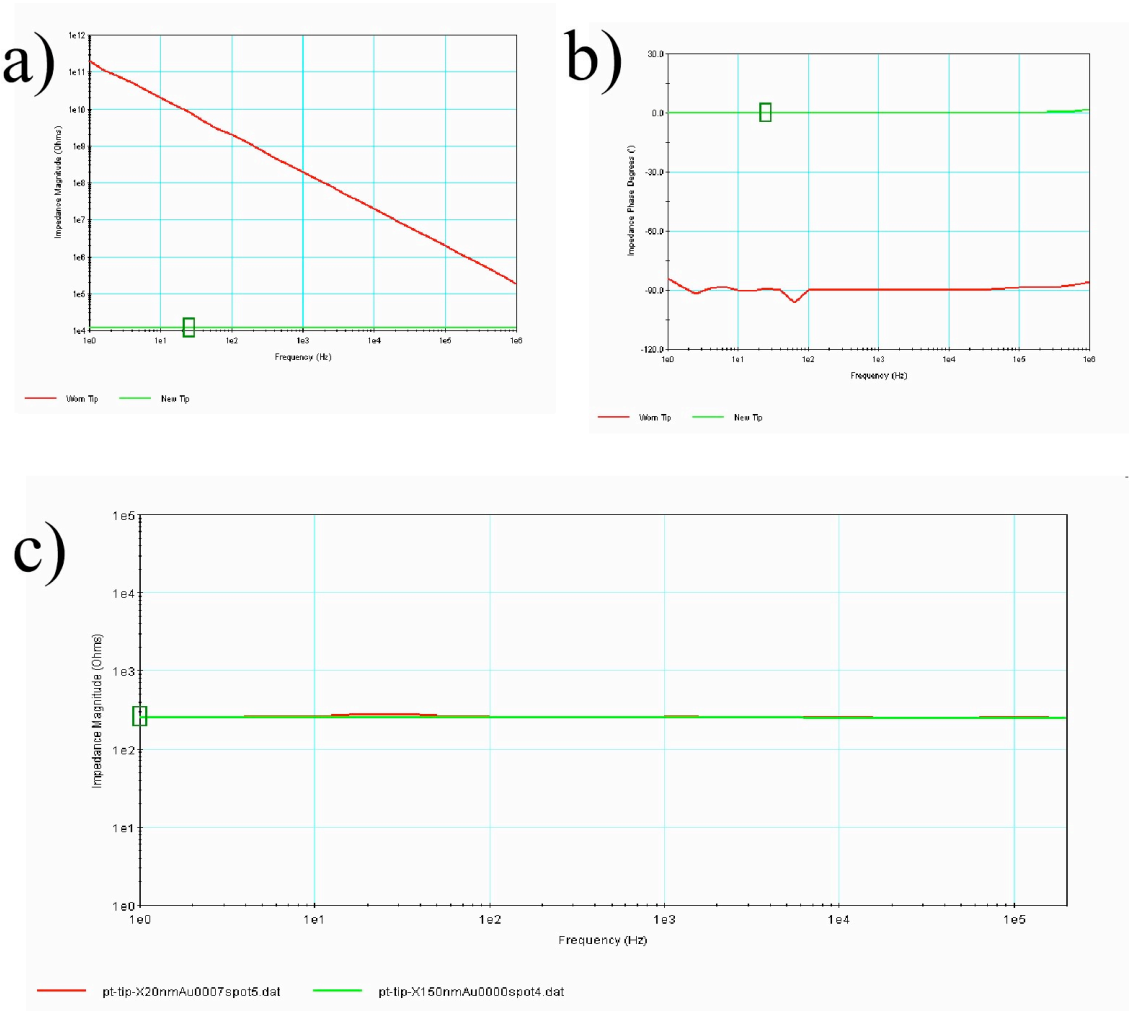


Figure 5-16. Before (green trace) and After (red trace) a) impedance spectra and b) phase shift spectra of platinum tip shorted onto bare gold region of substrate, with a 10 kohm current limiting resistor. c) Impedance spectra of 20 nm and 150 nm gold nanoparticles, with no current limiting resistors, to determine the contact impedance; the red trace is 20 nm gold nanoparticles, while the green trace is 150 nm gold nanoparticles.

Experiments to determine if the AFM had any effect on the impedance spectra collection were conducted. The external breadboard was connected on the base of the

AFM, to analyze various current limiting resistors while the AFM would be in contact with a bare region of the gold substrate. This would create a model circuit of two resistors in series, R_1 and R_2, who would have an equivalent resistance $R_{eq}=R_1+R_2$. Since one can use a known external current limiting resistor, R_1, and the impedance analyzer can measure the R_{eq}, this allows the user to easily calculate R_2, and use this value as an offset for the system. This setup would be analogous to having a high resistance wire connecting to the resistors on the breadboard, and collecting the impedance spectra. This configuration will also confirm that there was no hindrance created by using the impedance AFM, since if the impedance AFM is truly acting as a wire the impedance spectra of the resistors should be identical to the spectra of a resistor hardwired directly to the impedance analyzer. A series of spectra collected with the AFM acting as a long wire is shown in Figure 5-17. In the case of Figure 5-17a, the impedance spectra of resistors on a breadboard are shown with the AFM used as a wire, since the conductive tip is shorted to the conductive substrate. In Figure 5-17b, the impedance spectra of resistors on a breadboard directly hardwired to the FRA are shown. Since there is no difference between Figures 5-17a and 5-17b, Figure 5-17a simply masked the contact resistance and showed the correct values of the current limiting resistors. This confirms a correct instrumental setup was achieved.

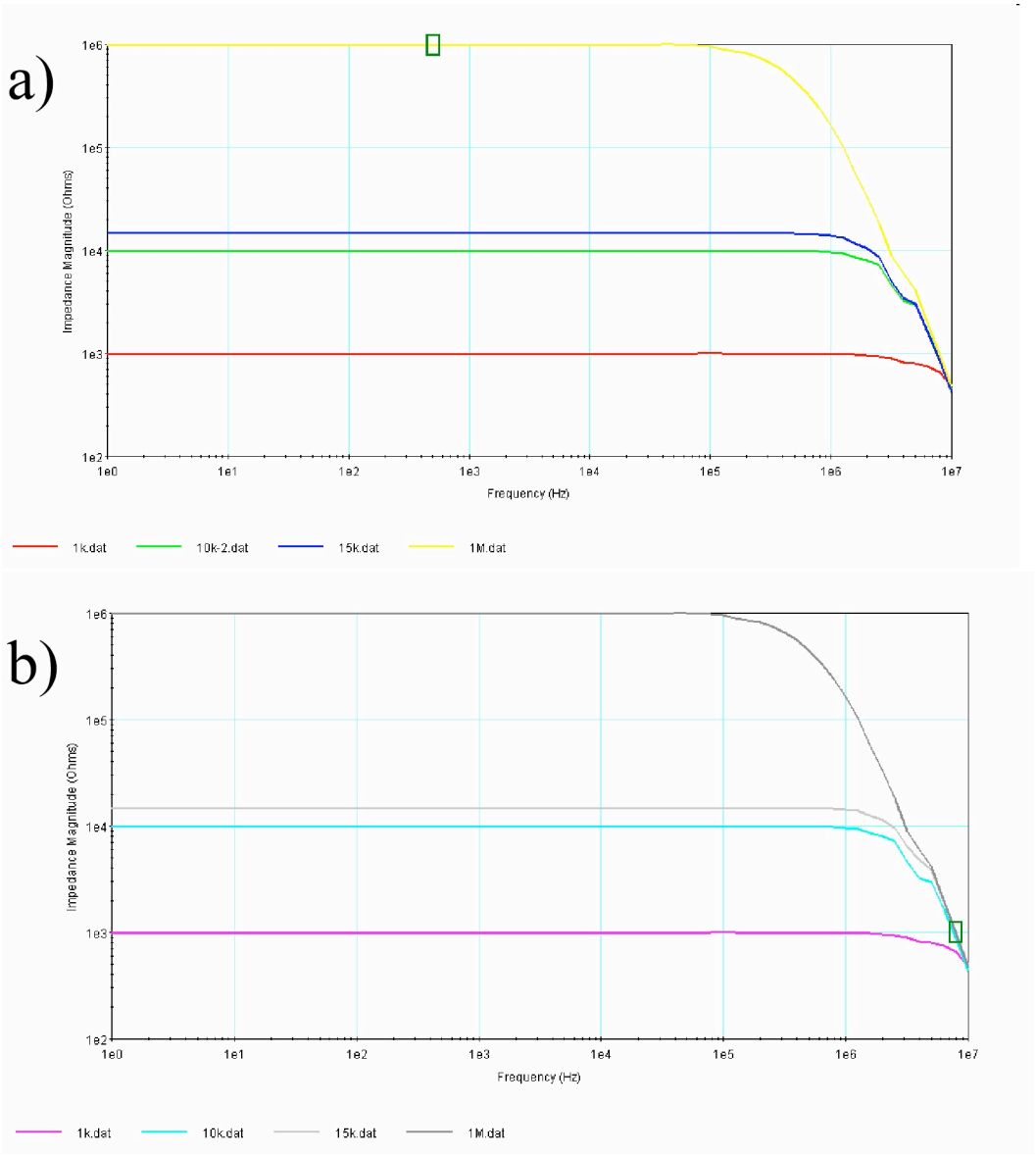


Figure 5-17. Resistors a) with AFM connected, and platinum AFM tip in contact with bare gold substrate at 100nN, the red trace is a 1kOhm resistor, the green trace is a 10kOhm resistor, the blue trace is a 15kOhm resistor, the yellow trace is a 1MOhm resistor. b) Resistors hardwired to the impedance analyzer, the pink trace is a 1kOhm resistor, the teal trace is a 10kOhm resistor, the light gray trace is a 15kOhm resistor, and the dark gray trace is a 1MOhm resistor.

The considerations of parasitic inductance from the AFM tip must be mentioned. Other inductances can be ignored because they are orders of magnitude smaller, and will

be discussed in more detail on page 163. One can induce a current across a capacitor by changing the voltage by the following equation (5-4)[129].

$$I = \frac{\partial V}{\partial t} \times C \quad (5\text{-}4)$$

At higher AC frequencies, the $\frac{\partial V}{\partial t}$ term gets much larger, even for very small capacitors. The current sensors can easily detect nanoamp and femptoamp currents. Therefore, at frequencies of 10^5 Hz and a parasitic capacitance of the AFM tip of approximately 10^{-15} farads, about a 10^{-10} amp current could be generated; on the order of 0.1 nanoamps or 100 femptoamp amps, this is enough current to generate sufficient noise in the circuit such that parasitic inductance must be considered. In the above estimation, the parasitic capacitance of the cantilever of about 10^{-15} F for an applied voltage of 10 mVV was estimated using the equation for parallel plate capacitors (5-5).

$$C = \frac{k\varepsilon_0 A}{d} \quad (5\text{-}5)$$

In equation (5-5), the term *k* is the dielectric constant of the material between the two parallel plates, *A* is the area of the plates, and *d* is the distance between them. By using the tip manufacturer's specifications for the particular model of AFM tip used in these experiments, a Mikromasch NSC-15 style cantilever, with a width of approximately 35 micrometers and a length of approximately 125 micrometers and a distance between this cantilever and the surface of about 20 micrometers based on the tip height[130], and knowing the permittivity of free space is about 8.854 x 10^{-12} and the dielectric constant of air is 1, the estimated capacitance would be about 1.9x10^{-15} F. The simplest ways of avoiding parasitic capacitance or parasitic inductance was to operate in lower frequency ranges.

e) Circuit modeling of AFM-based Impedance System

Impedance spectroscopy is a useful method in characterizing the electrical properties of non-conducting materials, such as inductance and capacitance, by monitoring the current responses with respect to the applied perturbing sinusoidal voltage signal. The impedance is defined as the ratio between the system voltage, $U(j\omega)$, and the corresponding current, $I(j\omega)$, whose unit is ohms[131]. As the stimulating system voltage is changing with the variance of the frequency, f, the obtained current and impedance are functions of the frequency. Numerically, the calculated impedance is represented by the sum of real and imaginary parts due to the sinusoidal response. The real element represents the resistance, R, and the imaginary element does reactance, X. The numerical expression is presented in equation (5-6).

$$Z(j\omega)=\frac{U(j\omega)}{I(j\omega)}=\mathrm{Re}(Z(j\omega))+\mathrm{Im}(Z(j\omega))=R+jX \tag{5-6}$$

where,

$$j=\sqrt{-1}\ and\ \omega=2\pi f$$

In analyzing the impedance spectroscopy data, the components of instrument contributing to the electrical signal are assigned as discrete electrical circuit elements and a model electrical circuit is constructed from the combination of these electrical circuit elements. The electrical circuit modeling of an instrument is the strongest advantage of the impedance spectroscopy, which enables to characterize the electrical property of the element of interest as well as to predict the impedance response. The analysis of the impedance spectroscopy data is performed by fitting a electrical circuit model to the experimental data, which determines the unknown electrical properties of interest. In

general, the electrical circuit model is nonlinear containing more than two unknown values. Thus, a vigorous data fitting process using nonlinear-least-square method is generally applied to determine the unknown values.

The schematic layout used in measuring the impedance data of nanoparticles and viruses is presented in Figure 5-18. When the conductive SPM tip contacts with the nanoparticle on the conductive gold substrate, three electrical elements contributing to the overall impedance are considered; (i) capacitance of nanoparticle(C_{NP}), (ii) capacitance of air existing between the SPM tip and gold substrate (C_{air}), and (iii) resistance of the instrument (R). The electrical circuit is comprised of series electrical elements connected in series. The electrical circuit is corresponding to the physical layout of the instrument. A similar electrical circuit model is also suggested in the STM study of gold nanoparticles[132, 133].

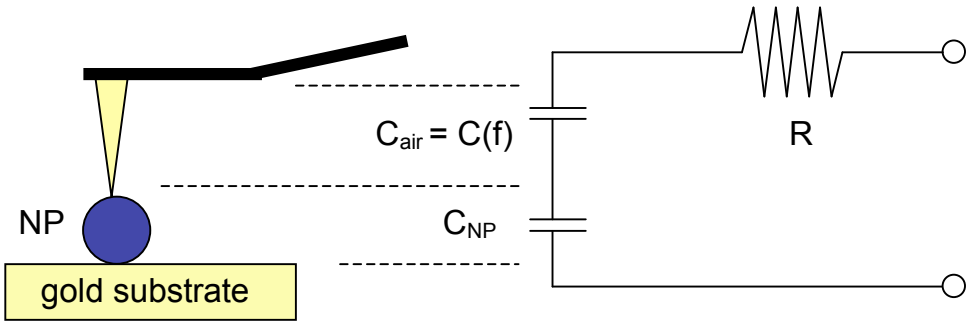


Figure 5-18. Schematic layout of contacting SPM tip on nanoparticle loaded on the conductive gold substrate (left). The corresponding electrical circuit model (right). The capacitance of air gap (C_{air}), capacitance of nanoparticle (C_{NP}), and resistance of the instrument (R) is connected in series.

From the characterization of the instrument, the inherent resistance of instrument, R, is determined to be 0.73 ohms, which is thought to be originated from the cables connecting the instrument. It is notable that there is a capacitance contribution from the air gap between conductive SPM tip and substrate. This air gap capacitance was observed

to change with variance of frequency from the complimentary experiments. The reason why the capacitance of air gap is dependent to the frequency is not clear. We propose a capacitance model in equation (5-7) in order to describe the frequency dependence from the impedance data represented.

$$C_{air} = \frac{C_{air,0}}{\left[1 + (f / f_c)^2\right]^m} \tag{5-7}$$

Where, the $C_{air,0}$ is capacitance at zero frequency, f_c is the critical frequency at which the slope of impedance changes, and m is arbitrary parameter.

From the impedance data of the air gap, above parameters fitting with the data were determined as follows; $C_{air,0} = 1.0148\times10^{-12}$ (F), $f_c = 3.5\times10^{-5}$ (Hz), and m = -0.696. The calculated impedance determined from above capacitance model and experimental data are plotted in Figure 5-19.

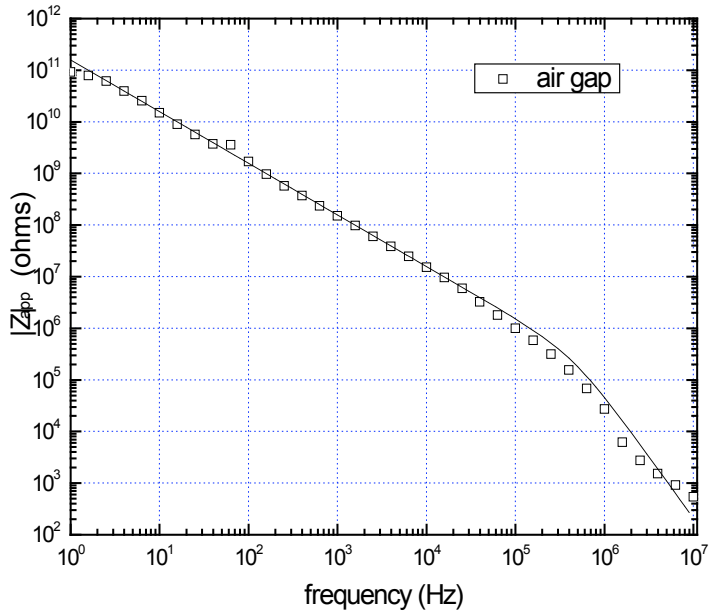


Figure 5-19. Bode diagram of the air gap between SPM tip and gold substrate. The white square represent experimental data and the solid line is the fitting line whose capacitance is described in equation (5-7).

Now, the impedance model of nanoparticle contacting with SPM tip (Figure 5-18) is expressed as the sum of the contributions from the resistance of instrument and from the apparent capacitance, C_{app}, which is the combination of the capacitances of air gap and nanoparticle. The numerical description of the impedance is given in equation (5-8).

$$Z = R - \frac{j}{\omega C_{app}} \tag{5-8}$$

where, the apparent capacitance is determined by

$$\frac{1}{C_{app}} = \frac{1}{C_{air}(f)} + \frac{1}{C_{NP}}$$

Using above model of impedance expressed by the combination of resistance and apparent capacitance, the capacitance of the nanoparticle was estimated by fitting impedance data. In Figure 5-20, the Bode diagram of a model negatively charged silica nanoparticle (d = 110nm) and its fitted line is present.

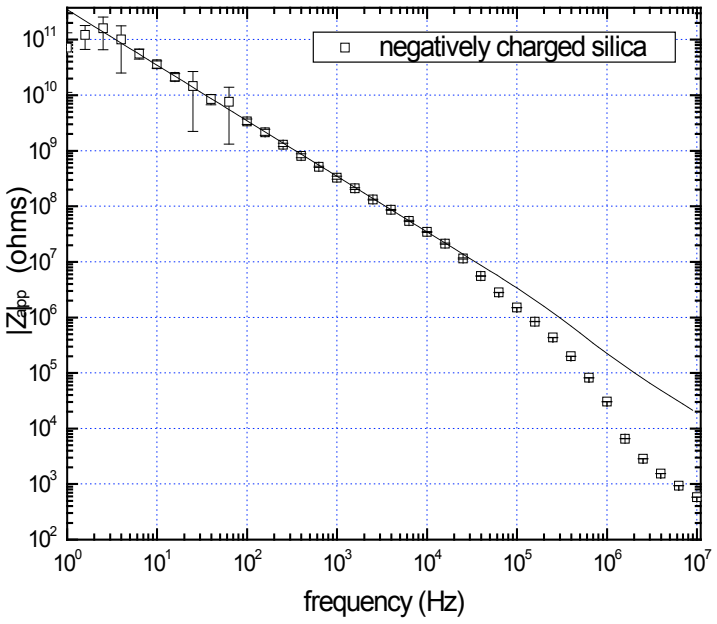


Figure 5-20. Bode diagram of the model negatively charged silica nanoparticle. The white square represent the experimental data and the solid line is the calculated values after data fitting.

It is obvious that the fitting highly deviates from the experimental data at high frequencies, which suggest other electrical elements should be considered to describe the impedance variations with respect to the frequency changes.

It was determined that there were parasitic inductances inherent to the instrument itself, parasitic inductances from the BNC cables, and parasitic inductances from the AFM connections and interface. The procedure by which this was determined included building up a series of test circuits and adding one component at a time, then fitting the impedance spectra data to circuit models that represented the physical setup being studied. The schematics of the three connections are shown in Figure 5-21.

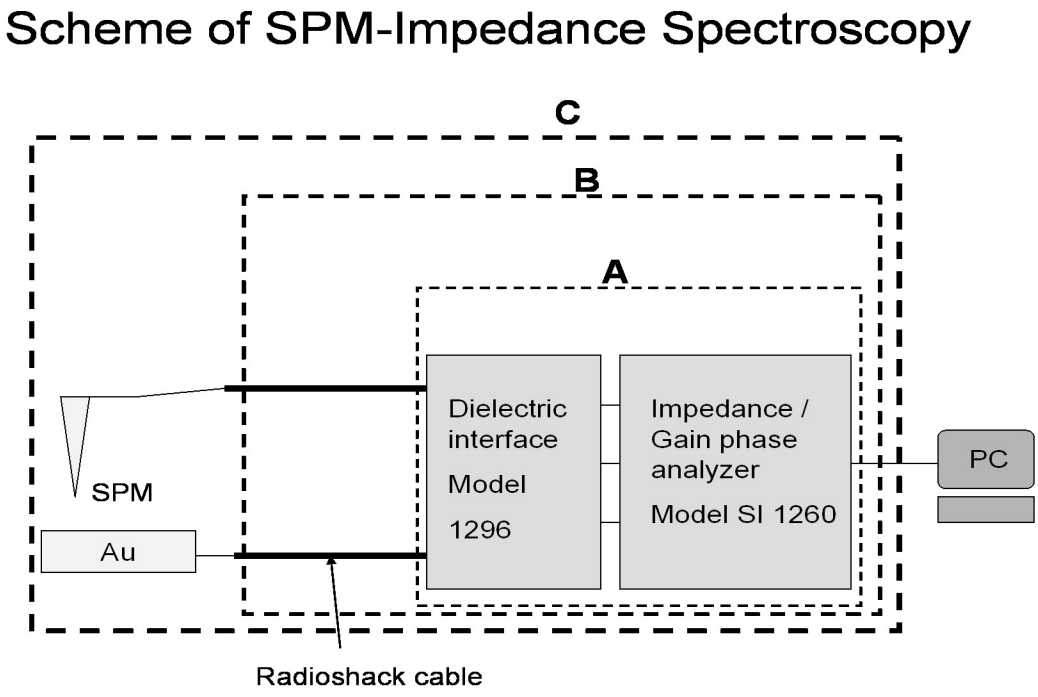


Figure 5-21. Scheme of SPM-Impedance Spectroscopy.

Initially, as depicted by box A in Figure 5-21, a resistor or capacitor was plugged into the BNC connectors on the front panel of the dielectric interface, and the circuit model included the resistor or capacitor plus a parasitic inductor term. Impedance data were fit by manual calculations of equations for the circuit model and least squares fitting to determine unknown parasitic inductance values. Then, as depicted by box B in Figure 5-21, a resistor or capacitor was plugged into the ends of BNC cables connected to the dielectric interface. This circuit model included a resistance from the resistor, a resistance and capacitance from the cables, and a parasitic inductance. Finally, as depicted by box C in Figure 5-21, the AFM was loaded with a conductive tip and conductive substrate and the tip was brought into contact with the substrate, and the AFM was used essentially as an overpriced wire in the circuit. The circuit model in this case included two capacitors in series, a contact resistance, and a parasitic inductance term. The parasitic inductance from configuration A was 9.43×10^{-7} H (Henries), while the parasitic inductance from configuration B was 4.03×10^{-6} H, and the parasitic inductance from configuration C was 4.70×10^{-5} H. In other words, the AFM connections and interface were the highest by an order of magnitude over the cables, which were an order of magnitude higher than the Solartron FRA. This parasitic inductance manifested itself at high frequencies above 500 kHz. Low frequency vibrations such as building floor vibrations or 60Hz noise from electric power lines and equipment running on AC power could be reduced by integrating the impedance measurement over longer times at each frequency. For example, by measuring the impedance for one second at one hertz, the impedance is measured over only one cycle. This could lead to large standard deviations when several spectra are compared or averaged. However, by measuring the impedance

for ten seconds at one hertz, the impedance is integrated over ten cycles, and can average out some of the noise that occurs during measurement. This increased time, however, must be balanced with the need to collect impedance spectra quickly before the thermal drift of the piezos in the scanner cause the AFM tip to drift off of the nanoparticle under study. A good compromise is described in the experimental details at the end of this chapter.

f) Conclusion

In conclusion, the first impedance AFM from Asylum Research was built in collaboration with their applications scientists, after several attempts to modify a Veeco Multimode failed. Such an impedance AFM is capable of measuring the impedance spectra of individual nanoparticles. Control experiments were performed to establish the working instrument was completed and operating successfully. The details of measuring the impedance spectra of single nanoparticles will be discussed in Chapter 6.

5. EXPERIMENTAL DETAILS

a) Installing the Frequency Response Analyzer

The Solartron 1260 Frequency Response Analyzer and 1296 Dielectric Interface should be installed according to the manufacturer's instructions. This includes all power cords, including the computer driving the instruments as well as the AFM and associated equipment, being plugged into the same electrical circuit run in the building so that they share the same ground to minimize ground loops and other potential noise sources. The GPIB cables connected on the back of the 1260 and 1296 boxes must be daisy-chained together, meaning the cable connecting the 1260 to the 1296 should be connected first,

and then the GPIB cable that goes to the USB interface should be connected on top of the GPIB cable on the back of the 1260.

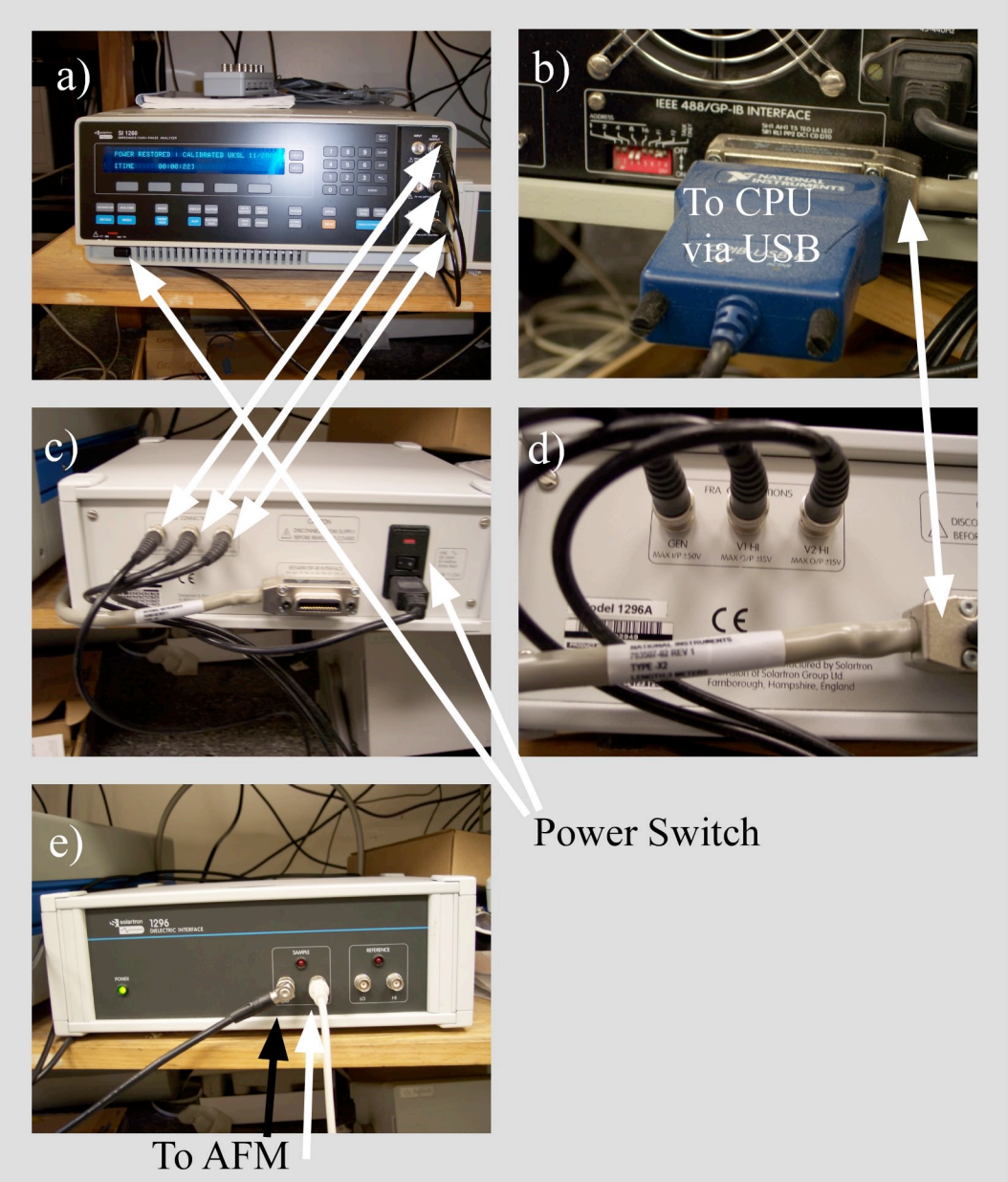


Figure 5-22. Photographs of how to install the Solartron 1260 Frequency Response Analyzer and 1296 Dielectric Interface. a) Front panel of the 1260, with the power switch on the lower left hand corner, and three BNC cables that run to the corresponding locations on the rear of the 1296. b) Rear panel of the 1260, showing the power cord, daisy-chained GPIB cable and GPIB-USB converter, and on the left the GPIB channel selector location. c) Rear panel of the 1296, with the three BNC cables from the front of the 1260 on the left, the GPIB cable in the center, and the power cord on the right. d) Zoomed in view of the three BNC cable connections on the rear of the 1296. e) Front

panel of the 1296, with the two BNC cables that run to three rear of the base of the AFM as shown in Figure 5-25

Remove any kinks in the cords, and prevent coiling of the cables to minimize interference. For the BNC cables, the front panel of the 1260 has 6 connectors. The three on the right labeled "HI" should be connected to the corresponding 3 BNC connectors on the back panel of the 1296, as seen by the arrows in Figure 5-22a and 5-22c. For example, the V1 HI on the 1260 front goes to the V1 on the 1296 back, the V2 HI on the 1260 front goes to the V2 on the 1296 back, and Generator Output on the 1260 front goes to the Generator on the 1296 back. Also see Figure 5-28 for further details on HI/LO connection schemes. Also make sure the USB cable is connected to the computer, and the National Instruments software drivers are installed. This will include the LabView software package.

On the front panel of the 1296, one can imagine the Hi connector as being the AC bias source, or similar to the positive electrode in a DC circuit, while the Lo connector is similar to the negative electrode in a DC circuit, which provides the modified signal a return path to the detector.

b) SMaRT Software

This is the proprietary software from Solartron Analytical (Farnborough, Hampshire, England, www.solartronanalytical.com), as of 9/26/05 a division of Ametek (Paoli, PA, www.ametek.com). This software both drives the instruments and records and displays the data collected. If the original installation CD for the software cannot be found, visit www.solartronanalytical.com and go to the "downloads" section link, then click on the "software" link, and download the latest version of SMaRT (as of 7/11/06,

v.2.8.0) or alternatively download the following link http://www.solartronanalytical.com/downloads/software/smart280.zip. After installing the hardware, make sure the GPIB listeners are on the correct GPIB channels in the SMaRT software. This only needs to be done one time as part of the installation process. A screen shot of each of the windows that will pop up when adjusting these settings are shown in Figure 5-23. To access the window, click on the Tools menu then click on Hardware Settings, or alternatively hit the F4 button. The correct settings, as shown in Figure 5-23a, under the interface tab are Model = Solartron 1296, Card No. = GPIB Card 0, and Address = 2. The correct settings under the FRA tab, as shown in Figure 5-23b, are Model = Solartron 1260, Card No. = GPIB Card 0, and Address = 12. Once these settings are correct, click ok.

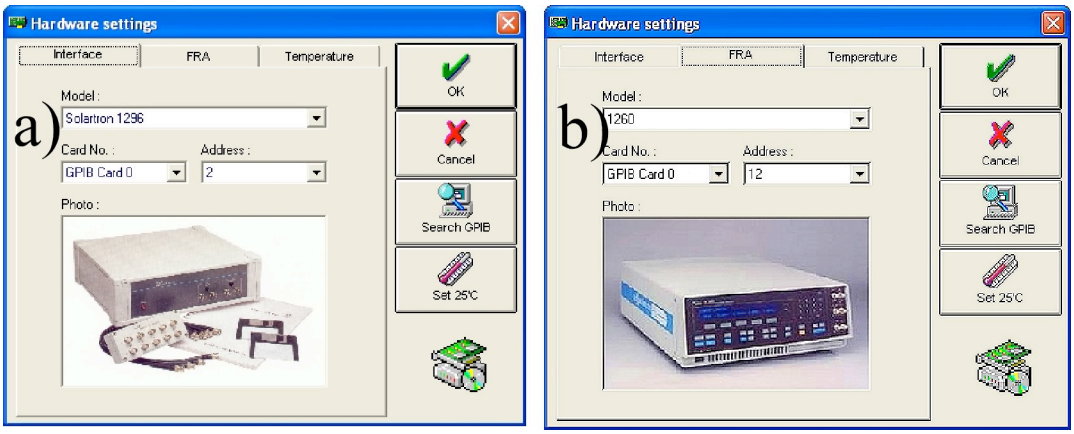


Figure 5-23. Initial configuration of the SMaRT software to find the hardware after installation showing the hardware settings a) interface tab and b) FRA tab.

There are project files in this software which contain a collection of experiment and data files. The experiment files contain the instructions for driving the instrument. All GPIB codes are sent automatically, and data is stored for you in the .dat files under the experiment being run. The software allows you to fix or sweep the AC Bias, DC

Bias, Frequency, change the integration time for impedance measurement, and loop instructions. When you first load the software, you will see a window like that in Figure 5-24a. Select Create a New Project to bring up the window in Figure 5-24b. Then, type in the name and comments for your project file. Then you will be brought to the project viewing screen, shown in Figure 5-24c.

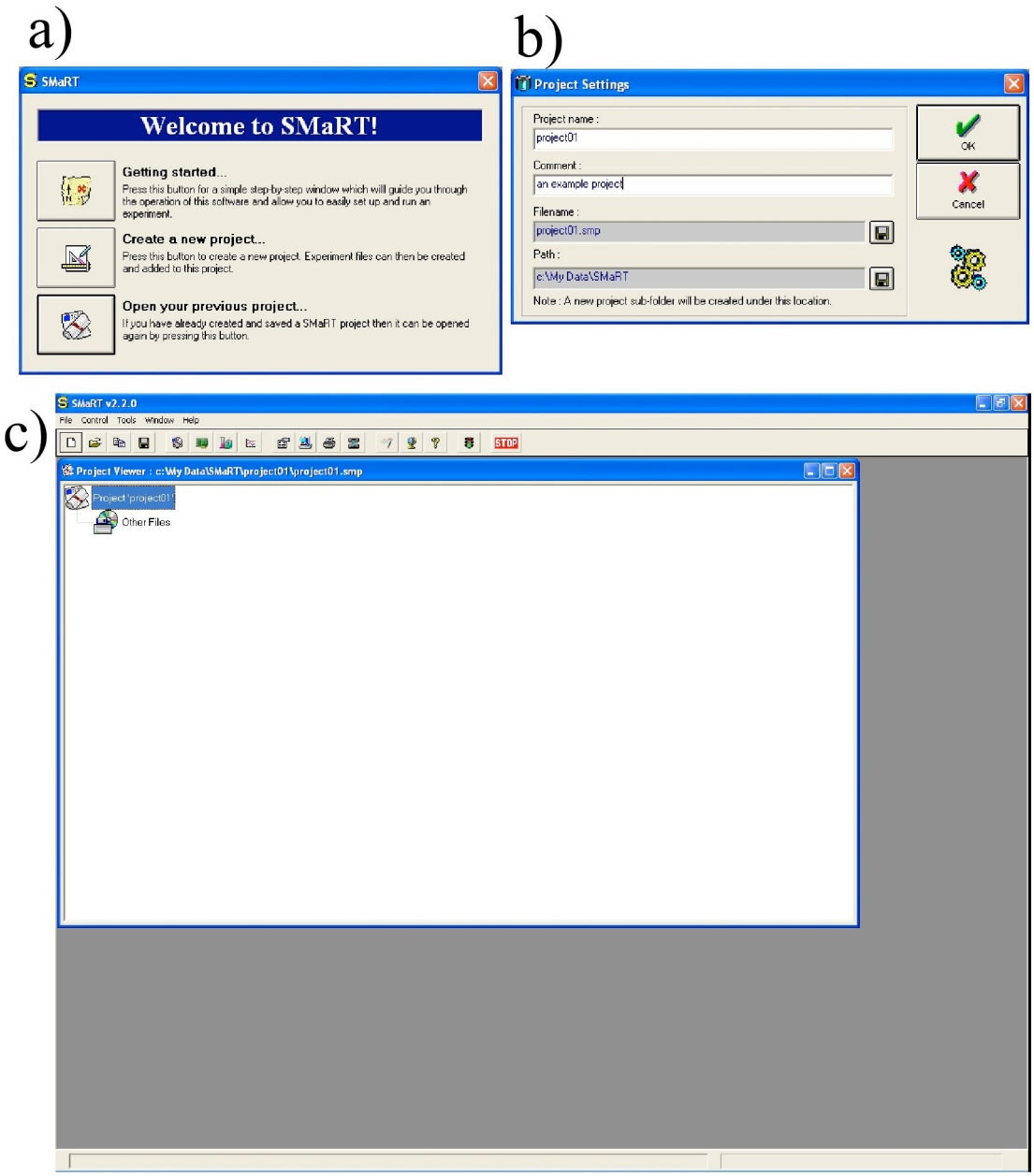


Figure 5-24. Initial screens of the SMaRT software.

SMaRT uses files called “experiments” to drive the hardware through a series of steps to collect the impedance spectra for you. A typical experiment file from SMaRT is shown below.

1)Set DC = 0.0V

2)Set AC = 0.01V

3)Sweep Frequency from 1Hz to 100Hz, 5 pts/decade

4)Measure Impedance, 10s

5)Next Frequency

6)Sweep Frequency from 100Hz to 10MHz, 10 pts/decade

7)Measure Impedance, 1s

8)Next Frequency

A series of screen shots of how to create an experiment file in the SMaRT software is shown below in Figure 5-24.

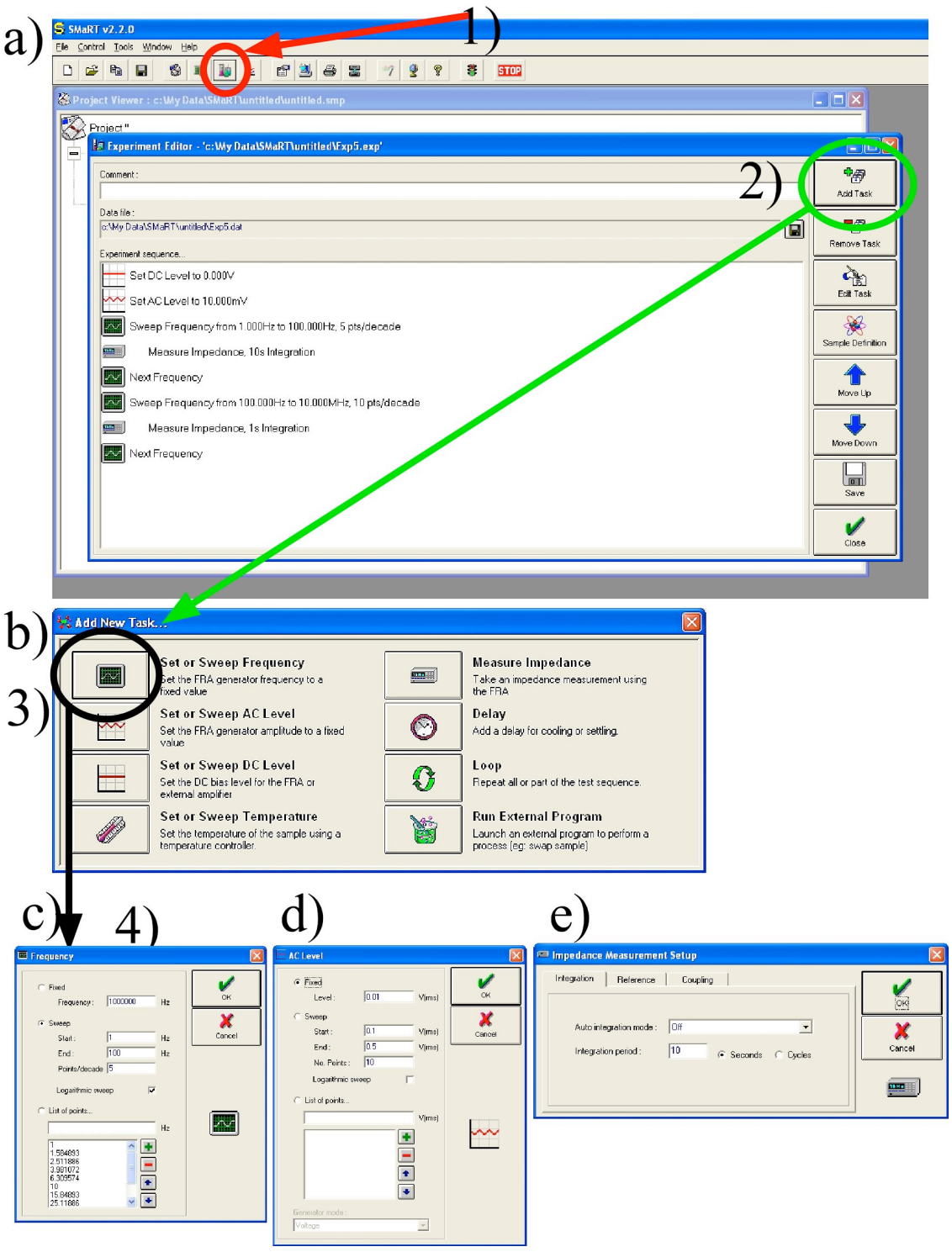


Figure 5-25. Screen shots from SMaRT.

First, one creates a new experiment either by selecting File, New, Experiment or by clicking on the icon of the beakers, highlighted by the red circle on the screen shot in

Figure 5-25a. This will bring up the experiment editor window, shown in the foreground of Figure 5-25a. Each line listed in the experiment is called a task. To edit a task, simply double click it and a window will pop up showing the choices available when editing this task. To add a new task, click the button labeled add task, highlighted by the green circle. A new window pops up, displayed in Figure 5-25b. Select the task to add, in this example the "set or sweep frequency" button is clicked, and then enter the desired parameters in the window that pops up. Examples of different tasks include set or sweep frequency in Figure 5-25c, set or sweep AC level in Figure 5-25d, and measure impedance in Figure 5-25e. Once a task's details are entered, it will be added to the list of tasks for the experiment. To change the order of the tasks, highlight a task to move, then click the buttons on the right side of Figure 5-25a labeled Move Up or Move Down depending on which direction you wish to move the task in the experiment.

The example experiment listed above typically takes about five and a half minutes to collect, and only describes a portion of setting up the SMaRT software to make the desired measurements. In later sections of this chapter, such as section 5-f of this chapter on page 189, details of picking points and engaging onto nanoparticles will be described. While it is of course desirable to have as many points per decade as possible, and it is desirable to have long integration times for the impedance measurements at low frequencies, these must be balanced with the need to collect spectra quickly. About six minutes per spectra can provide up to 40 spectra in a four hour work period, which was adequate to make statistically significant comparisons between samples. Typical experimental conditions to minimize 60 Hz noise include using longer integration times. Thus, the typical experiment described on page 174 includes long 10 second integration

times at low frequencies while only using shorter 1 second integration times at high frequencies.

Data can be exported in .csv formats for use in Excel or other software programs for data analysis. It is worth noting that the 1260/1296 instrument only measures the real and imaginary components of the impedance. All other values such as impedance magnitude, capacitance, admittance, tan delta or dielectric loss, and relative or absolute permittivity are calculated from these measurements. Therefore, if mathematical models are required where specific assumptions must be made, it is best to start with the data actually collected, the real and imaginary components of the impedance, and then operate on this data with transfer functions known by the user.

c) Writing custom software for Igor Pro on the Asylum MFP-3D system.

It may be worth the time to learn how to program custom panels in the Asylum AFM software. This avoids the cumbersome and time consuming process of exporting data, converting data between software program file formats, and having to navigate between multiple windows of software during operation of the instrument. This is fairly straightforward. One could copy areas of panels like the force curve "pick point" functions for a start. There are ways to have Igor send the GPIB codes to the Solartron system, which can be found on the internet. Good starting points include http://zone.ni.com/devzone/devzone.nsf/webproducts/a95c253dfb5fdb0986256786000be3c3, and http://zone.ni.com/devzone/conceptd.nsf/webmain/8F143577CCF9A31F86256804006800E6. The GPIB codes that are specific to the Solartron system can be found in the user manuals, while standard GPIB codes can be found online. It would be fairly simple,

assuming prior experience programming in languages such as Visual Basic or C++, to create panels within the Igor Software that replicate the functions performed by the SMaRT software, that let you sweep the AC frequency and fix or sweep the AC & DC biases, etc., and then save this data into waves in Igor with fairly easy ways of then displaying the spectra. While this sounds intimidating, it could make the end-user's life much easier for investing a month of work early on. Currently, one has two copies of software running simultaneously, and has to constantly switch back and forth between them in a fairly cumbersome process. Further, in order to handle the data correctly, one has to export the data from Smart into Excel or Igor for detailed analysis; if one collects the data in Igor directly, a much more efficient and robust analysis of the data can be performed. Excellent online help files are provided in the Asylum Software package for Igor Pro. Located under the Help Menu, MFP3D Help Files, MFP3D Advanced, there are several informative options. Suggested starting points include 3D Programming Start, MFP3D Programming, and How to Write User Functions. These help files will be most useful assuming the user has read at least Volume I - Introduction of the Igor Pro Manual, and reading Volume IV – Programming is also useful knowledge.

d) AC Impedance AFM Tip Holder (Asylum MFP-3D).

The AC Impedance AFM tipholder is the tipholder with a wire ending with a pin connector coming off a binding post screw on the circuit board side of the tipholder. A photo of the AC Impedance tipholder is shown in Figure 5-26.

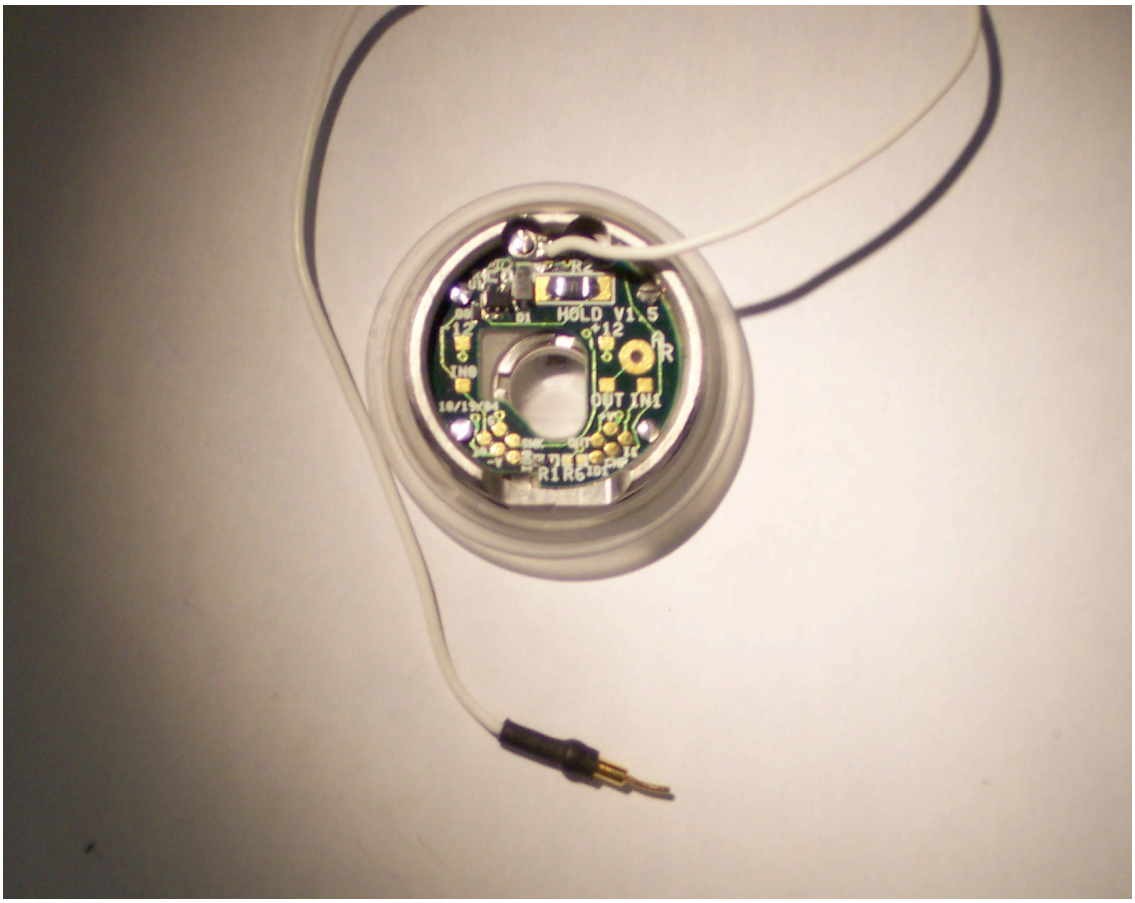


Figure 5-26. AC Impedance tip holder for Asylum MFP-3D Stand Alone AFM

This wire can be changed should the pin or wire get damaged by removing the flat-head screw and installing a spare. The round lug or eye opening is placed on the shaft of the screw before reinsertion. A Pt-coated tip (mikromash, NSC15-TiPt, Wilsonville, OR, USA) is loaded into the AC Impedance tip holder. Load the tipholder into the AFM head, making sure the wire is in the gap near the tip-holder-release button so that the wire is not pinched, and can move freely. Photographs of the correct way to install the impedance AFM tipholder into the head of the Asylum MFP-3D are shown in Figure 5-27. Figure 5-27a shows initially aligning the two rear ball bearings to the two grooves on the metal band on the tipholder, as the user would normally do when loading

a regular tipholder. Figure 5-27b shows the installed tip holder, after pressing the black rubber button to release the third ball bearing while lowering the tip holder into position, and then releasing the black rubber button to lock the tip holder in place with all three of the white ceramic ball bearings. Notice how the wire is in an opening next to the mechanism that moves the third ball bearing. It does not matter which opening is used to run the wire through, what is most important is to prevent the wire from being pinched and making sure that it can move freely, so that when the other end of the wire is being plugged in to the BNC connectors the wire is not damaged or the tip holder does not become dislodged and fall onto the sample below, ruining both the tip and the sample.

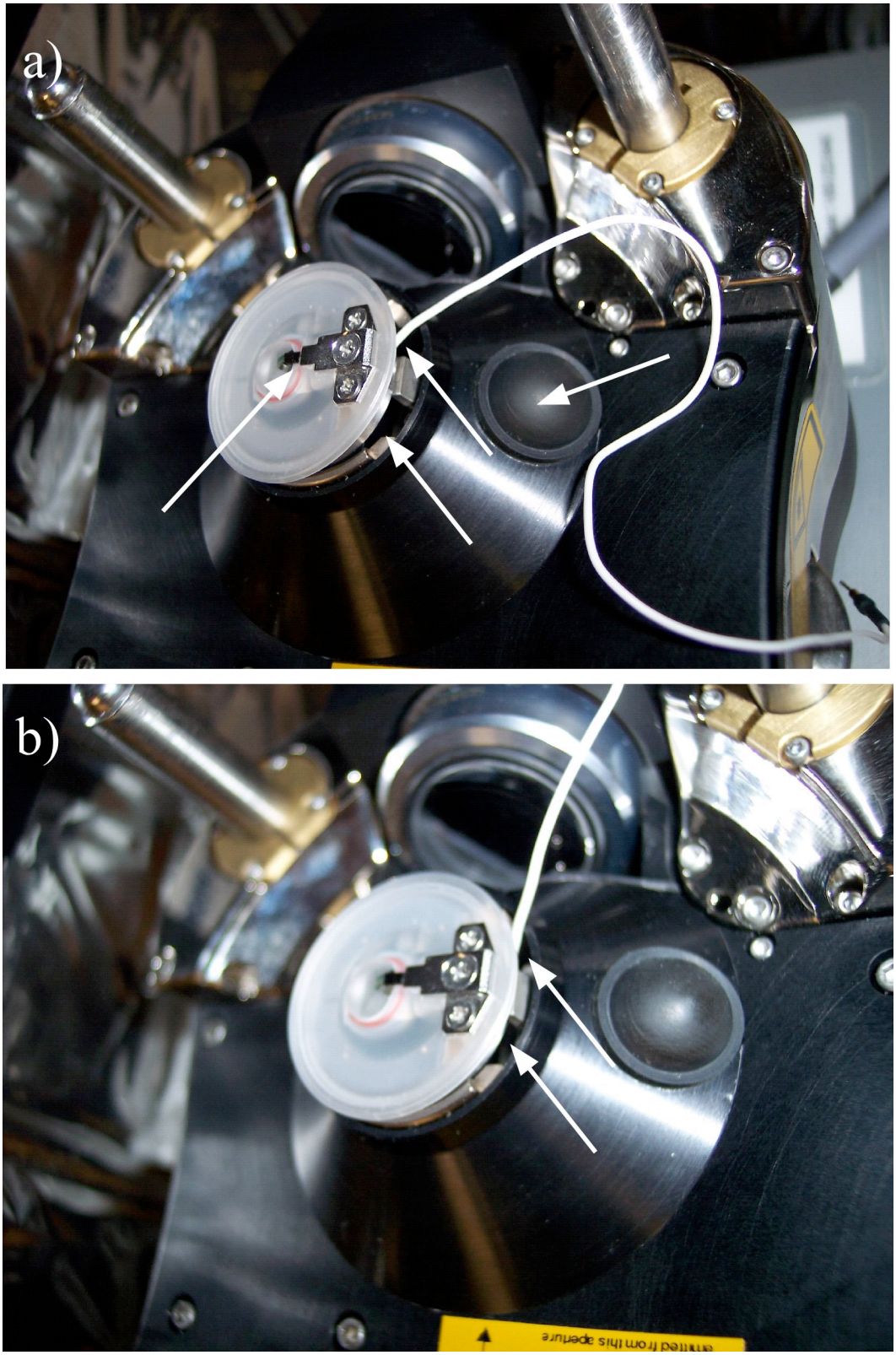


Figure 5-27. a) When loading the tipholder into the Asylum MFP-3D head with a conductive cantilever (left arrow), place the two grooves on the metal ring of the

tipholder onto the ball bearings on the left side of the head while it is upside down. Then, make sure the wire coming out of the tipholder is in one of the two openings (center two arrows) near the rubber button (right arrow) you push to secure the third ball bearing and lock the tip holder in place. b) A picture of the tipholder completely loaded, with the wire (upper arrow) not pinched or obstructed.

Always remember to plug in the pins from the tip holder and the sample to the correct BNC connector on the mounting plate on the back of the AFM base, depending on whether tip bias or sample bias is desired. If tip bias is desired, then make sure the BNC cable running to the HI connector on the front of the Solartron 1296 is plugged into the wire connected to the tip holder, and the BNC cable running to the LO connector on the front panel of the Solartron 1296 is plugged into the wire that leads to the sample. If sample bias is desired, then make sure the BNC cable running to the HI connector on the front panel of the Solartron 1296 is connected to the wire that leads to the sample, and the BNC cable running to the LO connector on the front panel of the Solartron 1296 is connected to the wire coming out of the tip holder. Also, when placing the head onto the scanner, make sure all the magnets on the slides are far enough away from the tip holder that scanning will not be obstructed, or the head will not have any weight supported by the magnets accidentally. Additionally, keep the two unshielded wires from crossing paths to minimize potential noise sources; these are the white wires shown in Figures 5-27, 5-28, 5-30. A figure showing how the connections should be made to the BNC connectors on the back of the base of the AFM is depicted in Figure 5-28. In this photo, there is a white BNC cable connected closest to the photographer with an unshielded white wire going to the external breadboard containing a current limiting resistor, and then another unshielded white wire leads from the breadboard to the sample. The impedance tip holder is loaded into the AFM head, and an unshielded white wire leads to

the rear BNC connector and the black BNC cable. In Figure 5-30, the BNC connector on the right hand side is the same as the BNC connector in the front in Figure 5-28.

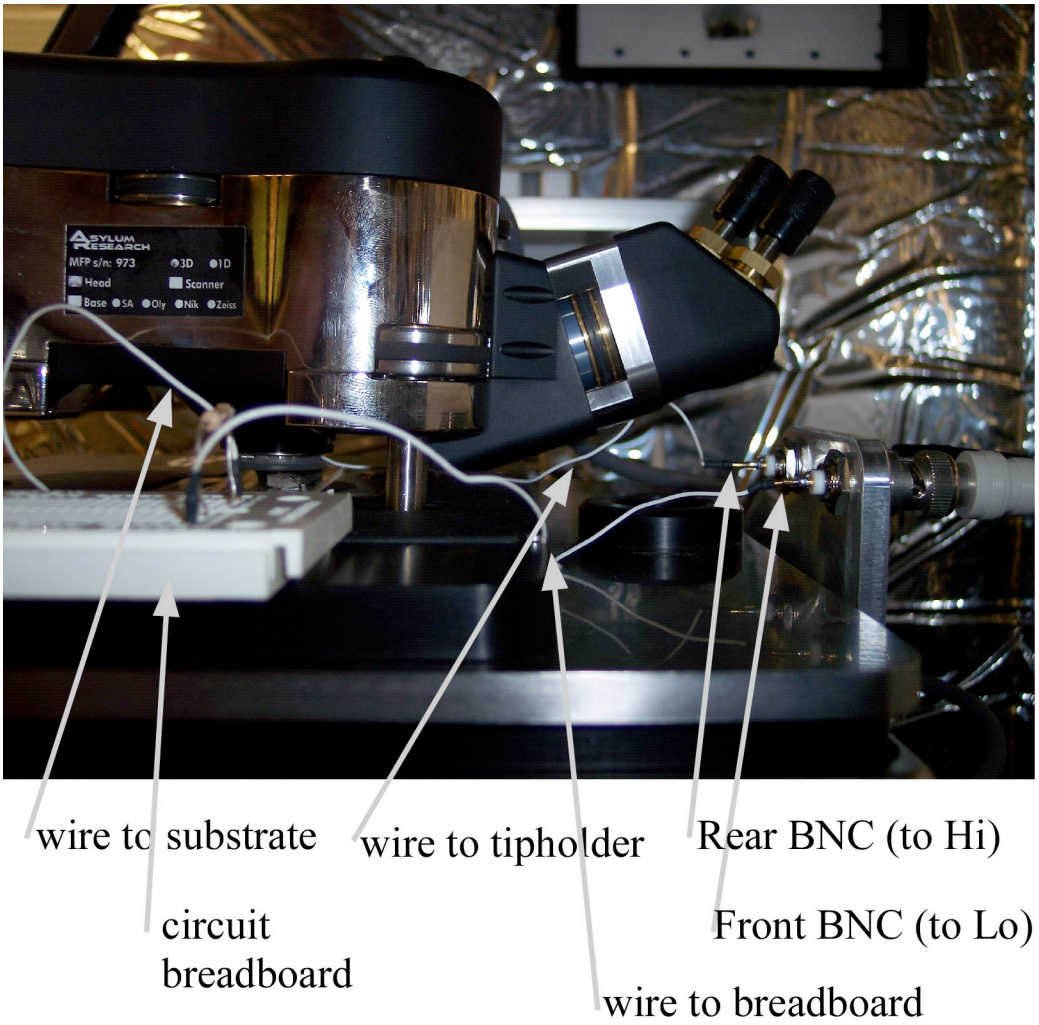


Figure 5-28. Side view of the Asylum MFP-3D AFM head loaded on the scanner with the impedance AFM connections including an external breadboard completed, in position to engage and begin scanning.

e) Sample Prep

Conductive metal substrates were used for all experiments conducted in this thesis research. If measuring an insulator either a conductor or semi-conductor substrate could be used because the dielectric constant of the circuits could be compared by comparing their relative capacitances using equation (5-2). While the shape of this electrode

material can be varied, maintaining a conductive path from the nanoparticles to the wires leading back to the FRA is crucial. Typically, gold substrates from Molecular Imaging (now Agilent AFM) which are deposited on a mica surface yield very atomically smooth substrates, and these substrates can be cut using scissors into various smaller sized pieces to examine multiple samples at lower cost. Another typical substrate can be purchased from Asylum Research, and are three circular gold pads deposited on a glass slide.

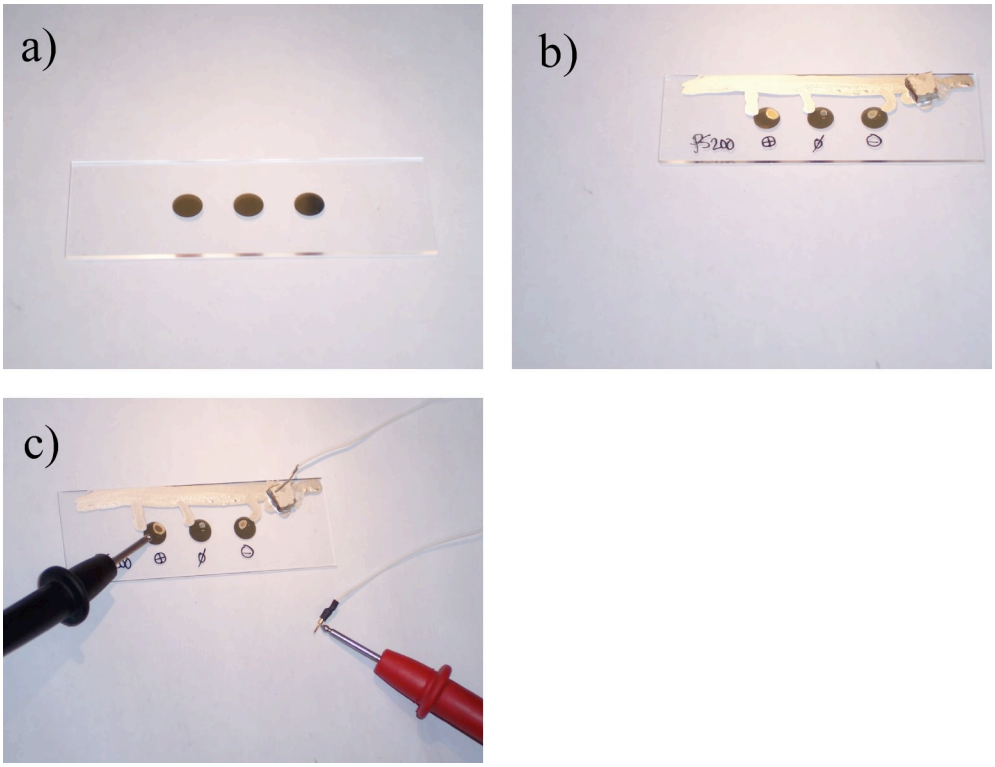


Figure 5-29. How to prepare a sample includes taking a) one gold substrate from Asylum Research, depositing samples on the gold pads, b) then painting silver epoxy paint paths from the gold pads to the magnet in one corner, and c) performing a continuity check to insure a conductive path has been made.

These are the substrates used for all of the experiments described in this thesis, as they are quite easy to work with, and are shown in Figure 5-29. Silver epoxy paint (Ted Pella, USA) was painted on the surface of the glass slide from the edge of the gold pad to a small magnet on the corner of the slide, which is held in place with the silver

paint. Make sure a small path of silver paint goes up the side of the magnet and onto the top to ensure a good conductive path, as shown Figure 5-29b. A small wire with a magnetic segment at one end and a pin at the other is attached to the magnet on the slide and plugged into the pin receptacle of the BNC connector on the base of the AFM. Take note of whether this wire to the sample is applying the bias or returning the signal to the FRA detector. While initially experiments were performed with both configurations, no noticeable difference could be found in either case. Despite this finding, it is still good practice to know whether you are applying tip bias or sample bias. It is also easy for BNC cables to get switched either on the front panel of the Solartron 1296 or on the plate on the back of the AFM base if there are multiple users performing experiments that require switching between tip bias and sample bias.

If at this point the user is worried about whether a good conductive path has been created, a hand-held multimeter can be used to perform a continuity check with one test probe contacting the outside edge of the gold surface (so as not to damage any of the atomically smooth areas to be used in imaging later), and hold the pin of the wire to the other test probe, and measure the resistance, as shown in Figure 5-29c. While this test is not necessary, it can be useful to build confidence that the skills of sample prep have been mastered sufficiently.

One note about using glass slides as sample substrates on the Asylum AFM. If the area of interest is anywhere other than the exact center of the slide, care must be taken to examine whether any part of the slide will lie outside the center metal section of the scanner. If this situation occurs (it definitely will if you are using one of the outside gold pads on the Asylum glass slide / gold substrates), you will have to shim the glass slide

containing the sample up so it clears the black regions of the scanner. This process is detailed step by step in Figure 5-30.

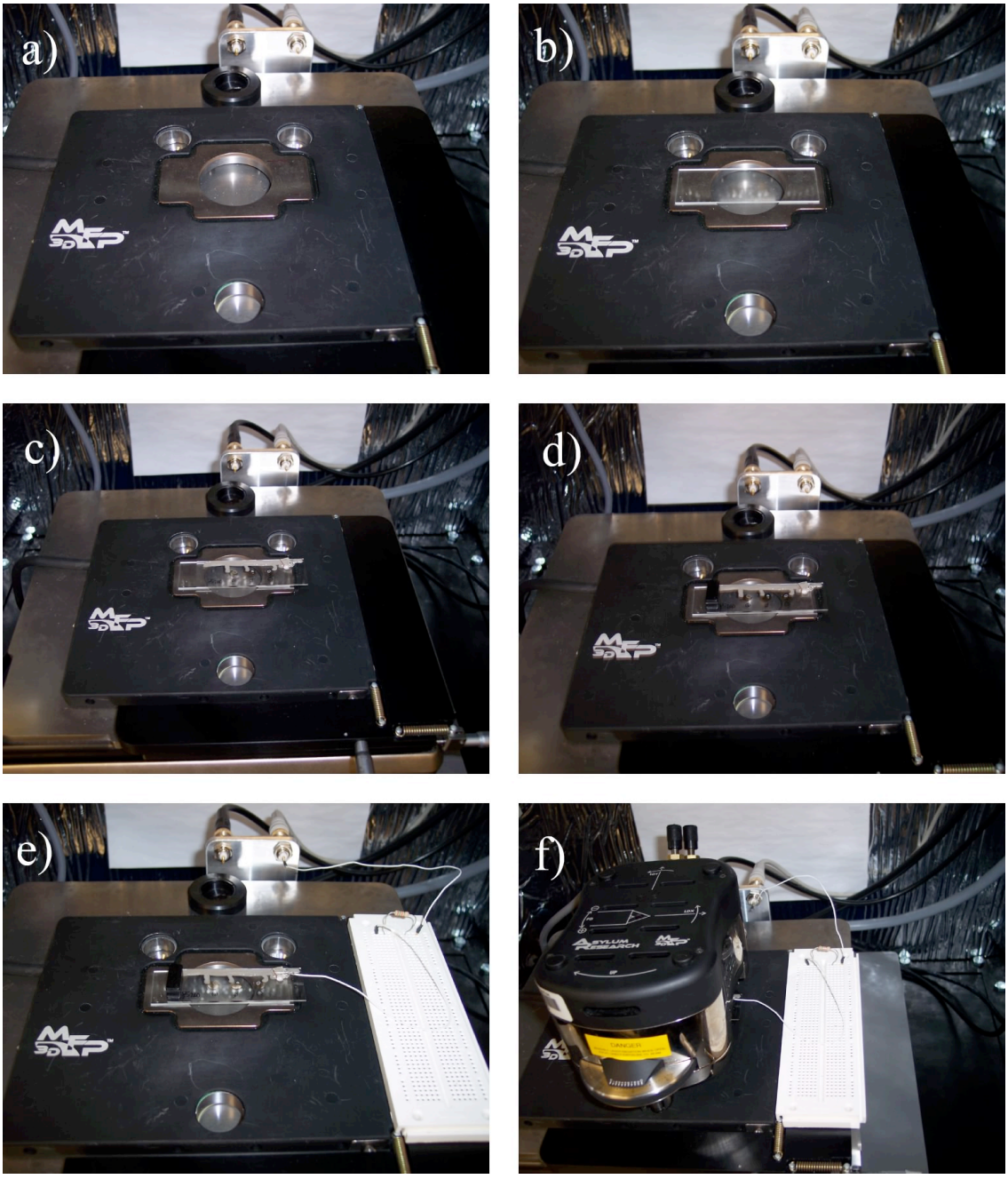


Figure 5-30. How to shim a slide, step by step.

To shim up a glass slide with a sample, place an empty glass slide so it fits normally on the metal section (Figure 5-30a) of the scanner as shown in Figure 5-30b. Then, place the slide containing the sample on top of this slide such that the area containing the sample will be centered for scanning, as shown in Figure 5-30c. Then attach the magnets as needed to hold the slide in place during scanning, as shown in Figure 5-30d. Finally, attach the wires connecting the sample to the BNC connectors (Figure 5-30e) and place the head on the scanner as shown in Figure 5-30f. If for some reason you do not shim the slide and you see strange distortions in the images, your slide is hitting the edge of the black region of the scanner. For some reasons, the metal scanner section is lower than the surrounding black scanner sections. The drag between the slide resting on these stationary black regions and the moving metal scanner regions in the x-axis direction will lead to this type of distortion.

Two configurations of loading a slide onto the scanner can be used, as shown in Figure 5-31. In the first case, as in Figure 5-31a, the sample is connected directly to the BNC. In the second case, as in Figure 5-31b, the sample has a current limiting resistor installed. Each setup has its own advantages. If the exact contact impedance is needed, no current limiting resistor should be used. If the exact contact impedance is not necessary, then the current limiting resistor should be used to protect the current sensors in the Solartron Frequency Response Analyzer and Dielectric Interface.

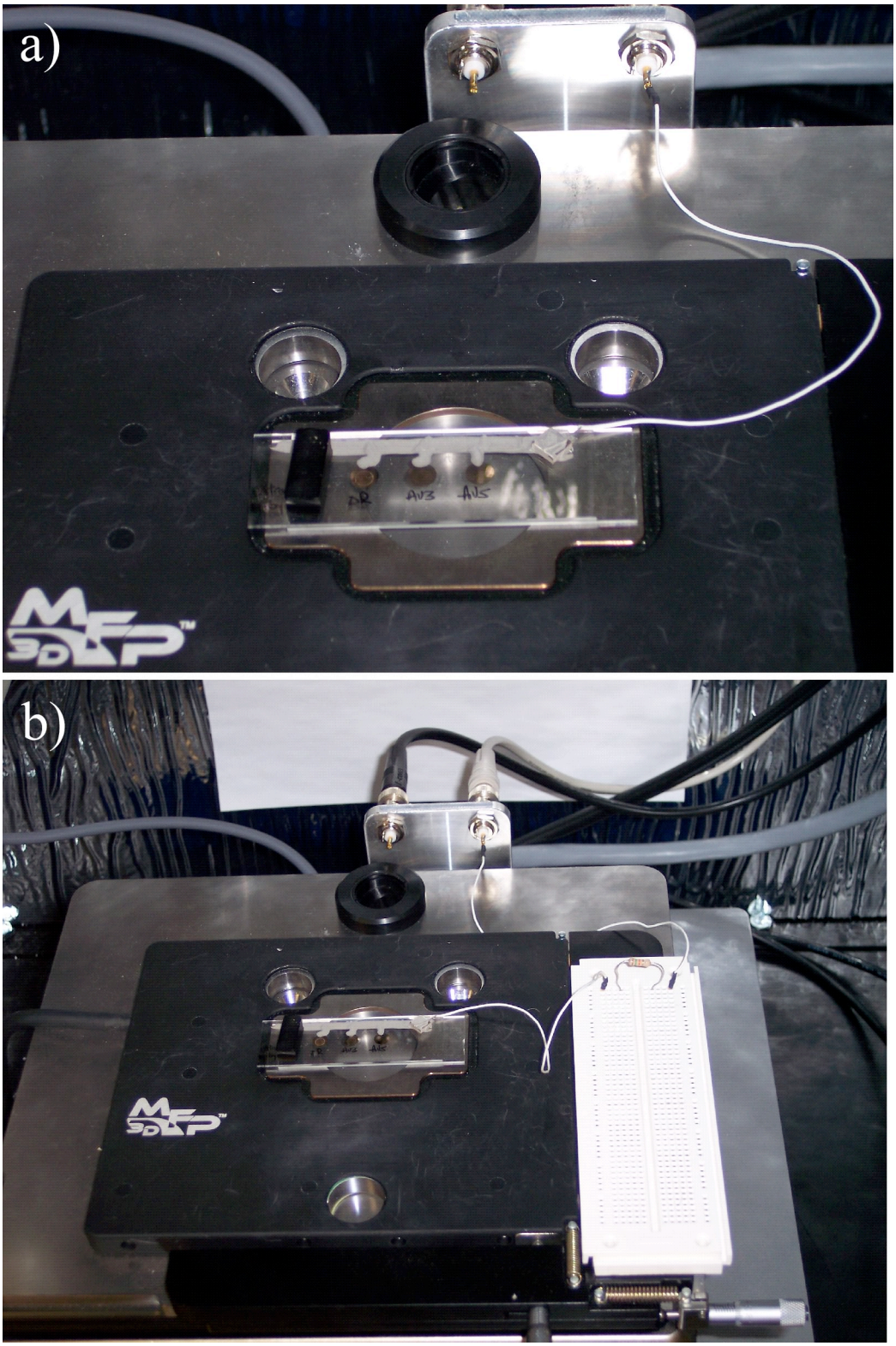


Figure 5-31. a) Direct connection of sample substrate to BNC. Notice the shim slide underneath the sample slide with the gold pads, such that the right hand gold pad can be imaged. b) Connection of a current limiting resistor via an external breadboard. The wire

from the sample is plugged into the breadboard, and any desired circuit elements can be added. In both of these photos, the slide with the gold pads is shimmed up by an empty glass slide underneath it, such that the sample deposited on the right hand gold pad can be imaged.

f) Process of collecting Impedance Spectra.

First auto-tune the cantilever to determine the resonant frequency of the cantilever just as one would normally do before taking a topographical image in AC mode or tapping mode. A screen shot of the result of this process is shown in Figure 5-31.

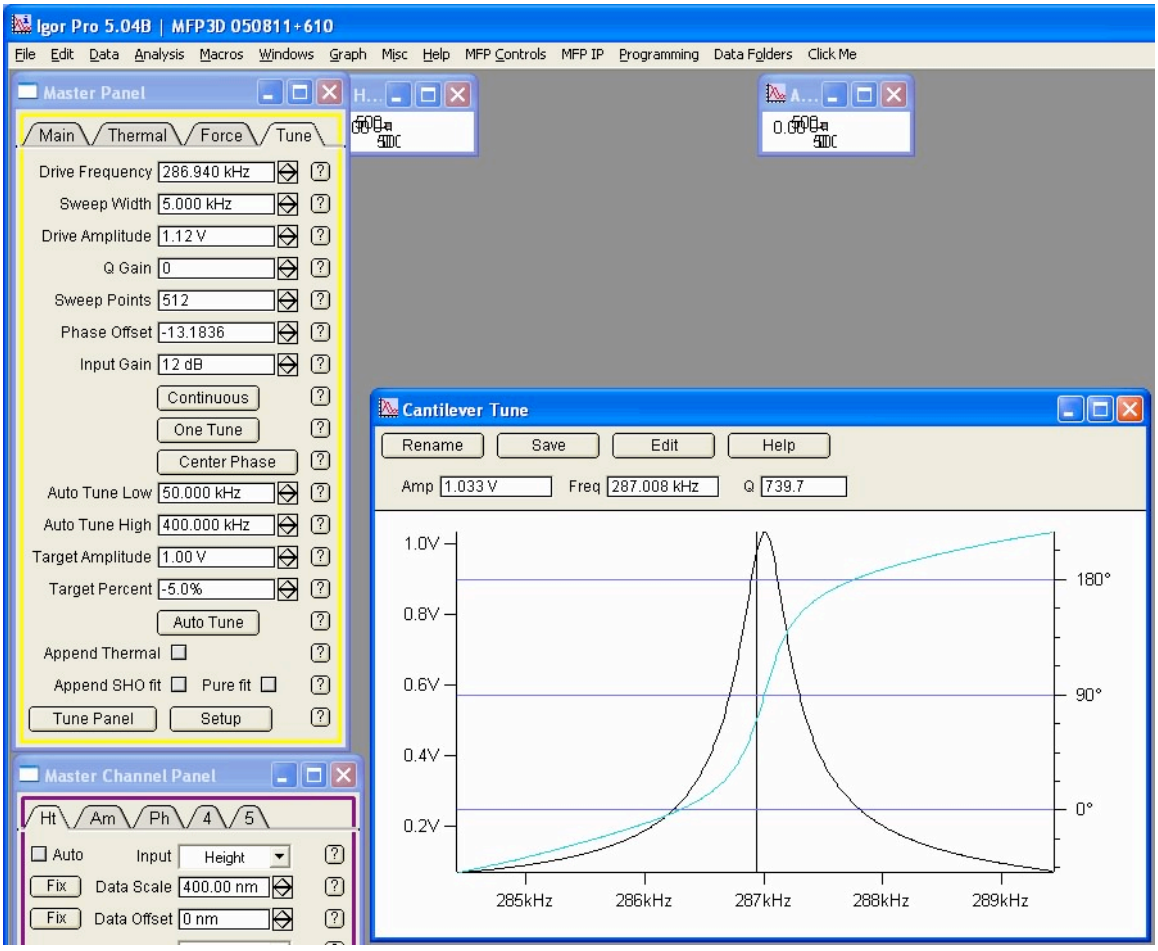
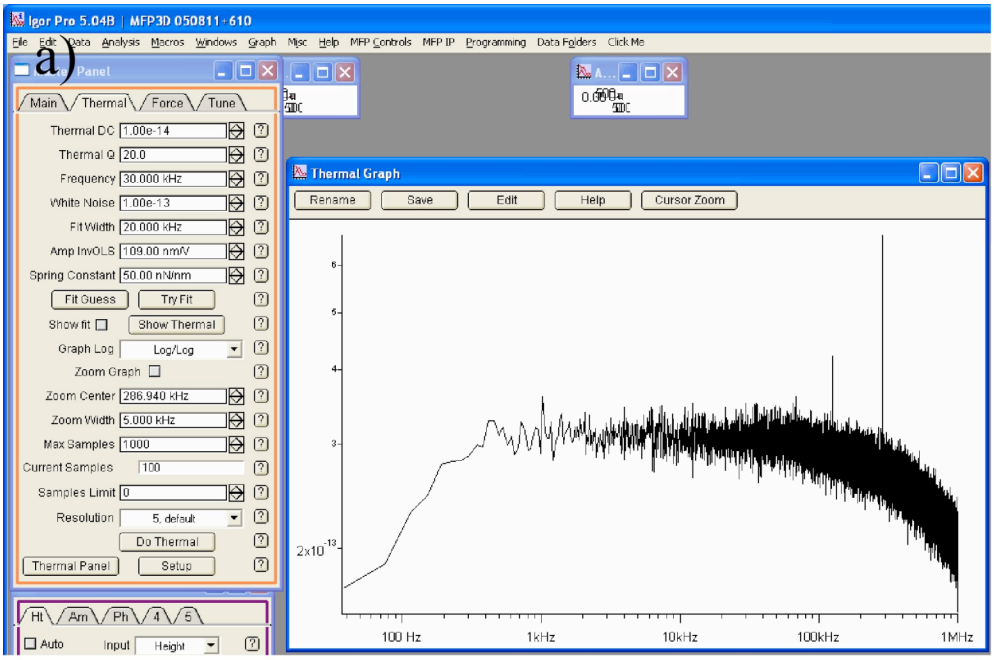


Figure 5-32. Screen shot of the auto tune process, showing a very nice resonant frequency peak.

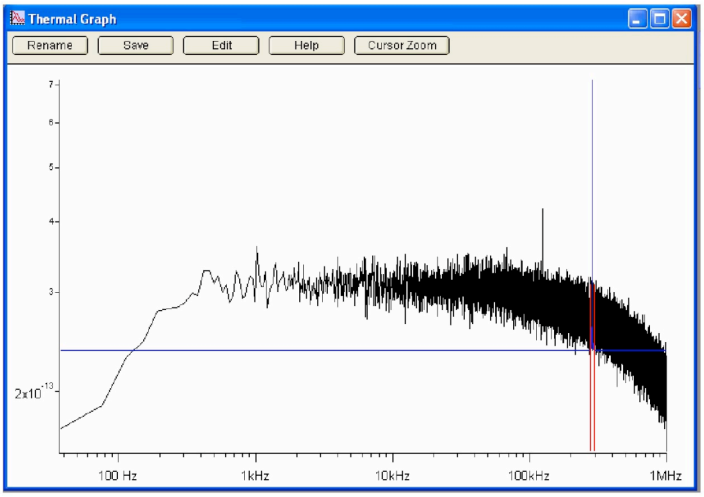
AC mode and tapping mode are the same form of imaging, however tapping mode is a trademarked term by Veeco and thus no other manufacturer can use this most descriptive term. Since the cantilever is being shaken to oscillate as it "taps" across the surface in a scan, one can imagine this oscillation represented electronically as an alternating current signal, or AC mode signal. Then collect a thermal tune of the cantilever to determine the spring constant or force constant of the tip, which will be used later when determining how to apply the desired contact force. A thermal tune is performed by clicking on the thermal tab of the master panel, as shown in Figure 5-33a. Click the Do Thermal button, then wait for at least 50 or so samples to be collected. After this, hit stop thermal, followed by the Fit Guess button. A blue line will show the software's estimation of the fit, as shown in Figure 5-33b. At this point, make sure the peak of the blue line is on the resonant frequency peak, previously determined from the auto tune. In the vast majority of cases, the software picks the correct peak. Finally, hit the Try Fit button to have the software calculate the spring constant for you, as shown in Figure 5-33c.

a)



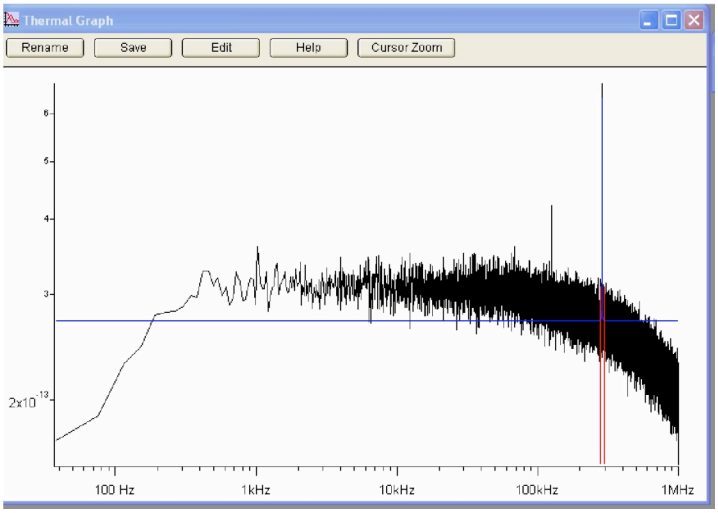
thermal tune

b)



fit guess

c)



try fit

Figure 5-33. Thermal tune screen shots, showing a) the process of collecting the thermal tune, b) applying a mathematical fit guess by the software, and c) trying the mathematical fit parameters.

Engage onto the surface as normal AC mode or tapping mode imaging requires, and collect a quick AC mode or tapping mode topographical image of your sample to determine whether you have particles of interest in the field of view. Zoom in on the appropriate areas, such that several target particles can be seen clearly in one field of view. Using the force tab of the master panel, pick points in the center of each particle that is to be measured. Withdraw the tip using the Withdraw button, select the first point to make a measurement, and click the Go There button. Using equation (5-3) for relative deflection volts, calculate what the contact mode setpoint should be as described on pages 152 and 153 of Chapter 5, and enter this value in the main tab of the master panel. Then simple engage, and the tip will move to contact the particle with the desired force. At this point, switch to the impedance software, start the experiment and give each data file a new filename. The software displays the data with a real-time plot. Once the spectra is collected, switch back to the Igor Pro MFP-3D software, withdraw the AFM tip, go to the next point, engage, collect the spectra, and repeat as many times as necessary.

Selection of particles was performed by picking points from the force curve panel, engaging in contact mode on the surface with a relative deflection value suited to give 100nN of contact force, but not starting any scanning or force curves. This ensured a good and reproducible electrical contact between the tip and the sample each measurement, and enabled the ability to remain engaged on the surface indefinitely while impedance spectra were being collected.

To determine the effects of parasitic inductance in the circuit models, step-wise measurements and models were built by adding components one by one to the experiment. First, reference resistors and capacitors were connected directly to the FRA. Second, BNC cables were used to connect to resistors and capacitors. Third, the BNC cables were connected to the AFM, which was shorted by bringing a gold conductive tip into direct contact with a gold conductive surface, and the same reference resistors and capacitors were characterized. By comparing all of these three cases, it was possible to determine the parasitic capacitance and parasitic inductance from each component in the instrument system. The parasitic inductance contributions explain the surprising rise in capacitance at high frequencies above 20 kHz. Clearly, an important consideration is the capacitance created by the cantilever leg and the chip being separated above the surface by air, which creates a parallel parasitic capacitance and can also increase the effects of parasitic inductance, since it is effectively an unshielded wire.

6. FUTURE APPLICATIONS OF AC IMPEDANCE MEASUREMENTS IN SOLUTION

Measurements utilizing AC impedance have been used to study redox chemistry of solutions[134-141]. Liquid mode imaging of AFM samples in a hydrated environment can provide useful information and a more realistic image of what a sample looks like in solution. Therefore a logical next step would be to characterize materials in solution at the nanoscale. However, several non-trivial technical challenges must be overcome before successful measurements can be made.

If one desires to measure nanoparticles in liquid with the tip in direct physical contact, the conductivity of the solvent should be considered. Even with ultra pure water the resistance of water is 18 mega ohms. If there is an easier way for the electric field to pass from tip to substrate than a highly resistive path directly through the nanoparticle sample, concerns about whether the AC bias will short circuit through the solvent to bare regions of the substrate surface should be raised.

Electrode shape could become a consideration at this point. If this short circuiting effect is prohibiting the collection of impedance spectra, one could attempt to force all of the current to travel through the sample by attaching a sample larger in size than the electrode to the surface of the electrode. The exposed area of electrode would only be in contact with the nanoparticle or sample, with none of the surrounding solution able to provide a short circuit path.

Other electrode shape consideration could include designing a shielding guard ring around the circular electrode where sample will be deposited. Careful design of electrode shape would help to minimize the fringing effects that occur on the edges of electrodes. Reducing the fringing of the electric field would help to orient the field lines in a parallel fashion through the sample. Larger areas of parallel electric field lines could lead to easier mathematical modeling calculations in both liquid and air.

Coaxial tips, if ever invented, could be a tremendous advantage to this liquid mode effort and even to air measurements. Coaxial tips would have a conductive wire in the center of the pyramid of silicon on the tip that is only exposed at the apex of the pyramid. Essentially, this would provide the surface for imaging. Challenges with this

type of tip could potentially include rapid tip wear since the imaging would be with a soft gold tip rather than a hard silicon tip.

The challenges of obtaining a liquid mode topographical image should be considered. In liquid mode, the resonant frequency of a cantilever is dampened into the audible range (typically the resonant frequency will fall between 4-20 kHz, usually between 8-12 kHz) due to the greater viscosity of water compared to air. The auto tune panel must be adjusted to provide a sweep range from about 1 kHz to 50 kHz, rather than the usual 50 kHz to 400 kHz. Alternatively, one can tune the cantilever manually. When doing this, the tune plot will not be in the usual single peak shape like that shown in Figure 5-31. There will be several noisy peaks close together. The user will have to pick a peak that has no shoulder peaks and has a large amplitude range to work with. Often, after selecting the drive frequency from this peak, the image will not show the response the user is accustomed to. If this is the case, a different peak can be selected and a subsequent different drive frequency can be used, until a satisfactory image can be obtained. Recent work on in-situ liquid mode scanning probe microscopy has been completed that successfully completed high resolution images in liquid[142]. The keys to a high resolution liquid image from this paper were using a 0.1nN silicon nitride AFM tip at a resonant frequency of 9kHz, using scan rates from 0.5 to 0.8Hz, and using integral gains from 0.6 to 1. It could also be worthwhile to investigate suggestions made by Aslyum Research to coat the AFM tip with nail polish to provide an insulating layer that leaves much less open surface area for parasitic capacitance[143, 144].

Chapter 6

IMPEDANCE AFM FOR BIOSENSING: TOWARDS A TRIPLY REDUNDANT SINGLE VIRUS BIOSENSOR.

1. INTRODUCTION

This chapter provides a proof-of-principle that a triply redundant single virus biosensor is feasible. A scheme that uses physical size, biological recognition, and electrical characterization of the single virus is proposed. The AFM tip provides the size of the virus from the height images, while an antibody functionalization on the conductive substrate or the AFM tip provides the biological specificity, and the metal coating on the AFM tip allows for electrical characterization of the individual virus. Physical size information of viruses is available in scientific literature, and biological specificity is well known through commercially available antibodies. However, electrical characterization of insulating and dielectric nanoparticles individually remains largely unexplored.

Impedance characterization of viruses should reveal that different viruses have subtle differences in electrical properties. Viruses are made up of various combinations of different proteins. Since each protein has its own dipole moment and dielectric constant, this individual difference should yield an overall difference in dipole moment and dielectric constant from virus species to virus species, similar to bacterial cells[95]. Further differences should be expected by the variation in size providing a different thickness of protein layers which should affect the resistance as a function of virus size.

In order to gain an understanding of the fundamental science behind the electrical characterization of single viruses, the impedance AFM was used as a model system for future biosensor applications. The studies of single nanoparticle characterization as a model for studies of single viruses by impedance AFM will be described in this chapter.

The polymers used were selected as a model system due to the well known properties of the materials in bulk systems, and their insulating nature with dielectric constants of approximately 2.4-2.6 for polystyrene(PS), 2.7-3.2 for polymethylmethacrylate(PMMA), and 2.5-3.5 for silica[145]. The impedance responses to different sizes of similar materials, as well as to different materials of like particle sizes, were characterized using AC Impedance AFM.

The instrument's layout is shown in Figure 6-1. The electrically isolated path to the tipholder increased the sensitivity of the impedance measurements by eliminating interference from the electronics associated with the operation of the AFM. Using signal access modules or breakout boxes typically introduced noise from the AFM electronics since the frequency response analyzer, or FRA, was measuring the impedance of the controller or base in addition to the sample's impedance. The dielectric interface added to the frequency response analyzer allowed measurement of over 100 teraohm (10^{14} ohm) impedances, extending the operating range of impedances of the FRA by several orders of magnitude. The versatile Asylum MFP-3D AFM base can be easily modified so that any electronic characterization instrument can be interchanged via BNC connections at the base. To further capitalize on the open architecture of the Asylum MFP-3D software interface, the end user can write custom panels to drive any electrical characterization

instrument that accepts GPIB codes. Such user panels could thereby providing seamless operation of all instrument components from one software interface.

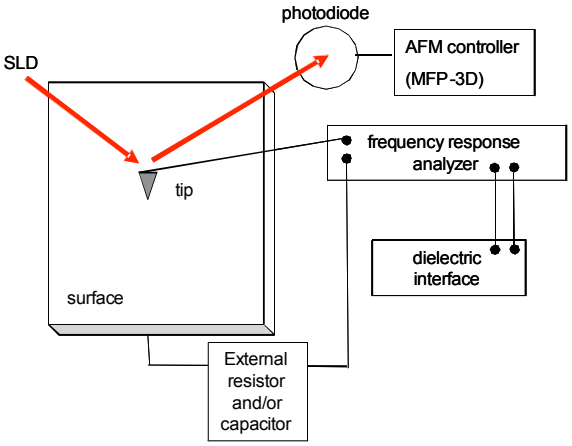
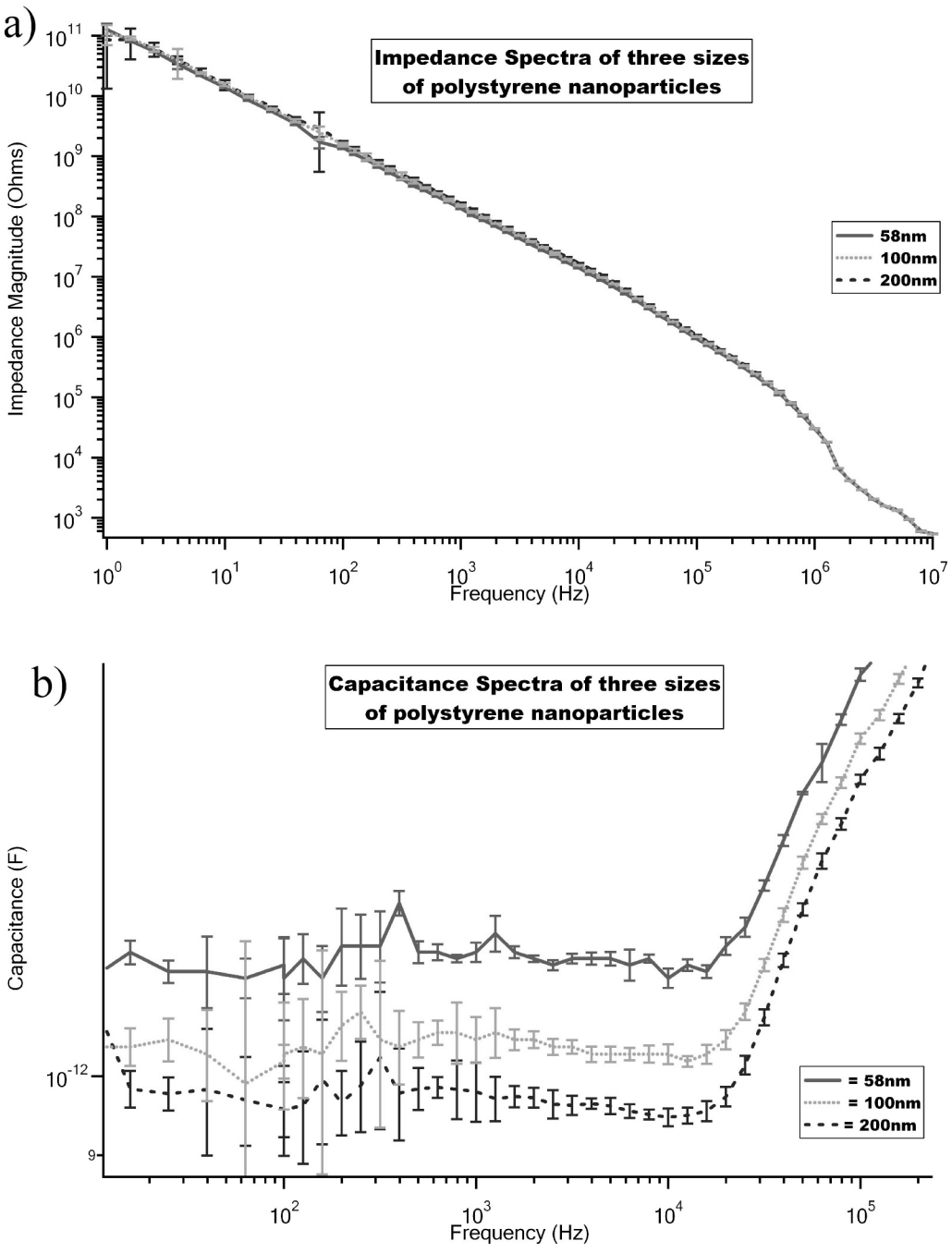


Figure 6-1. Illustration of the impedance AFM configuration, such that AFM operation is possible while providing a direct electrical path from the impedance analyzer through the sample and back to the detector input.

2. AC IMPEDANCE STUDIES OF POLYSTYRENE, PMMA, AND SILICA NANOPARTICLES IN THREE DIFFERENT SIZES.

a) Polystyrene (PS)

Impedance measurements were performed on nanoparticles with various sizes and materials. First an area of the gold electrode surface on which the nanoparticles are deposited is scanned in tapping mode. Next, the tip is positioned over the particle and brought into contact at a specified force with the particle, as described previously in Chapter 5. Figure 6-2 shows the impedance and capacitance of 58, 100 and 200 nm unmodified polystyrene particles deposited on gold surfaces. The spectra of over fifty particles is averaged to show the traces in Figure 6-2, with error bars showing one standard of deviation at each frequency measured.


a)
Impedance Spectra of three sizes of polystyrene nanoparticles
Impedance Magnitude (Ohms)
Frequency (Hz)
58nm
100nm
200nm
b)
Capacitance Spectra of three sizes of polystyrene nanoparticles
Capacitance (F)
Frequency (Hz)
= 58nm
= 100nm
= 200nm

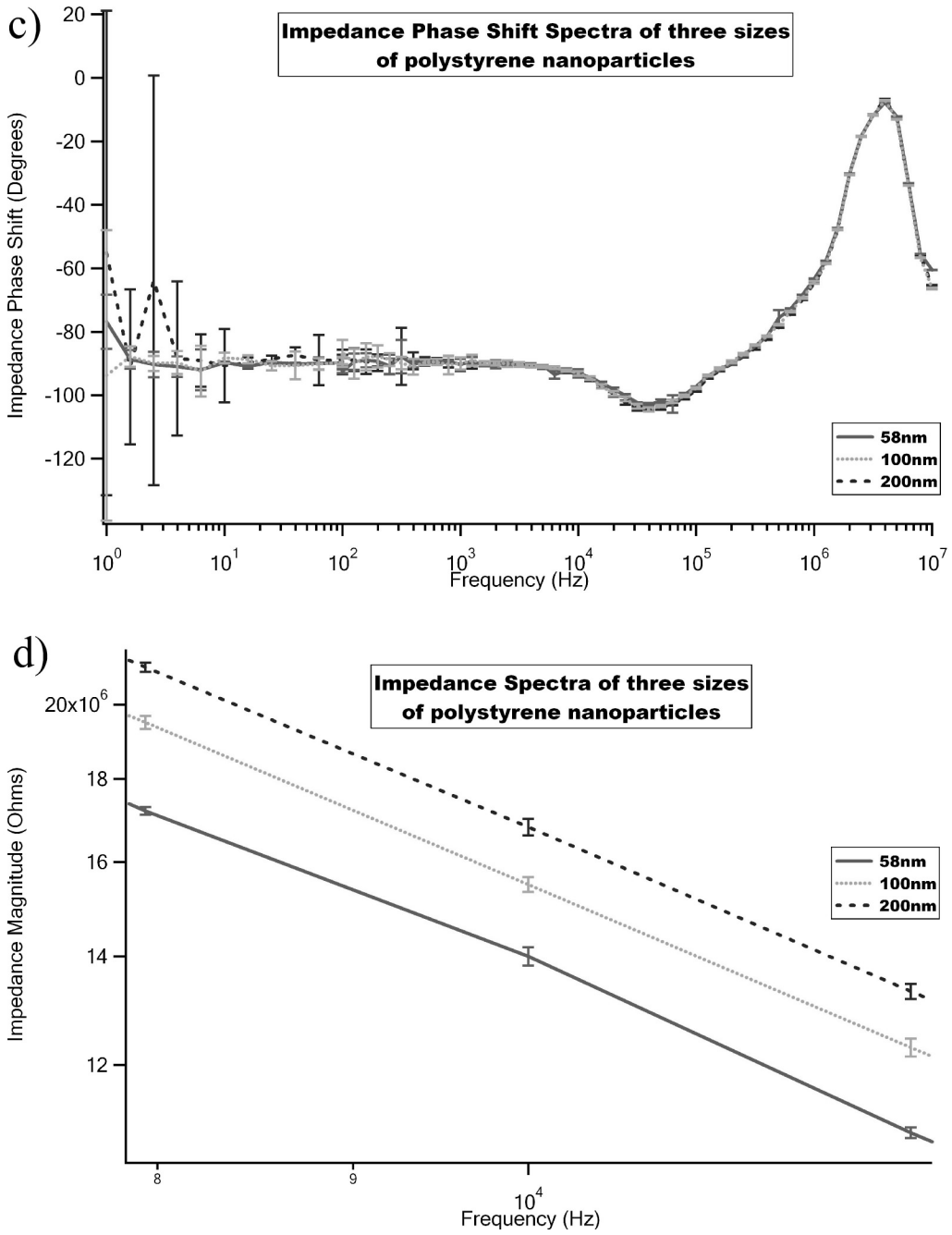


Figure 6-2. a) Impedance, b) capacitance, c) impedance phase shift, and d) magnified impedance spectra for three different sizes of polystyrene nanoparticles, with diameters of Solid trace = 58nm, Dotted trace = 100nm, Dashed trace = 200nm.

While the impedance plot of the whole spectra in Figure 6-2a appeared to have all three traces overlaid, the zoomed in region of Figure 6-2d showed more clearly a

statistically significant difference between the three samples. It was observed that the impedance magnitude of the 58nm diameter polystyrene nanoparticles was lower than the impedance of the 100nm diameter polystyrene nanoparticles, which was lower than the measured impedance of the 200nm diameter polystyrene nanoparticles. These results were summarized in the first column of Table 6-1.

The impedance phase shift spectra for the three sizes of polystyrene nanoparticles were shown in Figure 6-2c. The phase shift was observed to be -90 degrees over a large region of the low frequency end of the spectra, which suggested a purely capacitive interaction. Further details of the phase shift will be discussed with Figure 6-4 in this chapter.

Topographical images of each type of particle characterized in Figure 6-2 were obtained and shown in Figure 6-3. The height AFM image for 58nm diameter polystyrene nanoparticles was shown in Figure 6-3a, and the section analysis of this image was shown in Figure 6-3b. The line used to take the section analysis was drawn and shown on Figure 6-3a. The height of these nanoparticles was approximately the expected diameter. The height image for the 100nm diameter polystyrene nanoparticles was shown in Figure 6-3c, and the section analysis of this image was shown in Figure 6-3d. While the height did not perfectly match the diameter, the particles were still 100nm across. In Figure 6-3e the height image of the 200nm diameter polystyrene nanoparticles was shown, and the section analysis of this image was shown in Figure 6-3f. The section analysis for the 200nm polystyrene particles showed good agreement with both the height and width of the particles.

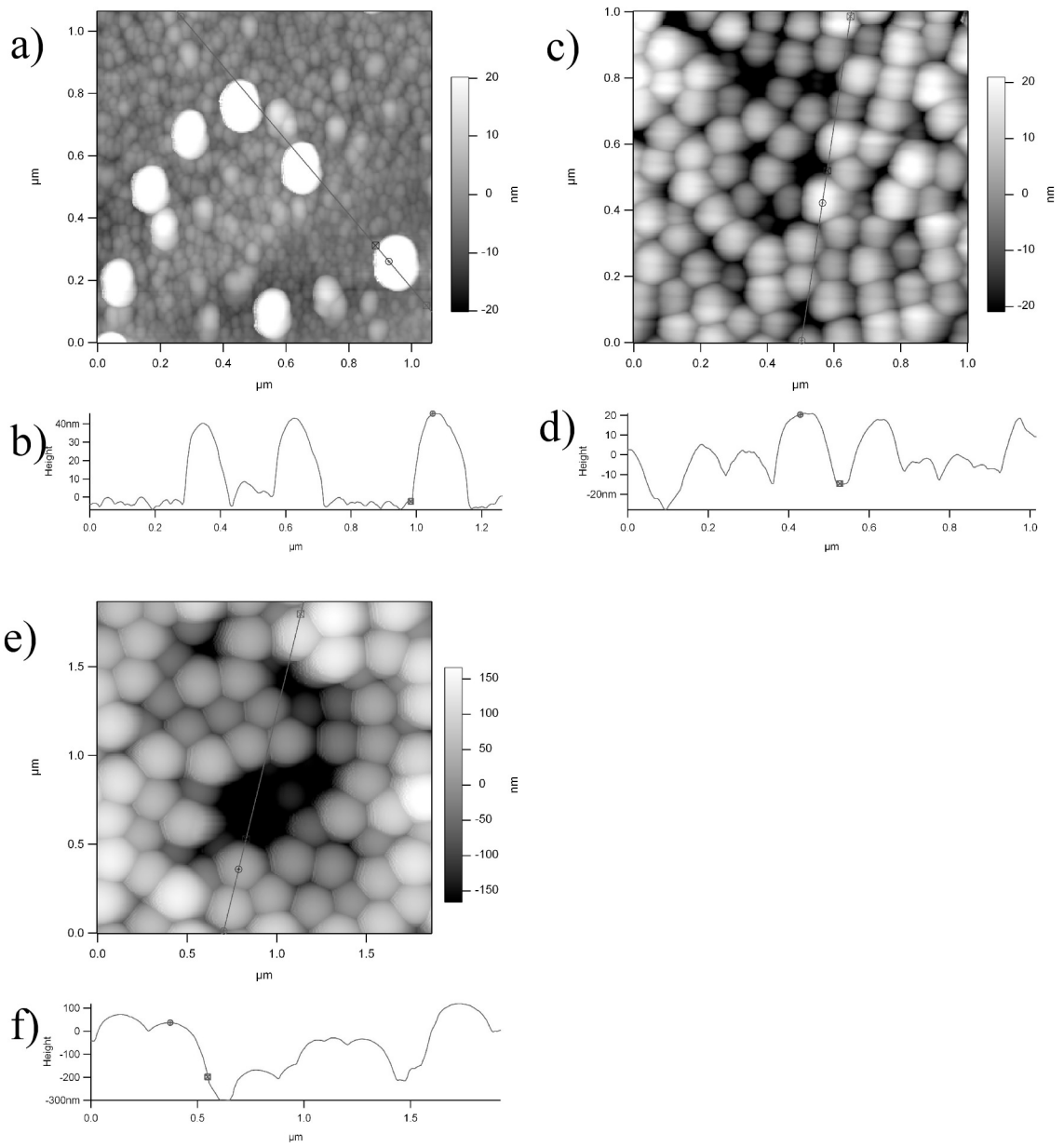


Figure 6-3. a) AFM height image and b) cross section of 58nm polystyrene; c) AFM height image and d) cross section of 100nm polystyrene; e) AFM height image and f) cross section of 200nm polystyrene.

The statistically significant difference in impedance between the three sizes of polystyrene nanoparticles was confirmed looking at the capacitance spectra values in Figure 6-2b. The trend in this figure mimicked what would be expected in a bulk system from a parallel plate capacitor model, where the distance between the two plates was

inversely proportional to the capacitance. The capacitance (C) at any given frequency (f) is calculated from the impedance (Z) and the phase angle (φ) using the relationship

$$C = \frac{1}{2\pi f Z \sin\phi} \quad (6\text{-}1)$$

The decrease in capacitance with increasing particle size was due to the increased separation between the tip and the surface (the two plates of the capacitor) by the equation

$$C = \frac{k\varepsilon_0 A}{d} \quad (6\text{-}2)$$

where C is the capacitance, k is the dielectric constant, ε_0 is the permittivity of free space, A is the area of the electrodes, and d is the distance between the electrodes. An illustration of this model can be found in Figure 6-4a.

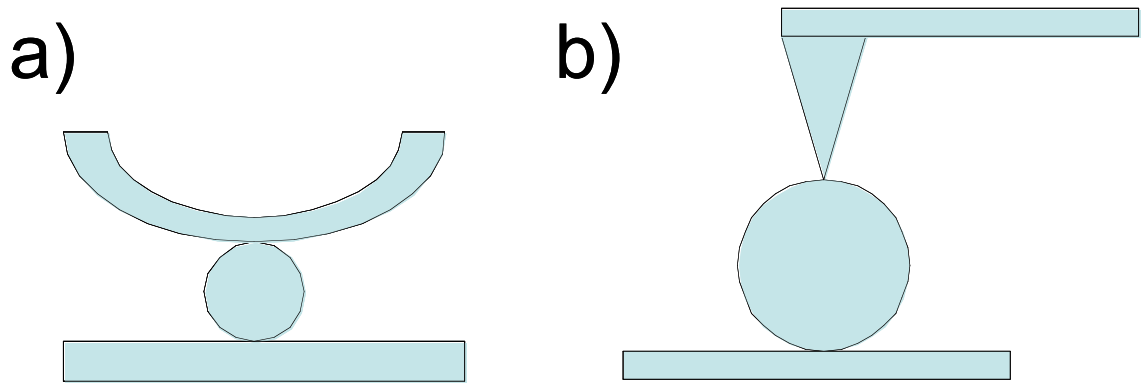


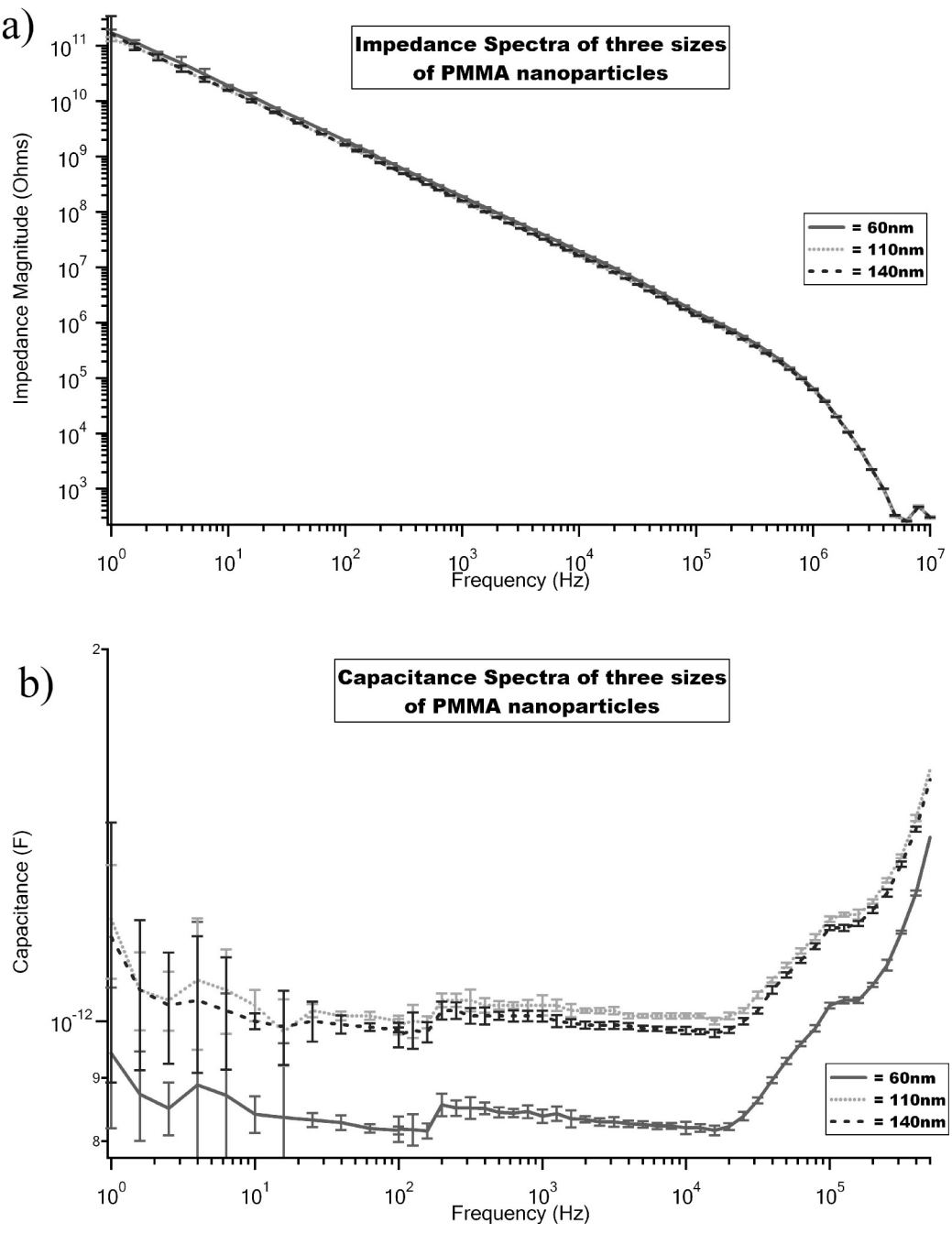
Figure 6-4. Illustrations of a) parallel plate model, and b) spherical model of AFM tip to substrate capacitance with a nanoparticle dielectric separating the two.

An alternative model of the capacitance between the AFM tip and the electrode substrate could be called the spherical model. An illustration of this model is shown in Figure 6-4b. When the radius of the nanoparticle is larger than the radius of curvature of the AFM tip the AFM tip acts like a point above a spherical dielectric resting on top of an

infinite plane of surface charge. This model is more similar to a point charge above an infinite plate charge, with the primary difference being the addition of the spherical dielectric material. In this model, the capacitance is no longer proportional to the inverse of the nanoparticle radius, but instead becomes directly proportional to the nanoparticle radius. Further details of this model will be discussed later in this chapter on page 235.

b) Polymethylmethacrylate (PMMA)

In the case of polymethylmethacrylate (PMMA), or Plexiglas, the data collected are shown in Figure 6-5. In Figure 6-5a, the three impedance traces appear overlaid, but in Figure 6-5d the smallest particles of 60nm diameter PMMA have statistically significant higher impedances from the other sizes. The two sizes of 110nm and 140nm diameter PMMA particles are nearly overlapping. Surprisingly, in the case of PMMA the opposite trend of the polystyrene data is observed. In Figure 6-5b the capacitance spectra were shown. Here, the capacitance decreased with smaller sized particles. This could be a result of several possibilities. It is not known precisely how the dielectric constant of materials changes at the nanoscale, if at all. Perhaps there is size dependence to the dielectric constant of nanomaterials. Another possibility is the remaining surfactant molecules on the nanoparticles after they were dried. Since the two different materials were sourced from different vendors, it is possible different surfactants were used in the manufacturing process. These different surfactant molecules could have different molecular charges, electron densities, or dielectric constants that could alter the impedance measurements. Further, if there were some inconsistencies in the layer of surfactant molecules leftover as residue on the particles as some function of the nanoparticle size, there could have been different impedance measurements observed.


a)
Impedance Spectra of three sizes of PMMA nanoparticles
Impedance Magnitude (Ohms)
Frequency (Hz)
= 60nm
= 110nm
= 140nm
b)
Capacitance Spectra of three sizes of PMMA nanoparticles
Capacitance (F)
Frequency (Hz)
= 60nm
= 110nm
= 140nm

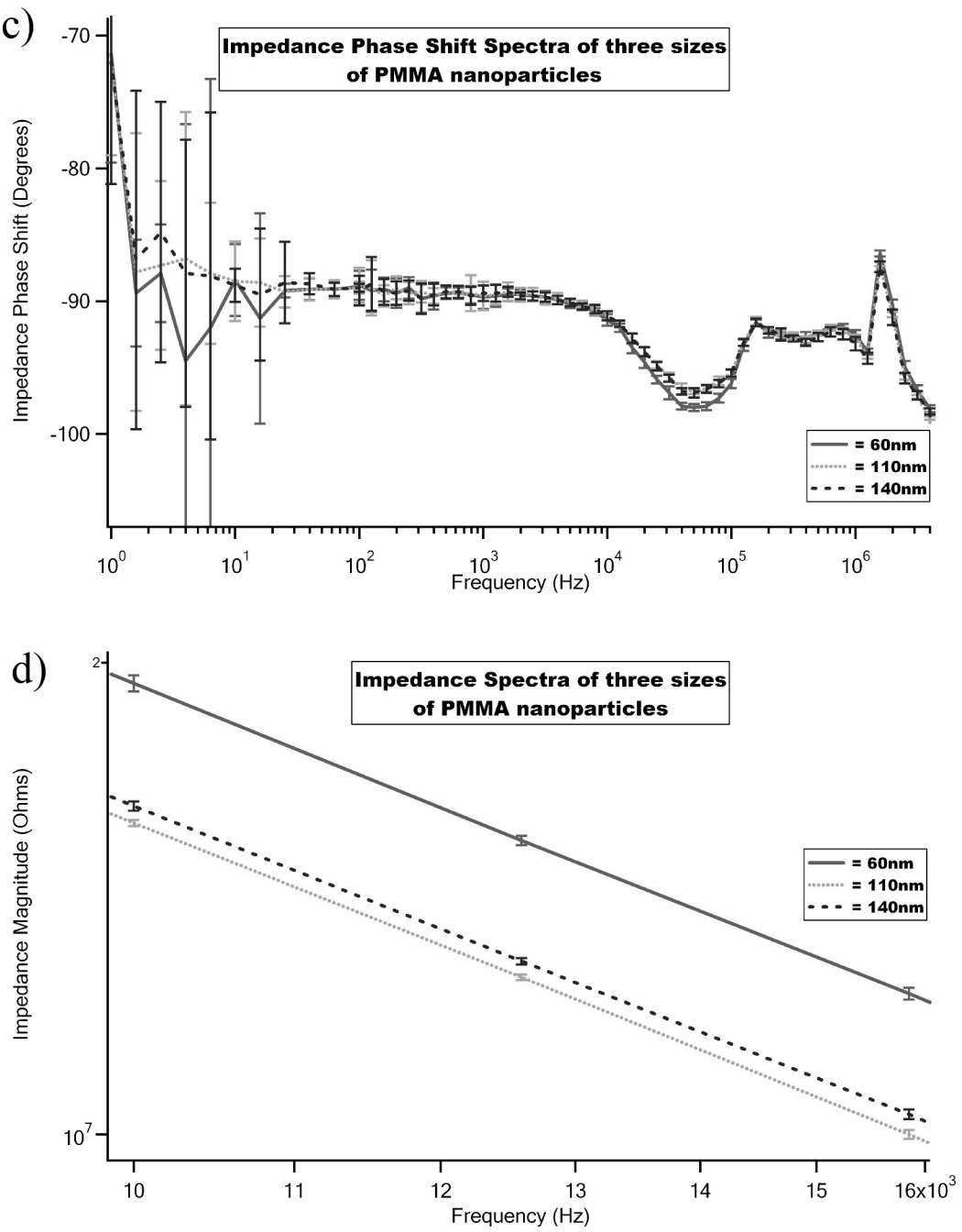


Figure 6-5. a) Impedance, b) capacitance, c) impedance phase shift, and d) magnified impedance spectra of three sizes of polymethylmethacrylate (PMMA). Diameters are Solid traces = 60nm, Dotted traces = 110nm, Dashed traces = 140nm.

It is worth noting that in Figures 6-2c and 6-5c, the impedance phase shift at low frequencies is nearly -90 degrees. The impedance phase shift can provide clues as to the

capacitive or resistive nature of the circuit elements when modeling the device under test. The phase shift of the impedance measurement relates to the impedance vector quantity. The angle between the real component of the impedance and the impedance vector magnitude, as shown in Figure 6-6a, is measured as the phase shift.

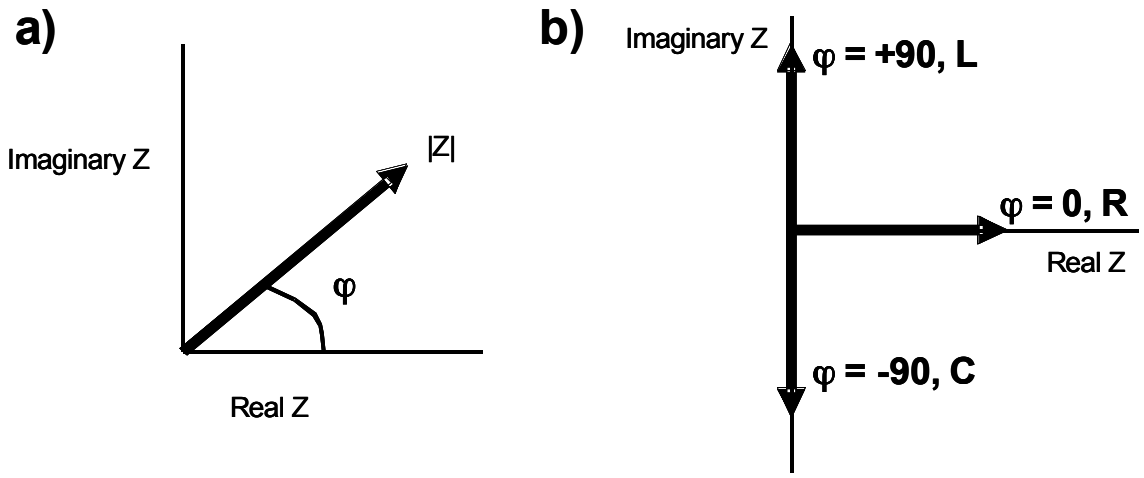


Figure 6-6. Impedance vector quantity. a) example of impedance vector, b) example of vectors for pure resistors, pure capacitors, and pure inductors.

Simply imagining a pure resistor, the expected phase shift would be 0 degrees, while a pure capacitor would provide a phase shift of -90 degrees, and a pure inductor would provide a phase shift of +90 degrees[129]. An inductor can be imagined physically as a straight wire with a second wire coiled around it. Figure 6-6b shows example impedance vectors for pure resistors (R), pure capacitors (C), and pure inductors (L). Since the impedance phase shifts at low frequencies are observed to be nearly -90 degrees, this suggests a model circuit that is almost purely capacitive. At higher frequencies, such as those above 10^4 Hz, there is a deviation from -90 degrees of phase shift. This decrease in phase indicated that some other circuit elements must be considered. As suggested by the use of the word "pure" to describe capacitors and other

circuit elements, a circuit under test could behave, for example, partially as an inductor and partially as a capacitor.

In the case of the polystyrene, the phase shift decreases slightly, and then spikes upward to approach 0 degrees between 10^6 and 10^7 Hz. The phase shift data suggest that the effects of parasitic capacitance were increasing from 10^4 to 10^6 Hz, indicated by the increase of the phase shift from -90 degrees closer to +90 degrees. Parasitic inductance contributions from the parasitic capacitance are discussed on page 162 of chapter 5. In the case of PMMA, the phase shift decreases slightly at frequencies above 10^4 and then remains below -90 degrees at all higher frequencies. The most likely cause of this change in phase shift at high frequencies was some breakdown of the real capacitor from ideal to non-ideal. It is not immediately known why the PMMA exhibited a different shift than the polystyrene; however, differences in surfactant could have provided different electrical effects.

The topographical images of the three different sizes of PMMA nanoparticles studied by impedance spectroscopy are shown in Figure 6-7. The 60nm diameter PMMA nanoparticles were shown in Figure 6-7a with a height image and Figure 6-7b with a section analysis of Figure 6-7a. While it was not clearly single particles shown in this section analysis, the range from the top of the particles to the surface is approximately 60nm, which was the expected value. In Figure 6-7c, the 110nm diameter PMMA nanoparticles were shown, and the corresponding section analysis was displayed in Figure 6-7d. The nanoparticles appeared to be very close to 110nm in both height and width, which was in good agreement with the expected values. In this image, the nanoparticles were more dispersed, and were only a monolayer thick where deposited.

Unfortunately, some polydispersity of diameters was observed, however only particles close to a diameter of 110nm were selected for impedance spectroscopy characterization. In Figure 6-7e the height image of the 140nm PMMA was shown, with the corresponding section analysis shown in Figure 6-7f. The height image appeared to depict a densely packed monolayer of particles that were slightly smaller in height than the predicted 140nm. While the dense packing of particles made precise determination of individual particle width difficult, it was estimated by measuring the distance from the center of one particle to the center of an adjacent particle. This particle width estimation was also slightly less than the expected 140nm diameter. The discrepancy between the manufacturer product specifications and the actual product could account for the unexpected trends observed in impedance and capacitance in Figure 6-5. If the particles labeled as 140nm were actually smaller than the particles labeled as 110nm, then the trend in capacitance from highest to lowest would be in order of increasing size. While this corrected trend was consistent across all sizes, it was still in the opposite direction as that observed with polystyrene.

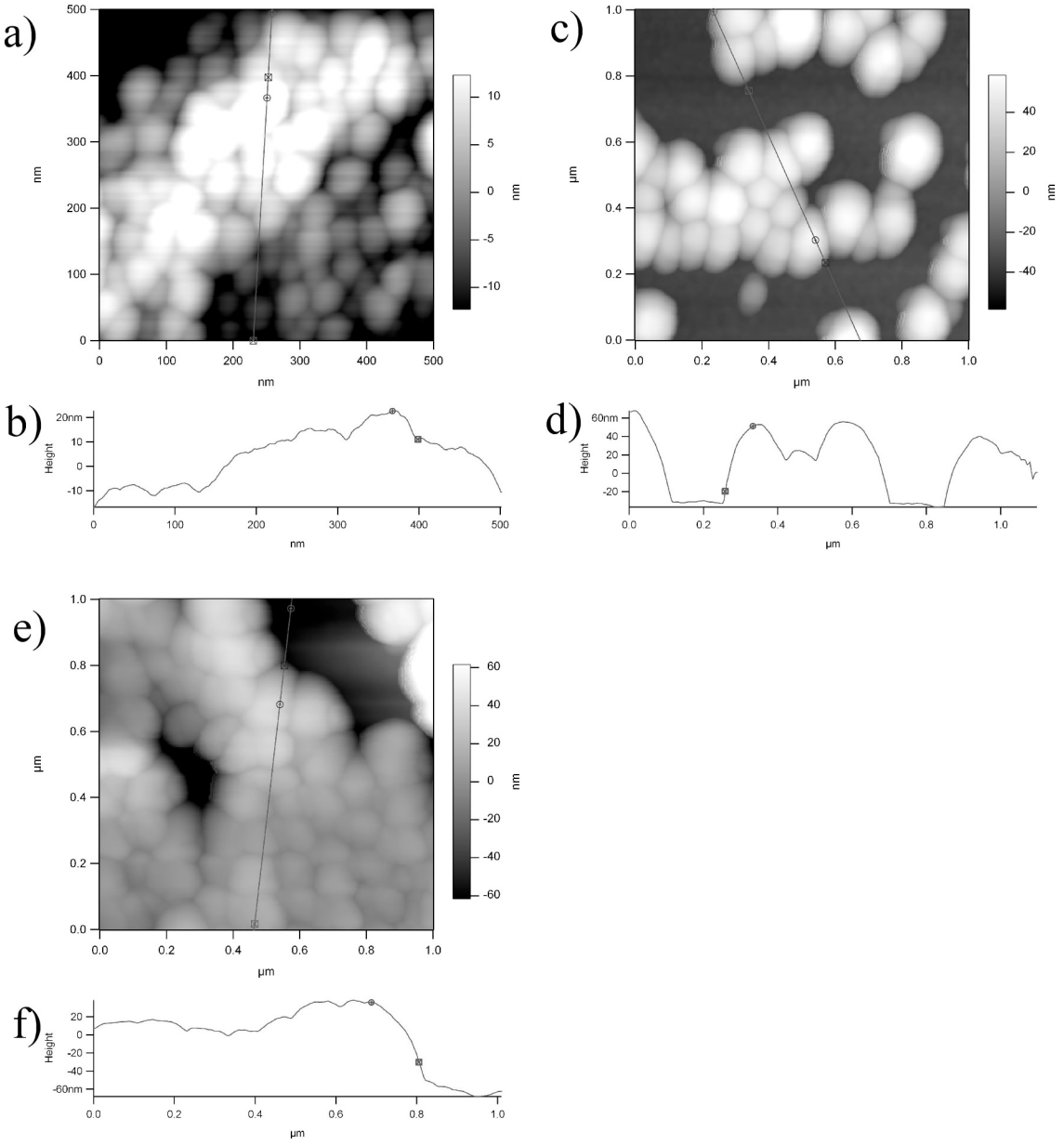
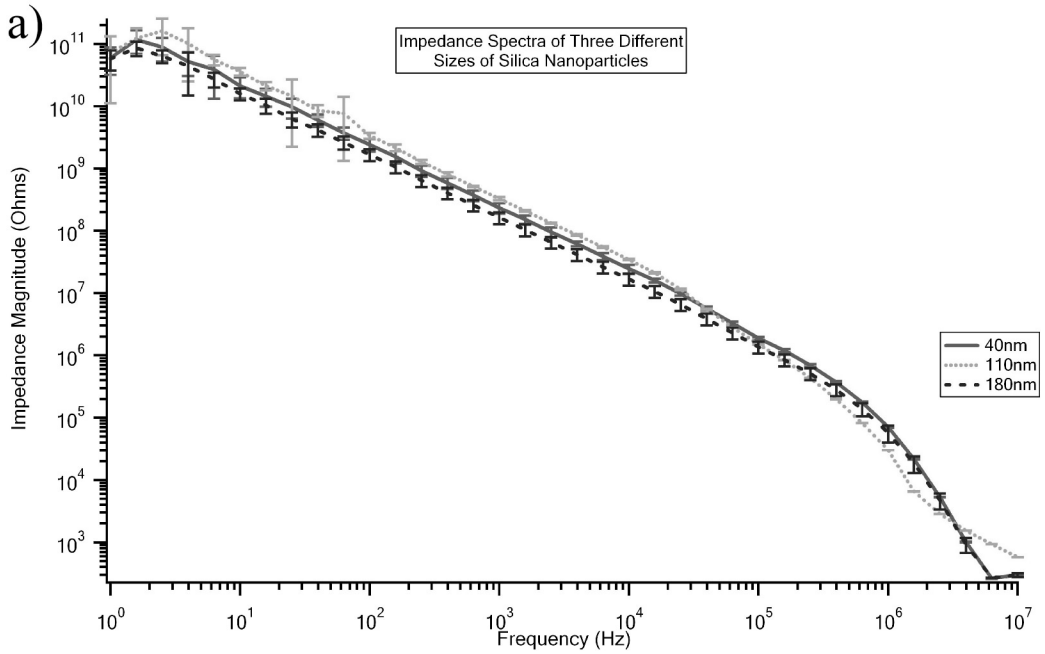


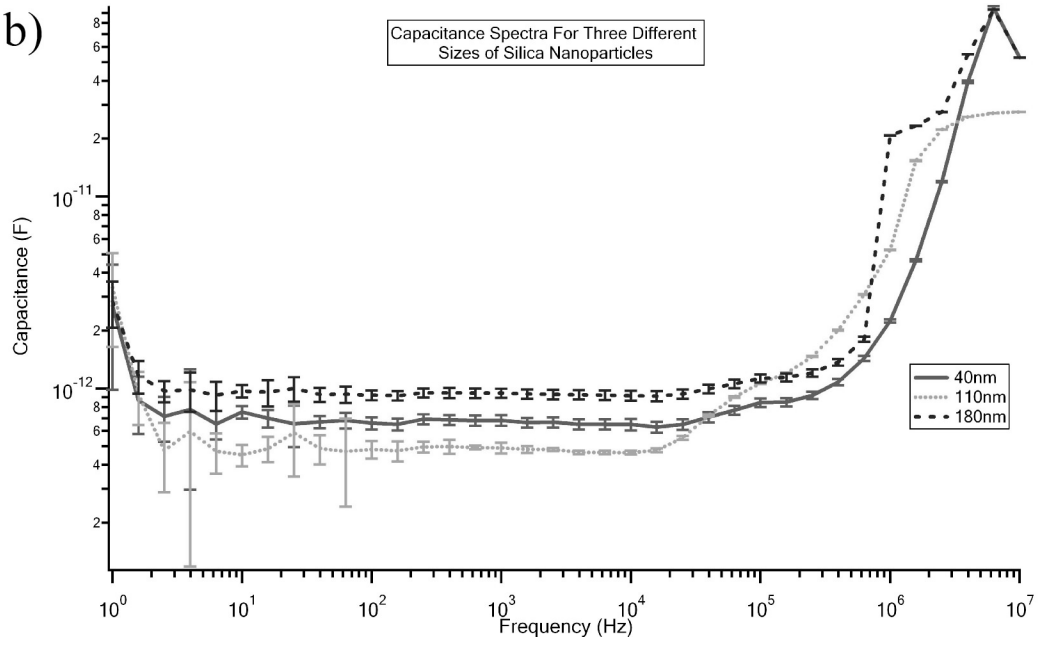
Figure 6-7. a) AFM height image and b) cross section of 60nm PMMA; c) AFM height image and d) cross section of 110nm PMMA; e) AFM height image and f) cross section of 140nm PMMA.

c) Silica

A third material was studied in three different sizes for nanoscale impedance properties. Silica nanoparticles were prepared in 40nm, 110nm, and 180nm diameters. The impedance spectra shown in Figure 6-8a appeared to have three overlapping traces,

however when a small region was magnified as in Figure 6-8c, the statistically significant differences between the spectra become visible. In this case for silica, the impedance values from highest to lowest were 110nm, 40nm, and 180nm. This order clearly did not fit with the parallel plate capacitor model, and further there was no trend between the size and the capacitance of the material. As discussed previously in the case of PMMA, it was not known whether the dielectric constant of materials can change at the nanoscale. Alternatively, there could have been different amounts of surfactant residue leftover from the drying process on the nanoparticles, and these varied amounts of surfactant molecules could have affected the impedance. The capacitance spectra of the three sizes of silica nanoparticles were shown in Figure 6-8b. Since the trends of the capacitance values for both PMMA and silica did not agree with the simplistic parallel plate capacitor model, future research should focus on identifying specifically what variables might have affected the capacitance measurement. In Figure 6-8d, the phase shift of the three different sizes of silica nanoparticles are shown. All three samples showed capacitive interactions dominating the spectra. Future work should also focus on the development of a model that would include a reasonable explanation of the trends observed in all three of these nanoscale materials studied at different sizes.


a)
Impedance Spectra of Three Different Sizes of Silica Nanoparticles
Impedance Magnitude (Ohms)
Frequency (Hz)
40nm
110nm
180nm


b)
Capacitance Spectra For Three Different Sizes of Silica Nanoparticles
Capacitance (F)
Frequency (Hz)
40nm
110nm
180nm

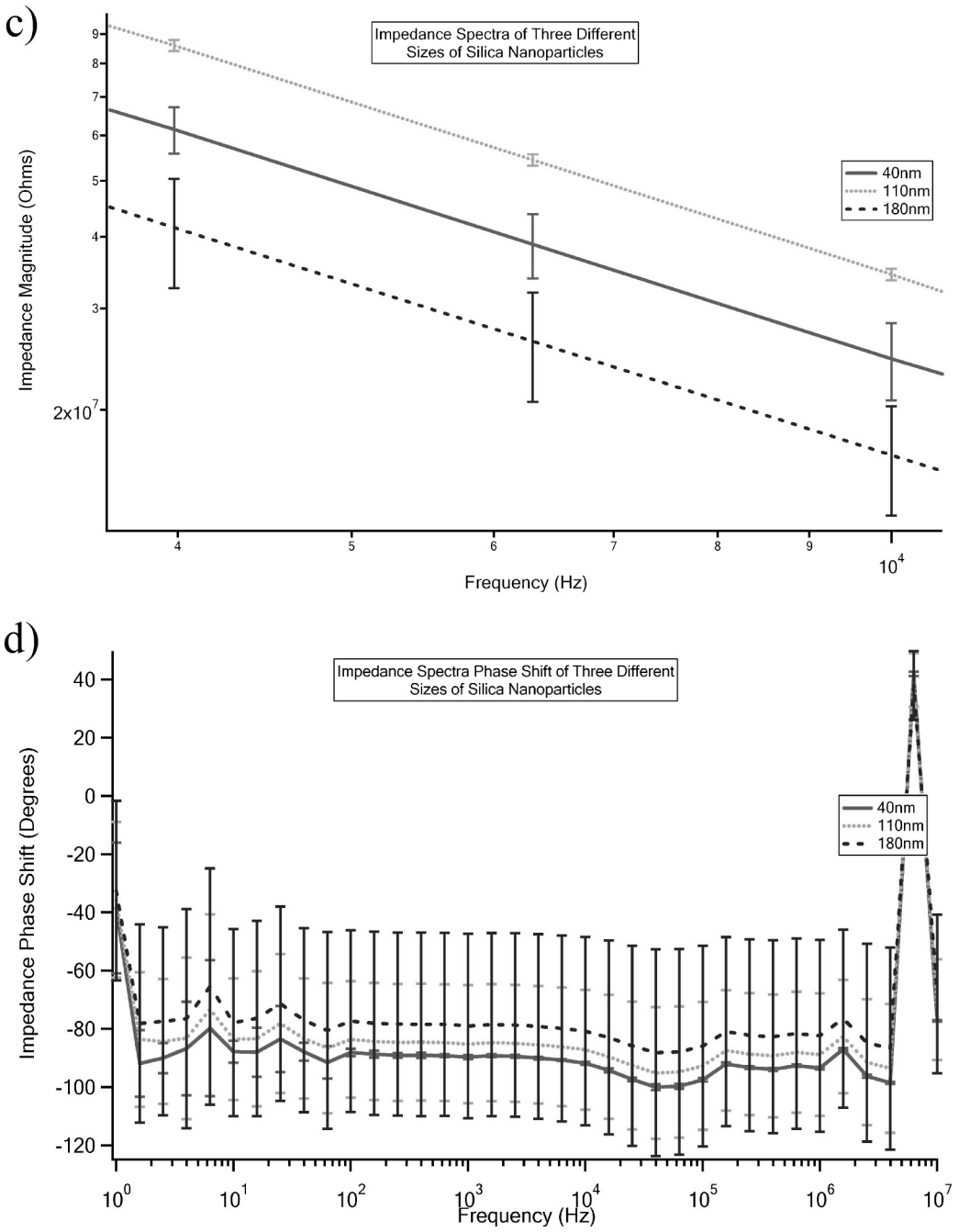


Figure 6-8. Silica nanoparticles at three different sizes. a) Impedance spectra, b) capacitance spectra, c) magnified impedance, and d) phase shift spectra.

Topographical images of the three sizes of silica nanoparticles were shown in Figure 6-9. The height image for the 40nm silica nanoparticles was shown in Figure 6-9a, while the section analysis was shown in Figure 6-9b. Both the height and width of

the nanoparticles appeared to be in good agreement with the predicted result. A packed monolayer of particles appeared to be deposited based on the height AFM image. The height image for the 110nm silica nanoparticles was shown in Figure 6-9c, with the corresponding section analysis shown in Figure 6-9d. The height image depicted single particles deposited on the surface in a well-dispersed pattern. The height and width from the section analysis corresponded well with the expected values. In Figure 6-9e, the height image for the 180nm silica nanoparticles was shown, and the corresponding section analysis was displayed in Figure 6-9f. In this height image, several particles appeared to have aggregated together, however the height from the top of the particles to the surface was in good agreement with the expected value, despite a difficult to interpret particle width.

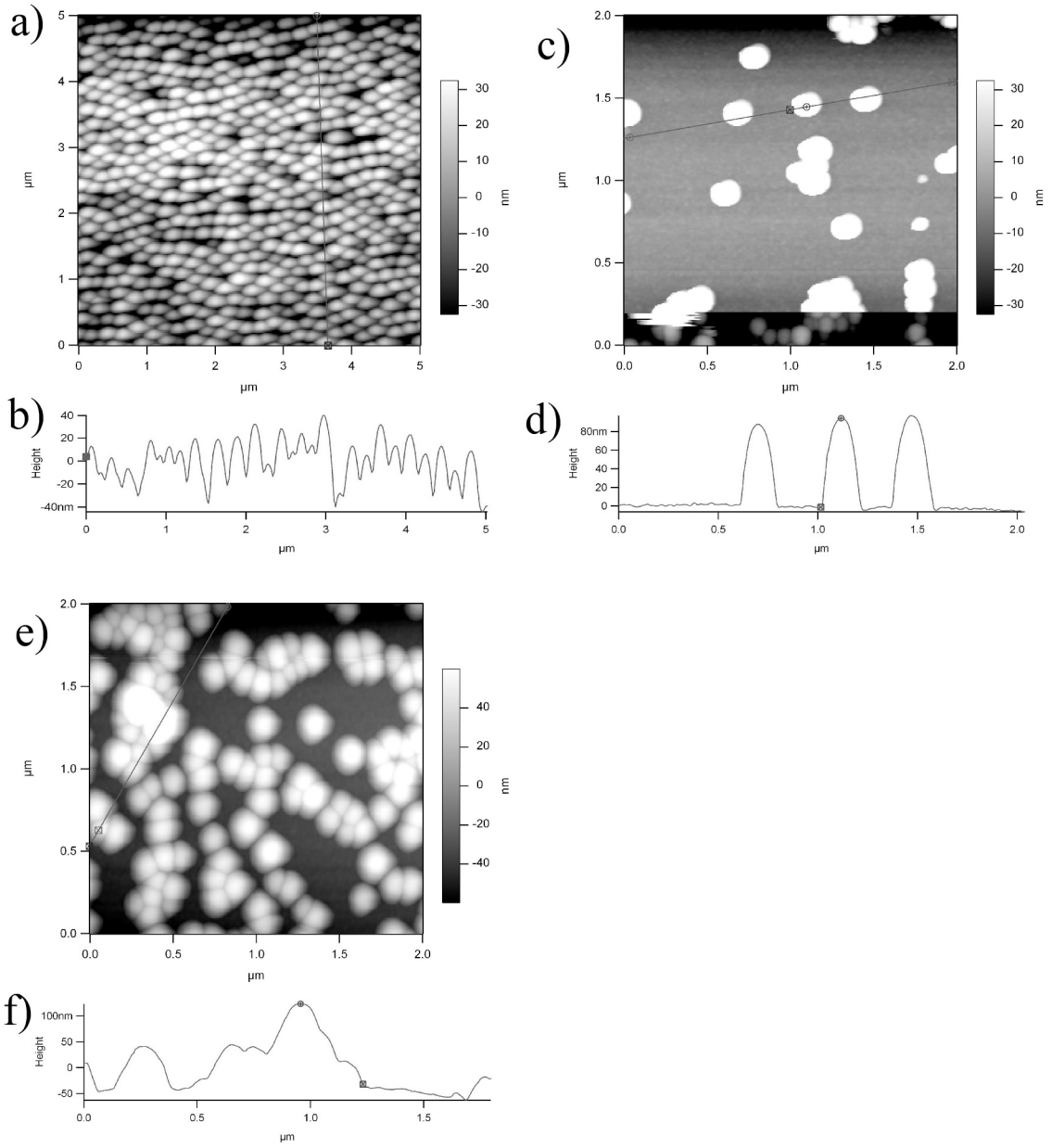


Figure 6-9. a) AFM height image and b) cross section of 40nm silica; c) AFM height image and d) cross section of 110nm silica; e) AFM height image and f) cross section of 180nm silica.

Table 6-1 summarizes the results of the three different sizes of nanoparticles for the three different materials studied. The first column lists the exact diameter in nanometers of each material studied in that grouping, and the last column describes the relationships between the three materials for that particular size grouping.

Table 6-1. Capacitance of Different Sizes of Materials

Particle Size (ps, pmma, silica) in nm	**Capacitance of PS, 10kHz**	**Capacitance of PMMA, 10kHz**	**Capacitance of Silica, 10kHz**	**Order of Capacitance**
58, 60, 40	1.14e-12	8.20e-13	6.48627e-13	ps > pmma > silica
100, 110, 110	1.03e-12	1.01e-12	4.63261e-13	ps ~ pmma >> silica
200, 140, 180	9.46763e-13	9.83e-13	9.18093e-13	pmma > ps > silica

An examination of these three materials at the smallest two size ranges revealed that the capacitance observed for similar sized nanoparticles went from polystyrene to PMMA to silica in order of highest to lowest capacitance. If one compares the parallel plate model described in equation (6-2), and approximates the same size for the nanoparticles as a constant *d* term and assumes all SPM tips have the same area in contact with the nanoparticles *A*, then a directly proportional relationship between the capacitance and dielectric constant is revealed. The dielectric constants of the three materials from highest to lowest are silica, PMMA, and polystyrene. Surprisingly, this was exactly the opposite order as would be expected in the case of bulk materials.

Previously, the parallel plate capacitor model was described. On page 235 the sphere model will be described in detail. In the case where the nanoparticle radius is smaller than the radius of curvature of the tip, the nanoparticle is small compared to the tip. An illustration of these relative sizes is shown in Figure 6-4a. However, as the AFM tip is used to study nanoparticles with radii greater than the radius of curvature of the tip,

the nanoparticle is large compared to the tip. An illustration of these relative sizes are shown in Figure 6-4b. The main noteworthy mathematical items here are the parallel plate capacitor model uses an inversely proportional relationship between the particle diameter and measured capacitance, while the sphere model uses a directly proportional relationship between the particle diameter and measured capacitance. However, there clearly should be some transition from the plate model to the sphere model where the radius of the nanoparticle is approximately the radius of the AFM tip. Figure 6-10 shows speculation as to the effect on the capacitance of the particles as a function of the particle radius is shown, incorporating the plate model in the lower radii and the spherical model in the higher radii. The dotted line in the middle of Figure 6-10 depicts the transition area from plate model to spherical model. The capacitance is not shown as function of nanoparticle radius R in this region due to the uncertainty of which model might have a more dominant effect.

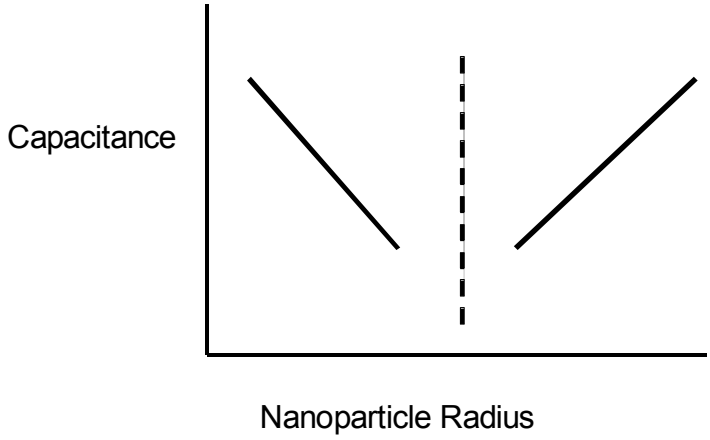


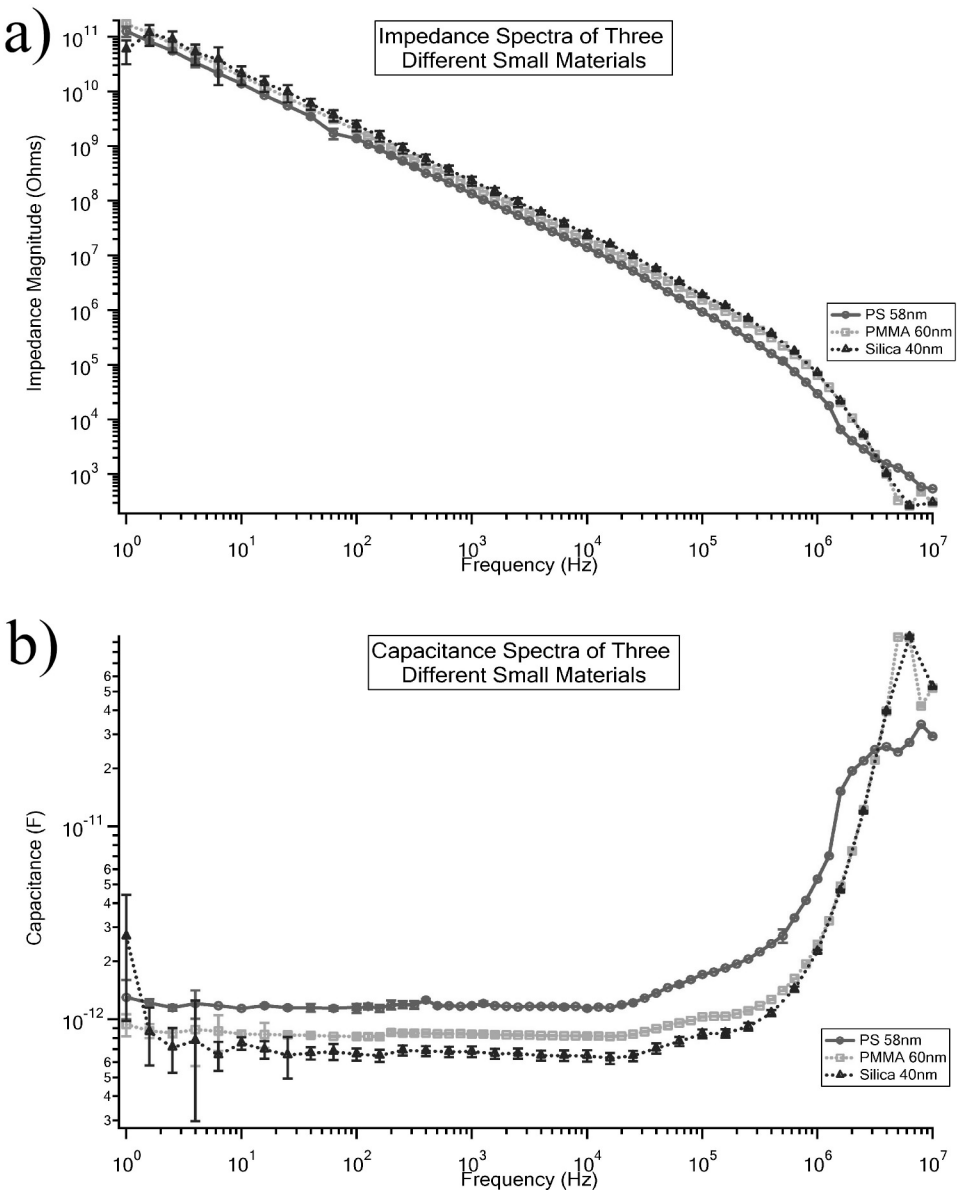
Figure 6-10. Change from plate to sphere model. C is a function of the inverse of R until the transition at the dotted line, then C becomes a function of R.

One reason for this discrepancy could be that the dielectric constant of materials changes at the nanoscale, however detailed discussion of this idea will come later in page

235. Another explanation for this discrepancy would have been the variations in area of the SPM tips if using the parallel plate model. Since each SPM tip was manufactured to be within certain size ranges, there was inherent variability in the area that was at the apex of the tip and being assumed to be one of the two parallel plates. While variations in contact force could have changed the area of the tip in contact with the sample, this consideration was removed by using a constant contact force from sample to sample.

When comparing the three different materials, one would expect to see the dielectric constant of the material provide a proportional relationship to the capacitance as seen in equation (6-2), assuming the particles were the same size. In Figures 6-11, 6-12, and 6-13, the trends of three different materials of approximately small, medium, and large sizes, respectively, are compared.

In Figure 6-11, different materials were compared with sizes of 60nm PMMA, 58nm for polystyrene, and 40nm silica. In Figure 6-11a, the impedance traces are hard to distinguish, however in Figure 6-11c the highest to lowest impedance was silica, PMMA, and polystyrene respectively. In Figure 6-11b, the three capacitance values from highest to lowest were polystyrene, PMMA, and silica. This was the inverse trend compared to the impedance, as would be expected by the inverse relationship between the impedance and capacitance. This trend is opposite of that which is expected from the bulk dielectric constants and the parallel plate capacitor model. In Figure 6-11d, the phase shift spectra shows that capacitive effects dominate the spectra.


a)
Impedance Spectra of Three Different Small Materials
Impedance Magnitude (Ohms)
Frequency (Hz)
PS 58nm
PMMA 60nm
Silica 40nm
b)
Capacitance Spectra of Three Different Small Materials
Capacitance (F)
Frequency (Hz)
PS 58nm
PMMA 60nm
Silica 40nm

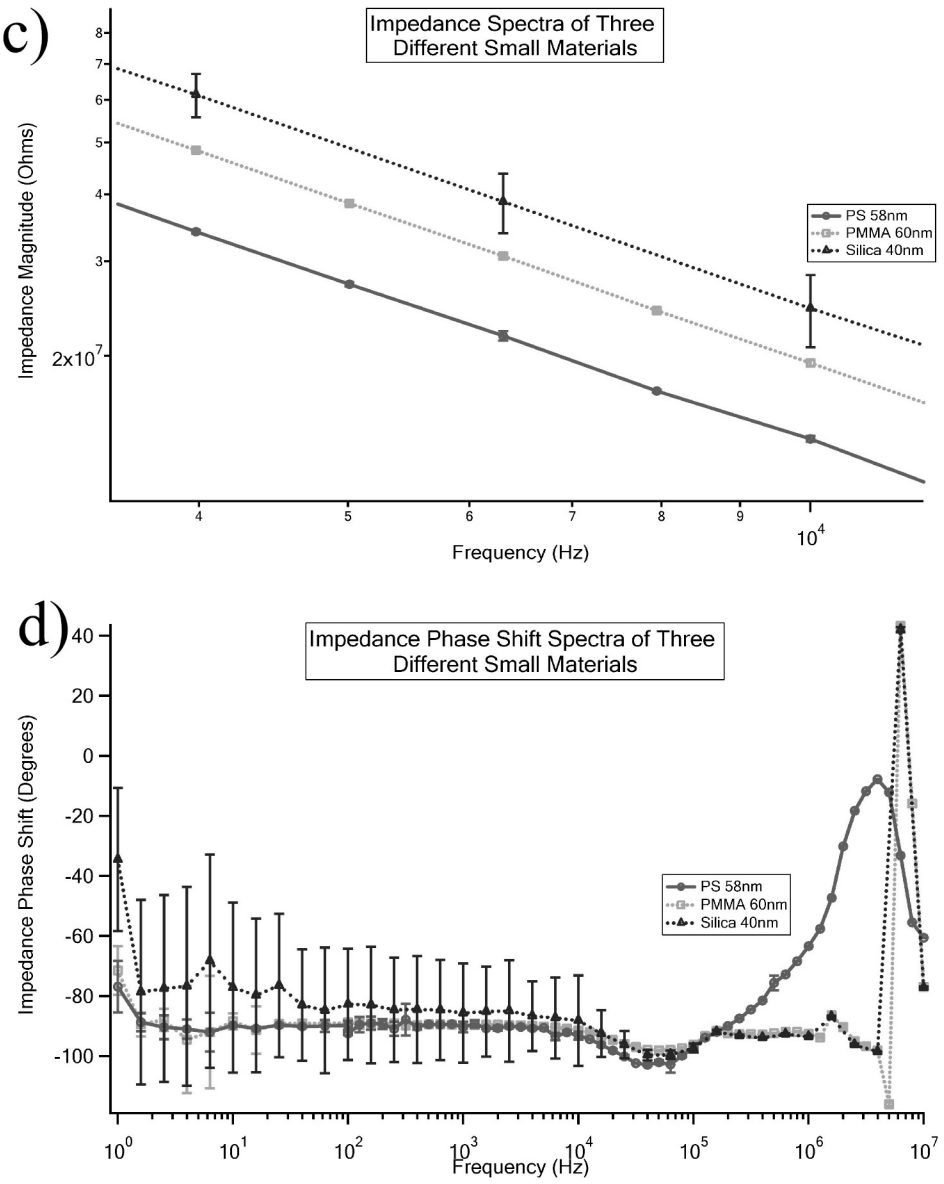
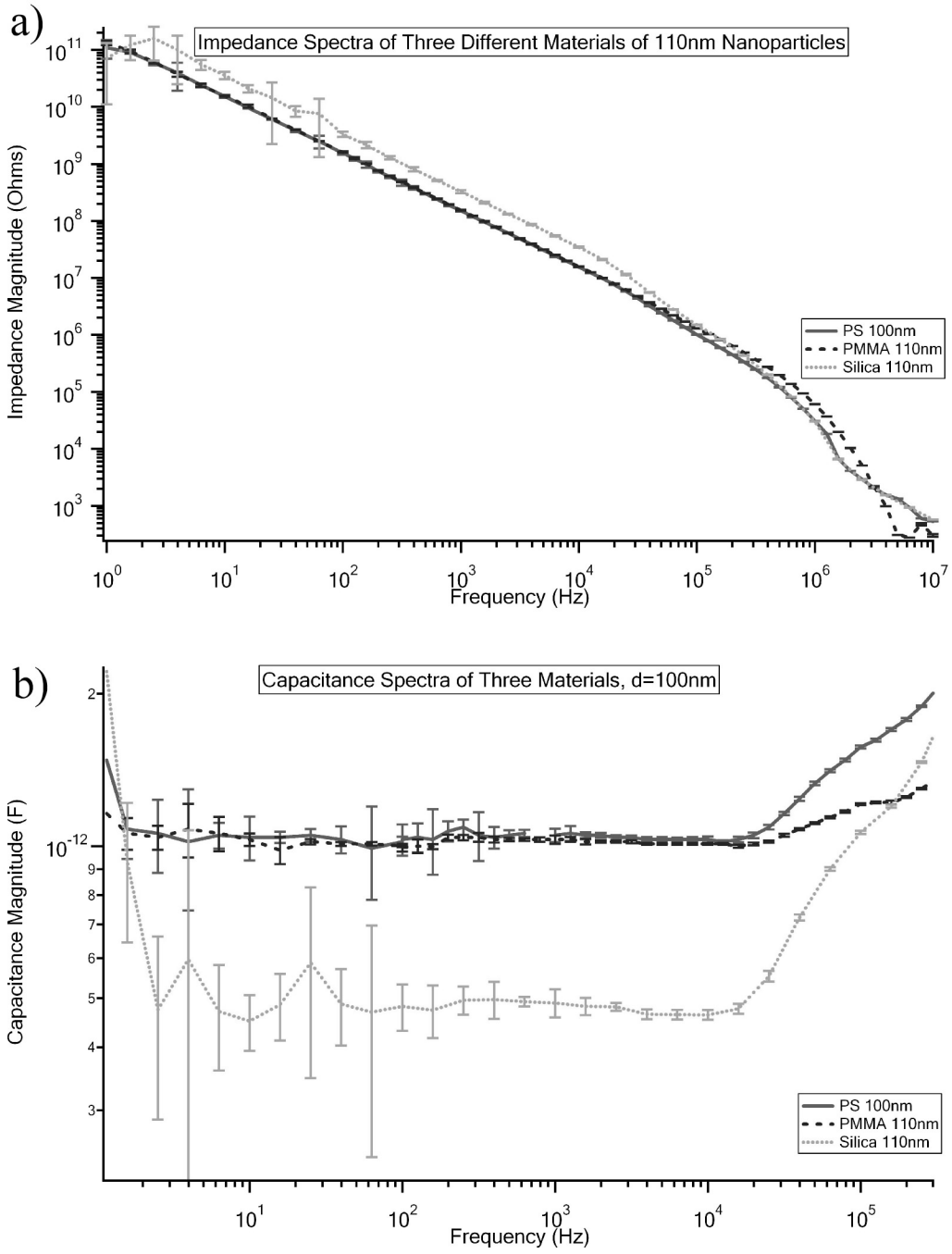


Figure 6-11. a) impedance, b) capacitance, c) magnified impedance, and d) phase shift spectra of smaller nanoparticles of three different materials.

In Figure 6-12, different materials were compared with sizes of 100nm for polystyrene, 110nm for PMMA, and 110nm for silica. In Figure 6-12a, silica had a much higher impedance than either polystyrene or PMMA, which were almost completely overlaid. Examination of the magnified impedance image in Figure 6-12c confirmed this approximation. In Figure 6-12b, the silica had a correspondingly lower capacitance value

than the nearly identical values for polystyrene and PMMA. If the dielectric constant of the materials at the nanoscale (approximately 100 nanometers diameter) followed the same trend as reported for bulk materials and mentioned on page 191, then the predicted order of capacitance values from highest to lowest would be silica, pmma, and then polystyrene. Unfortunately, the dielectric constant measurements reported provided ranges of values rather than exact values, leaving a large degree of uncertainty.


a)
Impedance Spectra of Three Different Materials of 110nm Nanoparticles
Impedance Magnitude (Ohms)
Frequency (Hz)
PS 100nm
PMMA 110nm
Silica 110nm
b)
Capacitance Spectra of Three Materials, d=100nm
Capacitance Magnitude (F)
Frequency (Hz)
PS 100nm
PMMA 110nm
Silica 110nm

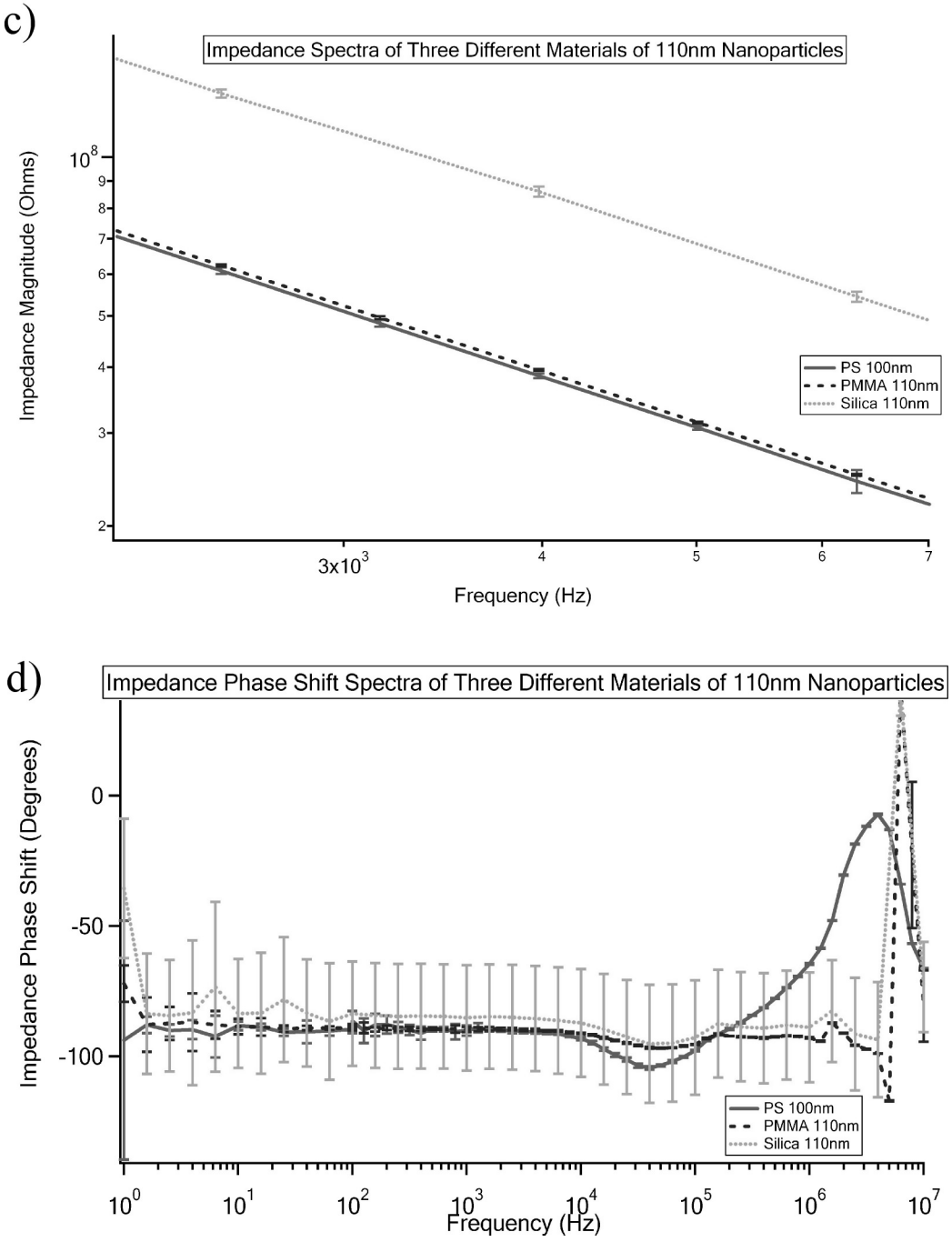
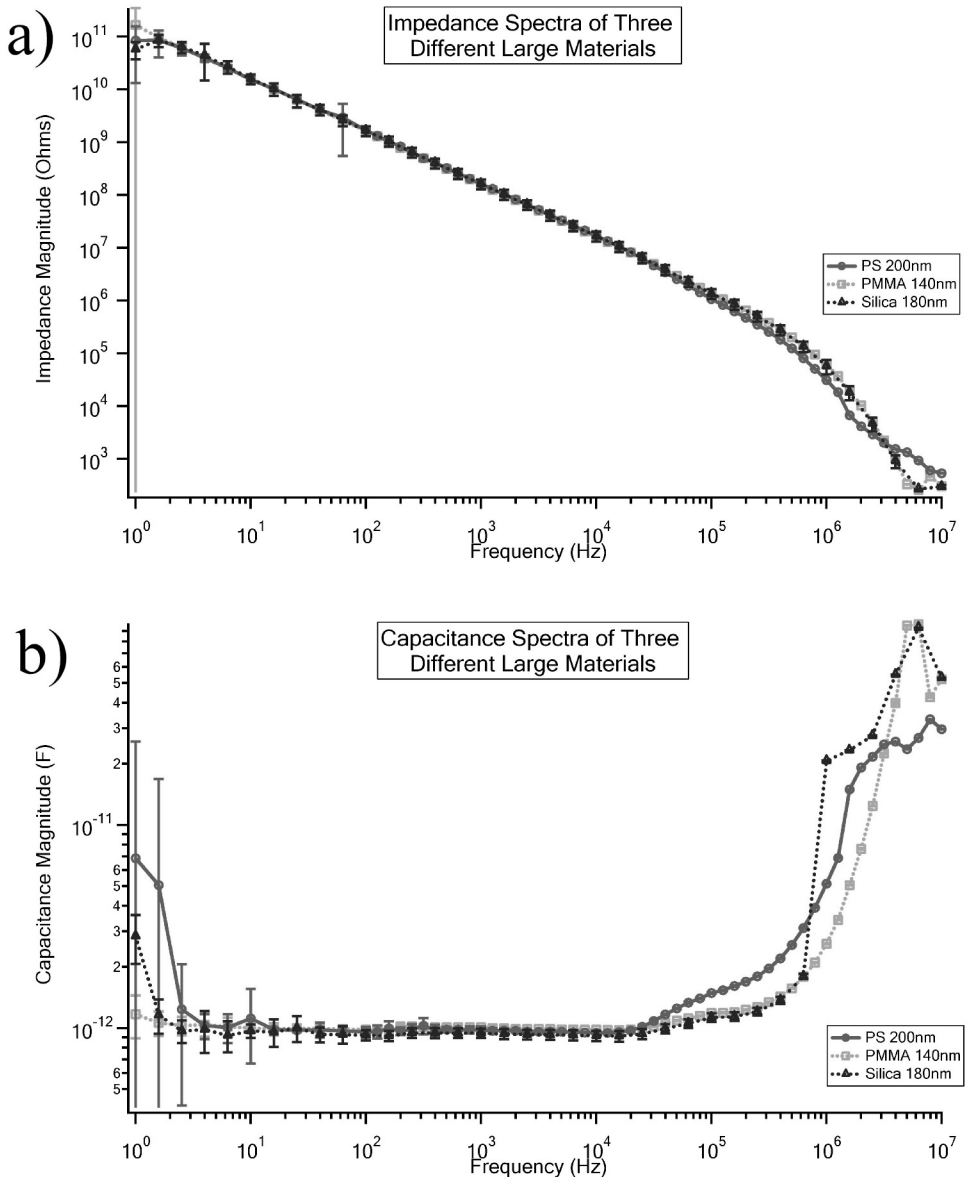


Figure 6-12. a) Impedance, b) capacitance, c) magnified impedance, and d) phase shift spectra comparison of different materials approximately 100nm in diameter. Solid trace = 100nm PS, dashed trace = 110nm PMMA, dotted trace = 110nm silica.

In Figure 6-13, three different materials of large nanoparticles are compared. In Figure 6-13a, the impedance spectra of 200nm polystyrene, 180nm silica, and 140nm

PMMA are compared. The impedance spectra are hard to distinguish, however in the magnified impedance spectra shown in Figure 6-13c, it is possible to see that the order of materials from highest to lowest impedance is still indistinguishable. The phase shift spectra, shown in Figure 6-13d, indicate that capacitive effects are dominating the impedance spectra. The capacitance spectra in Figure 6-13b shows the three larger sized nanoparticles do not show a statistically significant difference in capacitance between the three materials.


a)
Impedance Spectra of Three Different Large Materials
Impedance Magnitude (Ohms)
Frequency (Hz)
PS 200nm
PMMA 140nm
Silica 180nm
b)
Capacitance Spectra of Three Different Large Materials
Capacitance Magnitude (F)
Frequency (Hz)
PS 200nm
PMMA 140nm
Silica 180nm

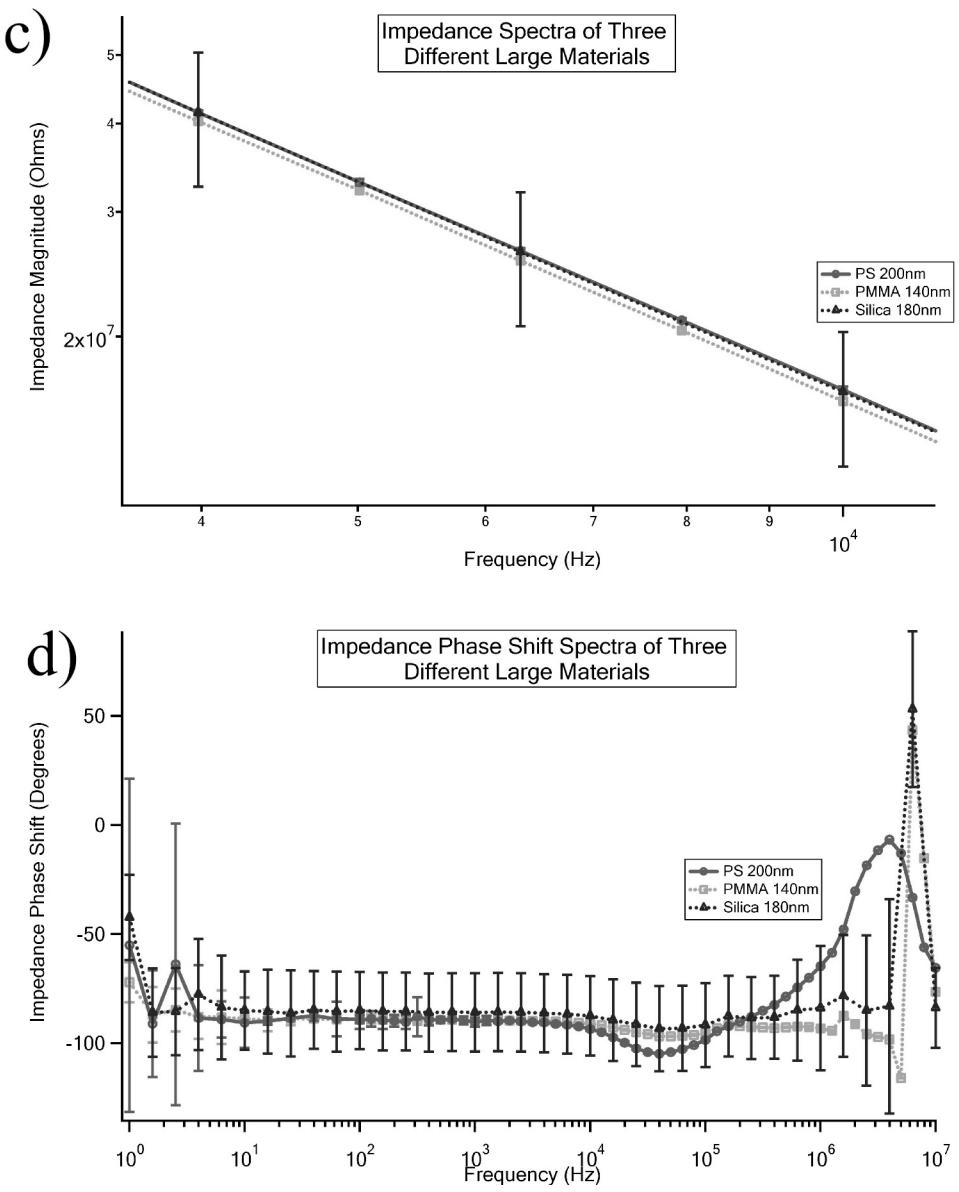
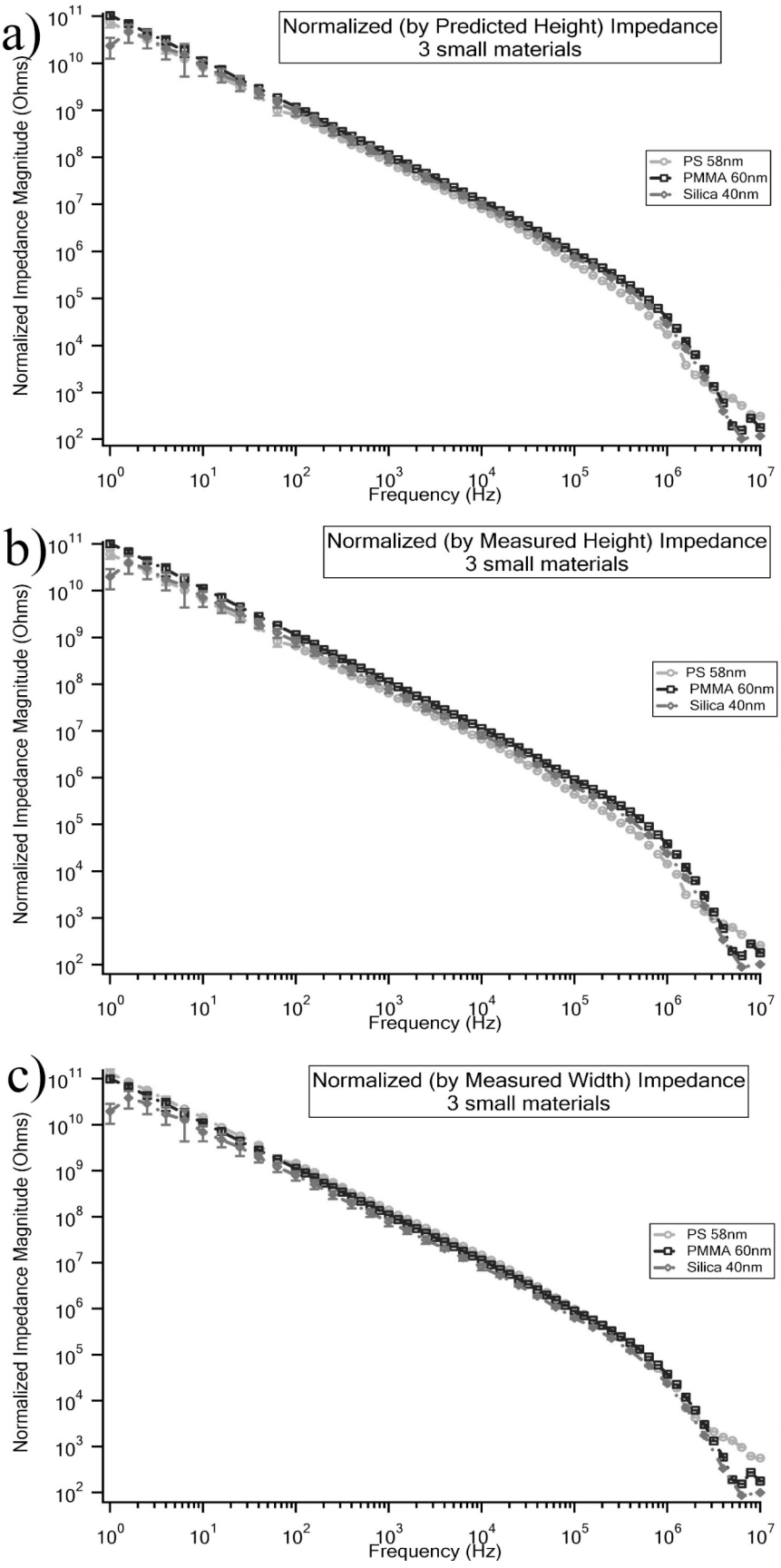


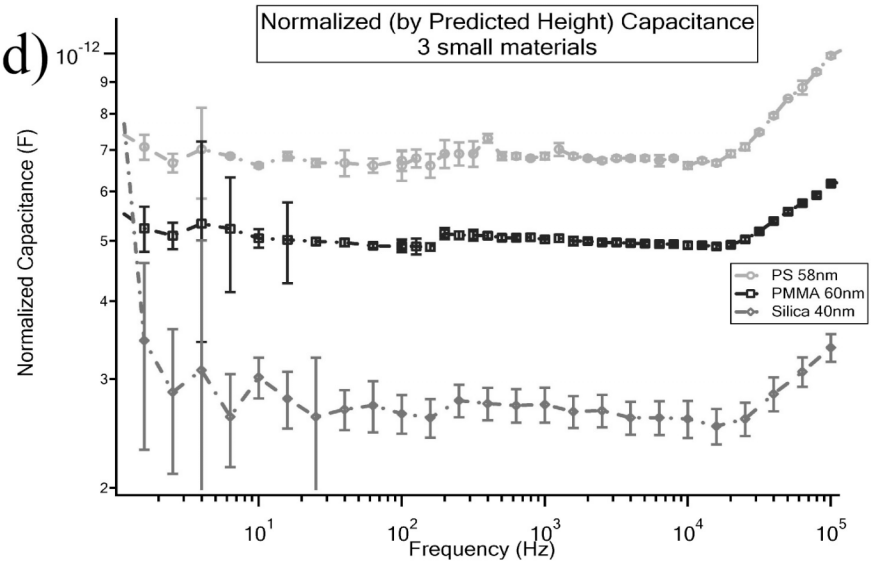
Figure 6-13. a) impedance, b) capacitance, c) magnified impedance, and d) phase shift spectra of three different materials of large nanoparticles size.

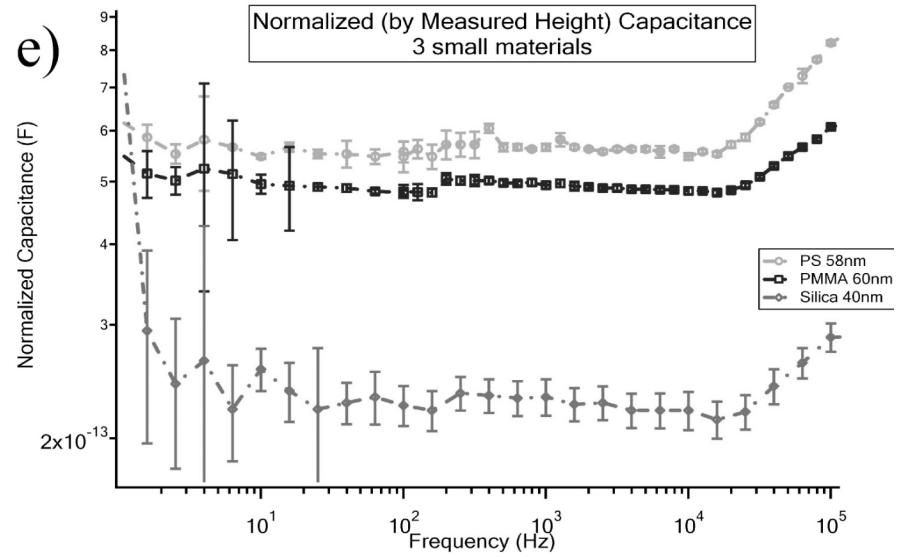
In Figures 6-14, 6-15, and 6-16 the impedance and capacitance plots of the three different materials are shown normalized with respect to three different parameters. In the first normalization, the predicted height or nanoparticle diameter is used to compare the relative dielectric constants between the materials. In the second normalization, the height measured from the AFM section analysis of example nanoparticles is displayed.

In the third normalization, the nanoparticle diameter as measured from the width of the AFM section analysis is used to normalize the impedance and capacitance spectra of the three different materials to compare their relative dielectric constants. While all three methods of data normalization are shown in this thesis for comparison, the normalization method that is most likely the closest approximation is that of the measured AFM height in the section analysis. This is most accurate if the parallel plate capacitor model is envisioned, since the distance between the two plates is accurately measured by the AFM.

In Figure 6-14, the normalized data for the three different materials of small nanoparticles are shown. In the three normalized sets of impedance spectra, it is hard to distinguish the different materials in Figures 6-14a, 6-14b, and 6-14c. In the capacitance spectra, normalization by the three different methods produced the same trend between materials, with polystyrene, PMMA, silica ranking highest to lowest normalized capacitance. Figures 6-14d, 6-14e, and 6-14f are also measures of the relative dielectric constants between the materials.


a)
Normalized (by Predicted Height) Impedance
3 small materials
Normalized Impedance Magnitude (Ohms)
Frequency (Hz)
PS 58nm
PMMA 60nm
Silica 40nm
b)
Normalized (by Measured Height) Impedance
3 small materials
Normalized Impedance Magnitude (Ohms)
Frequency (Hz)
PS 58nm
PMMA 60nm
Silica 40nm
c)
Normalized (by Measured Width) Impedance
3 small materials
Normalized Impedance Magnitude (Ohms)
Frequency (Hz)
PS 58nm
PMMA 60nm
Silica 40nm


d)
Normalized (by Predicted Height) Capacitance
3 small materials
Normalized Capacitance (F)
Frequency (Hz)
PS 58nm
PMMA 60nm
Silica 40nm


e)
Normalized (by Measured Height) Capacitance
3 small materials
Normalized Capacitance (F)
Frequency (Hz)
PS 58nm
PMMA 60nm
Silica 40nm

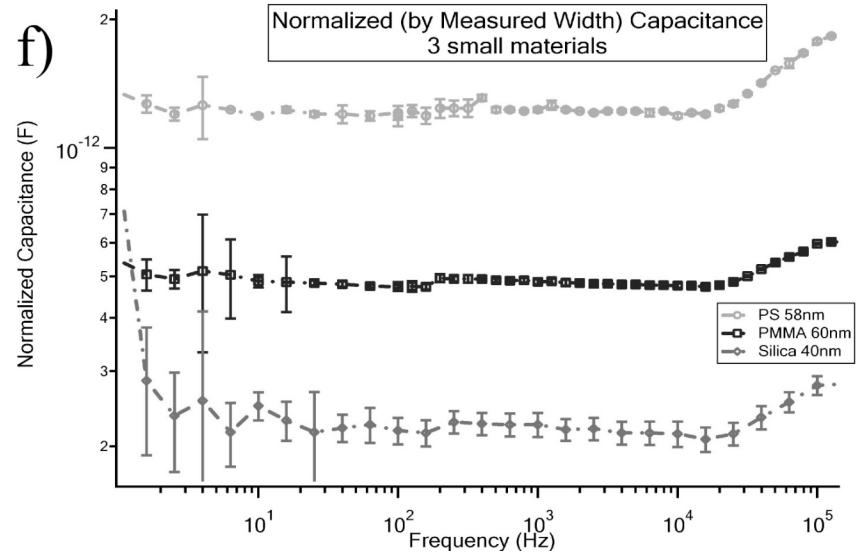
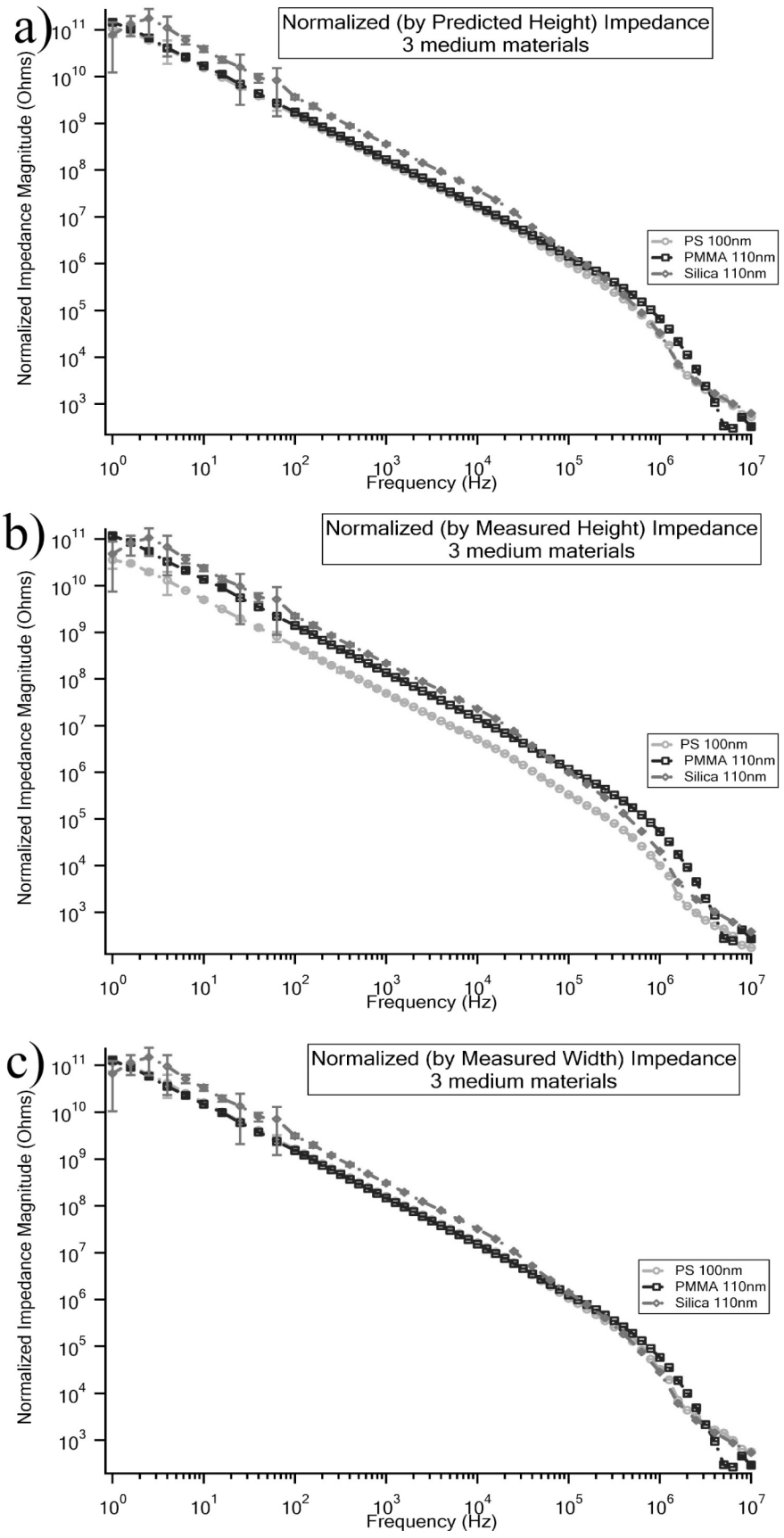
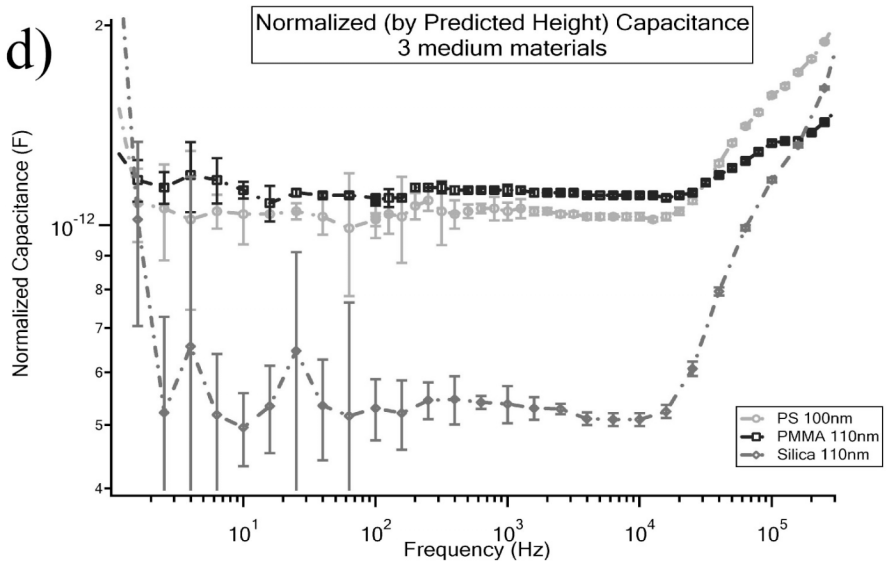
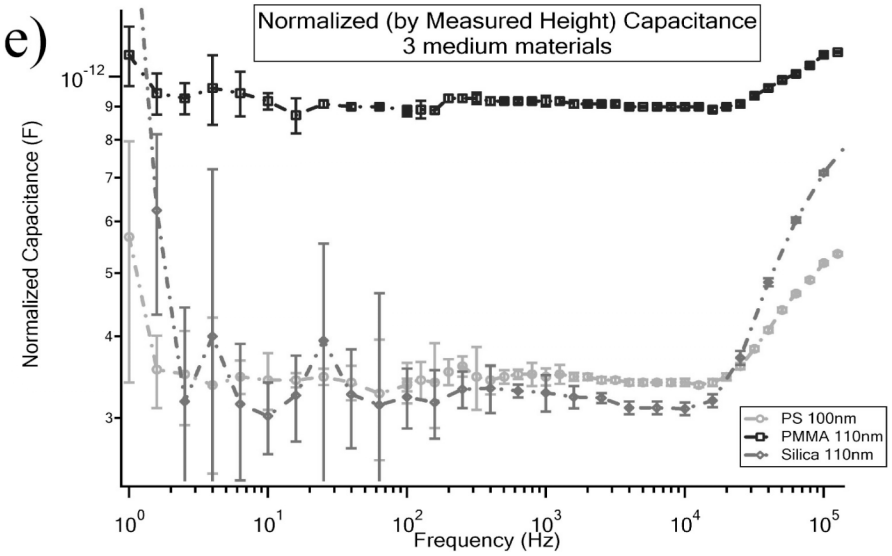

f)
Normalized (by Measured Width) Capacitance
3 small materials
Normalized Capacitance (F)
Frequency (Hz)
PS 58nm
PMMA 60nm
Silica 40nm

Figure 6-14. Impedance spectra normalized by a) predicted height, b) measured height, and c) measured width of nanoparticles. Capacitance spectra normalized by d) predicted height, e) measured height, and f) measured width of three different materials of small nanoparticles. Silica = 40nm, PMMA = 60nm, PS = 58nm.

In Figure 6-15, the impedance and capacitance spectra of three different materials of medium sized nanoparticles are normalized by three different values. In the three normalized sets of impedance spectra, it is hard to distinguish the different materials in Figures 6-15a, 6-15b, and 6-15c. In the capacitance spectra, normalization by the three different methods produced different trends between materials. In Figure 6-15d, normalization by the predicted height, and Figure 6-15e, normalization by the measured height, the order of capacitance values from highest to lowest material was PMMA, polystyrene, and silica. However, in Figure 6-15f, normalization by the measured width, the trend matched that of Figure 6-14 and all three of the small nanoparticle methods of normalization, with polystyrene, PMMA, silica ranking highest to lowest in order of normalized capacitance. Similarly to Figure 6-14, Figures 6-15d, 6-15e, and 6-15f are also measures of the relative dielectric constants between the materials. It is not immediately clear why the different methods of normalization would yield different relative dielectric constant orders. It is also not immediately clear why different sizes of nanoparticles would yield different relative dielectric constant orders. However, one reason that could offer an explanation for both observations is the uncertainty of nanoscale electrical properties, and if there is some size dependence of the dielectric constant at the nanoscale.


a)
Normalized (by Predicted Height) Impedance
3 medium materials
Normalized Impedance Magnitude (Ohms)
Frequency (Hz)
PS 100nm
PMMA 110nm
Silica 110nm
b)
Normalized (by Measured Height) Impedance
3 medium materials
Normalized Impedance Magnitude (Ohms)
Frequency (Hz)
PS 100nm
PMMA 110nm
Silica 110nm
c)
Normalized (by Measured Width) Impedance
3 medium materials
Normalized Impedance Magnitude (Ohms)
Frequency (Hz)
PS 100nm
PMMA 110nm
Silica 110nm


d)
Normalized (by Predicted Height) Capacitance
3 medium materials
Normalized Capacitance (F)
Frequency (Hz)
PS 100nm
PMMA 110nm
Silica 110nm


e)
Normalized (by Measured Height) Capacitance
3 medium materials
Normalized Capacitance (F)
Frequency (Hz)
PS 100nm
PMMA 110nm
Silica 110nm

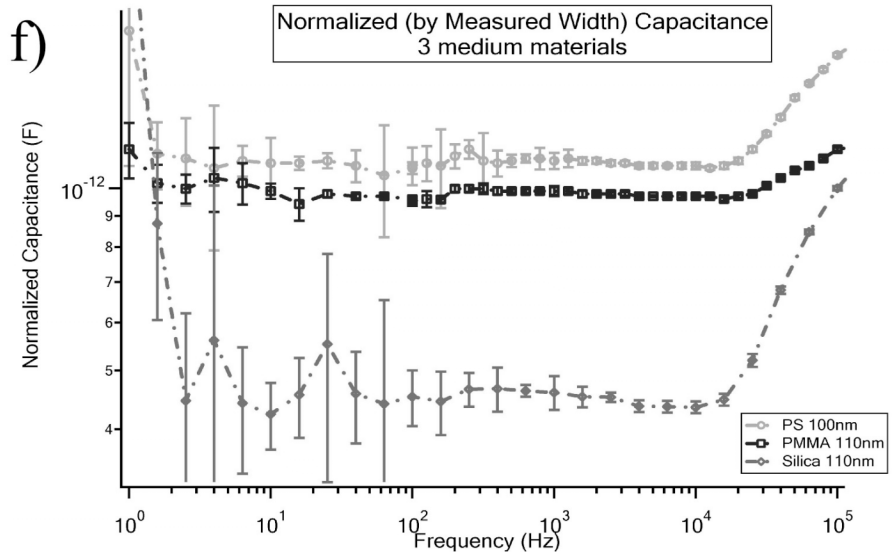
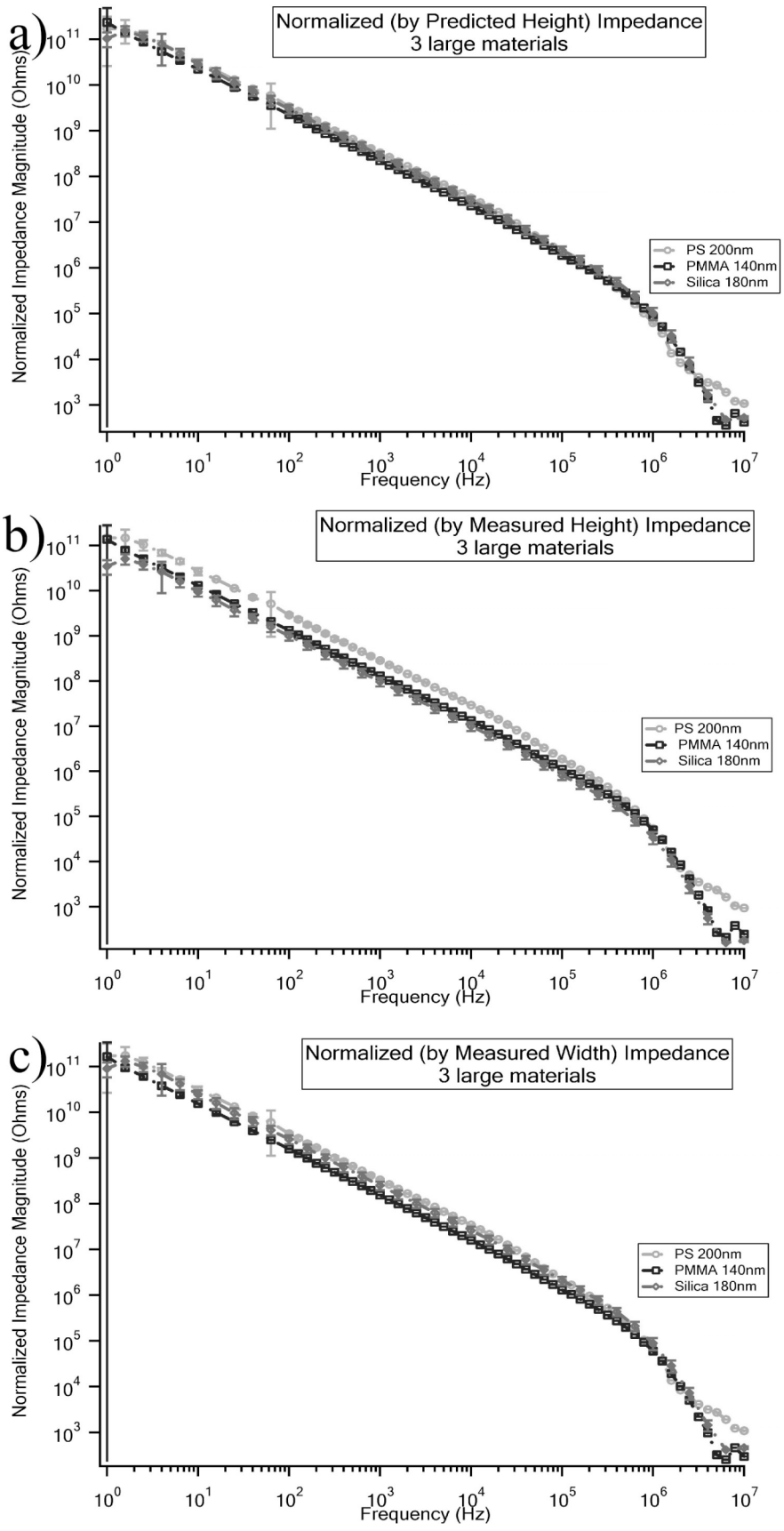
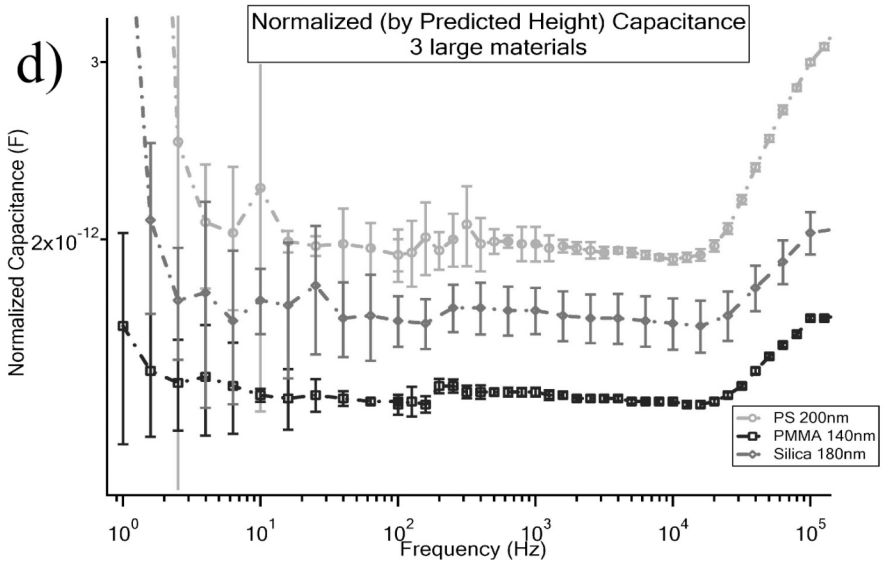
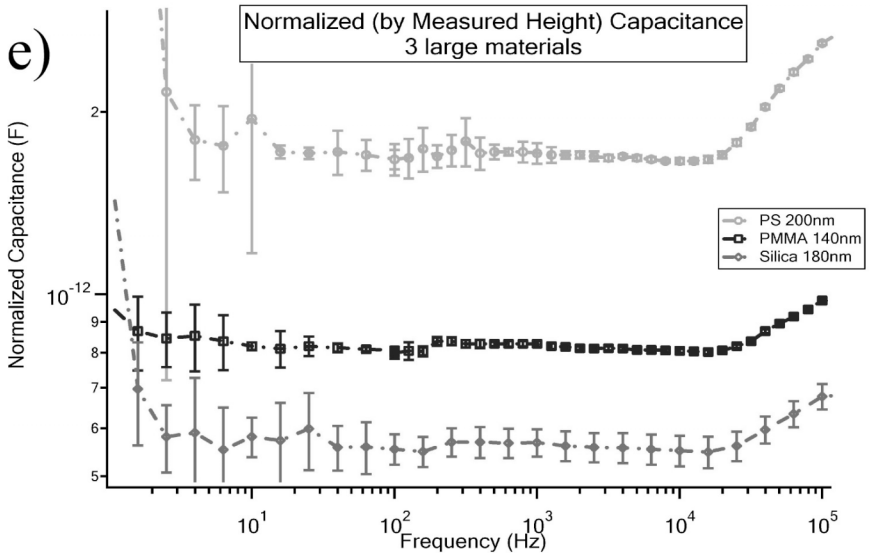

f)
Normalized (by Measured Width) Capacitance
3 medium materials
Normalized Capacitance (F)
Frequency (Hz)
PS 100nm
PMMA 110nm
Silica 110nm

Figure 6-15. Impedance spectra normalized by a) predicted height, b) measured height, and c) measured width of nanoparticles. Capacitance spectra normalized by d) predicted height, e) measured height, and f) measured width of three different materials of medium nanoparticles. Silica = 110nm, PMMA = 110nm, PS = 100nm.

In Figure 6-16, the impedance and capacitance spectra of three different materials of larger sized nanoparticles are normalized by three different values. In the three normalized sets of impedance spectra, it is hard to distinguish the different materials in Figures 6-16a, 6-16b, and 6-16c. In the capacitance spectra, normalization by the three different methods produced different trends between materials. In Figure 6-16d, normalization by predicted height, and Figure 6-16f, normalization by measured width, the order of highest to lowest capacitance materials was polystyrene, silica, and PMMA. However, in Figure 6-16e, normalization by measured height, the trend agreed with Figure 6-14 and Figure 6-15f, with polystyrene, PMMA, silica ranking highest to lowest normalized capacitance. While it is not immediately clear why there are differences between all three sizes of materials and methods of normalization, another reason could lie in the discrepancy between measured height, measured width, and predicted height. Compounded by the previously mentioned unknown and perhaps nanoscale size dependence of dielectric constants, it is not possible at this time to precisely determine the exact dielectric constants of the nanoparticles.


a)
Normalized (by Predicted Height) Impedance
3 large materials
Normalized Impedance Magnitude (Ohms)
Frequency (Hz)
PS 200nm
PMMA 140nm
Silica 180nm
b)
Normalized (by Measured Height) Impedance
3 large materials
Normalized Impedance Magnitude (Ohms)
Frequency (Hz)
PS 200nm
PMMA 140nm
Silica 180nm
c)
Normalized (by Measured Width) Impedance
3 large materials
Normalized Impedance Magnitude (Ohms)
Frequency (Hz)
PS 200nm
PMMA 140nm
Silica 180nm


d)
Normalized (by Predicted Height) Capacitance
3 large materials
Normalized Capacitance (F)
3
2x10^-12
PS 200nm
PMMA 140nm
Silica 180nm
10^0
10^1
10^2
10^3
10^4
10^5
Frequency (Hz)


e)
Normalized (by Measured Height) Capacitance
3 large materials
Normalized Capacitance (F)
2
10^-12
9
8
7
6
5
PS 200nm
PMMA 140nm
Silica 180nm
10^1
10^2
10^3
10^4
10^5
Frequency (Hz)

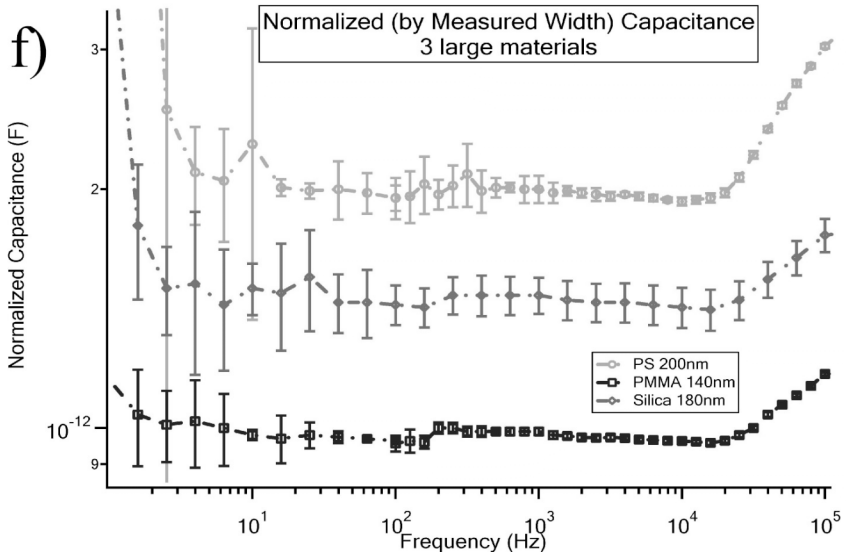

f)
Normalized (by Measured Width) Capacitance
3 large materials
Normalized Capacitance (F)
3
2
10^-12
9
PS 200nm
PMMA 140nm
Silica 180nm
10^1
10^2
10^3
10^4
10^5
Frequency (Hz)

Figure 6-16. Impedance spectra normalized by a) predicted height, b) measured height, and c) measured width of nanoparticles. Capacitance spectra normalized by d) predicted height, e) measured height, and f) measured width of three different materials of large nanoparticles. Silica = 180nm, PMMA = 140nm, PS = 202nm.

Table 6-2 summarizes the normalized capacitance values, for all three sizes of all three materials, by each of the three different methods of normalization. The three methods of normalization were predicted nanoparticle height, measured nanoparticle height, and measured nanoparticle width. The data shown in Table 6-2 were measured at 10 kHz.

Table 6-2. Normalized Capacitance values, measured at 10kHz.

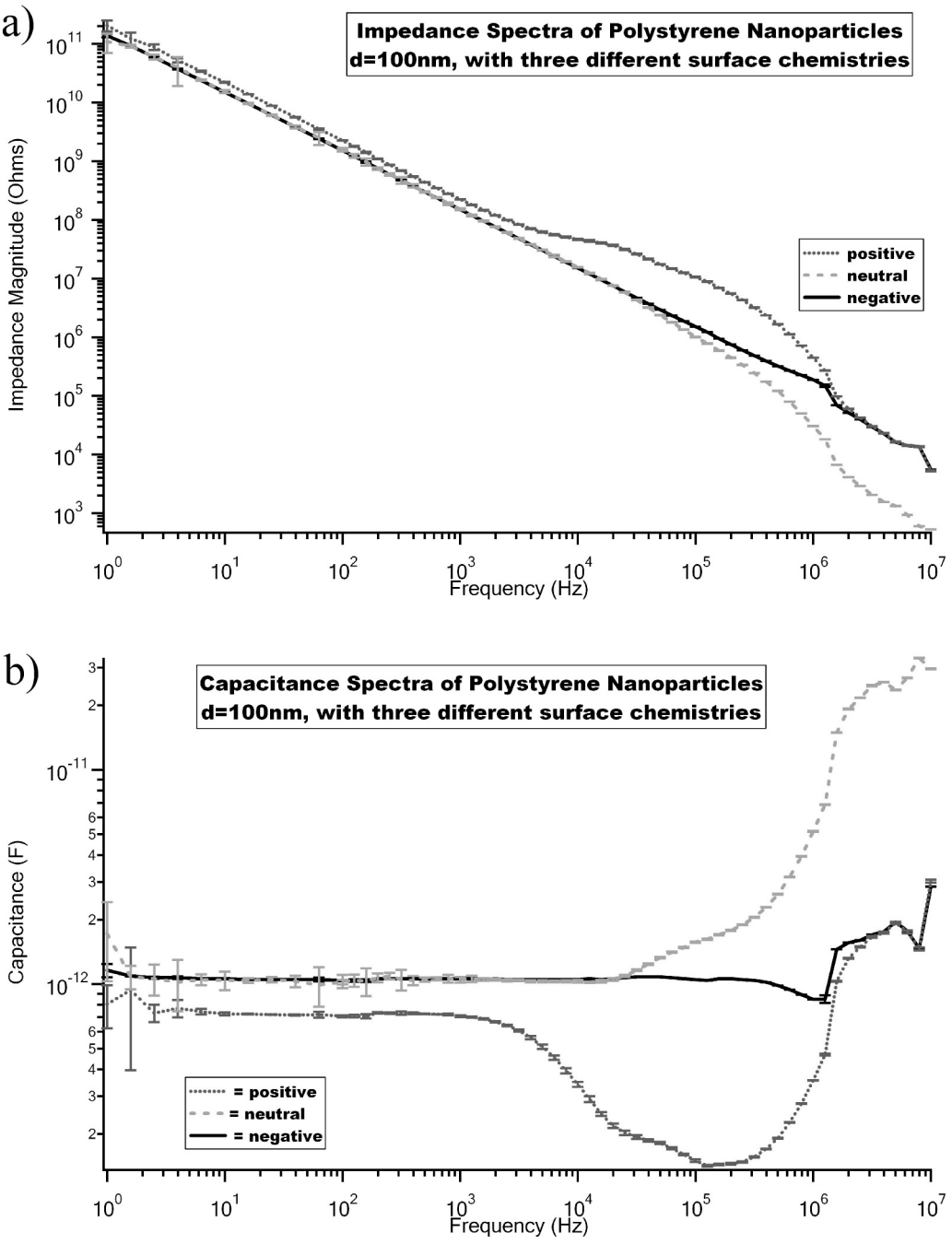
Material	Measured Capacit-ance	Normalized Capacitance by Predicted Height	Normalized Capacitance by Measured Height	Normalized Capacitance by Measured Width
PS 58nm	1.14e-12	6.61e-13	5.47e-13	1.19e-12
PS 100nm	1.03e-12	1.03e-12	3.40e-13	1.09e-12
PS 200nm	9.47e-13	1.91e-12	1.66e-12	1.93e-12
PMMA 60nm	8.20e-13	4.92e-13	4.84e-13	4.76e-13
PMMA 110nm	1.01e-12	1.11e-12	8.99e-13	9.70e-13
PMMA 140nm	9.83e-13	1.38e-12	8.06e-13	9.63e-13
Silica 40nm	6.49e-13	2.59e-13	2.21e-13	2.14e-13
Silica 110nm	4.63e-13	5.10e-13	3.10e-13	4.35e-13
Silica 180nm	9.18e-13	1.65e-12	5.51e-13	1.42e-12

3. AC IMPEDANCE STUDIES OF POLYSTYRENE AND SILICA NANOPARTICLES WITH DIFFERENT SURFACE CHEMISTRIES

To further examine this concept of different dielectric constants varying the impedance and capacitance spectra, modifications were made to the surface chemistry of polystyrene and silica nanoparticles in an attempt to change the dielectric constant of these materials. If the parallel plate capacitor model were used as described in equation 6-2, there was a directly proportional relationship between the dielectric constant of the materials and their capacitance, and therefore impedance, if the particles were of the same size.

Two sizes of polystyrene nanoparticles, 100 nm as shown in Figure 6-17 and 200nm as shown in Figure 6-19, which had been modified with amino and carboxy groups, were studied. Those modified polystyrene nanoparticles were purchased from Polysciences, Inc. The nanoparticles modified with amino groups resulted in an overall more positive charge with respect to the unmodified polystyrene nanoparticles, while the nanoparticles modified with carboxy groups resulted in a more negative charge. The smaller size of 58nm polystyrene was not functionalized. One size of silica nanoparticles, 110nm, was also functionalized with amino or carboxy groups. Details of the surface chemistry are detailed in the experimental section. These nanoparticles were characterized and displayed in Figures 6-21 and 6-22. Other sizes of silica were not studied for effects of surface chemistry modifications, nor were any PMMA nanoparticles.

a) Polystyrene, 100nm


a)
Impedance Spectra of Polystyrene Nanoparticles
d=100nm, with three different surface chemistries
Impedance Magnitude (Ohms)
Frequency (Hz)
positive
neutral
negative
b)
Capacitance Spectra of Polystyrene Nanoparticles
d=100nm, with three different surface chemistries
Capacitance (F)
Frequency (Hz)
= positive
= neutral
= negative

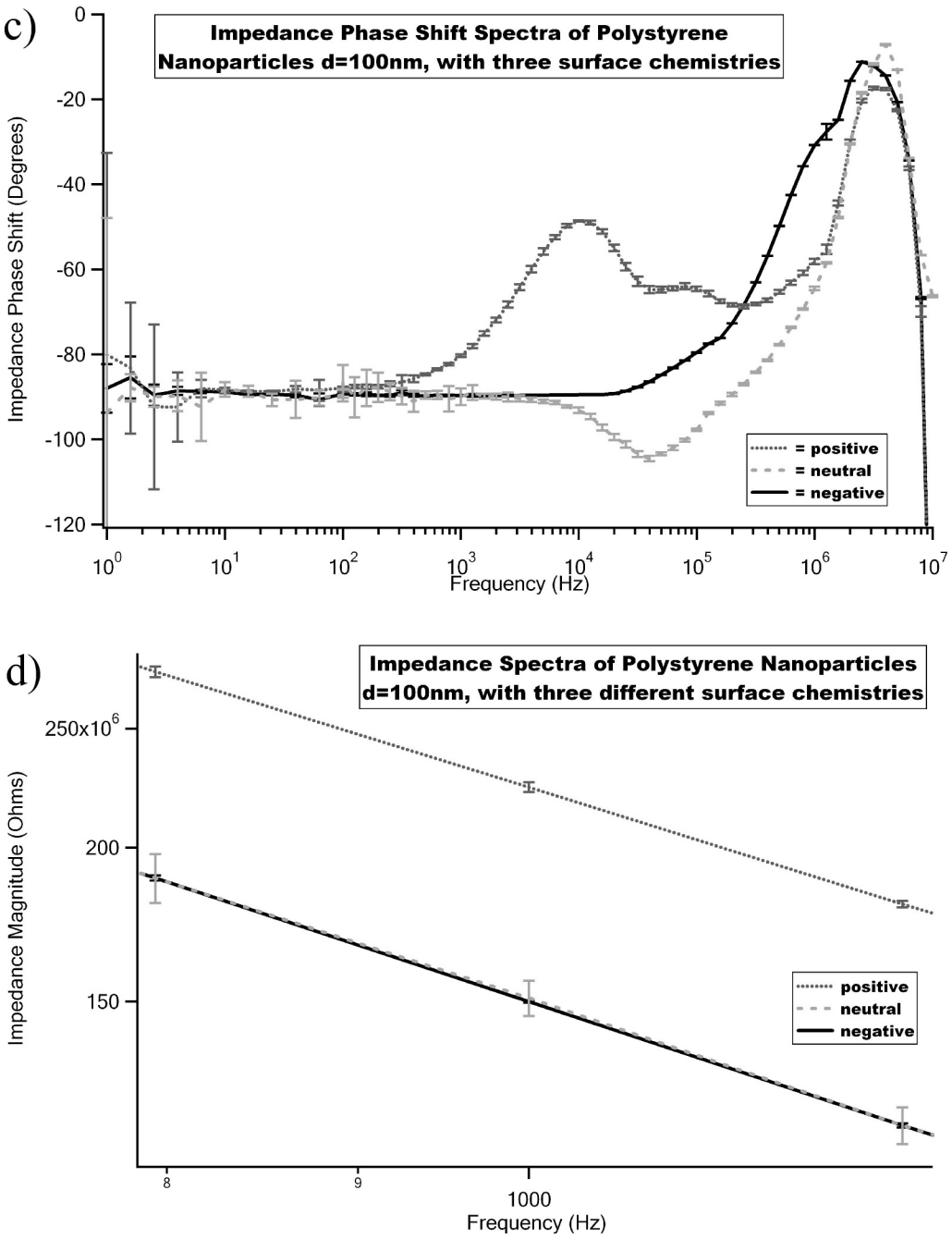


Figure 6-17. a) Impedance, b) capacitance, c) impedance phase shift, and d) magnified impedance spectra of three surface chemistries of d=100nm polystyrene nanoparticles. Dotted traces are amino- functionalized polystyrene yielding a more positive surface charge, Dashed traces are not functionalized yielding a neutral control, and Solid traces are carboxy- functionalized yielding a more negative surface charge.

In Figure 6-17, 100nm diameter polystyrene nanoparticles with three different surface chemistries were observed. In Figure 6-17a, the impedance spectra was shown. In frequencies lower than 10^4 Hz, a difference was slightly noticeable between those nanoparticles that had a more positive surface charge density due to the functionalization with amino groups, and the unmodified and negative particles. In Figure 6-17d, the magnified impedance spectra revealed that there were in fact a statistically significant difference between the positive nanoparticles and the overlapping negative and neutral nanoparticles. At high frequencies, above 10^4 Hz, more distinct separations of the spectra occurred.

In Figure 6-18, AFM height images and section analyses were shown for the three different 100nm diameter polystyrene nanoparticles. In Figure 6-18a, the height image for the polystyrene nanoparticles functionalized with amino groups was shown, with the corresponding section analysis shown in Figure 6-18b. The height image showed well dispersed single particles. The section analysis revealed the height of the particles was about 120nm, while the width of the particles was also larger than expected. The height image of unmodified 100nm polystyrene nanoparticles was shown again in Figure 6-18c, with the section analysis shown again in Figure 6-18d. In Figure 6-18e, the height image for the polystyrene nanoparticles functionalized with carboxy groups was shown, and the corresponding section analysis was shown in Figure 6-18f.

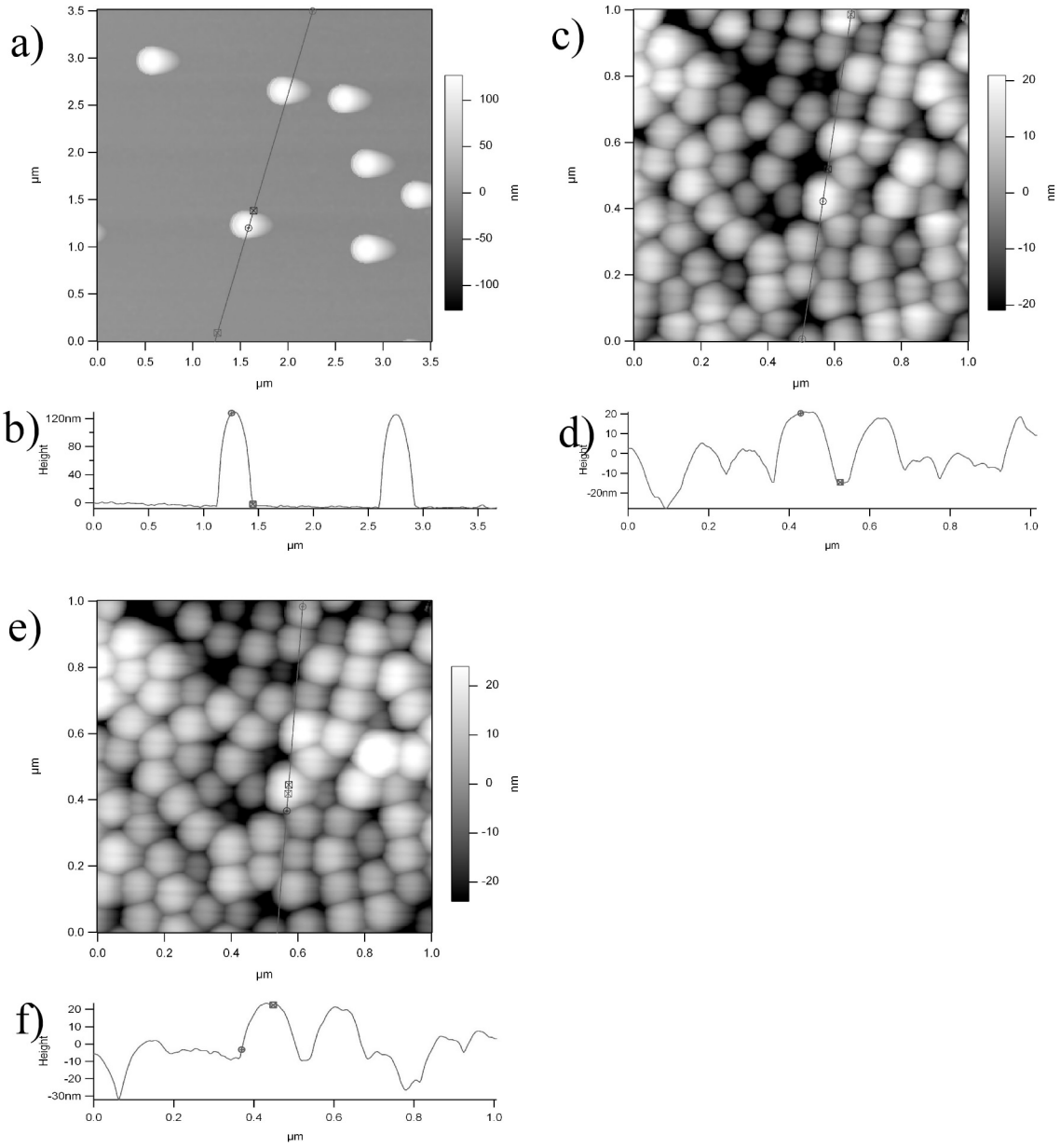


Figure 6-18. a) AFM height image and b) cross section of 100nm amino functionalized polystyrene, or "positive" polystyrene; c) AFM height image and d) cross section of 100nm unmodified polystyrene, or "neutral" polystyrene; e) AFM height image and f) cross section of 200nm carboxy functionalized polystyrene, or "negative" polystyrene.

The capacitance spectra, shown in Figure 6-17b, revealed three different behaviors of capacitance at high frequencies. In the phase shift spectra in Figure 6-17c, some clues began to appear that could reveal why there were such dramatic differences in

spectra. The phase shift of the positively functionalized nanoparticles increased from -90 degrees to -45 degrees of phase shift around 10^4 Hz. As previously described, -90 degrees of phase shift was the result from a capacitive circuit. However -45 degrees was also an interesting case. A phase shift of -45 degrees occurs when a Warburg impedance is present[146]. A Warburg impedance occurs when there is diffusion of reactive elements, or charges, in the circuit. This impedance is typically low at higher frequencies, and increases at lower frequencies. Since at high frequencies the diffusing elements do not have as far to move to diffuse, the impedance is lower. Conversely, at lower frequencies, the reactants must diffuse over longer distances, and this increases the Warburg impedance. If the diffusion layer is infinite, the Warburg impedance is termed infinite, and follows equation (6-3).

$$Z = \sigma(\omega)^{-\frac{1}{2}}(1 - j) \quad (6\text{-}3)$$

The Warburg coefficient in the equation (6-3) above is defined in equation (6-4).

$$\sigma = \frac{RT}{n^2 F^2 A\sqrt{2}}\left(\frac{1}{C_0^*\sqrt{D_0}} + \frac{1}{C_R^*\sqrt{D_R}}\right) \quad (6\text{-}4)$$

In equations (6-3) and (6-4), ω = radial frequency, D_O = diffusion coefficient of the oxidant, D_R = diffusion coefficient of the reductant, A = surface area of the electrode, n = number of electrons transferred, and C^* = bulk concentration of the diffusing species (moles/cm^3).

If the Warburg impedance is finite, then equation (6-5) below is used to describe the impedance.

$$Z_O = \sigma\omega^{-\frac{1}{2}}(1 - j)\tanh\left(\delta\left(\frac{j\omega}{D}\right)^{\frac{1}{2}}\right) \quad (6\text{-}5)$$

With d = Nernst diffusion layer thickness, and D = an average value of the diffusion coefficients of the diffusing species. This finite Warburg impedance case applies in most real cases, where there is some layer of material the charge must diffuse through. In the case of the positive polystyrene nanoparticles, a layer of amino-functionalized polystyrene molecules was located on the surface, which could have created this Warburg impedance. Perhaps the reason that only the positively charged polystyrene exhibited this behavior has to do with the flow of negatively charged electrons being affected by the positively charged amino groups on the surface of the polystyrene nanoparticles.

The impedance phase shift spectra of the three surface chemistries of 100nm polystyrene nanoparticles shown in Figure 6-17c showed a behavior that trended towards a pure resistor at high frequencies between 10^6 and 10^7 Hz. The shape of the phase shift spectra for the carboxy-functionalized nanoparticles was opposite what would be expected for an "ideal" real capacitor. At higher frequencies, a real capacitor will exhibit some change in impedance and capacitance. These changes by real capacitors yield behavior more like constant phase elements, or CPE's. The impedance of a capacitor is shown in equation (6-6) below,

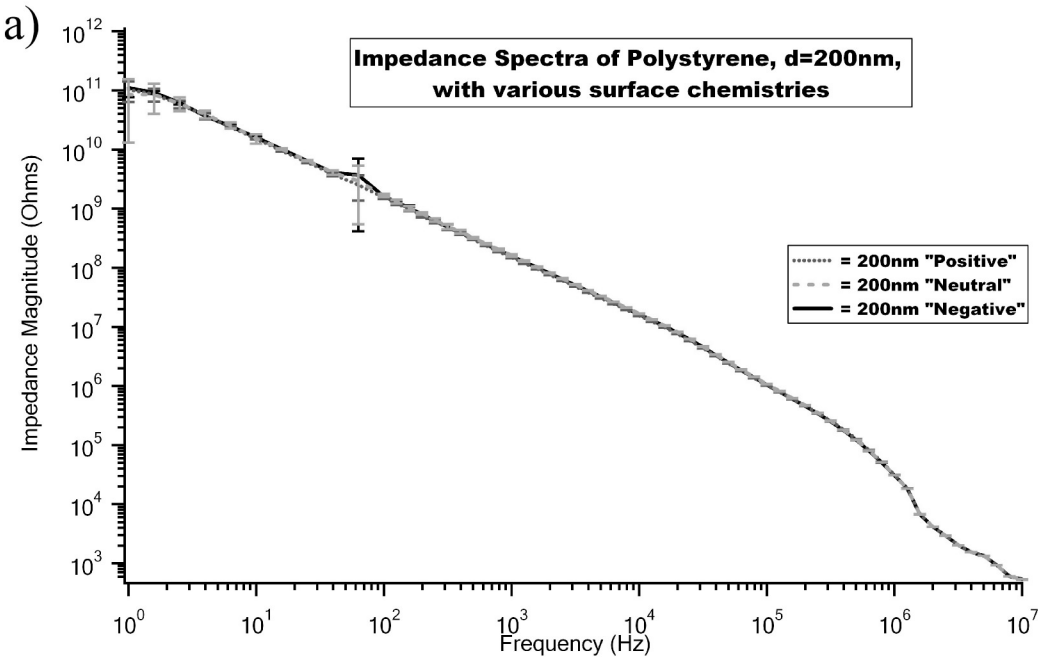
$$Z = \left(\frac{1}{j\omega C} \right)^{-\alpha} \quad (6\text{-}6)$$

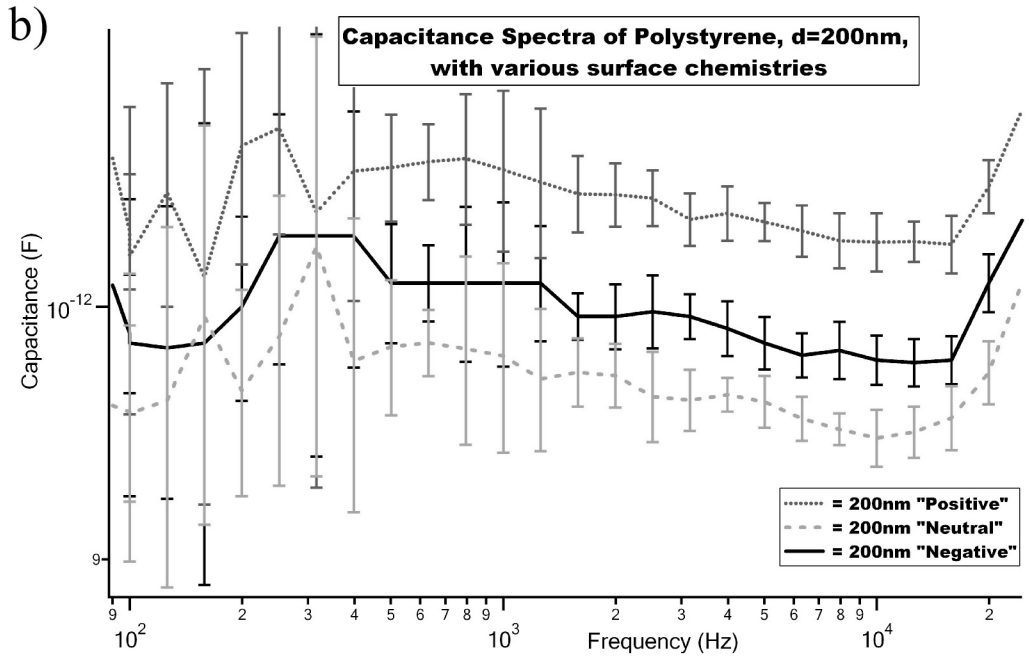
where the exponent, alpha, is equal to one, the capacitor behaves in an ideal fashion[147]. In the case of a CPE, the exponent, alpha, is less than one. The so-called "double layer capacitor" found on the surface of real electrodes often behaves like a CPE

rather than like a real capacitor. Thus, a CPE could perhaps best describe the functionalized nanoparticles deviation from an ideal capacitor.

b) Polystyrene, 200nm

In Figure 6-19, three different surface chemistries of 200 nanometer diameter polystyrene nanoparticles were studied. In the case of this larger size of polystyrene, the positive particles had the highest capacitance, followed by the negative then the neutral particles in order of decreasing capacitance. This trend was not a similar trend to the case of 100 nm polystyrene. One reason proposed for this difference could be that the shift in capacitance between unmodified and modified states of surface chemistry was a reflection of the absolute value of the effective surface charge on the particles. For example, if arbitrarily only 10% of the surface was functionalized with positive surface charge groups while arbitrarily 20% of the surface was functionalized with negative surface charge groups, the net shift in charge of the positive particles would be less than the net shift in charge of the negative particles. This could be further complicated by the issue of the negatively charged surfactants used in the manufacturing process of synthesizing the nanoparticles. These residue surfactants could provide a baseline negative charge for the unmodified particles labeled as neutral, and the addition of positively charged amino surface groups would lead to seemingly arbitrary final absolute values for the surface charge of each of the particles.


a)
Impedance Spectra of Polystyrene, d=200nm,
with various surface chemistries
Impedance Magnitude (Ohms)
Frequency (Hz)
= 200nm "Positive"
= 200nm "Neutral"
= 200nm "Negative"


b)
Capacitance Spectra of Polystyrene, d=200nm,
with various surface chemistries
Capacitance (F)
Frequency (Hz)
= 200nm "Positive"
= 200nm "Neutral"
= 200nm "Negative"

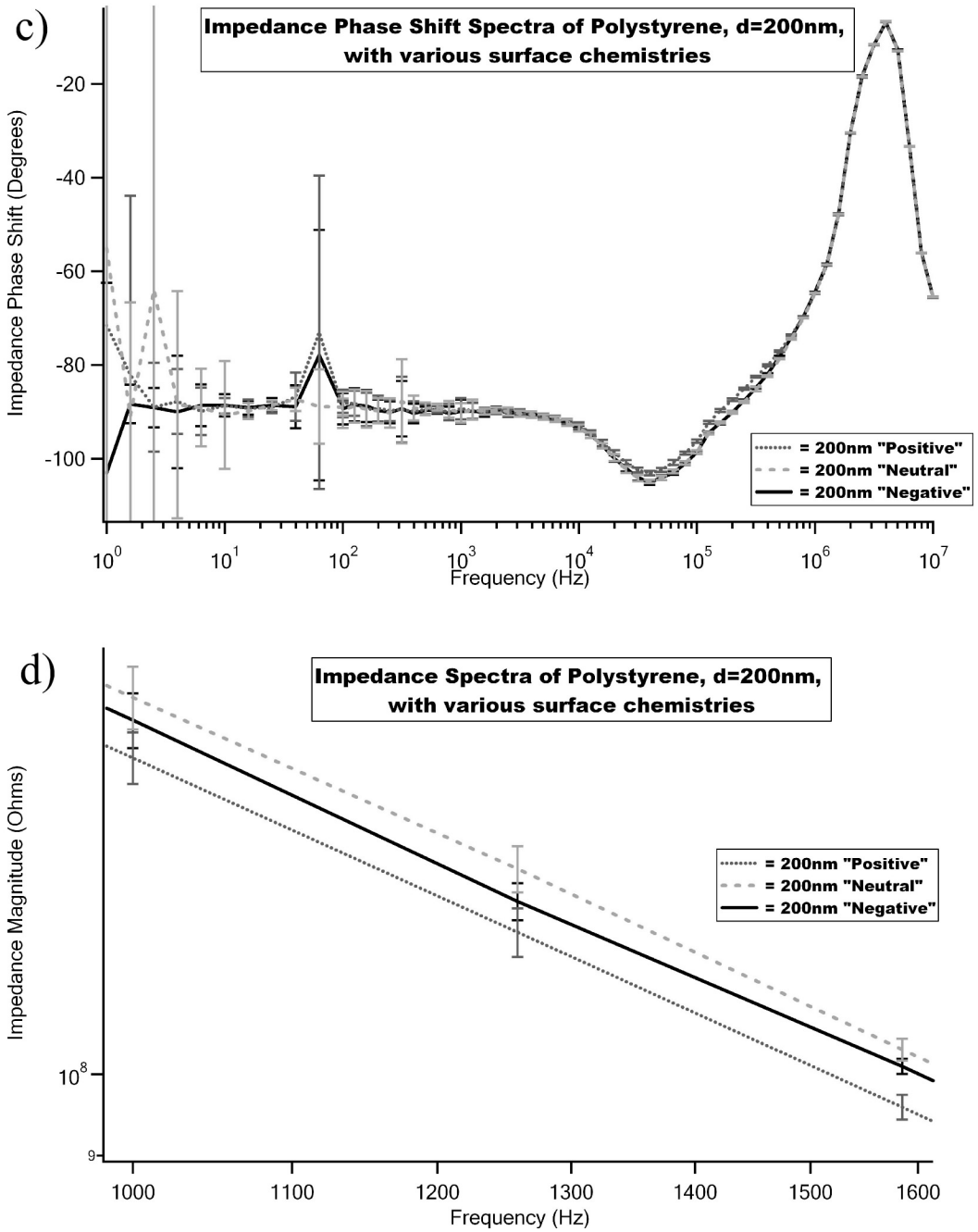


Figure 6-19. a) Impedance, b) capacitance, c) impedance phase shift, and d) magnified impedance spectra for three surface chemistries and therefore surface charges of polystyrene nanoparticles with diameters of 200nm. Dotted traces are amino-functionalized polystyrene yielding a more positive surface charge, Dashed traces are not functionalized yielding a neutral control, and Solid traces are carboxy- functionalized yielding a more negative surface charge.

In Figure 6-20, the AFM images of the three types of 200nm diameter polystyrene nanoparticles were shown. In Figure 6-20a the height image of the 200nm polystyrene nanoparticles functionalized with amino groups, or the positive nanoparticles, were shown. The corresponding section analysis is shown in Figure 6-20b. The height image of the unmodified 200nm polystyrene nanoparticles, or the neutral nanoparticles, was shown again in Figure 6-20c, with the corresponding section analysis shown again in Figure 6-20d. In Figure 6-20e, the height image of the 200nm polystyrene nanoparticles functionalized with carboxy groups, or the negative nanoparticles, was displayed. Figure 6-20f showed the section analysis for Figure 6-20e. All three nanoparticles show good agreement between height and width with expected values from the section analysis. The height images in all three cases revealed monolayers packed on the surface with aggregated particles that provided incomplete surface coverage.

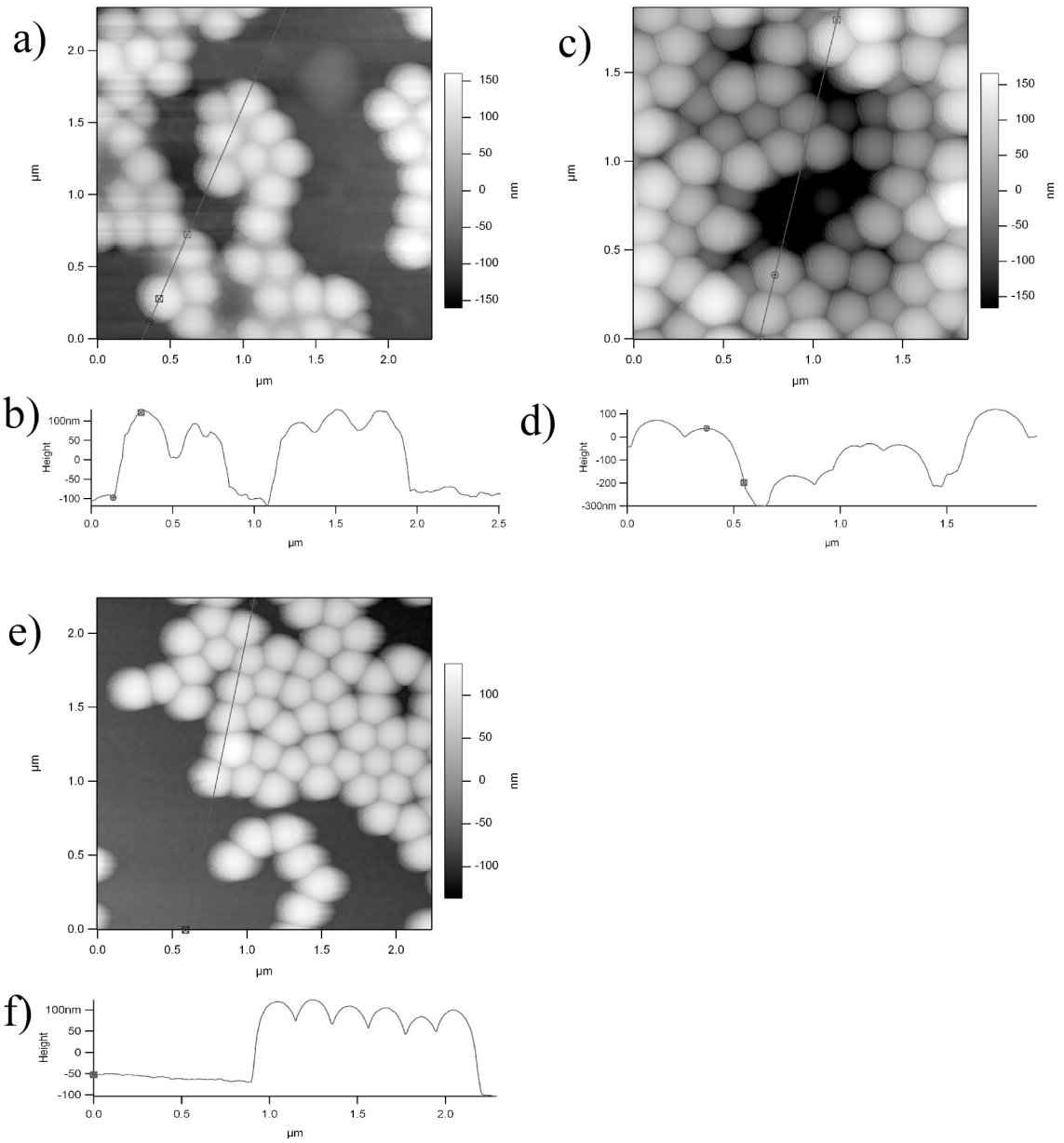


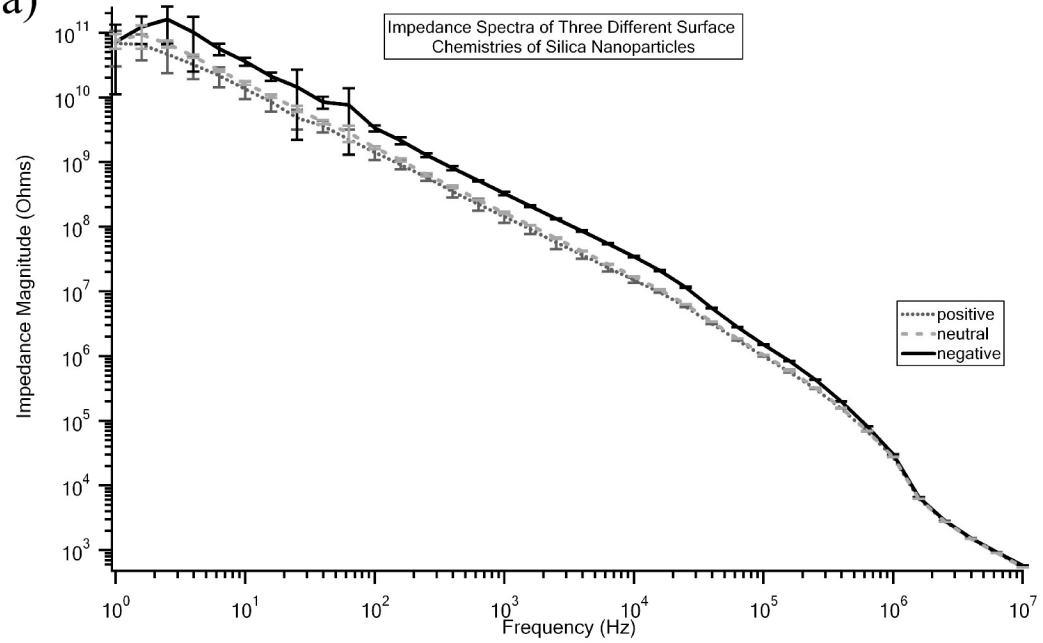
Figure 6-20. a) AFM height image and b) cross section of 200nm polystyrene nanoparticles modified with amino groups, or "positive" polystyrene; c) AFM height image and d) cross section of unmodified 200nm polystyrene nanoparticles or "neutral" polystyrene; e) AFM height image and f) cross section of 200nm polystyrene nanoparticles modified with carboxy groups, or "negative" polystyrene.

c) Silica

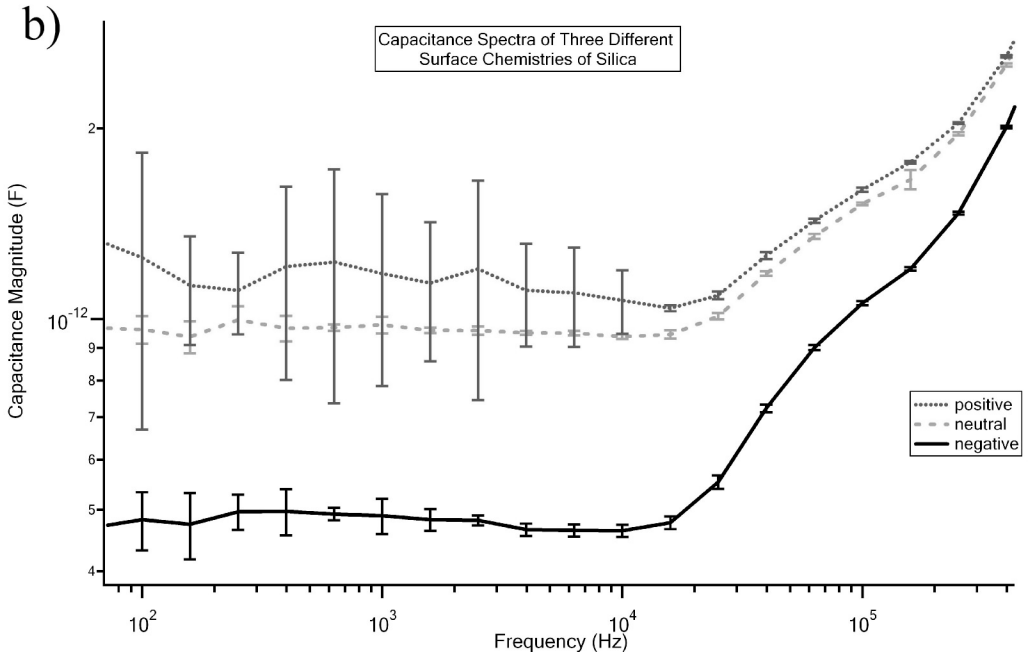
In Figure 6-21, the silica nanoparticles were functionalized with a more positive surface charge chemistry by adding amino functional groups, and were functionalized

with a more negative surface charge chemistry by adding carboxy groups. In the case of silica, the data for different surface charges showed a higher capacitance for the carboxy functionalized nanoparticles in Figure 6-21b. The impedance showed a noticeable difference in the entire spectrum in Figure 6-21a, and a clear statistically significant difference in the magnified area of the spectrum shown in Figure 6-21c. In all of these cases, the change in chemical composition of the material should change the dielectric constant of the nanoparticle, thereby changing the capacitance. From this data it is clear that the capacitance of the nanoparticles is dependant not only on their size, but on the composition or material of the particle. The trend in the case of silica indicated adding negative charge decreases the capacitance. In Figure 6-21d, the phase spectra interestingly show a much more mixed value between purely capacitive and purely resistive phase shift. Unlike most purely capacitive impedance spectra obtained in the course of this study, with phase shifts staying very close to -90 degrees, these phase spectra exhibit a mixture of capacitive and resistive (or inductive) components in the spectra. This could be due to the different chemical composition of the silica nanoparticles as compared to the polymer nanoparticles.

a)


Impedance Spectra of Three Different Surface Chemistries of Silica Nanoparticles
Impedance Magnitude (Ohms)
Frequency (Hz)
positive
neutral
negative

b)


Capacitance Spectra of Three Different Surface Chemistries of Silica
Capacitance Magnitude (F)
Frequency (Hz)
positive
neutral
negative

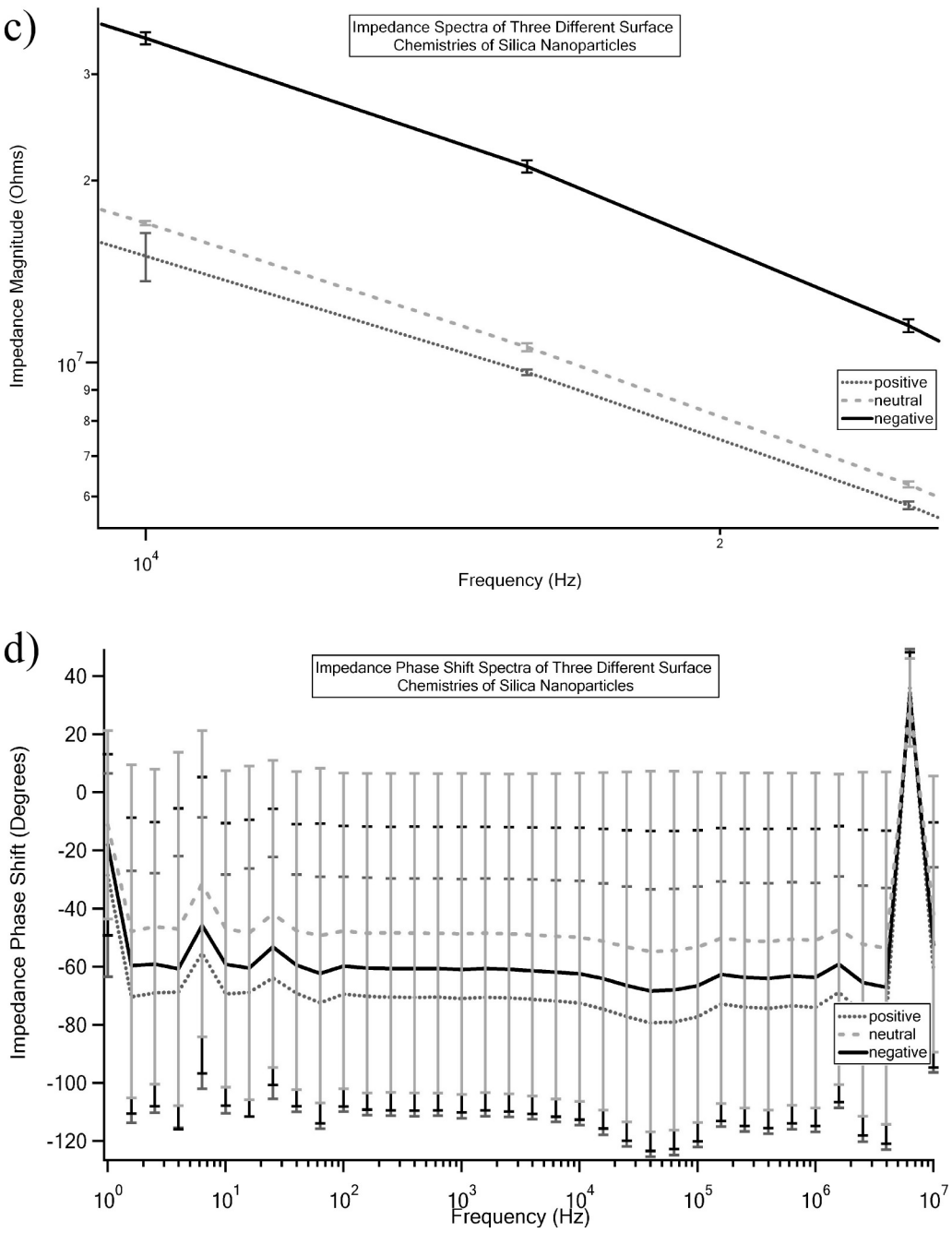


Figure 6-21. a) Impedance, b) capacitance, c) magnified impedance, and d) phase shift spectra for three different surface chemistries of silica nanoparticles.

The AFM images of the silica nanoparticles with different surface chemistries are shown in Figure 6-22. In Figure 6-22a, the height image of the 110nm silica

nanoparticles functionalized with amino groups, or the positive nanoparticles, were shown. The corresponding section analysis is shown in Figure 6-22b. The height image of the unmodified 110nm silica nanoparticles, or the neutral nanoparticles, was again shown in Figure 6-22c, with the corresponding section analysis shown in Figure 6-22d. In Figure 6-22e, the height image of the 110nm silica nanoparticles functionalized with carboxy groups, or the negative nanoparticles, was displayed. Figure 6-22f showed the section analysis for Figure 6-22e.

Interestingly, the modified silica nanoparticles aggregated together more than the unmodified silica nanoparticles, which appeared to remain monodisperse. In all three cases, monolayers of nanoparticles were deposited on the surface based on the AFM height images. Further, the section analysis in all three cases provided good agreement between the measured height and expected height, as well as good agreement on the particle width.

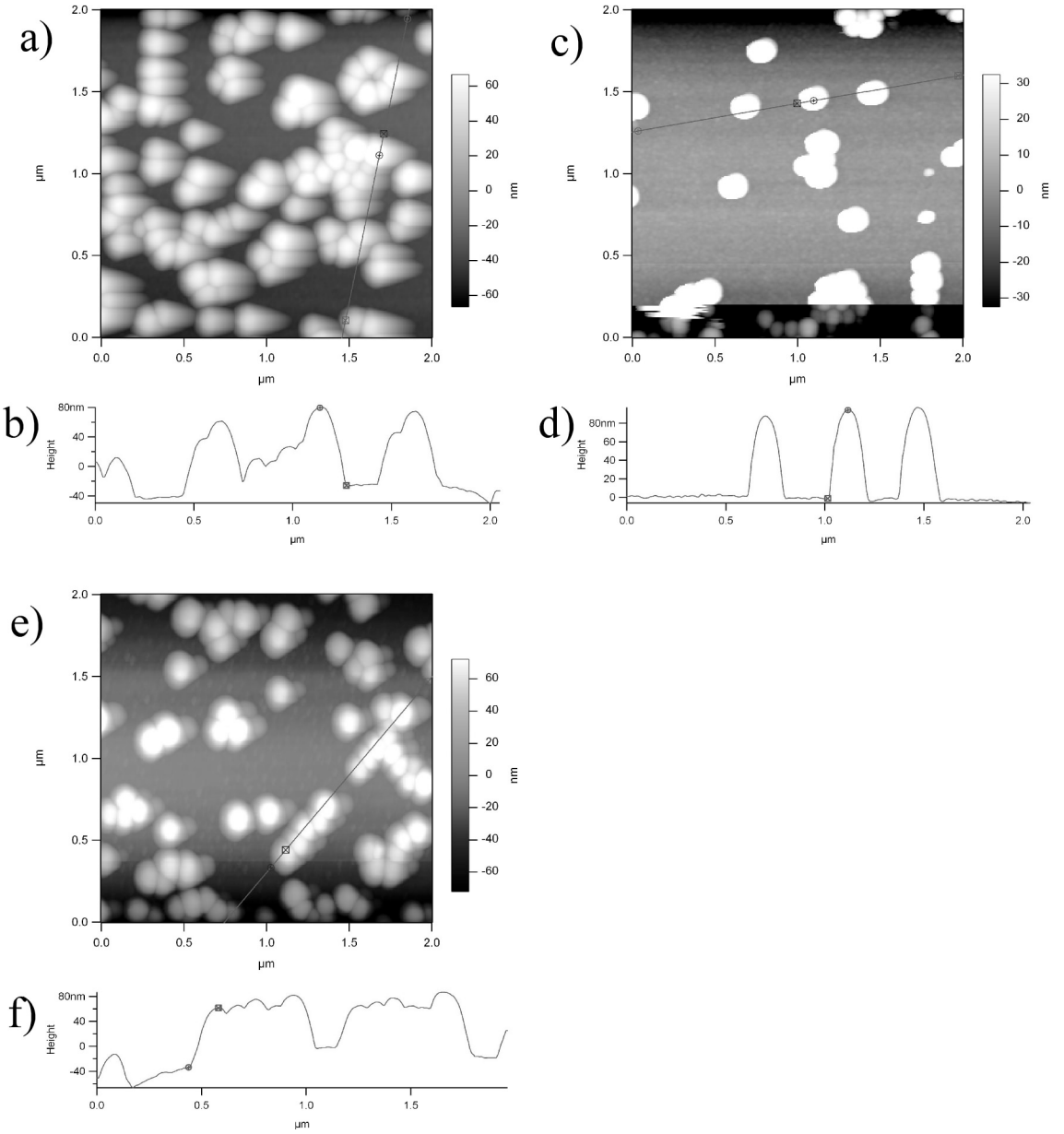


Figure 6-22. a) AFM height image and b) cross section of 110nm silica modified with amino groups, or "positive" silica; c) AFM height image and d) cross section of unmodified 110nm silica, or "neutral" silica; e) AFM height image and f) cross section of 110nm silica modified with carboxy groups, or "negative" silica.

The results of Figures 6-17, 6-19, and 6-21 were summarized in Table 6-3. The trend of highest to lowest capacitance as a function of surface charge for each material was shown in the right hand column. The terms positive, neutral, and negative were used

in quotations since there was not a clear understanding of what the precise surface charge of the particles would be in air based on the surfactant molecules, surface chemistry, and debate over whether molecules could hold charge in air without counter ions present to effectively provide a net neutral charge.

Table 6-3. Capacitance of different surface chemistries

Material, and diameter	"Positive" (+) Capacitance, 10kHz	"Neutral" (0) Capacitance, 10kHz	"Negative" (-) Capacitance, 10kHz	Highest to Lowest Capacitance
PS, 100nm	3.40e-13	1.03e-12	1.05e-12	(-) = (0) > (+)
PS, 200nm	1.0273e-12	9.46763e-13	9.78e-13	(+) > (-) > (0)
Silica, 110nm	1.07e-12	9.38e-13	4.63e-13	(+) > (0) > (-)

4. A POINT-TO-PLATE MODEL FOR CAPACITANCE OF AIR GAP

One of the challenges to creating an accurate theoretical model was determining the electric field near the AFM tip and the sample. If the electric field, *E*, can be calculated, then it is possible to obtain the potential difference, *V*, by

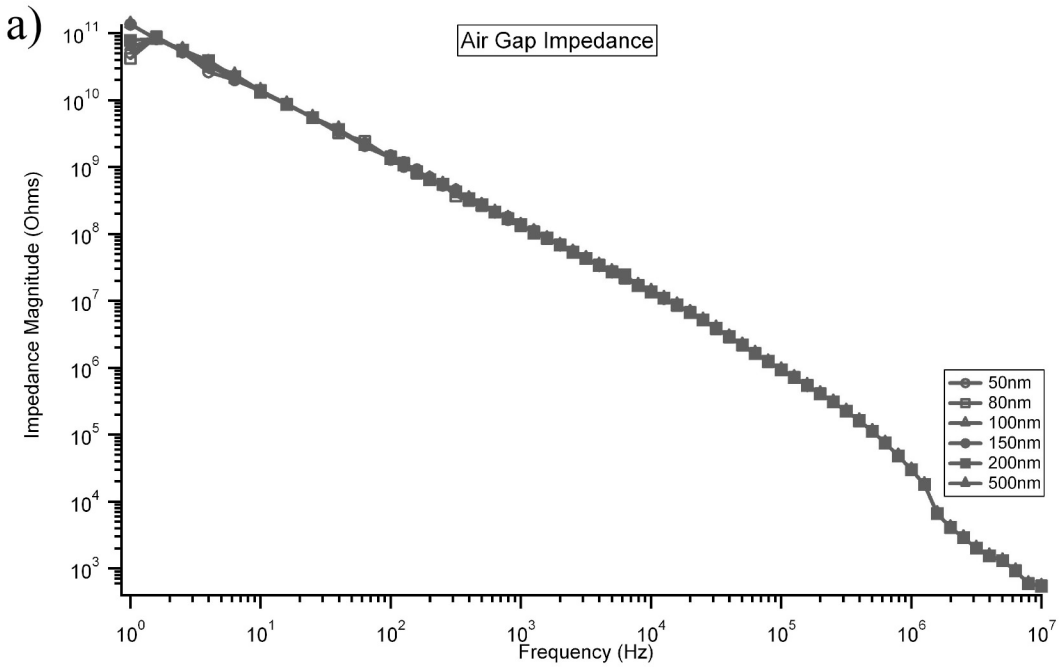
$$V = -\int E \cdot dl \quad (6\text{-}7)$$

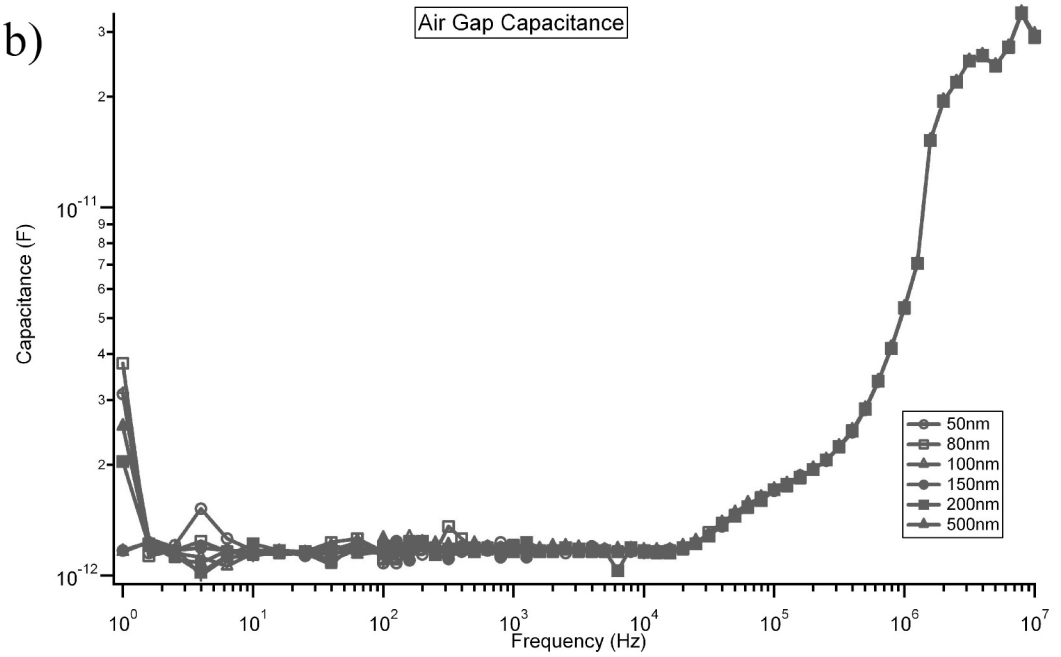
and then use $C=Q/V$ to calculate and predict the capacitance and the dielectric constant. Modeling this electric field included several considerations. One component to this model was considering a point electrode above a plate electrode as the configuration

of the capacitor. The equation for the electric field at a point above an infinite plate with surface charge σ does not depend on the distance of the point above the plate,

$$\hat{E} = \frac{\sigma}{2\varepsilon_0}\hat{n} \quad (6\text{-}8)$$

where $\hat{n}$ is a unit vector normal to the surface[129]. This model was reasonable when considering both the radius of curvature of the AFM tip, 4×10^{-8} m, and the radius of the spherical gold electrode pad, 3×10^{-3} m. The difference in size between the AFM tip and gold electrode was approximately five orders of magnitude. This situation approximated a point test charge above an infinite plane. The validity of this model was confirmed when the AFM tip was held at various heights from 50nm to 500nm above the surface and a constant capacitance value was measured, as shown in Figure 6-23.


a)
Air Gap Impedance
Impedance Magnitude (Ohms)
Frequency (Hz)
50nm
80nm
100nm
150nm
200nm
500nm


b)
Air Gap Capacitance
Capacitance (F)
Frequency (Hz)
50nm
80nm
100nm
150nm
200nm
500nm

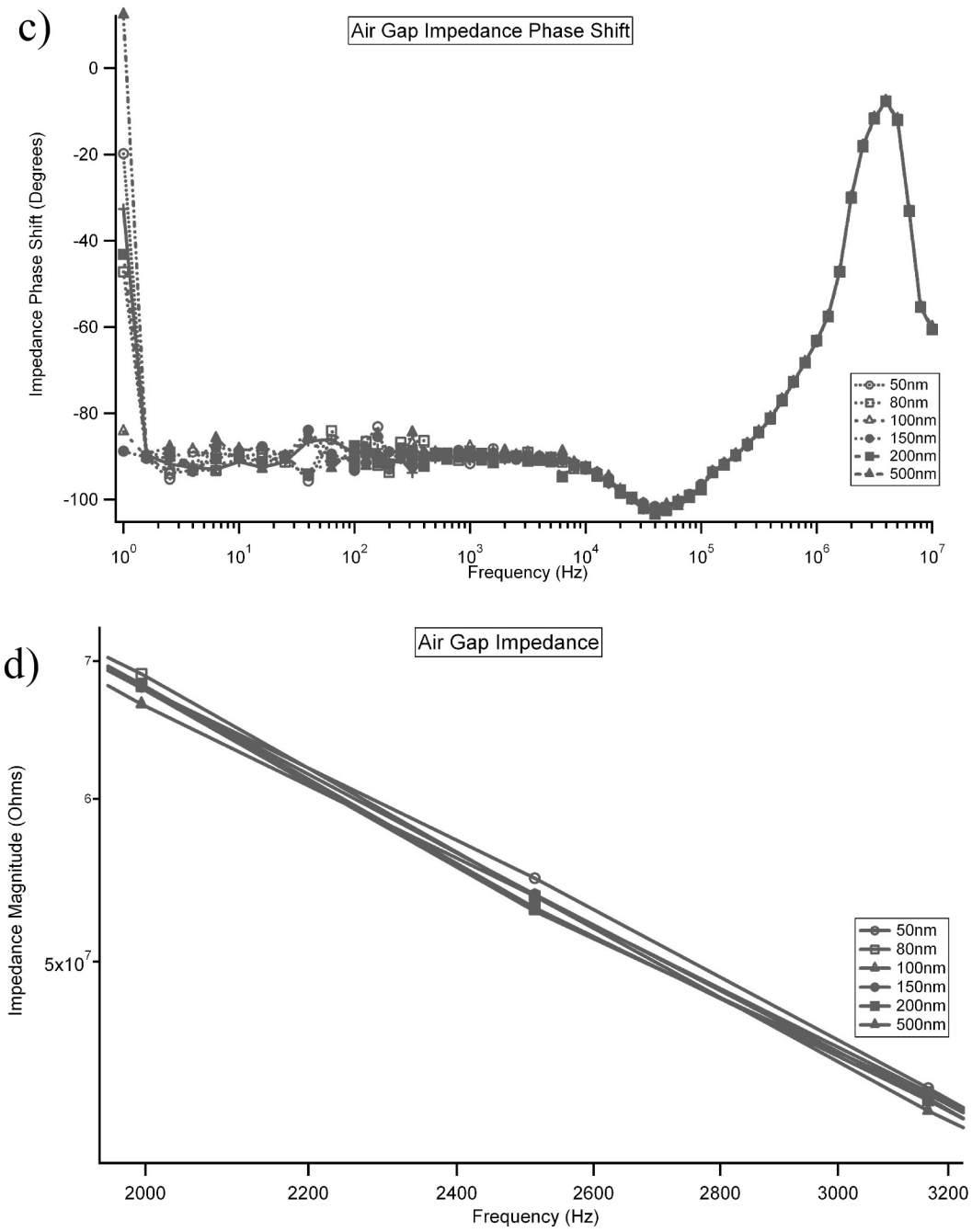


Figure 6-23. Air gap spectra. a) impedance, b) capacitance, c) impedance phase shift and d) magnified impedance for 50nm, 80nm, 100nm, 150nm, 200nm, and 500nm air gaps.

Changes in surface charge densities led to changes in the electric field and therefore the potential, the capacitance, and the impedance. When a model of the

nanoparticle as a spherical dielectric material in between two conducting planes was used, the parallel plate capacitor model was a reasonable assumption when the radius of the nanoparticle was smaller than the radius of curvature of the tip. However, in the cases where the nanoparticle was larger than the size of the AFM tip, a model of a point-plate capacitor with a spherical dielectric material between the point and the plate, as depicted in Figure 6-24b, was more suitable. This model was different from the model described in equation (6-8) and characterized in Figure 6-23, since there is no spherical dielectric material in that model. An illustration of the strictly point-plate capacitor is shown for comparison in Figure 6-24a.

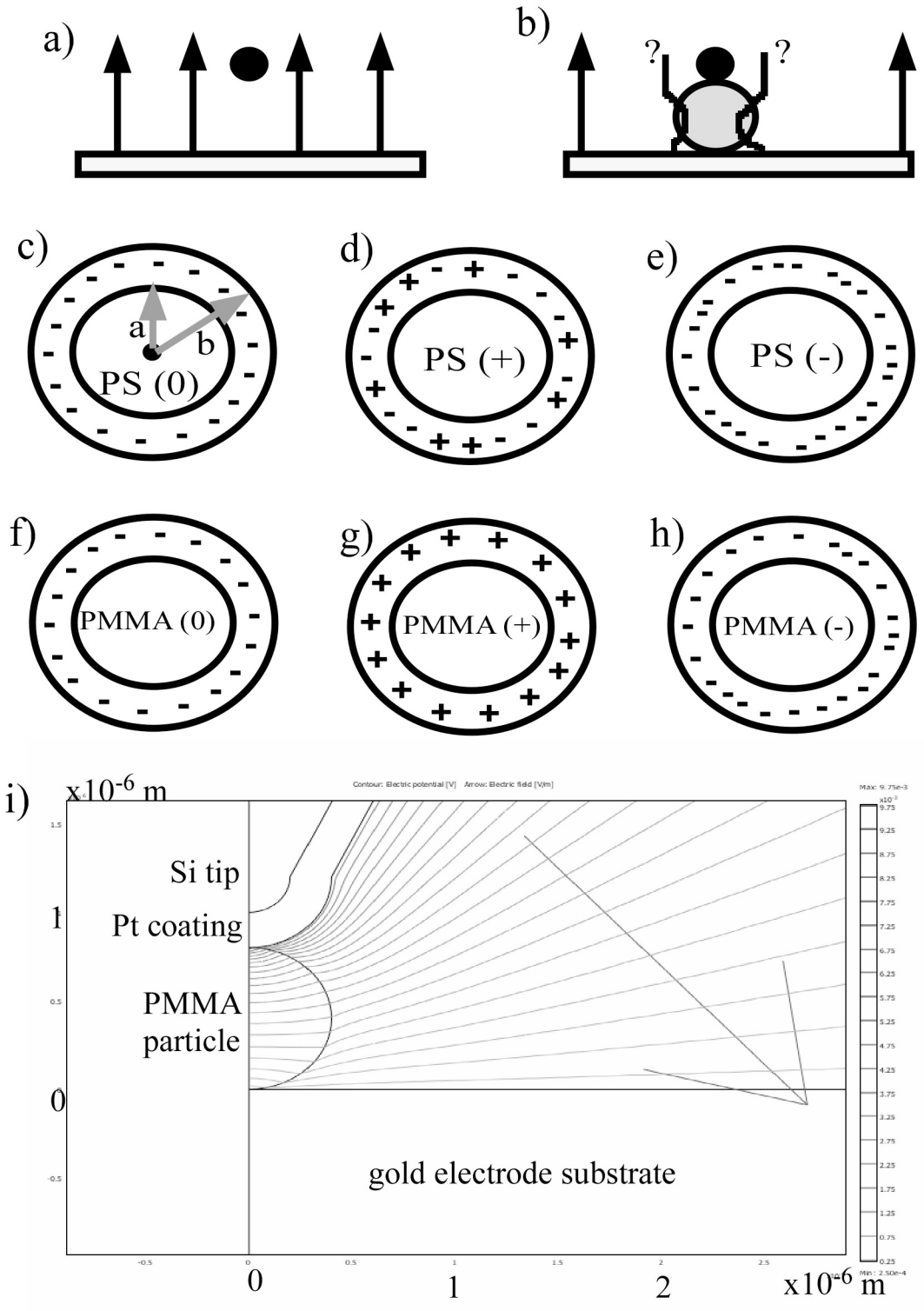


Figure 6-24. a) cartoon of field lines of a point charge above an infinitely large plate charge. b) cartoon of field lines in the case of the afm spherical model of capacitance. illustration of how surface charge of surfactant molecules could create a double layer in the cases of c) unmodified polystyrene, d) amino functionalized polystyrene, e) carboxy

functionalized polystyrene, f) unmodified PMMA, g) amino functionalized PMMA, and h) carboxy functionalized PMMA. i) COMSOL Multiphysics model, with only the AFM tip biased, and zoomed in around the tip and PMMA nanoparticle and gold substrate.

However, a point-plate capacitor model would be an oversimplified assumption for the case of modifying the surface chemistry of the nanoparticles. In the case under study, the so-called "core-shell" model was perhaps more appropriate. A simple case would be if the unmodified nanoparticle was an uncharged sphere of uniform dielectric constant. However, it is likely that the surface of the dried nanoparticles contains negatively charged surfactant molecules. A representation of the resulting dried nanoparticle was depicted in Figure 6-24c. Modification of the surface chemistry by adding amino groups, depicted in Figure 6-24d, or carboxy groups, depicted in Figure 6-24e, would make the charge density on the surface of the resulting nanoparticle either less negative or more negative, respectively with respect to the unmodified nanoparticle. It is possible to imagine a model of a spherical dielectric material with dielectric constant k_1 and radius a nm, surrounded by another spherical dielectric material with dielectric constant k_2 and radius b nm, where the thickness of the outer layer is b-a nm, is more appropriate. The changes in either the thickness of this outer layer or its charge density would affect the overall dielectric constant of the nanoparticle medium. This change in charge density would in turn modify the electric field and potential above the gold electrode and below the AFM tip, and thus the capacitance as shown in Figure 6-9.

$$C = \frac{4\pi\varepsilon_a\varepsilon_b}{\frac{1}{a} - \frac{1}{b}} \quad (6\text{-}9)$$

In the case of PMMA, the unmodified nanoparticle also had a negatively charged surfactant molecule. The possibility exists that a more complete functionalization with

amino groups occurred on the surface of the PMMA compared to the surface of the polystyrene. This would create a change from the unmodified PMMA nanoparticle, depicted in Figure 6-24f, and the amino functionalized nanoparticle, depicted in Figure 6-24g. The possibility exists also that a less complete functionalization with carboxy groups occurred on the surface of the PMMA when compared to the polystyrene. This would result in a carboxy functionalized nanoparticle, depicted in Figure 6-24h, that was not significantly different in charge density compared to the unmodified nanoparticle. These speculations offer potential explanations for the seemingly random behavior of the impedance spectra response among different materials. In Figure 6-17c, the phase shift of the three different functionalizations of 100 nm polystyrene nanoparticles was uniquely different compared to other samples. The reaction of the surface of the nanoparticles and therefore different levels of surfactants bound to the surface of the nanoparticles could have caused the decreased phase shift compared to the neutral or unreacted polystyrene.

A further consideration to the measurement of the polystyrene nanoparticles is the residual surfactant layer from the manufacturing process that creates a small layer of negative charge. The surfactant is present in all three species of polystyrene nanoparticles, amino functionalized, carboxy functionalized, and unfunctionalized. Therefore, there is a constant amount of negative surface charge density included in the measurement of any particle, and it is more appropriate to discuss the relative changes in surface charge density rather than claiming that the polystyrene nanoparticle had an absolute positive or negative surface charge density. While it is quite difficult to precisely determine what the charge of the proprietary surfactant molecule would be in

air, and what effects a wetting meniscus layer of humidity condensation from the AFM tip would introduce, assuming that these properties are constant from sample to sample still allows the measurement of how the surface chemistry changes are affecting the electrical properties of the nanoparticles.

Mathematical models using the commercially available software package COMSOL Multiphysics were also studied. The results from these calculations are shown in Figure 6-24i. In Figure 6-24i, the equipotential lines are drawn based on a calculation where the AFM tip was biased with 10mV and the substrate was held to ground. Equipotential lines are simply contours that have a constant value of potential, to allow visualization of the changes in potential through space. The arrow drawn is a normal vector through the equipotential lines. The main triangle of the cantilever was defined as silicon, with a twenty nanometer thick layer of platinum covering the silicon. The bottom rectangle was defined as gold, the electrode material used in the experiments. The nanoparticle sphere was defined as PMMA, and the remaining volume was defined as air. The defined dielectric constants, electrical permittivity and resistivity were used from defined libraries in the COMSOL software package. Further calculations should be performed that allow for changing dielectric constants as the electric potential applied changes. The take home message from Figure 6-24i is that while the equipotential lines are fairly uniform through the nanoparticle and parallel to the substrate, on the sloped portion of the AFM tip and through the air down to the substrate below the equipotential lines deviate from parallel. This suggests that the models used for electric fields may need more descriptive mathematical terms to compensate for this deviation, making a mixture of models perhaps the most appropriate calculation.

5. AC IMPEDANCE SPECTROSCOPY STUDIES OF VIRUSES

a) In general

So far, impedance characterization of single nanoparticles has been described in an attempt to gain a more fundamental understanding of electrical properties of nanomaterials. However, to reach the goal of developing a better biosensor, studies must be performed on single viruses. A summary of these studies is shown in Figure 6-25, and Table 6-4.

Viruses have a complex structure made up of either a DNA or RNA core, surrounded by structural capsids proteins, and in some cases an envelope of more proteins and glycoproteins. Since each species of virus has unique structural capsid proteins, each virus should in principle have a different dielectric constant. Since virions are insulators, this would allow the determination of unknown viruses by their electrical properties using impedance spectroscopy, as a difference capacitance should be observed with each species. Further differences can be identified by the presence or absence of the envelope layer of glycoproteins. These glycoproteins in principle should have a different dielectric constant than the proteins that make up the capsid. Since all these layers are different, they should affect the total capacitance, even though the percentage of contribution from each layer may vary. The DNA, being negatively charged and most likely trapping some water content inside the capsid, can be treated as a spherical conductor, which is surrounded by an insulating dielectric sphere. When an envelope is present on the virus, this conducting sphere of DNA is surrounded by two dielectric spheres, each with its own dielectric constant and charge density. Since proteins and

glycoproteins typically have some associated electrostatic charges, further discrimination could be possible. A significant challenge, therefore, is deconvoluting the complex layers of signals intertwined in the impedance spectroscopy measurement.

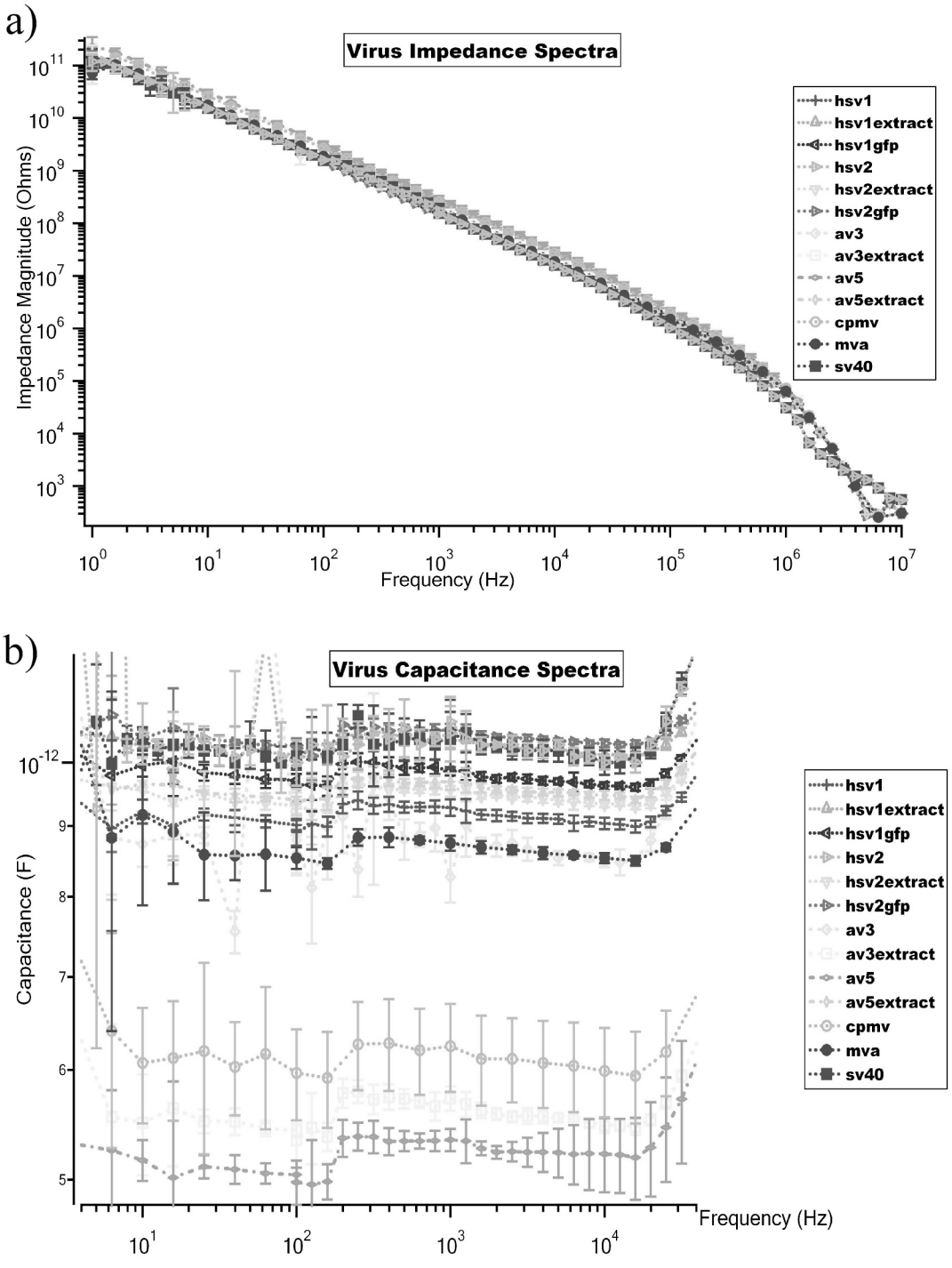
Herpes Simplex Virus Type 1 (HSV-1) is known to cause cold sores around the mouth, and Herpes Simplex Virus Type 2 (HSV-2) is known to cause genital herpes[1]. In both of these cases, spread of the virus can occur when patients do not actively exhibit symptoms, thereby spreading the disease unknowingly. Herpes viruses are double stranded DNA viruses, icosahedral or spherical in shape, and have a diameter approximately 110-120nm. Herpes viruses have an envelope layer.

Adenovirus is a virus that causes up to 10% of acute respiratory infections in children, with infections also possible in the eyes, intestines and urinary tract[111]. Adenovirus is also a double stranded DNA virus, icosahedral or spherical in shape, and has a diameter of approximately 65-75nm. Adenoviruses have an envelope layer. Adenovirus Type 3 was associated with childhood pneumonia in Korea from 1991-1999[148]. Human Adenovirus Type 5 was first isolated from the adenoids, and is non-carcinogenic[1].

Simian Virus 40 (SV40) is a natural virus that is typically asymptomatic in otherwise healthy monkeys[112]. Interest in SV40 increased in the early 1960's after its discovery as a contaminant in some 98 million injected polio vaccines. Studies have shown SV40 associated with mesothelioma tumors, or lung cancer, as well as some brain and bone tumors[113-115]. SV40 is a double stranded DNA virus, icosahedral or spherical in shape, approximately 45-55nm in diameter. SV40 does not have an envelope layer.

Cowpea mosaic virus, or CPMV, is a plant virus that is 25nm across, and icosahedral in shape. The genome of CPMV is approximately 10.4 kb, or 10,400 base pairs. CPMV is a single stranded RNA virus[1]. Vaccinia virus, or MVA, has been used in the past for vaccination against smallpox. It is an oval shaped virus, about 270nm by 360nm. It is a double stranded DNA virus[1].

In regards to using these properties solely for the means of identifying pathogens, it is clear that a large library of spectra should be collected as a reference for comparison to unknown spectra. While the impedance and capacitance spectra showed the most promise for identifying pathogens, the phase shift spectra was not suitable for identification of unknown pathogens. Instead, the phase shift spectra served as a control that electrical continuity was maintained on the AFM tip and on the substrate electrode by looking for the -90 degree phase shift to confirm a capacitive circuit. However, it is likely many viruses will still not be identifiable solely on impedance data, and thus using other criteria such as physical size or antibody recognition remain important components of a successful method. The phase shift data for the viruses followed one of two trends. Viruses that approached a phase shift of zero at high frequency then decreased towards -90 degrees at the highest frequencies included HSV-2, AV3, and SV40. Viruses that stayed at -90 degrees phase shift longer, then spiked above 0 degrees phase shift at the highest frequencies included all other samples.


a)
Virus Impedance Spectra
Impedance Magnitude (Ohms)
Frequency (Hz)
hsv1
hsv1extract
hsv1gfp
hsv2
hsv2extract
hsv2gfp
av3
av3extract
av5
av5extract
cpmv
mva
sv40
b)
Virus Capacitance Spectra
Capacitance (F)
Frequency (Hz)
hsv1
hsv1extract
hsv1gfp
hsv2
hsv2extract
hsv2gfp
av3
av3extract
av5
av5extract
cpmv
mva
sv40

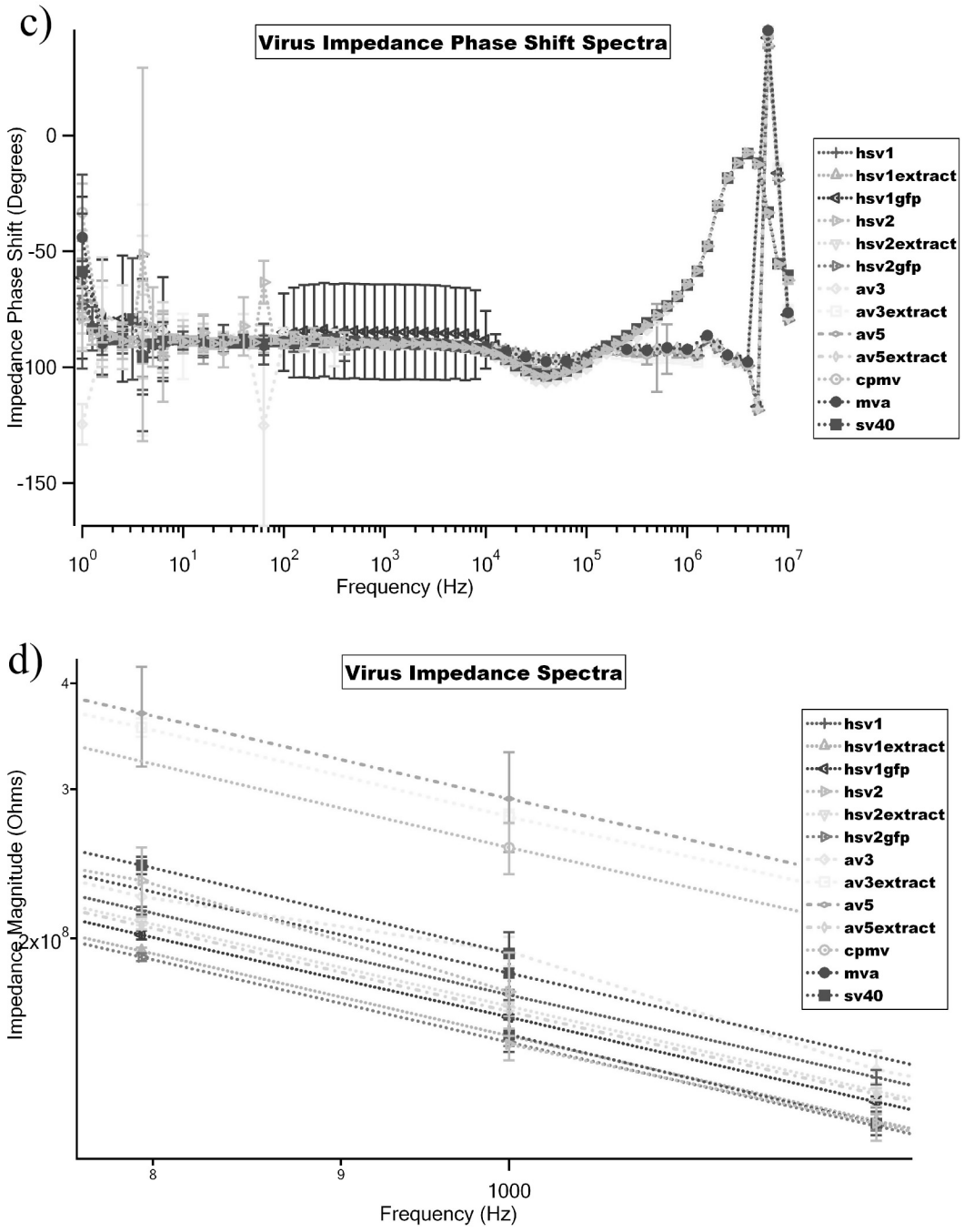


Figure 6-25. Spectra for all viruses characterized of a) impedance, b) capacitance, c) impedance phase shift. d) A region of the impedance spectra is magnified to show the differences between impedance spectra more clearly.

Table 6-4. Capacitance of Viruses at 10 kHz.

Virus	**Capacitance (F) at 10 kHz**	**Virus Size (nm)**	**Virus Shape**	**Envelope Present?**	**DNA/RNA virus?**
hsv2	1.07000E-12	110	Spherical	Yes	dsDNA
sv40	1.04000E-12	55	Spherical	No	dsDNA
hsv2gfp	1.03222E-12	110	Spherical	Yes	dsDNA
hsv1extract	1.01232E-12	100	Spherical	No	dsDNA
hsv1gfp	9.61581E-13	110	Spherical	Yes	dsDNA
av5extract	9.47000E-13	65	Spherical	No	dsDNA
hsv2extract	9.32466E-13	100	Spherical	No	dsDNA
hsv1	9.03753E-13	110	Spherical	Yes	dsDNA
mva	8.53141E-13	270 x 360	Oval	No	dsDNA
av3	8.48000E-13	75	Spherical	Yes	dsDNA
cpmv	5.99000E-13	25	Icosahedral	No	ssRNA
av3extract	5.46883E-13	65	Spherical	No	dsDNA
av5	5.21683E-13	75	Spherical	Yes	dsDNA
Virus	**Capacitance (F) at 10 kHz**	**Virus Size (nm)**	**Virus Shape**	**Envelope Present?**	**DNA/RNA virus?**

Topographical images of all of the viruses studied to create Table 6-4 were collected. In Figure 6-26 some of the AFM data is displayed. MVA, CPMV, and SV40 were all shown in this figure. In Figure 6-26a, the height image for Vaccinia is

displayed, with the corresponding section analysis shown in Figure 6-26b. The height image for CPMV is shown in Figure 6-26c, with the corresponding cross section analysis shown in Figure 6-26d. SV40 has its height AFM image shown in Figure 6-26e, with the corresponding section analysis shown in Figure 6-26f. The remainder of the viruses from Table 6-4 and Figure 6-25 will have their AFM data discussed as their impedance spectra are described in more detail.

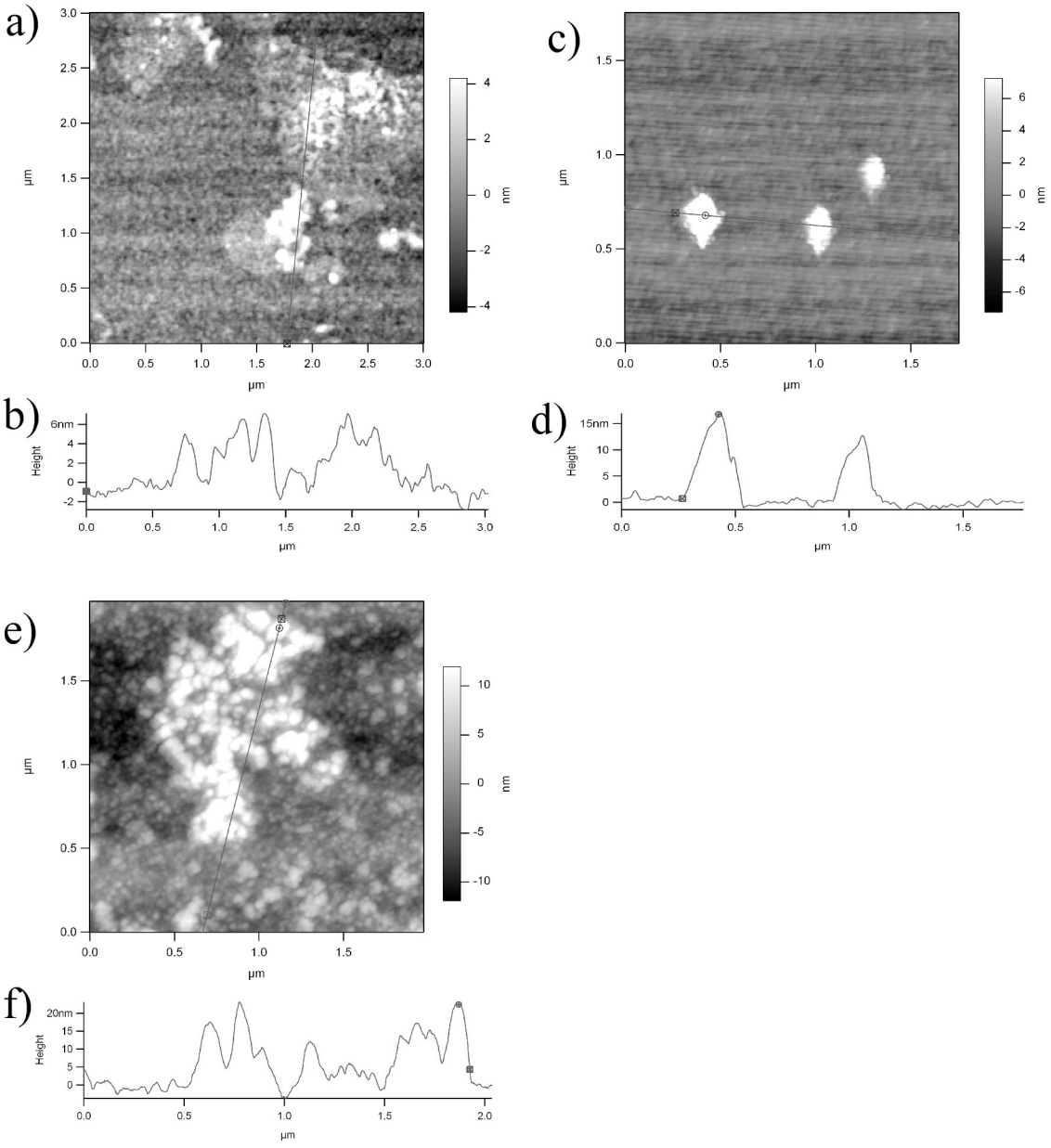


Figure 6-26. AFM height and section analysis data for three viruses. a) Height image and b) section analysis for Vaccinia (MVA). c) Height image and d) section analysis for Cowpea Mosaic Virus (CPMV). e) Height image and f) section analysis for Simian Virus 40 (SV40).

b) HSV-1

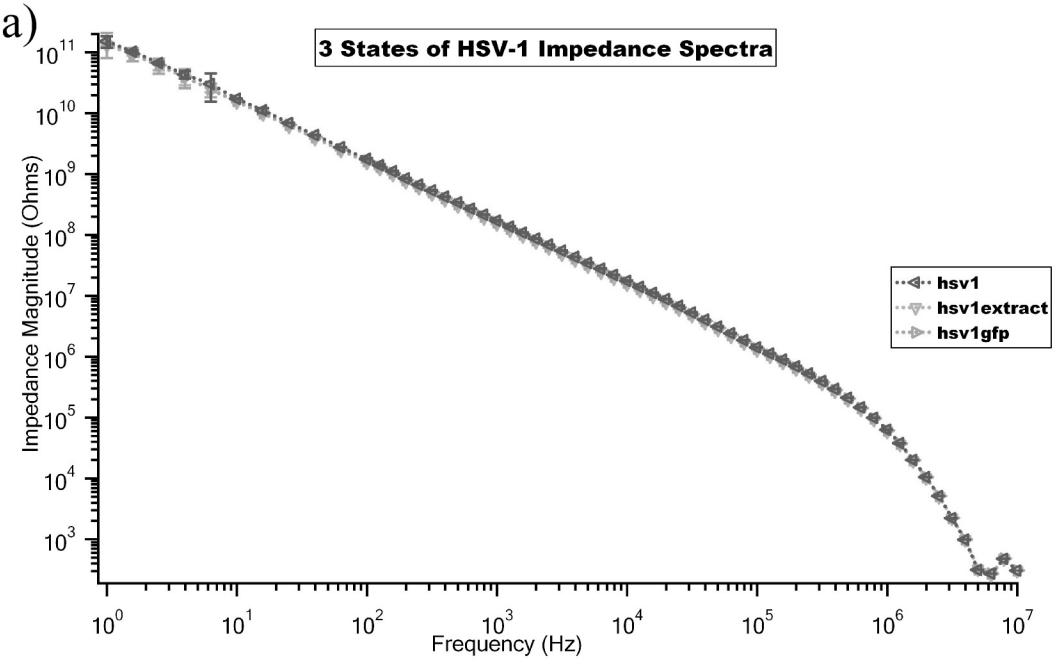
Biologists and virologists have shown as virus capsid proteins bind certain receptors or drugs, quantifiable changes in surface charge occur[149]. This could allow monitoring of fundamental properties of viruses throughout their lifecycle since adding layers of materials (such as envelope proteins) with different dielectric constants should change the overall capacitance of the materials. Since the model system of polystyrene showed that not only do changes in size of particles affect impedance spectra but also changes in the surface chemistry create a corresponding shift, it is possible to propose a system that collects a library of spectra with different biological conditions in order to monitor the health or state of a virus under analysis. As a proof of principle, three types of HSV-1 virions were studied, including native or wild type, capsid extracted, and GFP-mutant. The impedance spectra are displayed in Figure 6-27a, and a magnified area of the impedance spectra is displayed in Figure 6-27d. The capacitance spectra are displayed in Figure 6-27b, while the phase shift spectra is displayed in Figure 6-27c. The native HSV-1 was characterized and plotted as the dotted trace with triangular markers pointing towards the left.

To determine what the effects of the envelope would have on the impedance spectra, a Freon extraction was performed to remove the envelope layer[150]. The remaining capsid structures were studied by impedance, and plotted as the dotted trace

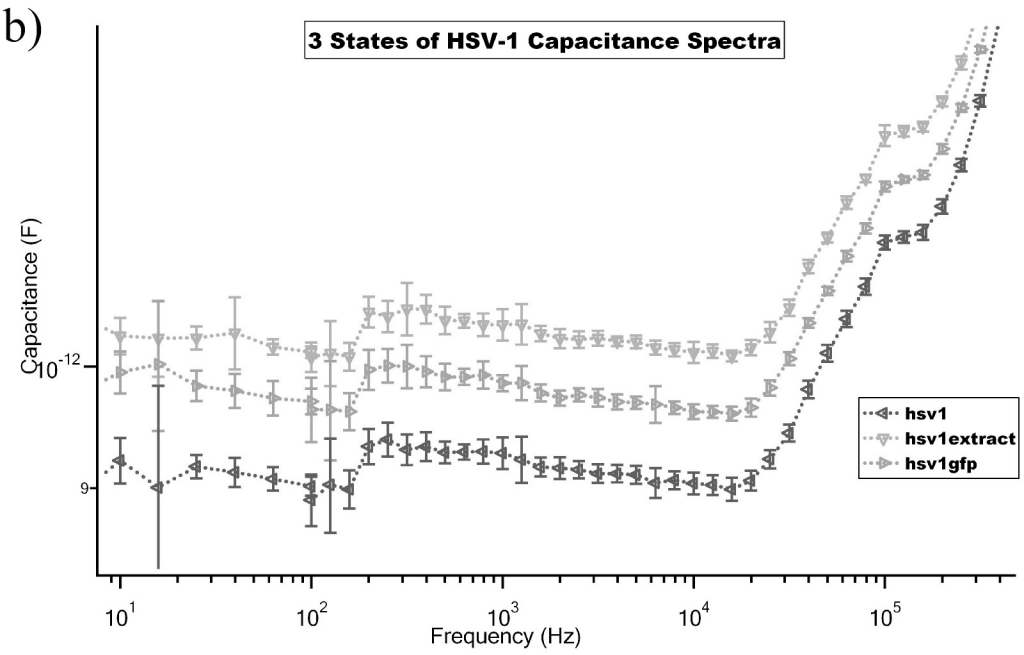
with triangular markers pointing downward. A clear increase in capacitance was observed.

Finally, in order to study whether a mutant strain of virus would be distinguishable from a native strain, the capsid protein VP26 was modified such that it contained a fusion to Green Fluorescent Protein (GFP). This mutant protein is estimated to produce between 300 and 600 copies of the GFP-VP26 fusion protein in the capsid structure[151]. This amount of GFP expression provides a significant enough change to the material composition of the virus that a statistically significant shift in capacitance is observed by the dotted trace with the triangular markers pointing towards the right. Since GFP has an isoelectric point less than seven, approximately 6.1 to 6.4 depending on the species the GFP was obtained from, there is a slight negative charge under neutral pH conditions to the overall GFP protein[152]. One can enter the amino acid sequence into the ProtParm website (http://www.expasy.org/tools/protparam.html) to have the pI calculated automatically. By adding several hundred slightly negative proteins, the expectation of a shift in capacitance would be established since the charge density and dielectric constant of the capsid should change. This expectation was confirmed by the observation that the GFP mutant form of the HSV-1 virion had an increase in capacitance. This trend is the opposite of the control experiments, and appears to contradict the information obtained from them.

a)


3 States of HSV-1 Impedance Spectra
Impedance Magnitude (Ohms)
Frequency (Hz)
hsv1
hsv1extract
hsv1gfp

b)


3 States of HSV-1 Capacitance Spectra
Capacitance (F)
Frequency (Hz)
hsv1
hsv1extract
hsv1gfp

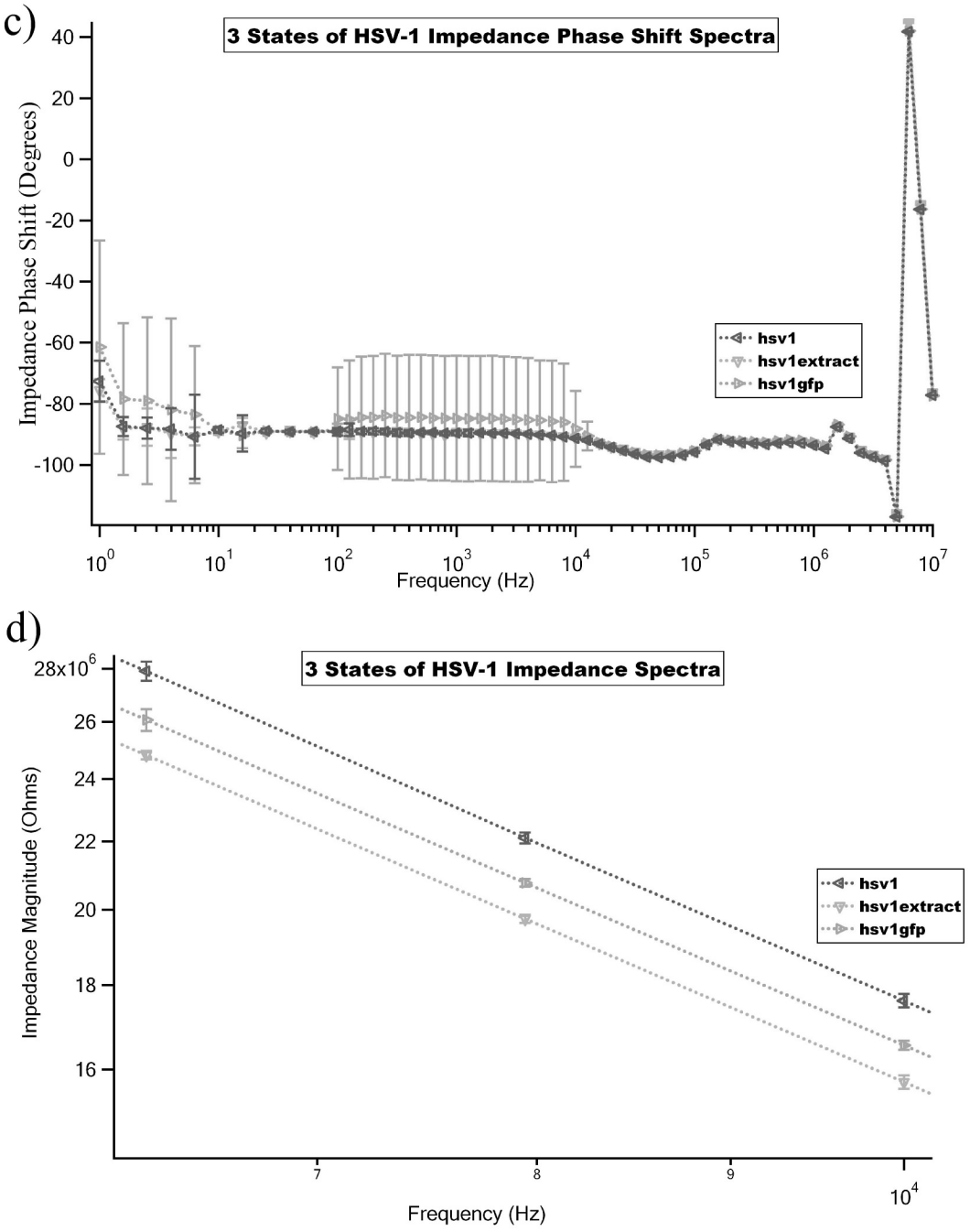


Figure 6-27. Three types of HSV-1 virions.

Topographical images of these three types of HSV-1 virions were collected, and are displayed in Figure 6-28. In Figure 6-28a, the height image of the native HSV-1 virions were displayed, with the corresponding section analysis shown in Figure 6-28b.

It was an interesting observation that the virions had approximately the correct width but appeared to have collapsed when dried in air, perhaps unable to support their own weight. The height of the virions in the section analysis appeared to be nearly an order of magnitude too small. In Figure 6-28c, a height image of the capsid extracted from native HSV-1 was shown, with the corresponding section analysis shown in Figure 6-28d. The capsids of the HSV-1 virions appeared to be taller in the section analysis than the native HSV-1 virions, however the capsids were still shorter than expected. The height image showed monodisperse virions, with the expected width. In Figure 6-28e, the height image of the HSV-1 GFP mutant strain of virion is shown, with the corresponding section analysis shown in Figure 6-28f. The GFP mutant appeared to be the correct height and width from the section analysis. However, the height image showed large aggregations of multiple viruses.

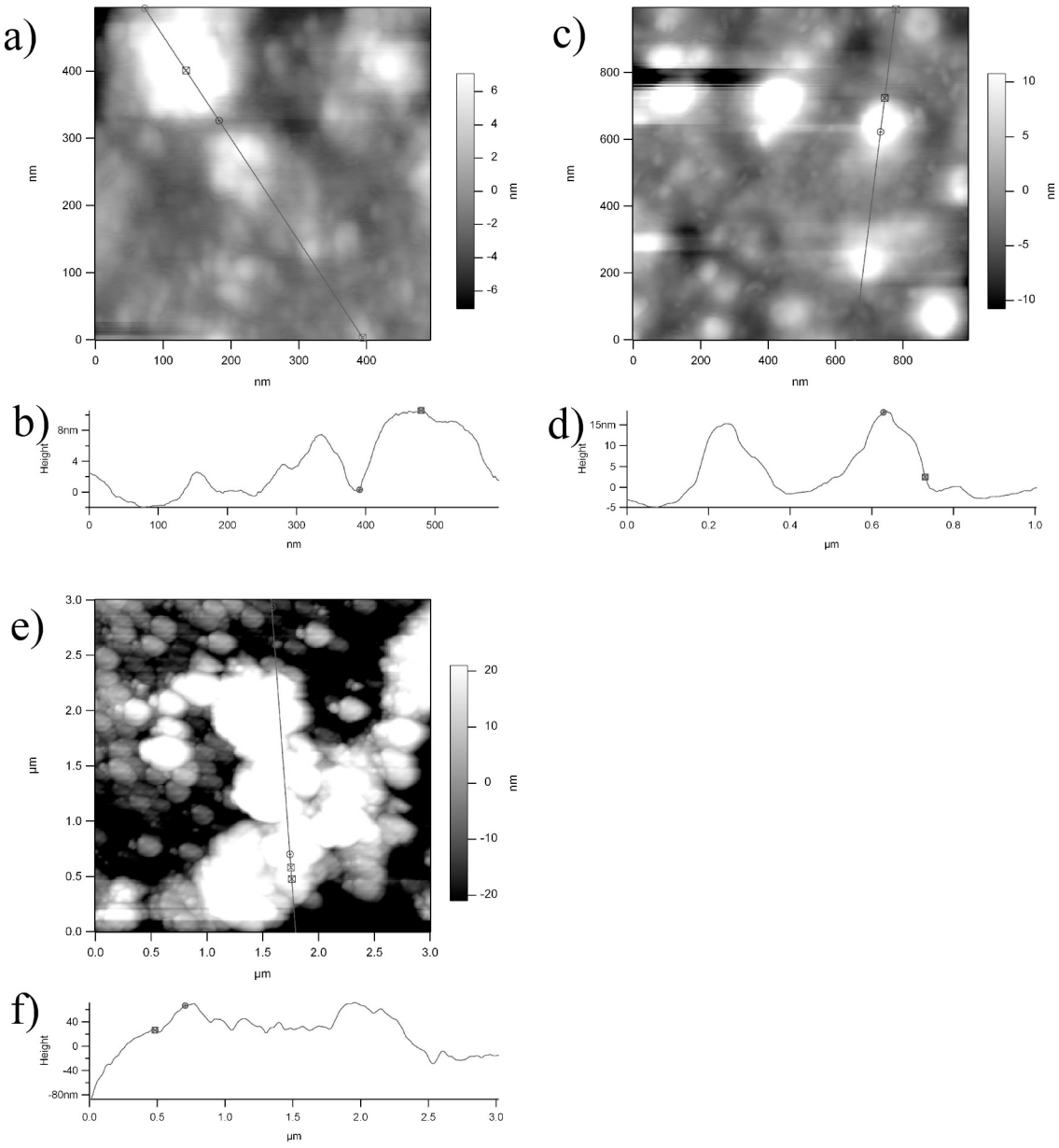


Figure 6-28. AFM images of three types of HSV-1 virions. a) Height and b) section analysis of native HSV-1 virions. c) Height and d) section analysis of the capsids extracted from the HSV-1 virions. e) Height and f) section analysis of the HSV-1 GFP mutant virions.

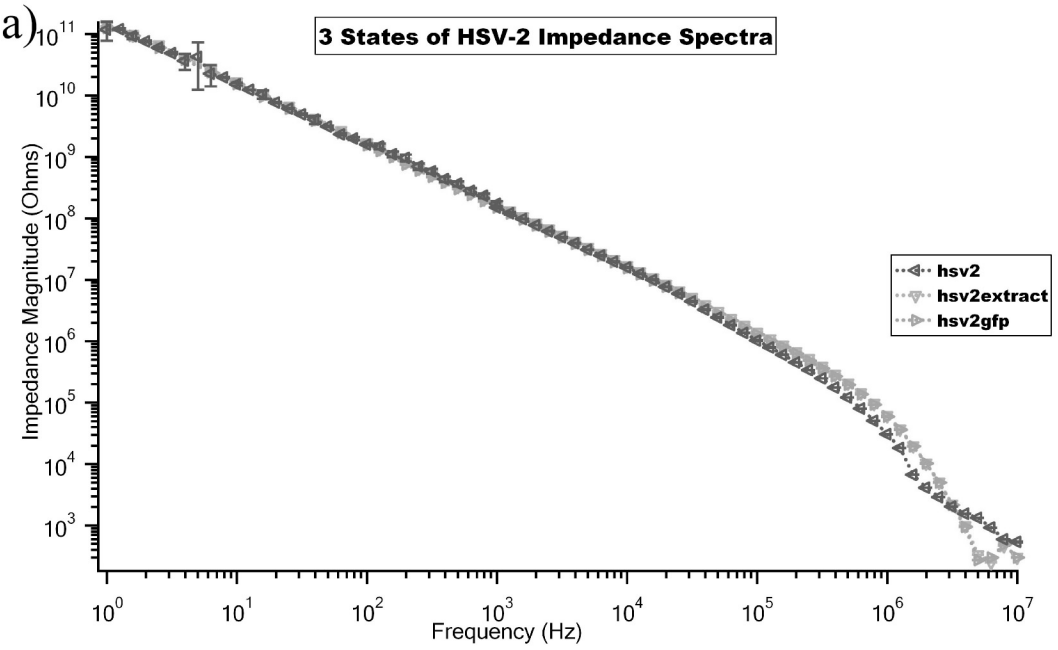
c) HSV-2

The same series of experiments were performed on HSV-2 virions. The impedance spectra were shown in Figure 6-29a, and a magnified region of those spectra

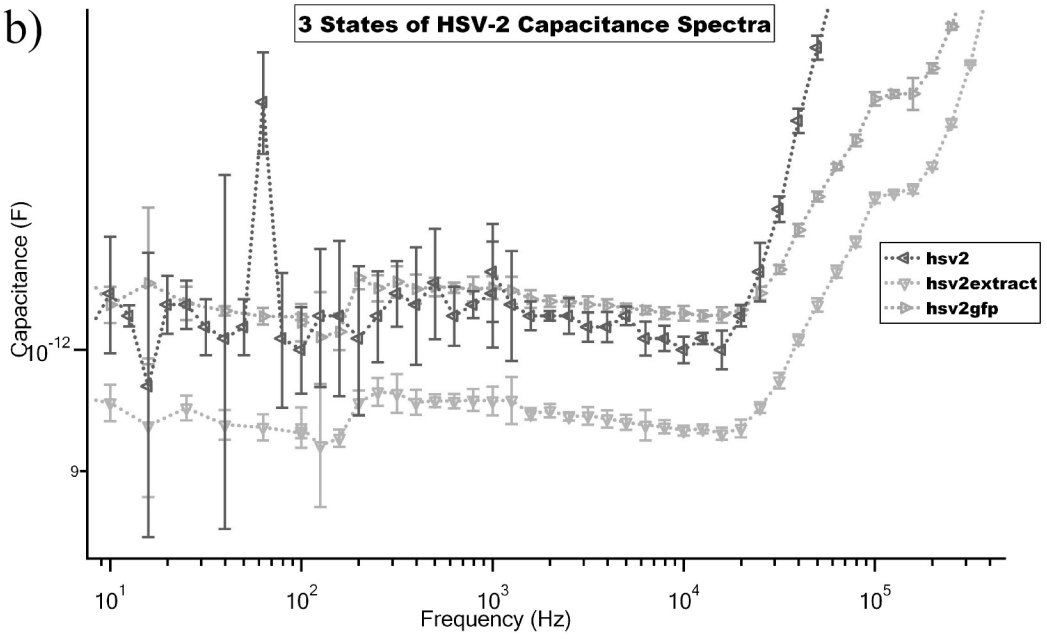
was shown in Figure 6-29d. The capacitance spectra were shown in Figure 6-29b, and the phase shift spectra were shown in Figure 6-29c. The native HSV-2 was shown in the dotted trace with the triangular markers that pointed towards the left. The HSV-2 capsids that were extracted from the native HSV-2 were plotted on the dotted trace with the triangular markers that pointed downward. The HSV-2 GFP mutant virions, which had the same rate of expression of mutant VP26-GFP copies of protein as HSV-1, were plotted on the dotted trace with the triangular markers that pointed towards the right. In the case of HSV-2, there was not a statistically significant difference in capacitance between the native HSV-2 and the GFP mutant of HSV-2, in contrast to the results observed with HSV-1. This was especially surprising considering the GFP should have modified the dielectric constant and charge density of the capsid. However, the precise isoelectric point and dielectric constant of the native HSV-2 capsid was not known. This creates the possibility, albeit unlikely, that the native HSV-2 capsid was equal in dielectric constant to the surrounding envelope layer's dielectric constant. Therefore the addition of more material of the same dielectric constant may not significantly modify the observed overall capacitance by the introduction of the GFP.

In the removal of the HSV-2 envelope, a significant decrease in capacitance was observed when compared to the native HSV-2 virions. This decrease in capacitance suggested that the envelope glycoproteins in HSV-2 were somehow different electrically than the HSV-1 envelope glycoproteins.

a)


3 States of HSV-2 Impedance Spectra
Impedance Magnitude (Ohms)
Frequency (Hz)
hsv2
hsv2extract
hsv2gfp

b)


3 States of HSV-2 Capacitance Spectra
Capacitance (F)
Frequency (Hz)
hsv2
hsv2extract
hsv2gfp

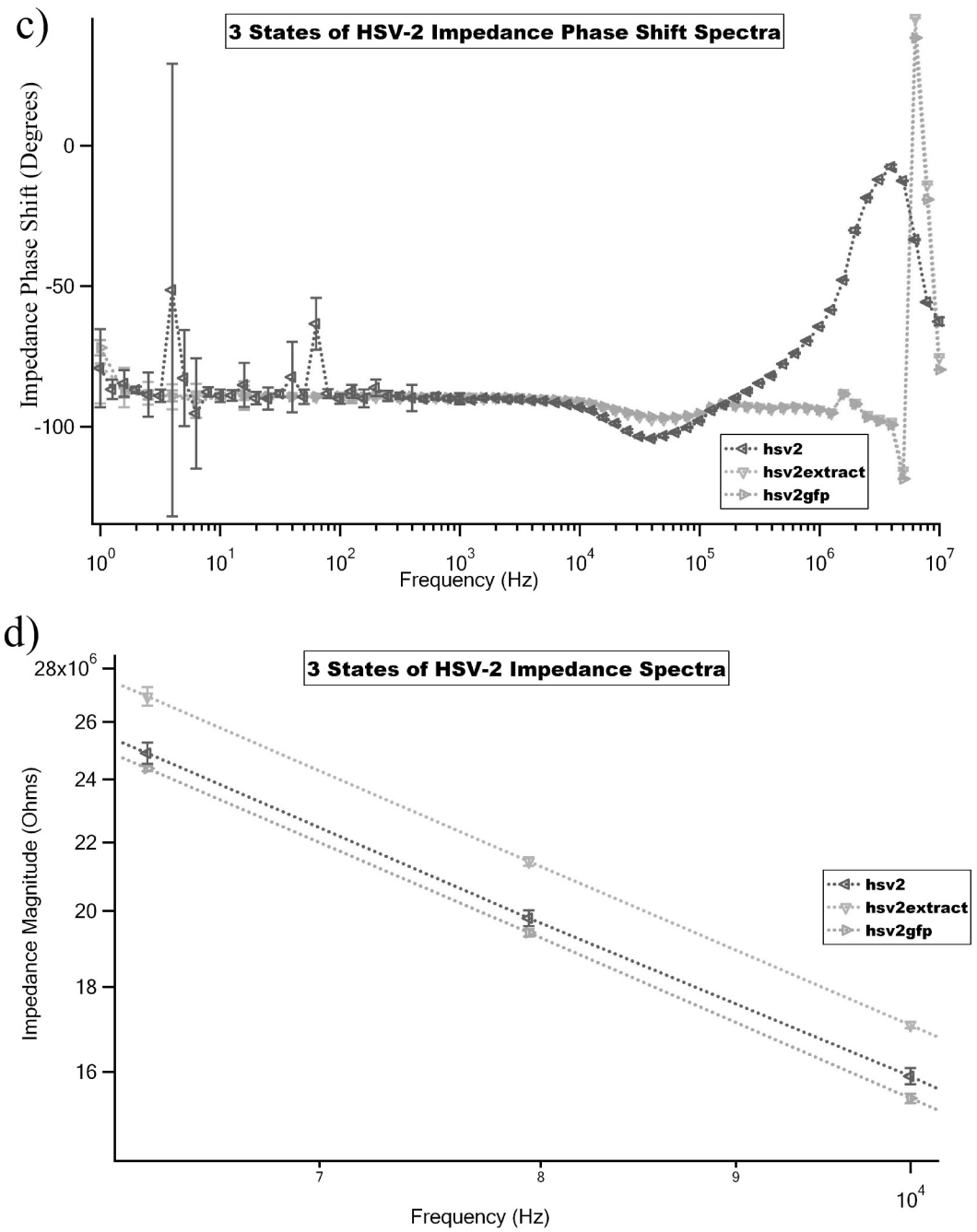


Figure 6-29. Three states of HSV-2 virions. a) Impedance, b) capacitance, c) phase shift, and d) magnified impedance spectra of three types of HSV-2 virions.

Topographical images were collected of the three types of HSV-2 virions, and the results were displayed in Figure 6-30. In Figure 6-30a, the height image of the native HSV-2 virions was displayed, with the corresponding section analysis shown in Figure 6-

30b. The height image of the capsids extracted from the native HSV-2 virions was displayed in Figure 6-30c, with the corresponding section analysis displayed in Figure 6-30d. The height image of the GFP mutant form of HSV-2 virions was displayed in Figure 6-30e, with the corresponding section analysis displayed in Figure 6-30f. The native HSV-2 appeared to have several virions aggregated together and dried on top of some of the growth buffer solution. When this image was shown to Asylum Research, experts in AFM characterization of biological samples replied that this result was quite common, and was the best possible result. The capsids appeared more monodisperse than the native virions, although it appeared the capsids had dried on some kind of supporting layer. The GFP mutant HSV-2 virions appeared to aggregate as well, although not to the degree that the native HSV-2 virions did. The section analysis for both the GFP mutant and native HSV-2 virions were expected widths, however the heights were about one-third the expected values. The decreased height suggested that the HSV-2 virions were collapsing under their own weight when dried out in air, however not to the degree that HSV-1 did. The height and width of the HSV-2 capsid were the expected values, with the height being reduced from the diameter of the enveloped virus. One possible explanation for the finding that the capsid maintains its height when dried out in air could stem from the fact that the capsid was structural, and supported its own weight. However, when the non-structural envelope layer was added, the capsid was not strong enough to support the added weight and collapsed.

Some observations on strains were worth mentioning. Intuitively, it may have been tempting to believe that all HSV, or all Adenovirus, are similar in structure and size and therefore would have similar impedance spectra. However, not all virus strains are

similar. For example, HSV-1 infects the eyes and mouth, while HSV-2 infects the genitals. Further, the mechanism by which these infections progress, the mechanism by which each strain enters latency, the mechanism by which each strain is reactivated from latency, and the neuronal cell type that each strain prefers to live its latent life in are all different between HSV-1 and HSV-2. The differences in biology must be accompanied by changes in the proteins and especially envelope glycoproteins to enable the different functionalities of each strain. Since each of these different glycoproteins would have different amino acid sequences, they should have different dielectric constants and charge densities, which would affect the overall virus dielectric constants and charge densities.

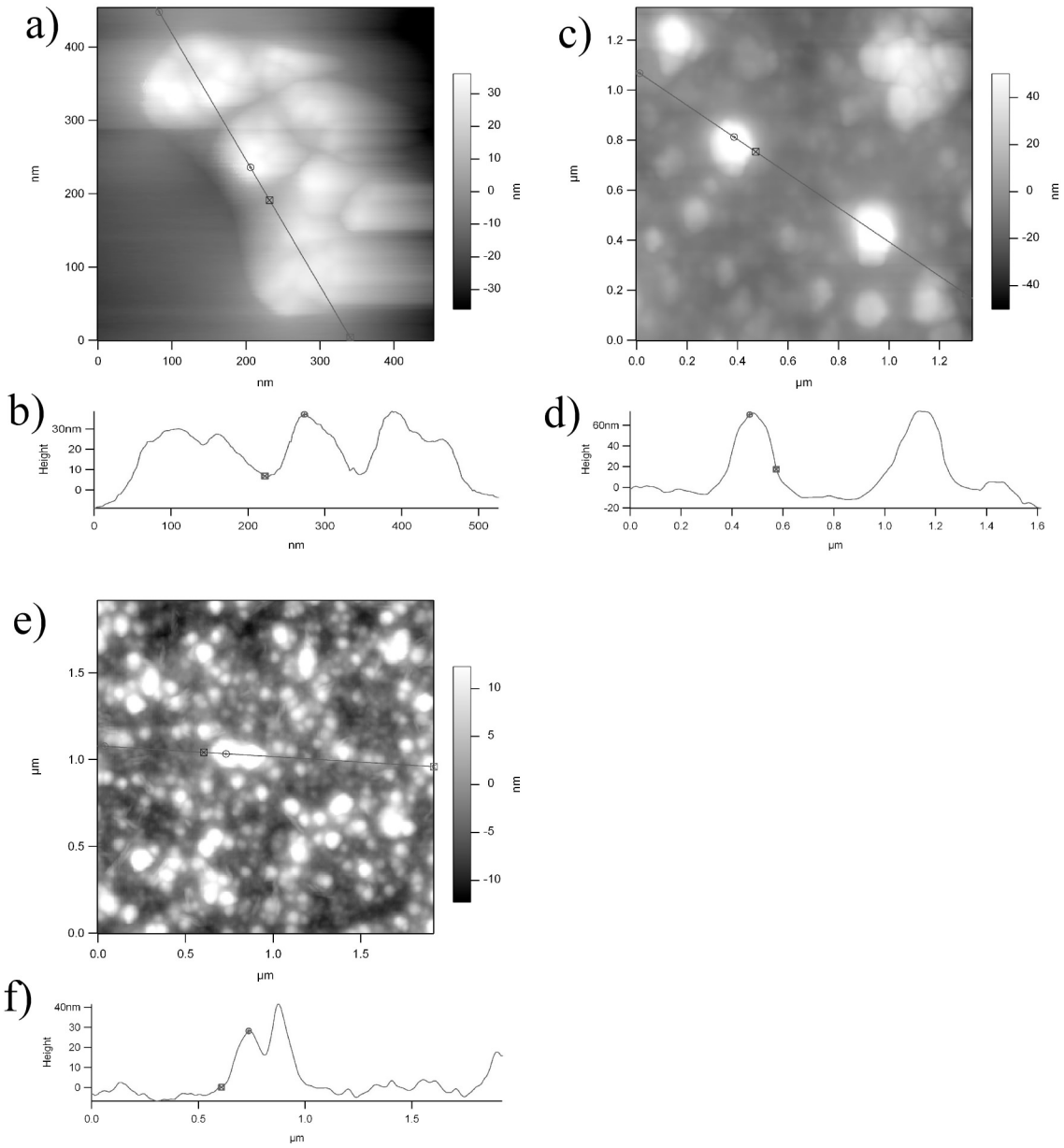
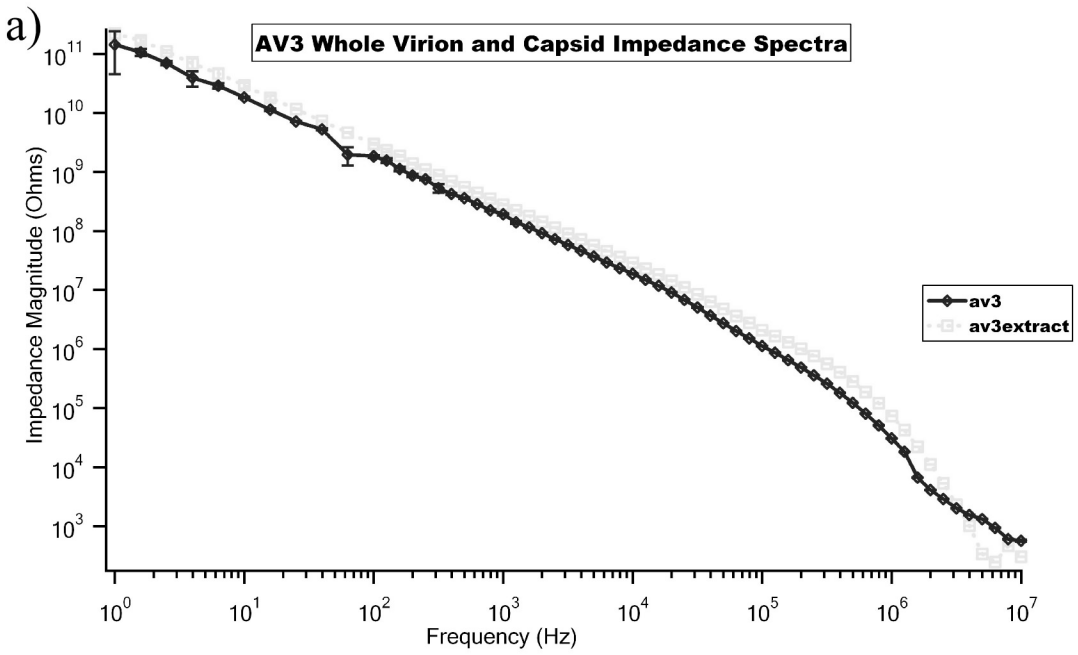


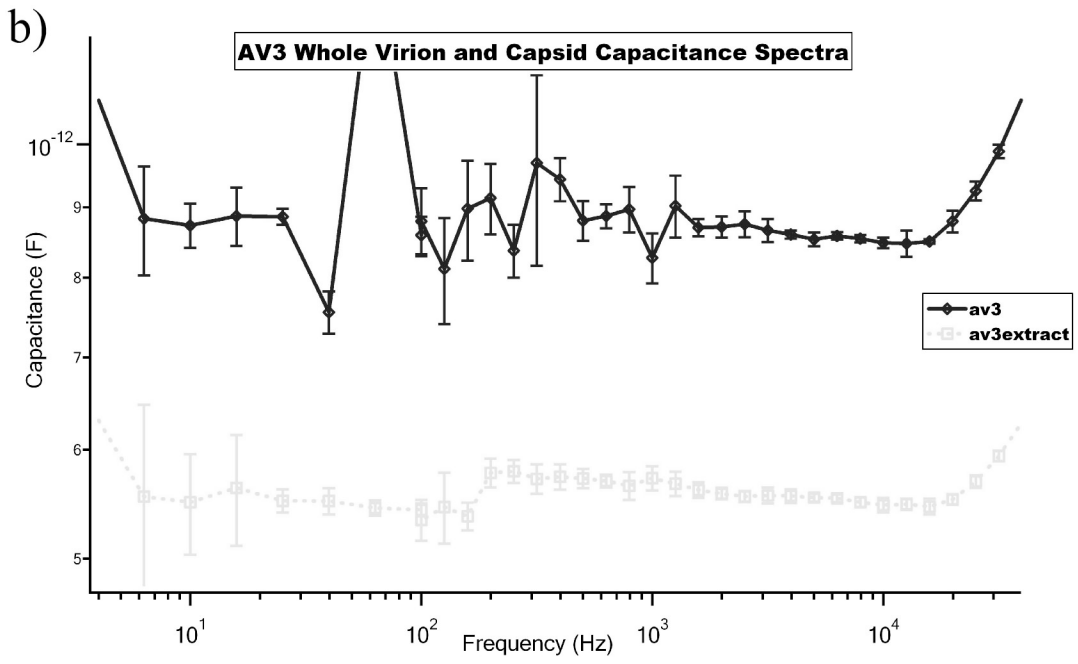
Figure 6-30. Three types of HSV-2 virions. a) Height and b) section analysis of native HSV-2 virions. c) Height and d) section analysis of the capsids extracted from the HSV-2 virions. e) Height and f) section analysis of the HSV-2 GFP mutant virions.

d) Adenovirus Type 3

Two strains of Adenovirus were studied in a more limited fashion than the two strains of HSV. Since no access to GFP mutant forms of either strain of Adenovirus used was available, only the effects of removing the envelope from the capsid were studied.

In Figure 6-31, Adenovirus Type 3 was characterized by impedance spectroscopy both with and without its envelope layer. In Figure 6-31a, the impedance spectra were plotted, and a region of the impedance spectra was magnified and displayed in Figure 6-31d. The capacitance spectra were plotted in Figure 6-31b, while the phase shift spectra were plotted in Figure 6-31c. The native Adenovirus Type 3 was shown as the dark gray trace, while the Adenovirus Type 3 capsid was shown as the light gray trace in Figure 6-31. In the case of Adenovirus Type 3, the removal of the envelope layer resulted in a significant decrease in capacitance. The removal of the glycopeptides in the envelope layer likely changed the dielectric constant of the virus, and thus altered the capacitance observed.


a)
AV3 Whole Virion and Capsid Impedance Spectra
Impedance Magnitude (Ohms)
Frequency (Hz)
av3
av3extract


b)
AV3 Whole Virion and Capsid Capacitance Spectra
Capacitance (F)
Frequency (Hz)
av3
av3extract

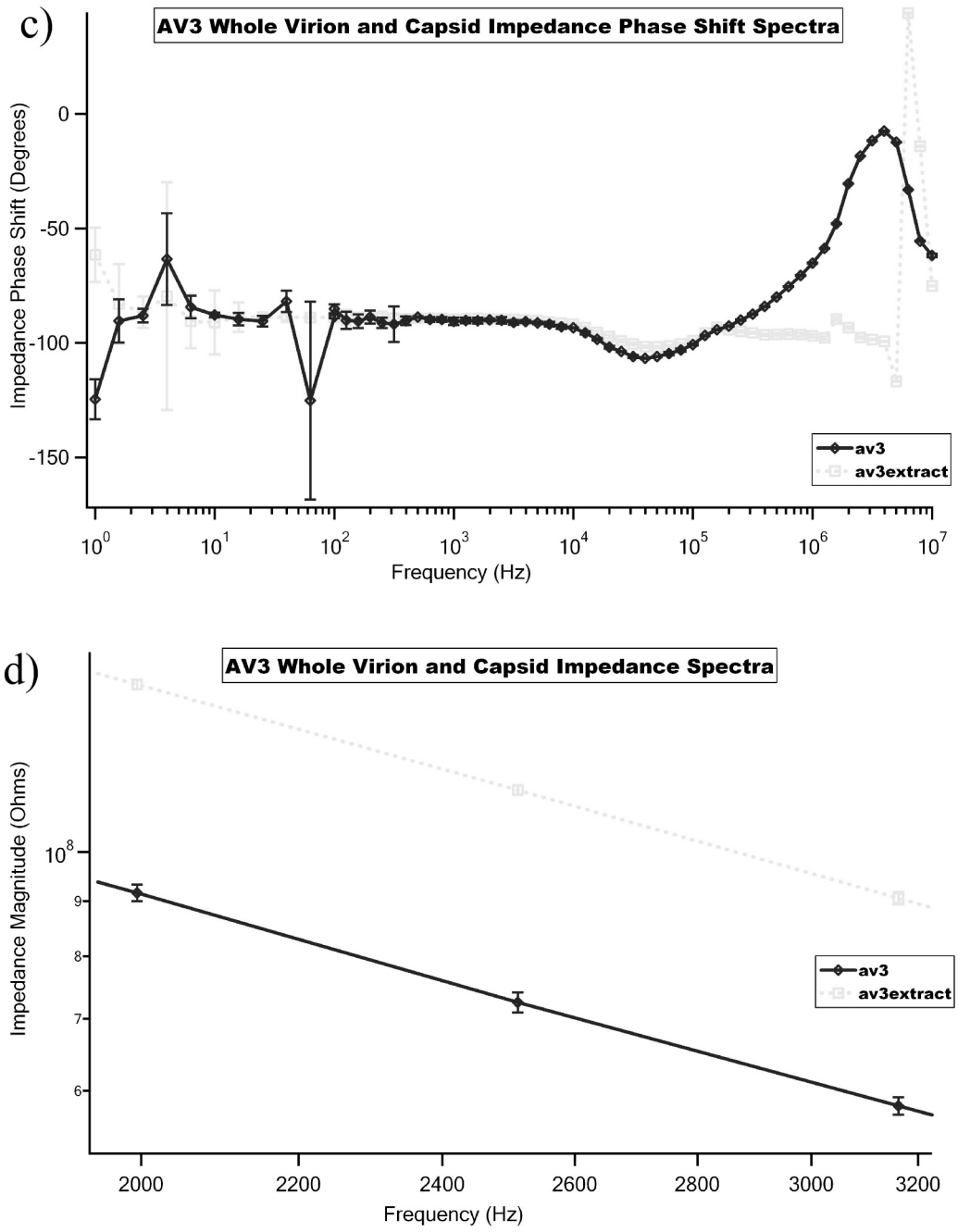


Figure 6-31. Two types of Adenovirus Type 3 virions. a) Impedance, b) capacitance, c) phase shift, and d) magnified impedance spectra of two types of AV3.

The native Adenovirus Type 3 virions were imaged by AFM, and shown in Figure 6-32. The section analysis revealed height was again lower than expected, but provided good agreement with the expected width. The height image revealed that several viruses

aggregated together and appeared to dry on top of the growth buffer. The Adenovirus Type 3 capsids were imaged by AFM before and after impedance spectra collection. This experiment was conducted to determine if there were any mechanical deformation effects of using the 100nN contact force for several minutes or if the application of an AC bias of about 10mV for several minutes would alter the structure. From the height image, the capsids appeared to be more spread out and wider than the native virions. The height was slightly higher than the native virions from the section analysis, and the height did not change between the before and after impedance measurement images. The height image did not reveal any damage to the capsids as a result of impedance measurements, in agreement with the section analysis. The most noticeable difference between the before and after height images was the thermal drift that occurred.

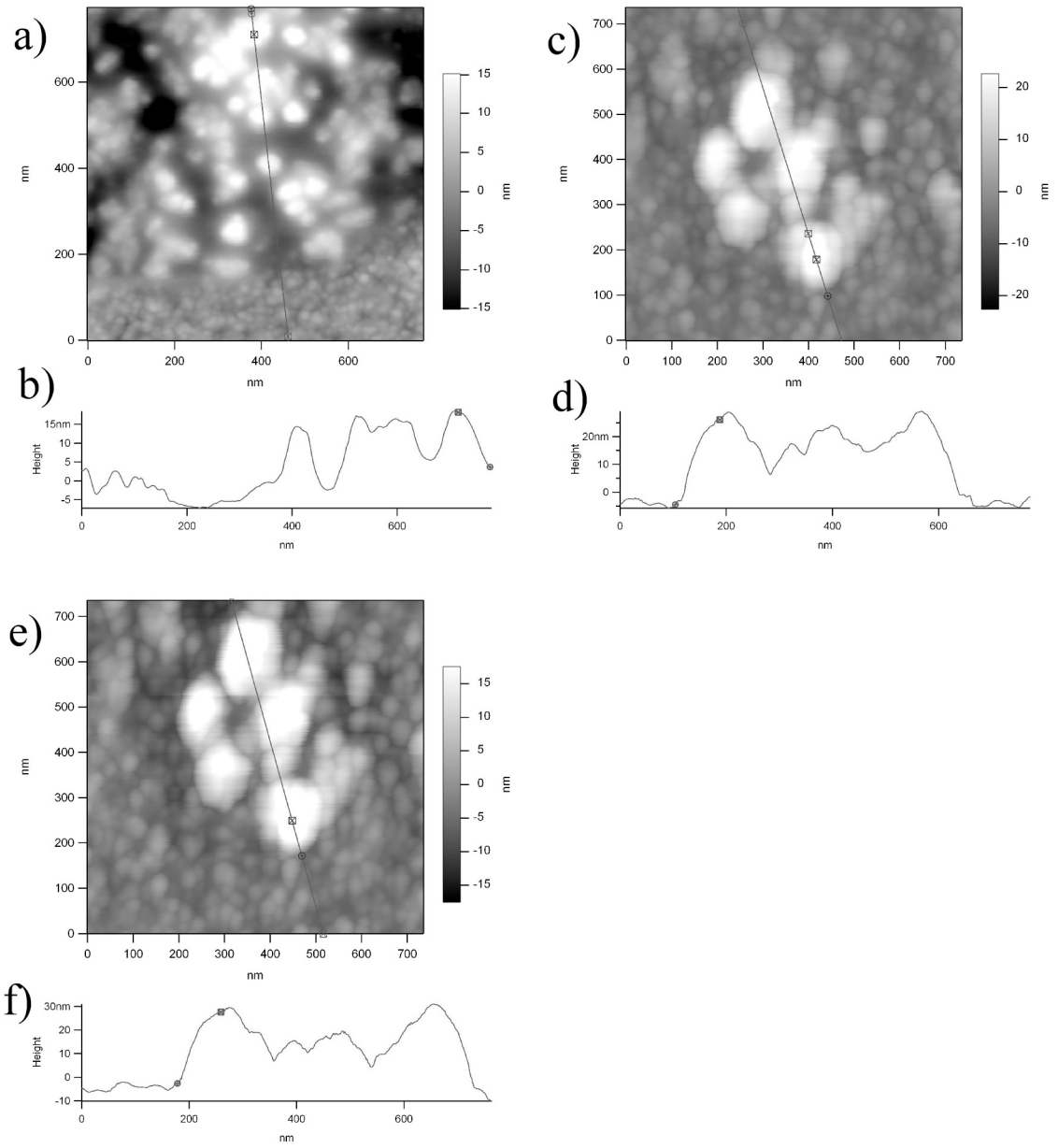


Figure 6-32. Two types of Adenovirus Type 3 virions. a) Height and b) section analysis of native AV3 virions. c) Height and d) section analysis of the capsids extracted from the AV3 virions before impedance spectra were collected. e) Height and f) section analysis of the capsids extracted from the AV3 virions after impedance spectra were collected.

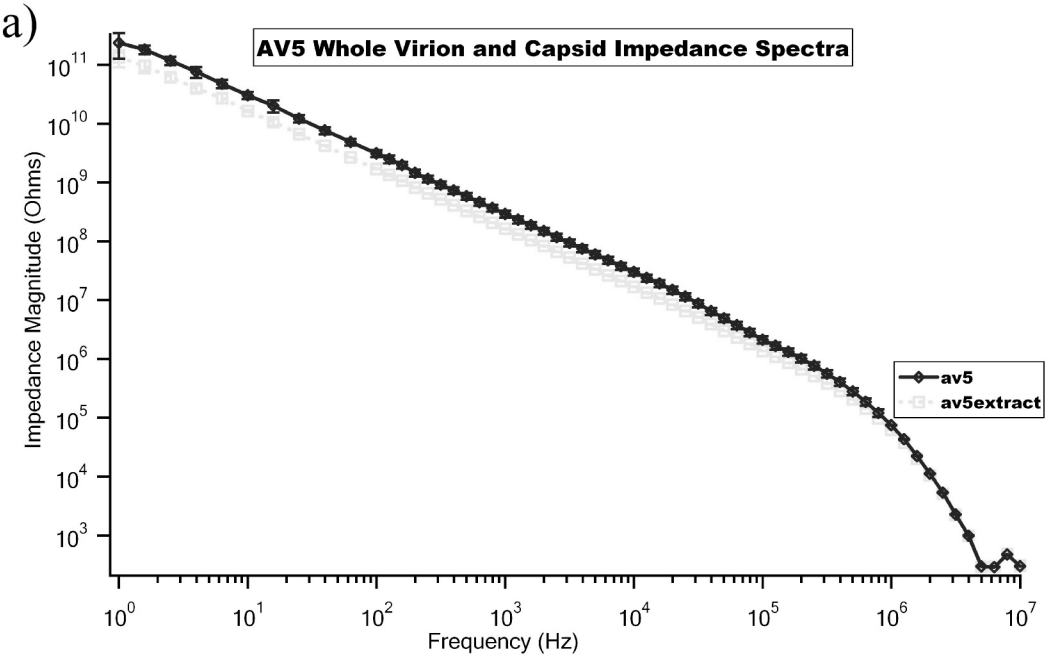
e) Adenovirus Type 5

Adenovirus Type 5 was studied with and without its envelope layer by impedance spectroscopy. The results were shown in Figure 6-33. The dark gray trace was the native

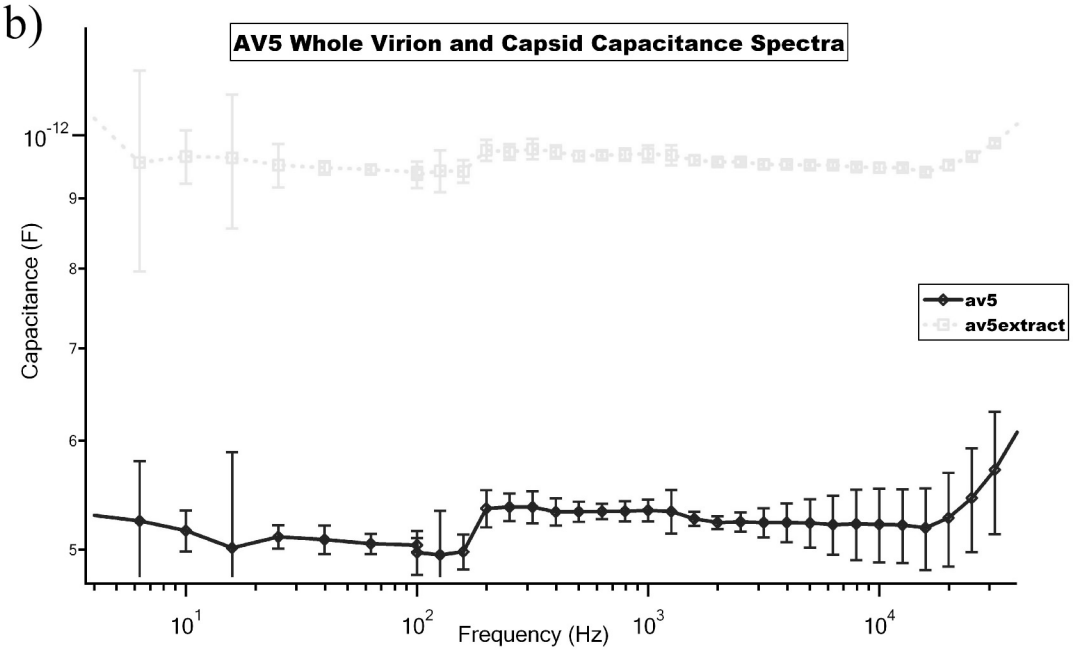
Adenovirus Type 5, while the light gray trace was the capsid extracted from the Adenovirus Type 5. In Figure 6-33a, the impedance spectra were shown with a magnified area of the spectra shown in Figure 6-33d. The capacitance spectra were shown in Figure 6-33b, while the phase shift spectra were shown in Figure 6-33c.

The capsid extracted from the Adenovirus Type 5 exhibited an increased capacitance compared to the native virions. While this was a shift in the opposite direction as that observed with Adenovirus Type 3, as previously mentioned in the discussion about HSV the envelopes between different strains of viruses should contain different glycoproteins and therefore have different effects on the dielectric constant of the native virions. Since the overall dielectric constant of the envelope layers was not known, it is possible each envelope caused an opposite shift in either the dielectric constant or the charge density of the native virions.

a)


AV5 Whole Virion and Capsid Impedance Spectra
Impedance Magnitude (Ohms)
Frequency (Hz)
av5
av5extract

b)


AV5 Whole Virion and Capsid Capacitance Spectra
Capacitance (F)
Frequency (Hz)
av5
av5extract

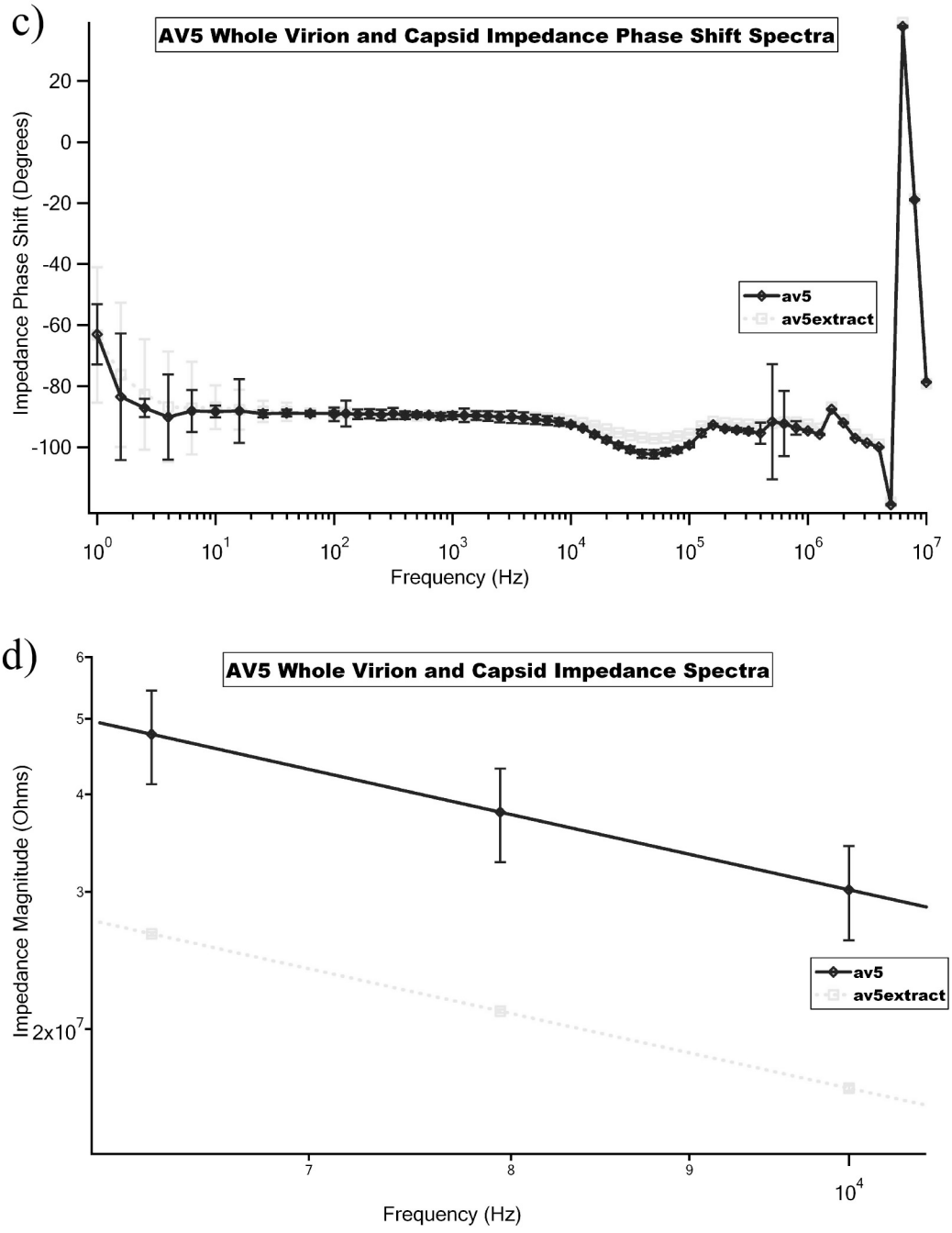


Figure 6-33. Two types of Adenovirus Type 5. a) Impedance, b) capacitance, c) phase shift, and d) magnified impedance spectra of three types of AV5 virions.

Topographical images of Adenovirus Type 5 were collected. In Figure 6-34a, the height image of the native Adenovirus Type 5 virions was displayed, with the corresponding section analysis in Figure 6-34b. The height image of the capsid extracted

from Adenovirus Type 5 was shown in Figure 6-34c, with the corresponding section analysis shown in Figure 6-34d. In both section analyses the height was consistent, however there was a small change in the width of the capsid. It also appeared from the height images that the shape of the capsid was different from the shape of the native virion. The capsid appeared more oval-like than the spherical native virion.

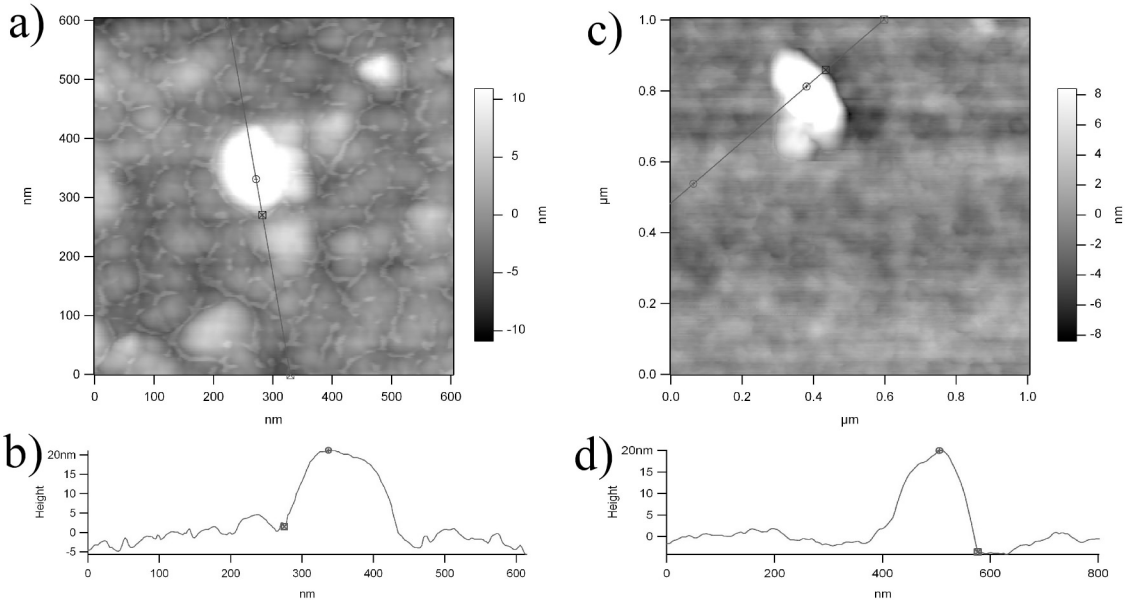


Figure 6-34. Two types of Adenovirus Type 5 virions. a) Height and b) section analysis of native AV5 virions. c) Height and d) section analysis of the capsids extracted from the AV5 virions.

In total, the data of these thirteen different virions suggested that as changes to the material composition of the virion occur, they should be able to generate observable changes in capacitance and impedance spectra. While at this time it was not clear why the removal of envelope results in capacitance shifts in opposite directions, it is also not known precisely what the dielectric constants of the envelope layer for each strain are or what the dielectric constants for the capsids of each strain are. It was possible the dielectric constants for each capsid or each envelope are different enough from one

another to produce the shifts in opposite directions. Nevertheless, the ability to collect a library of spectra to compare unknown virions to would allow at least some level of classification of virions. The best method of detection would not rely solely on electrical data alone, however. The combination of physical size, biological recognition, and electrical properties would allow a robust method of identification based on three criteria.

An experiment was run where a DC bias was applied on top of the AC bias, and this DC bias was swept from -5V to +5V. In the case of the impedance measurements previously described there was no DC bias offset, and the AC bias was only 10mV. The AC bias was below the Johnson noise limit from thermal noise of 26mV, and therefore did not electrically perturb the systems under study. However, if there were any polarizable materials, an increase in dielectric constant should occur as the dipoles aligned along the field lines and became capable of stabilizing more charge on the plates of the capacitor (the AFM tip and electrode substrate). Overall, no changes in impedance were observed at any DC bias offset, despite some noise likely from thermal drift. Therefore, there is not a dipole that is inducible by an external electric field that could allow for an increased dielectric constant and therefore higher capacitance. As shown in Figure 6-35, the capacitance was approximately constant at all DC biases. The peak at the beginning near -5V is likely from the tip drifting off of a particle then drifting back onto one near the start of the scan. Over 150 impedance spectra were collected over a 12 hour period, making thermal drift unavoidable. The thermal drift is likely the cause of the unexpected spikes in the capacitance and various DC biases, being localized as the tip drifts near the edge of the virus then back towards the center for other measurements and thus creating the sharp spikes in the capacitance.

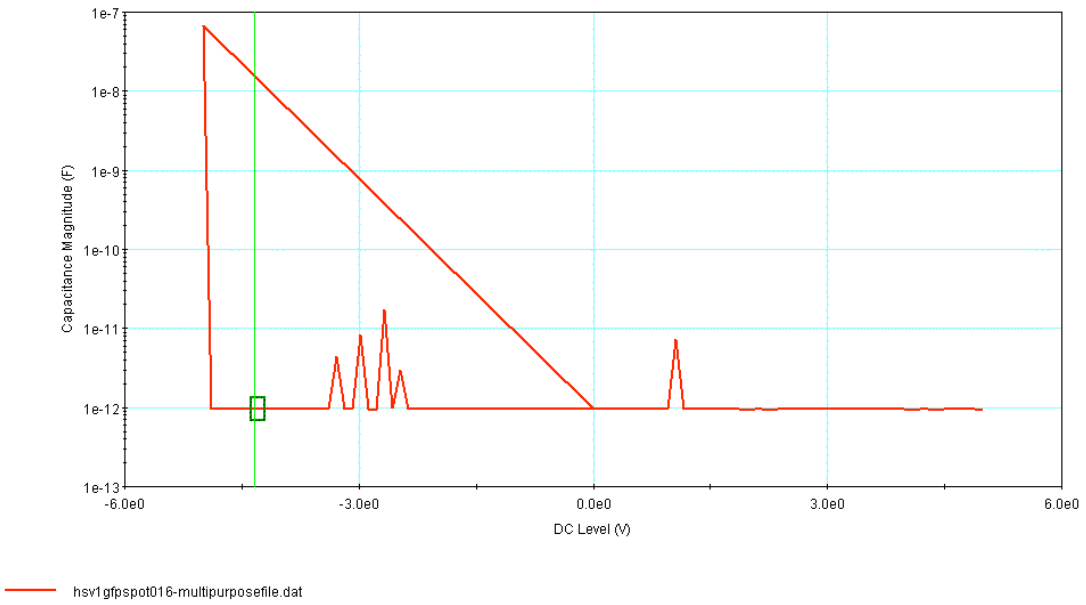


Figure 6-35. DC sweep from -5V to +5V, of HSV-1+GFP mutant.

6. CONCLUSION

In conclusion, there has been significant progress made towards the goal of using impedance/AFM to measure the electrical response of nanomaterials. An impedance/AFM instrument, in collaboration with Asylum Research, has been designed, developed and implemented. This instrument allows for extremely sensitive impedance measurements to be made on individual nanoparticles. Using polystyrene and other insulating nanoparticles as a model system, we have demonstrated that this technique is sensitive to both the size and the material of nanoparticles. Although the direction of the shift in impedance was not consistent, changes in nanoparticle size resulted in changes in impedance, as well as changes in material resulted in changes in impedance. We have also shown that this technique can differentiate between viruses by combining the

impedance data and the AFM images of the viruses. Presently this data is not enough to discriminate viruses by itself, due to the unknown relation between the observed capacitance and the virus structure. In the future, we hope to extend this technique to quantitatively determine properties of nanomaterials such as their dielectric constant, which are important for many applications of these new materials in devices.

7. EXPERIMENTAL DETAILS

To develop a suitable interface between the AFM and the impedance analyzer that would not compromise extreme sensitivity requirements, a stand-alone MFP-3D AFM (Asylum Research, Santa Barbara, CA, USA) was fitted with a custom modification. Use of an external circuit board allowed the addition of current-limiting resistors when testing highly conductive samples.

Platinum coated tips with a radius of curvature of less than 40nm and spring constant near 40 N/m were used for AFM imaging and electrical measurements (Mikromasch NSC15-Ti/Pt, Wilsonville, OR, USA; Nanosensors PPP-NCHPt, NanoAndMoreUSA, Lady's Island, SC, USA). Non-contact or AC mode images were collected to find particles of interest to minimize tip wear and lengthen the useful life of the metal coating on the AFM tips. Points were selected using the force curve panel to move the tip precisely through the closed-loop scanner to the center of the nanoparticles selected. A constant force of 100 nN was used for all the experiments.

Polystyrene nanoparticles of 58nm, 100nm, and 202nm, as well as all amino functionalized and carboxy functionalized polystyrene nanoparticles were used as

received (Polysciences, Warrington, PA, USA). Polymethylmethacrylate nanoparticles of 60nm, 110nm, and 140nm were used as received (Bangs Labs, Fishers, IN).

Model silica nanoparticles were synthesized by Stöber's process. The detailed mechanism and kinetics on the preparation of monodisperse silica nanoparticles are well summarized in the reference[153]. In order to prepare silica nanoparticle ethanol suspension with different sizes, the molar ratio of silica precursor and water was kept constant while the molar ratio of ammonium hydroxide was changed. The concentration of water and TEOS (tetraethyl orthosilicate, Aldrich: silica precursor) are kept 5.0 M and 0.2 M, respectively while the NH_4OH concentration changed from 0.01 to 0.5 M. Generally, the higher concentration of NH_4OH results in the larger nanoparticles.

All the chemicals were mixed overnight to complete the reaction. After the reaction, the mixture changed to be milky indicating the silica nanoparticle formation. The synthesized silica nanoparticles were centrifuged (8,000 rpm, 20 minutes) and washed with pure ethanol to remove unreacted chemicals.

The synthesized silica nanoparticles are negatively charged covered with hydroxyl groups. The negative surface charge was modified to be positive by introducing amine-terminated silica modifier. A volume of 0.3 mL of 3-aminopropyltrimethoxysilane (Gelest, 90%) and 5 mL ethanol were added to 5 mL of silica suspension. This mixture stirred for 1 day at room temperature following centrifugation and re-suspension in ethanol. The surface charge was shielded to be neutral by attaching hydrophobic alkyl chains on the surface. Esterification at the silica nanoparticle surface with stearyl alcohol was carried out at 180-200 ºC under nitrogen.

After the esterification, the surface-modified silica was centrifuged and re-suspended in n-hexane.

All purchased particles were diluted to 10^7 particles/mL; based on the manufacturer's specifications of initial particle concentration in particles/mL, serial dilutions to the final concentration of 10^7 particles/mL were performed; ultimately, the precise concentration of particles in the final solution was not known, as it was not measured after preparation; however, the precise concentration is not required to be known when one is interested in depositing particles in a dispersed monolayer onto a substrate, since there are broad ranges of concentration for which deposition of nanoparticles on surfaces will create suitable samples for AFM analysis of single nanoparticles, and therefore it was logically determined that knowing the precise concentration was not only not required, but very time consuming for no appreciable gain to gathering of the experimental data for impedance spectra collection. Then, 10uL of solution was deposited on gold substrates (Asylum Research, Santa Barbara, CA, USA). For each size and polymer of nanoparticle in a figure, at least fifty unique particles from different sample preparations were characterized. During the study different conductive tips were used on different days and different sample preps. The impedance spectra collected were averaged with error bars and shown at each frequency observed in the collection of the spectra.

Adenovirus Type 5 (AV5) were used as received from American Type Cell Culture (VR-1516). Herpes simplex virus type 2 (HSV-2) strain 333 was grown in Vero cells as described[121]. Adenovirus Type 3 (AV3) (ATCC# VR-847) was used as received from the American Type Culture Collection (Manassas, VA). Titered stocks of influenza

vaccine strains B, simian virus 40 (SV40), and Vaccinia (MVA) were obtained from Drs. Andrew Lewis, Zhiping Ye, and Michael Merchlinsky (all at FDA/CBER), respectively. HSV-1 and HSV-2 GFP mutants were obtained from Andrea Bertke (FDA/CBER). To create a series of spiked samples for analysis, 10-fold serial dilutions in 1X PBS were performed from virus stocks with known concentrations.

The envelopes of the virions were removed by a Freon extraction. Freon was used as received from Fisher, and added to a virus stock solution in a 1:1 volume:volume ratio. The mixture was vortexed for 30 seconds, then centrifuged at 14k rpm for 30 seconds. The aqueous layer was collected, which contained the capsids.

Humidity was controlled for all impedance AFM experiments by monitoring the humidity inside the acoustic isolation hood chamber. If the humidity was above 35%, nitrogen was pumped into the hood to lower the humidity. Experiments at several humidity levels were performed systematically from 10% to 90% humidity, however no difference in impedance was observed (data not shown). To increase the humidity, a simple ultrasonic humidifier, typically used for a room in a house, was fitted with a connection to plumb a pipe into the acoustic hood such that the humid air could be flowed into the acoustic hood chamber and increase the humidity.

A Solartron 1260 Frequency Response Analyzer with a Solartron 1296 Dielectric Interface (AMETEK, Paoli, PA, USA) was used for impedance and capacitance spectra collection. Circuit modeling was performed using Origin. An applied AC bias of 10mV was used to stay below the Johnson noise at room temperature of 26mV, thereby minimizing electrical perturbations to the materials in the system. There was no DC bias voltage applied. The impedance measurement was integrated over 10 seconds for each

frequency below 100Hz, in an attempt to average out low frequency noise sources such as building vibrations or AC power lines. The impedance measurement was integrated for 1 second at each frequency at and above 100Hz.

Chapter 7

CONCLUSION

Significant progress has been achieved in several areas, including gaining a better understanding of the self-assembly of peptide nanotubes, how to align these peptide nanotubes using various nanolithography techniques, the development of an impedance AFM for an Asylum Research platform, and the application of impedance AFM towards developing better biosensors and gaining a fundamental understanding of the electrical properties of individual nanoparticles.

The mechanism of peptide nanotube self assembly and formation as hypothesized was reinforced, while at the same time evidence was found that could lead to the discovery of alternative and complimentary methods of nanotube formation. In order to better understand the mechanism of tube formation, future experiments could be performed that are more quantitative in nature for determining nanotube yield. Further, attempts to self-assemble materials on patterned substrates could seed the growth of nanotubes into specific patterns. Computational chemistry studies could also provide clues as to how intermolecular hydrogen bonds form and strengthen the growing nanotubes.

The peptide nano-rings containing gold nanoparticles inside their cavities were aligned on dithiol SAMs patterned as an array by AFM-based nanolithography. The peptide nano-rings were self-assembled as lines on these SAMs, and gold nanoparticles inside the nanorings also formed lines with the spacing between these nanoparticles as the peptide nano-rings functioned as spacers. This type of fabrication will provide

improved tunability in their optical properties of resulting nanoparticle-assembled arrays. In addition, optimization of the inter-particle distance of nanoparticles in the array with various spacers may allow one to design new types of photonics with desired optical properties. However, for those optical applications, the stability and the rigidity of the nano-rings will be more desirable to be improved since some of the nano-rings were deformed during the self-assembly and this deformation caused the uneven spacing of the nanoparticles on the array. For realistic photonic applications, the nanoparticle assembly needs to be accomplished without deformation because they require the perfect alignment of nanoparticles with minimum defects. The additions of hydrogen-bonding functional groups or polymerizing groups to the monomer may increase the rigidity of the nano-rings, which may help overcome this problem.

A rapid, efficient, multiplexed peptide nanotube-based pathogen assay has been developed. A limit of detection for the technique has been determined by creating standard curves for several types of viruses, with a typical limit of detection on the order of 100 pfu/mL. Demonstration of the multiplex ability of the assay was performed as a proof of principle that the number of target pathogens that can be analyzed is as high as the number of photodetectors available on the flow cytometer being used. The versatility of this antibody-antigen interaction could allow other target analytes beyond pathogens, for example core-shell nanoparticles with biomarkers on the surface could be detected, sorted, and counted using this assay. The rapid visualization of the aggregates by fluorescence microscopy can also allow simple bench-top identification of the presence of target analytes. This assay clearly fills the pressing need to quantify in-tact whole virus both rapidly and sensitively, and in a multiplexed fashion.

Future directions for this project could include detection of small molecules with multiple binding sites: biotin/avidin pair would be best start, with well-known 4:1 ratio could provide excellent proof of principle. This approach could be applied to counting functionalized nanoparticles as well. It would be extremely beneficial to examine using non-symmetric nanotubes as scaffolds in order to achieve only sea-urchin structures. This provides a more direct measurement possibility by simply counting the number of sea-urchin structures and knowing that each structure contains only one virus, not requiring any averaging of the fluorescence intensity of large network structures. This could hopefully more control over the structures, as well as then allow biologists to use their popular sandwich-style assays to further amplify this assay. Further benefits could come from using more rigid nanotubes, and establishing better control over the size of the nanotubes in both diameter and in length. This could perhaps enable the next step of accurate single virus detection in up to one mL samples.

Significant progress has been achieved in the design and construction of an impedance AFM instrument in collaboration with Asylum Research. Electrically isolated paths from external instrumentation to the AFM tip and substrate have been constructed. Easy connection by BNC cables was designed into the system. Benefits of the sensored closed loop X, Y, and Z piezos made precise selection of particles possible. Methods of reproducible contact force were also derived, so as to minimize physical deformation of samples at the location of impedance spectra collection.

There are several future directions that could be undertaken for this biosensor project. One direction could include building a glove box around the AFM. Such an airtight chamber could allow gases with different dielectric constants and resitivities than

air to be exchanged. Studies could then be systematically performed to determine if the effects of the parasitic inductance and parasitic capacitance could be altered by having a different medium surrounding the nanoparticle. The effects of humidity could also be precisely controlled, and studies on the effects of humidity on impedance measurements could therefore be performed.

It is also possible to imagine making these measurements in liquid environments instead of in air. The use of liquids to provide a different dielectric constant in the surrounding medium than air could allow a broader sample size for the study. Some of the challenges potentially could include if the liquid is more conductive than the insulating sample under analysis, it is possible that short circuiting could occur. Also, consideration must be given to the liquids being used and any chemical or electrochemical reactions they could create with the sample. Further consideration must be given to the interaction of the liquids with the gaskets and seals in the fluid cell of the AFM, such that compatible chemicals are used so no seals are compromised. If such liquids could be found that overcome these obstacles, impedance measurements could be made in a liquid environment. Flow through experiments could then be performed where the height of the AFM tip is varied to see the effects on trapping particles between the tip and the substrate. Also, experiments to create a prototype biosensor using the AFM to detect the binding event of the virus between the AFM tip and the substrate could be performed.

Complimentary flow through experiments could be performed inspired by the work of Dr. Hamers from the University of Wisconsin-Madison. The work of Dr. Hamers used high frequency electric fields to align bacterial cells between electrodes

then used lower frequency AC bias signals to perform impedance measurements on the cells. This work could be applied to trapping viruses between the AFM tip and a substrate. This work would be greatly aided by the addition of a confocal fluorescent microscope to mount the base of the AFM on, so live video of the light microscopy images could be captured. One could use the GFP-mutant forms of HSV-1 and HSV-2 so viruses could be visualized by the light microscope, and the alignment of the viruses in the electric fields could be monitored. Calculation of different frequencies required to align particles of different sizes than bacterial cells would be required, and further optimization of experimental details like the frequency ranges to make the impedance measurements and the effects of making the impedance measurements in a liquid environment should also be considered.

When examining these flow-through types of experiments, fundamental studies on microfluidics could also be performed. These studies could be computational, perhaps using COMSOL Multiphysics, to predict the flow of virus particles through various channel shapes and with different liquid medium flow rates. This could lead towards better design and construction of the microfluidic cells that could incorporate detection of native virions in solution based on three levels of criteria (biological recognition, physical size, and electrical characterization by impedance spectroscopy). The effects of antibodies trapping the virions as they flow through various sized channels could be predicted, as well as how larger contaminating particles could potentially obstruct smaller channels designed to trap the smaller virions. By using the combinations of partial differential equations that COMSOL Multiphysics is excellent as solving, predictions could be made regarding the use of AC electric fields to dielectrophoretically separate

particles in microfluidic channels. Many of the challenges in the area of dielectrophoresis have been discussed in the scientific literature.

Other areas to improve the impedance AFM studies could include designing a better electrode substrate. Using an electrode that is approximately the size of the target nanoparticle, an outer electrode could be included that can act as a guard ring to shield against fringing effects on the electric field. This guard ring electrode would help to orient the field lines through the sample and up to the AFM tip in a more uniform fashion. Having a more uniform electric field could perhaps simplify the computational work required. Further reductions in computational work stem from the removal of the complicated point-plate capacitor model, and potential return to the well known parallel plate model. A more uniform electric field could also help to use the empty cell capacitance method of determining the dielectric constants of nanomaterials. If the empty cell capacitance varies as a function of the air gap between the electrodes in the cell, the ratio of the two capacitance values would be the ratio of the dielectric constants. Since the dielectric constant of air is known to be equal to one, this simple ratio can allow the determination of unknown dielectric constants. Such an experimental setup could be the first way to verify experimentally the theoretical calculations about changes in dielectric constants at the nanoscale.

A second benefit of having a small electrode shape with an outer guard ring electrode comes in a reduction in parasitic inductance and capacitance. The origin of the parasitic capacitance was the large area of the exposed conductive substrate underneath the cantilever leg. By eliminating this large area of substrate with a new electrode design, the parasitic capacitance should be either greatly reduced or eliminated entirely.

Another benefit of a smaller electrode design could apply to liquid mode impedance AFM measurements. If a small enough metal electrode surface could be fabricated that a bound virus could prevent short circuiting through the solvent, one could imagine a DC-bias be used to identify binding of virus by spike in resistance, then switch over to AC-bias to characterize impedance spectra.

If such an electrode could not be designed, ways of altering the parasitic capacitance could be achieved by different AFM cantilever selection. The AFM cantilevers used in this research were 125um x 35um. One way to reduce the parasitic capacitance would be by a reduction in the area of the parallel plates in the capacitor. This could be achieved by using a smaller cantilever. Conversely, one of the challenges to measuring high dielectric constant nanoparticles was the circuit model that estimated the highest measurable capacitance of a nanoparticle was dependent on the magnitude of the parasitic capacitance. In order to increase this parasitic capacitance, cantilevers such as the Mikromasch series 17 tips, over 400um x 35um, could allow slightly higher capacitance measurements. It could also be fruitful to discuss custom fabrication of tips with different AFM tip vendors. Tips that could have even longer and wider cantilevers, while still maintaining a spring constant that allowed reasonable tapping mode imaging, could potentially be fabricated.

Some suggestions that would be easy to perform experimentally for future directions of impedance AFM include adding layers of complexity to the virus measurements. By using an antibody functionalized AFM tip, the effects of the antibody layer could be determined on bare gold substrates before measuring viruses. Other ideas include using an antibody functionalized substrate and an unfunctionalized tip, or using

an antibody functionalized substrate with an antibody functionalized tip. The capacitance of this antibody layer could be characterized before addition of viruses. After addition of viruses, the removal of growth buffers and non-specifically bound cellular debris could be performed without the risk of losing the virions under investigation. This could provide a cleaner AFM topographical image, and less uncertainty about the effects of the residual growth buffers on the impedance measurements.

A quick, down and dirty experiment that could be performed includes a Freon extraction of the GFP mutant HSV-1 and HSV-2 and collection of the capsid impedance spectra. Observing any trends in the capacitance shifts could provide more clues on how the presence of GFP in the capsid affects the impedance spectra.

A more complex set of experiments could include comparing the force applied by the AFM tip and the effect on mechanical deformation of the sample and if there are any corresponding changes in the electrical or impedance properties. While the challenge lies in combining nanoindentation style experiments with impedance measurement experiments, the procedures required would still be relatively straightforward experimentally. By systematically varying the contact mode deflection setpoint, when engaging on a nanoparticle of interest the force applied by tip to the particle would be varied. Obtaining a topographical image after applying the force would allow a comparison between the before nanoindentation state and after nanoindentation state. Collection and comparison of impedance spectra could be performed at systematically varied contact forces to determine if there is any link between physical deformation and electrical properties. These studies of the size of the nanoindentation formation vs. the impedance spectra shift could also be paired with a complimentary set of experiments.

By using different materials with a different Young's Modulus, a comparison could be made between the Young's Modulus and the impedance among different materials.

Another down and dirty experiment could be the study of whether the tip height above a nanoparticle has any effect on the impedance measurement. If the field above an infinite plate is uniform, then the height of the point test charge above that plate does not affect the impedance or capacitance at the nanoscale since there is a uniform electric field above the plate. However, by inserting a spherical dielectric into this electric field, this field would no longer be uniform. It could be very informative to determine at what height above the nanoparticle a return to the "uniform" electric field would occur.

In the future, more sensitive current amplifiers may be developed. If this should happen, it could become possible to perform I-V curves and current mapping using traditional DC conductive AFM techniques. This could allow simpler methods of designing biosensors as well, since most hand-held devices are battery powered and therefore operate using DC circuitry.

Other studies this impedance AFM could excel at are analyses of microchips and nanochips. With the ever decreasing component size of circuit boards, having an accurate, precise nanopositioning system to bring a test probe into contact with specific areas of the circuit board could be useful in diagnosing failure points of a nanochip. By using the AFM to scan the surface of the chip and locate components of interest, the AFM probe could then be used to perform impedance analysis on specific regions of the circuitry. Alternatively, the AFM probe could be used as one of the test probes of a multimeter or any other electrical characterization device.

Studies of molecular electronics could benefit from the impedance AFM. By fabricating a self assembled monolayer, or SAM, of a molecular electronics candidate molecule, this material could be characterized electrically by the impedance AFM. The SAM could be on an electrode, or the SAM could be on a conductive nanoparticle such as a gold nanoparticle. Further considerations to study in molecular electronics would be the material of the AFM tip. The AFM tip could be coated with gold, platinum, tungsten, diamond-like carbon, or other conductive materials. Each material could have unique advantages and disadvantages when performing electrical characterization of molecular electronics molecule in terms of chemical reactivity with the molecule or contact resistance.

Using the concept of peptide SAMs on conductive nanoparticles could be a model system for studying changes in the envelope of a virus. Changing the peptide SAM on the conductive nanoparticle core could simulate changes in protein expression on the envelope. This model could also be used to simulate changes to the capsid proteins. Since the DNA core in the virion is likely conductive, the changes in protein expression in the capsid surrounding this conductive core could be simulated by changes in the peptide SAM around the conductive nanoparticle.

Impedance AFM studies would not have to be limited to viruses and nanoparticles. Characterization of cage molecules could shed light on the fundamental chemistry of these molecules. The electrical properties of these cage molecules both with and without molecules trapped inside could be studied. The information gathered in such studies of caged molecules could lead to new methods of data storage, if the presence or absence of such a trapped molecule could be recognized as a “1” or “0” data bit.

Alternatively, studies of cage molecules as drug delivery vehicles could show the before and after delivery relative concentrations of trapped drug molecules.

Other materials that could be studied by impedance spectroscopy include porphyrins layers. The metal ions that are trapped between porphyrins layers and their redox state could alter the electrical properties of the porphyrins film.

Still other materials to study by impedance AFM include live bacterial cells or eukaryotic cells. Changes *in vitro* in the expression of trans-membrane proteins could be studied. Alternatively, the AFM probe could be used to apply electric fields locally at various parts of the cell. One example could be applying an electrical bias at the axon of a neuron, or at the dendrite of a neuron, and comparing the biological and electrophysiological response of the neuronal cell.

Radio frequency electrical characterization could also be performed. The impedance AFM was designed as a versatile platform to allow exchange of external instrumentation designed for electrical characterization. If additional instruments were purchased that allowed the generation of radio frequency AC biases and the subsequent analysis of the modified signals, the impedance AFM could be used to characterize materials with radio frequency applications. Such applications could include cell phone transmitters or other signaling and receiving devices.

Point-by-point analysis was described in this work. However, impedance mapping should also be possible with appropriate instrumentation. If the sampling time for each impedance measurement is sufficiently fast, then impedance mapping is possible. The key challenge is the sample rate of the impedance instrument. As was described in the example with the phase analyzer in Chapter 5, low sample rates such as 3

Hz are prohibitive of impedance mapping. However, if a sample rate such as 128 Hz was possible, then a scan rate of 0.5 Hz would be possible during a 256 points per line scan.

In summary, this work increased fundamental scientific understanding in the areas of the self assembly of peptide nanotubes, the alignment of these nanotubes by nanolithography techniques, the design and development of an impedance AFM, and the implementation of using an impedance AFM to study electrical properties of individual nanoparticles that are insulators or dielectric materials as model systems for future virus biosensors.

REFERENCES:

1. Knipe, D.M., et al., *Fields Virology*. 4th ed. 2001. 3280.

2. Matsui, H. and B. Gologan, *Crystalline glycylglycine bolaamphiphile tubules and their pH-sensitive structural transformation.* Journal Of Physical Chemistry B, 2000. **104**(15): p. 3383-3386.

3. Matsui, H. and G.E. Douberly, *Organization of peptide nanotubes into macroscopic bundles.* Langmuir, 2001. **17**(25): p. 7918-7922.

4. Porrata, P., E. Goun, and H. Matsui, *Size-controlled self-assembly of peptide nanotubes using polycarbonate membranes as templates.* Chemistry Of Materials, 2002. **14**(10): p. 4378-4381.

5. Gao, X., et al., *Peptide Nanotubes: Simple Separation Using Size-Exclusion Columns and Use as Templates for Fabricating One-Dimensional Single Chains of Au Nanoparticles.* Advanced Materials, 2005. **17**(14): p. 1753-1757.

6. Gao, X. and H. Matsui, *Peptide-based nanotubes and their applications in bionanotechnology.* Advanced Materials (Weinheim, Germany), 2005. **17**(17): p. 2037-2050.

7. Matsui, H. and R. MacCuspie, *Metalloporphyrin nanotube fabrication using peptide nanotubes as templates.* Nano Letters, 2001. **1**(12): p. 671-675.

8. Matsui, H., S. Pan, and G.E. Douberly, *Fabrication of nanocrystal tube using peptide tubule as template and its application as signal-enhancing cuvette.* Journal Of Physical Chemistry B, 2001. **105**(9): p. 1683-1686.

9. Matsui, H., et al., *Bolaamphiphile nanotube-templated metallized wires.* Journal Of Physical Chemistry B, 2000. **104**(41): p. 9576-9579.

10. Djalali, R., Y. Chen, and H. Matsui, *Au nanowire fabrication from sequenced histidine-rich peptide.* Journal Of The American Chemical Society, 2002. **124**(46): p. 13660-13661.

11. Douberly, G.E., et al., *Fabrication of protein tubules: Immobilization of proteins on peptide tubules.* Journal Of Physical Chemistry B, 2001. **105**(32): p. 7612-7618.

12. Banerjee, I.A., L.T. Yu, and H. Matsui, *Location-specific biological functionalization on nanotubes: Attachment of proteins at the ends of nanotubes using Au nanocrystal masks.* Nano Letters, 2003. **3**(3): p. 283-287.

13. Matsui, H., P. Porrata, and G.E. Douberly, *Protein tubule immobilization on self-assembled monolayers on Au substrates.* Nano Letters, 2001. **1**(9): p. 461-464.

14. Matsui, H., et al., *Controlled immobilization of peptide nanotube-templated metallic wires on Au surfaces.* European Physical Journal D, 2001. **16**(1-3): p. 403-406.

15. Banerjee, I.A., L.T. Yu, and H. Matsui, *Application of host-guest chemistry in nanotube-based device fabrication: Photochemically controlled immobilization of azobenzene nanotubes on patterned alpha-CD monolayer/Au substrates via molecular recognition.* Journal Of The American Chemical Society, 2003. **125**(32): p. 9542-9543.

16. Chen, Y.F., et al., *Attachment of ferrocene nanotubes on beta-cyclodextrin self-assembled monolayers with molecular recognitions.* Langmuir, 2004. **20**(20): p. 8409-8413.

17. Yu, L.T., I.A. Banerjee, and H. Matsui, *Incorporation of sequenced peptides on nanotubes for Pt coating: smart control of nucleation and morphology via activation of metal binding sites on amino acids.* Journal Of Materials Chemistry, 2004. **14**(4): p. 739-743.

18. Djalali, R., Y.F. Chen, and H. Matsui, *Au nanocrystal growth on nanotubes controlled by conformations and charges of sequenced peptide templates.* Journal Of The American Chemical Society, 2003. **125**(19): p. 5873-5879.

19. Banerjee, I.A., L.T. Yu, and H. Matsui, *Cu nanocrystal growth on peptide nanotubes by biomineralization: Size control of Cu nanocrystals by tuning peptide conformation.* Proceedings Of The National Academy Of Sciences Of The United States Of America, 2003. **100**(25): p. 14678-14682.

20. Yu, L.T., I.A. Banerjee, and H. Matsui, *Direct growth of shape-controlled nanocrystals on nanotubes via biological recognition.* Journal Of The American Chemical Society, 2003. **125**(48): p. 14837-14840.

21. Yu, L.T., et al., *Size-controlled ni nanocrystal growth on peptide nanotubes and their magnetic properties.* Advanced Materials, 2004. **16**(8): p. 709-+.

22. Nuraje, N., et al., *Biological bottom-up assembly of antibody nanotubes on patterned antigen arrays.* Journal Of The American Chemical Society, 2004. **126**(26): p. 8088-8089.

23. Banerjee, I.A., et al., *Thiolated Peptide Nanotube Assembly as Arrays on Patterned Au Substrates.* Nano Lett., 2004. **4**(12): p. 2437-2440.

24. Disney, M.D., et al., *Detection of Bacteria with Carbohydrate-Functionalized Fluorescent Polymers.* J. Am. Chem. Soc., 2004. **126**: p. 13343-13346.

25. Medintz, I.L., et al., *Decoration of Discretely Immobilized Cowpea Mosaic Virus with Luminescent Quantum Dots.* Langmuir, 2005. **21**: p. 5501-5510.

26. Elkin, T., et al., *Immuno-Carbon Nanotubes and Recognition of Pathogens.* ChemBioChem, 2005. **6**: p. 640-643.

27. Patolsky, F., et al., *Electrical Detection of Single Viruses.* Proc. Natl. Acad. Sci. USA, 2004. **101**(39): p. 14017-14022.

28. Star, A., et al., *Electronic Detection of Specific Protein Binding Using Nanotube FET Devices.* Nano Lett., 2003. **3**(4): p. 459-463.

29. Biel, S.S. and H.R. Gelderblom, *Diagnostic Electron Microscopy is Still A Timely and Rewarding Method.* Journal of Clinical Virology, 1999. **13**(1-2): p. 105-119.

30. Kuznetsov, Y.G., et al., *Imaging of viruses by atomic force microscopy.* J. Gen. Virol., 2001. **82**: p. 2025-2034.

31. Nettikadan, S.R., et al., *Virus particle detection by solid phase immunocapture and atomic force microscopy.* Biochemical and Biophysical Research Communications, 2003. **311**: p. 540-545.

32. Givan, A., *Flow Cytometry: First Principles*. 2nd Edition ed. 2001, New York: Wiley-Liss.

33. Kellar, K.L. and M.A. Iannone, *Multiplexed microsphere-based flow cytometric assays.* Experimental Hematology, 2002. **30**(11): p. 1227-1237.

34. Rao, R.S., et al., *Comparison of Multiplexed Techniques for Detection of Bacterial and Viral Proteins.* Journal of Proteome Research, 2004. **3**: p. 736-742.

35. Yan, X., et al., *On the development of a microsphere-based multiplexed immunoassay for influenza virus typing and subtyping by flow cytometry.* International Congress Series, 2004. **1263**: p. 342-345.

36. McSharry, J.J., *Analysis of Virus-Infected Cells by Flow Cytometry.* Methods, 2000. **21**: p. 249-257.

37. Murray, C.B., C.R. Kagan, and M.G. Bawendi, *Synthesis and characterization of monodisperse nanocrystals and close-packed nanocrystal assemblies.* Annual Review of Materials Science, 2000. **30**: p. 545-610.

38. Yablonovitch, E., *Inhibited spontaneous emission in solid-state physics and electronics.* Physical Review Letters, 1987. **58**(20): p. 2059-2062.

39. Joannopoulos, J.D., P.R. Villeneuve, and S.H. Fan, *Photonic crystals: putting a new twist on light.* Nature, 1997. **386**(6621): p. 830.

40. Vlasov, Y.A., et al., *On-chip natural assembly of silicon photonic bandgap crystals.* Nature, 2001. **414**(6861): p. 289-293.

41. Murray, C.B., C.R. Kagan, and M.G. Bawendi, *Self-organization of CdSe nanocrystallites into three-dimensional quantum dot superlattices.* Science, 1995. **270**: p. 1335.

42. Colvin, V.L., *From opals to optics: Colloidal photonic crystals.* MRS Bull., 2001. **26**(8): p. 637-641.

43. Blanco, A., et al., *Large-scale synthesis of a silicon photonic crystal with a complete 3-dimensional bandgap near 1.5 micrometres.* Nature, 2000. **405**(6785): p. 437-440.

44. Lin, S.Y., et al., *A three-dimensional photonic crystal operating at infrared wavelengths.* Nature, 1998. **394**(6690): p. 251-253.

45. Liu, X., et al., *Arrays of magnetic nanoparticles patterned via "dip-pen" nanolithography.* Advanced Materials, 2002. **14**(3): p. 231-234.

46. Redl, F.X., et al., *Three-dimensional binary superlattices of magnetic nanocrystals and semiconductor quantum dots.* Nature, 2003. **423**(6943): p. 968-971.

47. Wonmok, L., et al., *Nanoparticle-mediated epitaxial assembly of colloidal crystals on patterned substrates.* Langmuir, 2004. **20**(13): p. 5262-5270.

48. Huang, J., et al., *Spontaneous formation of nanoparticle stripe patterns through dewetting.* Nature Materials, 2005. **4**(12): p. 896-900.

49. Kisailus, D., et al., *Functionalized gold nanoparticles mimic catalytic activity of a polysiloxane-synthesizing enzyme.* Advanced Materials, 2005. **17**(10): p. 1234-1239.

50. Brott, L.L., et al., *Ultrafast holographic nanopatterning of biocatalytically formed silica.* Nature, 2001. **413**(6853): p. 291-293.

51. Whitling, J.M., G. Spreitzer, and D.W. Wright, *A combinatorial and informatics approach to CdS nanoclusters.* Advanced Materials, 2000. **12**(18): p. 1377-1380.

52. Lee, S.-Y., et al., *Improved metal cluster deposition on a genetically engineered tobacco mosaic virus template.* Nanotechnology, 2005. **16**(7): p. 435-441.

53. Douglas, T. and M. Young, Advanced Materials, 1999. **11**(8): p. 679-681.

54. Chatterji, A., et al., *A Virus-Based Nanoblock with Tunable Electrostatic Properties.* Nano Lett., 2005. **5**(4): p. 597-602.

55. Walsh, D., et al., *Dextran templating for the synthesis of metallic and metal oxide sponges.* Nature Materials, 2003. **2**(6): p. 386-390.

56. Ken-Ichi, S., S. Hiroyuki, and S. Kiyotaka, *Specificity and biomineralization activities of Ti-binding peptide-1 (TBP-1).* Langmuir, 2005. **21**(7): p. 3090-3095.

57. Reches, M. and E. Gazit, *Casting Metal Nanowires Within Discrete Self-Assembled Peptide Nanotubes.* Science, 2003. **300**(5619): p. 625-627.

58. Lee, S.-W., et al., *Ordering of quantum dots using genetically engineered viruses.* Science, 2002. **296**(5569): p. 892-895.

59. Gao, X., et al., *Controlled Growth of Se Nanoparticles on Ag Nanoparticles in Different Ratios.* Advanced Materials, 2005. **17**(4): p. 426-429.

60. Deng, Z. and C. Mao, *DNA-Templated Fabrication of 1D Parallel and 2D Crossed Metallic Nanowire Arrays.* Nano Letters, 2003. **3**(11): p. 1545-1548.

61. Park, S.H., et al., Nano Lett., 2005. **5**(4): p. 693-696.

62. Sarikaya, M., et al., *Molecular biomimetics: nanotechnology through biology.* Nature Materials, 2003. **2**(9): p. 577-585.

63. Naik, R.R., et al., *Biomimetic synthesis and patterning of silver nanoparticles.* Nature Materials, 2002. **1**(3): p. 169-172.

64. Sumerel, J.L., et al., *Biocatalytically Templated Synthesis of Titanium Dioxide.* Chemistry of Materials, 2003. **15**(25): p. 4804-4809.

65. Banerjee Ipsita, A., L. Yu, and H. Matsui, *Room-temperature Wurtzite ZnS nanocrystal growth on Zn finger-like peptide nanotubes by controlling their unfolding peptide structures.* Journal of the American Chemical Society, 2005. **127**(46): p. 16002-3.

66. Coffman, E.A., et al., *Surface patterning of silica nanostructures using bio-inspired templates and directed synthesis.* Langmuir, 2004. **20**(20): p. 8431-8436.

67. Jin, S., et al., *Scalable Interconnection and Integration of Nanowire Devices without Registration.* Nano Lett., 2004. **4**(5): p. 915-919.

68. Long, D.P., J.L. Lazorcik, and R. Shashidhar, *Magnetically directed self-assembly of carbon nanotube devices.* Advanced Materials, 2004. **16**(9-10): p. 814-819.

69. Smith, P.A., et al., *Electric-field assisted assembly and alignment of metallic nanowires.* Applied Physics Letters, 2000. **77**(9): p. 1399-1401.

70. Chung, J., et al., *Toward large-scale integration of carbon nanotubes.* Langmuir, 2004. **20**(8): p. 3011-3017.

71. Huang, Y., et al., *Logic gates and computation from assembled nanowire building blocks.* Science, 2001. **294**(5545): p. 1313-1317.

72. Lay, M.D., J.P. Novak, and E.S. Snow, *Simple route to large-scale ordered arrays of liquid-deposited carbon nanotubes.* Nano Lett., 2004. **4**(4): p. 603-606.

73. Huang, L., S.J. Wind, and S.P. O'Brien, *Controlled Growth of Single-Walled Carbon Nanotubes from an Ordered Mesoporous Silica Template.* Nano Lett., 2003. **3**(3): p. 299-303.

74. Mbindyo, J.K.N., et al., *DNA-directed assembly of gold nanowires on complementary surfaces.* Advanced Materials, 2001. **13**(4): p. 249-254.

75. Braun, E., et al., *DNA-templated assembly and electrode attachment of a conducting silver wire.* Nature, 1998. **391**(6669): p. 775-778.

76. Rao, S.G., et al., *Nanotube electronics: large-scale assembly of carbon nanotubes.* Nature, 2003. **425**(6953): p. 36-37.

77. Caswell, K.K., et al., *Preferential end-to-end assembly of gold nanorods by biotin-streptavidin connectors.* Journal of the American Chemical Society, 2003. **125**(46): p. 13914-13915.

78. Wouters, D. and U.S. Schubert, *Nanolithography and nanochemistry: probe-related patterning techniques and chemical modification for nanometer-sized devices.* Angew. Chem., Intl. Ed. Engl., 2004. **43**(19): p. 2480-2495.

79. Liu, G.-Y., S. Xu, and Y. Qian, *Nanofabrication of Self-Assembled Monolayers Using Scanning Probe Lithography.* Accounts of Chemical Research, 2000. **33**(7): p. 457-466.

80. Ginger, D.S., H. Zhang, and C.A. Mirkin, *The evolution of dip-pen nanolithography.* Angewandte Chemie, International Edition, 2004. **43**(1): p. 30-35.

81. Zhong, Z., et al., *Nanowire Crossbar Arrays as Address Decoders for Integrated Nanosystems.* Science, 2003. **302**(5649): p. 1377-1380.

82. Chen, R.J., et al., *Noncovalent functionalization of carbon nanotubes for highly specific electronic biosensors.* Proc. Natl. Acad. Sci. USA, 2003. **100**(9): p. 4984-4989.

83. Fennimore, A.M., et al., *Rotational actuators based on carbon nanotubes.* Nature, 2003. **424**(6947): p. 408-410.

84. Qian, W., et al., *Icosahedral virus particles as addressable nanoscale building blocks.* Angewandte Chemie (International ed. in English), 2002. **41**(3): p. 459-462.

85. Mao, C., et al., *Virus-based toolkit for the directed synthesis of magnetic and semiconducting nanowires.* Science, 2004. **303**(5655): p. 213-217.

86. Slocik, J.M., J.T. Moore, and D.W. Wright, *Monoclonal Antibody Recognition of Histidine-Rich Peptide Encapsulated Nanoclusters.* Nano Letters, 2002. **2**(3): p. 169-173.

87. Douglas, T., et al., *Protein engineering of a viral cage for constrained nanomaterials synthesis.* Advanced Materials, 2002. **14**(6): p. 415-418.

88. Sano, K.-I. and K. Shiba, *A Hexapeptide Motif that Electrostatically Binds to the Surface of Titanium.* Journal of the American Chemical Society, 2003. **125**(47): p. 14234-14235.

89. Li, Z., et al., *Living templates for the hierarchical assembly of gold nanoparticles.* Angewandte Chemie, International Edition, 2003. **42**(20): p. 2306-2309.

90. Melosh, N.A., et al., *Ultrahigh-Density Nanowire Lattices and Circuits.* Science, 2003. **300**(5616): p. 112-115.

91. Javey, A., et al., *Ballistic carbon nanotube field-effect transistors.* Nature, 2003. **424**(6949): p. 654-657.

92. Layson, A., S. Gadad, and D. Teeters, *Resistance measurements at the nanoscale: scanning probe ac impedance spectroscopy.* Electrochimica Acta, 2003. **48**: p. 2207-2213.

93. Kalinin, S.V. and D.A. Bonnell, *Scanning impedance microscopy of an active Schottky barrier diode.* Journal of Applied Physics, 2002. **91**(2): p. 832-839.

94. Shao, R., S.V. Kalinin, and D.A. Bonnell, *Local impedance imaging and spectroscopy of polycrystalline ZnO using contact atomic force microscopy.* Applied Physics Letters, 2003. **82**(12): p. 1869-1871.

95. Beck, J.D., et al., *Manipulation and Real-Time Electrical Detection of Individual Bacterial Cells at Electrode Junctions: A Model for Assembly of Nanoscale Biosystems.* Nano Lett., 2005. **5**(4): p. 777-781.

96. O'Hayre, R., et al., *Quantitative impedance measurement using atomic force microscopy.* Journal of Applied Physics, 2004. **96**(6): p. 3540-3549.

97. O'Hayre, R., M. Lee, and F.B. Prinz, *Ionic and electronic impedance imaging using atomic force microscopy.* Journal of Applied Physics, 2004. **95**(12): p. 8382-8392.

98. Pingree, L.S.C., et al., *Nanoscale Impedance Microscopy - A Characterization Tool for Nanoelctronic Devices and Circuits.* IEEE Transactions on Nanotechnology, 2005. **4**(2): p. 255-259.

99. Cherniavskaya, O., et al., *Quantitative Noncontact Electrostatic Force Imaging of Nanocrystal Polarizability.* J. Phys. Chem. B, 2003. **107**: p. 1525-1531.

100. Sacha, G.M., et al., *Effective tip radius in electrostatic force microscopy.* Applied Physics Letters, 2005. **86**(12): p. 123101/1-123101/3.

101. Gordon, M.J. and T. Baron, *Amplitude-mode electrostatic force microscopy in UHV: Quantification of nanocrystal charge storage.* Laboratoire des Technologies de la Microelectronique, 2005. **72**(16): p. 165420/1-165420/14.

102. Kalinin, S.V., *Nanoscale electric phenomena at oxide surfaces and interfaces by scanning probe microscopy*. 2002. p. 448 pp.

103. Nam, J.-M., C.S. Thaxton, and C.A. Mirkin, *Nanoparticle-based bio-bar codes for the ultrasensitive detection of proteins.* Science, 2003. **301**: p. 1884-1886.

104. Shimizu, T., M. Kogiso, and M. Masuda, *Vesicle assembly in microtubes.* Nature, 1996. **383**(6600): p. 487-488.

105. Djalali, R., J. Samson, and H. Matsui, *Doughnut-shaped peptide nano-assemblies and their applications as nanoreactors.* Journal Of The American Chemical Society, 2004. **126**(25): p. 7935-7939.

106. Kogiso, M., et al., Langmuir, 1998. **14**: p. 4978.

107. Lee, K.-B., J.-H. Lim, and C.A. Mirkin, J. AM. CHEM. SOC., 2003. **125**: p. 5588.

108. Liu, G.-Y. and N.A. Amro, Proc. Natl. Acad. Sci. USA, 2002. **99**: p. 5165.

109. Frey, B.L. and R.M. Corn, Anal. Chem., 1996. **68**: p. 3187-3193.

110. Patel, N., et al., Langmuir, 1997. **13**: p. 6485-6490.

111. Ben-Joseph, E.P., S. Dowshen, and J. Klein. *Adenovirus*. August 2003 [cited 2006 07/17/06]; Available from: http://www.kidshealth.org/parent/infections/lung/adenovirus.html.

112. *Simian Virus 40 (SV40), Polio Vaccine, and Cancer*. April 22, 2004 [cited 2006 07/17/06]; Available from: http://www.cdc.gov/nip/vacsafe/concerns/cancer/default.htm.

113. Cicala, C., F. Pompetti, and M. Carbone, *SV40 induces mesotheliomas in hamsters.* The American journal of pathology, 1993. **142**(5): p. 1524-33.

114. Carbone, M., et al., *New molecular and epidemiological issues in mesothelioma: role of SV40.* Journal of Cellular Physiology, 1999. **180**(2): p. 167-172.

115. Jasani, B., et al., *Association of SV40 with human tumours.* Seminars in Cancer Biology, 2001. **11**(1): p. 49-61.

116. *Avian Influenza (Bird Flu)*. November 18, 2005 [cited 2006 07/17/06]; Available from: http://www.cdc.gov/flu/avian/gen-info/flu-viruses.htm.

117. Ali, S.H. and J.A. DeCaprio, *Cellular transformation by SV40 large T antigen: interaction with host proteins.* Seminars in Cancer Biology, 2001. **11**(1): p. 15-22.

118. Yang, C.-S., et al., *Simian virus 40 small t antigen mediates conformation-dependent transfer of protein phosphatase 2A onto the androgen receptor.* Molecular and Cellular Biology, 2005. **25**(4): p. 1298-1308.

119. *SV40 T-antigen antibody [PAb416] (ab16879) datasheet*. 2006 [cited 07/17/2006]; Available from: http://www.abcam.com/index.html?datasheet=16879.

120. *SV40 T-antigen antibody [PAb419] (ab16848) datasheet*. 2006 [cited 2006 07/17/06]; Available from: http://www.abcam.com/index.html?datasheet=16848.

121. Krause, P.R., et al., *Expression of the herpes simplex virus type 2 latency-associated transcript enhances spontaneous reactivation of genital herpes in latenly infected guinea pigs.* J. Exp. Med., 1995. **181**(1): p. 297-306.

122. Shin, J., et al., *Nonlinear transport imaging by scanning impedance microscopy.* Applied Physics Letters, 2004. **85**(18): p. 4240-4242.

123. Kalinin, S.V. and D.A. Bonnell, *Scanning impedance microscopy of electroactive interfaces.* Applied Physics Letters, 2001. **78**(9): p. 1306-1308.

124. Kalinin, S.V., R. Shao, and D.A. Bonnell, *Local Phenomena in Oxides by Advanced Scanning Probe Microscopy.* J. Am. Ceram. Soc., 2005. **88**(5): p. 1077-1098.

125. Kalinin, S.V., et al., *Potential and Impedance Imaging of Polycrystalline BiFeO3 Ceramics.* J. Am. Ceram. Soc., 2002. **85**(12): p. 3011-3017.

126. Staii, C., et al., *High Frequency Scanning Gate Microscopy and Local Memory Effect of Carbon Nanotube Transistors.* Nano Lett., 2005. **5**(5): p. 893-896.

127. Kalinin, S.V., et al., *Scanning probe microscopy imaging of frequency dependent electrical transport through carbon nanotube networks in polymers.* Nanotechnology, 2004. **15**: p. 907-912.

128. Kalinin, S.V., et al., *Tip-gating effect in scanning impedance microscopy of nanoelectronic devices.* Applied Physics Letters, 2002. **81**(27): p. 5219-5221.

129. Griffiths, D.J., *Introduction to Electrodynamics*. Third ed. 1999, Upper Saddle River, New Jersey: Prentice Hall. 562.

130. *Mikromasch Series 15 Datasheet*. [cited 2006 07/17/06]; Available from: http://www.spmtips.com/nsc15/ti-pt.

131. Katz, U. and I. Willner, Electronanalysis, 2003. **15**: p. 913.

132. Ingram, R.S., et al., Journal of the American Chemical Society, 1997. **119**: p. 9297.

133. Chen, S., et al., Science, 1998. **280**: p. 2098.

134. Guo, M., et al., *Monitoring of cell growth and assessment of cytotoxicity using electrochemical impedance spectroscopy.* Biochimica et Biophysica Acta, General Subjects, 2006. **1760**(3): p. 432-439.

135. Arnott, J.B., G.J. Browning, and S.W. Donne, *Study on Manganese Dioxide Discharge Using Electrochemical Impedance Spectroscopy.* Journal of the Electrochemical Society, 2006. **153**(7): p. A1332-A1340.

136. Adachi, M., et al., *Determination of Parameters of Electron Transport in Dye-Sensitized Solar Cells Using Electrochemical Impedance Spectroscopy.* Journal of Physical Chemistry B, 2006. **110**(28): p. 13872-13880.

137. Park, S.-M., et al., *Novel instrumentation in electrochemical impedance spectroscopy and a full description of an electrochemical system.* Pure and Applied Chemistry, 2006. **78**(5): p. 1069-1080.

138. Hu, C., S. Yuan, and S. Hu, *Studies on electrochemical properties of MWNTs-Nafion composite films based on the redox behavior of incorporated Eu3+ by voltammetry and electrochemical impedance spectroscopy.* Electrochimica Acta, 2006. **51**(15): p. 3013-3021.

139. Campuzano, S., et al., *Characterization of alkanethiol-self-assembled monolayers-modified gold electrodes by electrochemical impedance spectroscopy.* Journal of Electroanalytical Chemistry, 2006. **586**(1): p. 112-121.

140. Ragoisha, G.A. and A.S. Bondarenko, *Potentiodynamic electrochemical impedance spectroscopy.* Electrochimica Acta, 2005. **50**(7-8): p. 1553-1563.

141. Pan, S. and L. Rothberg, *Chemical control of electrode functionalization for detection of DNA hybridization by electrochemical impedance spectroscopy.* Langmuir, 2005. **21**(3): p. 1022-1027.

142. Zou, B., et al., *Self-Assembly of Crosslinked DNA-Gold Nanoparticle Layers Visualized by In-Situ Scanning Force Microscopy.* Advanced Materials, 2005. **17**: p. 1643-1647.

143. Jones, C.E., J.V. Macpherson, and P.R. Unwin, *In Situ Observation of the Surface Processes Involved in Dissolution from the (010) Surface of Potassium*

Ferrocyanide Trihydrate in Aqueous Solution Using an Integrated Electrochemical-Atomic Force Microscope. J. Phys. Chem. B, 2000. **104**: p. 2351-2359.

144. Macpherson, J.V., et al., *In-Situ Imaging of Ionic Crystal Dissolution Using an Integrated Electrochemical/AFM Probe.* Journal of the American Chemical Society, 1996. **118**: p. 6445-6452.

145. *Dielectric Constants of Materials*. 2006: http://www.clippercontrols.com/info/dielectric_constants.html.

146. *EIS Primer*. [cited 2006 07/17/06]; Available from: http://www.gamry.com/App_Notes/EIS_Primer/EIS_Primer.htm.

147. Horowitz, P. and W. Hill, *The Art of Electronics, 2nd Edition*. 2nd ed. 1989, New York, NY: Cambridge University Press. 1125.

148. Choi, E.H., et al., *Genetic heterogeneity of the hexon gene of adenovirus type 3 over a 9-year period in Korea.* Journal of Medical Virology, 2006. **78**(3): p. 379-383.

149. De Clercq, E., *Antivirals and antiviral strategies.* Nature Reviews Microbiology, 2004. **2**(9): p. 704-720.

150. Traore, O., et al., *Reverse Transcriptase PCR Detection of Astrovirus, Hepatitis A Virus, and Poliovirus in Experimentally Contaminated Mussels: Comparison of Several Extraction and Concentration Methods.* Applied and Environmental Microbiology, 1998. **64**(8): p. 3118-3122.

151. Enquist, L.W., et al., *Directional spread of an a-herpesvirus in the nervous system.* Veterinary Microbiology, 2002. **2266**: p. 1-12.

152. Ormo, M., et al., *Crystal structure of the Aequorea victoria green fluorescent protein.* Science, 1996. **273**: p. 1392-1395.

153. Brinker, C.J. and G.W. Sherer, *Sol-Gel Science: The Physics and Chemistry of Sol-Gel Processing*. 1989, San Diego: Academic Press.